

Element-specific Characterization of Magnetocaloric $\text{La}(\text{Fe}, \text{Si})_{13}$ -based Compounds

Der Fakultät für Physik der Universität Duisburg-Essen
zur Erlangung des akademischen Grades eines Doktors der
Naturwissenschaften (Dr. rer. nat.) vorgelegte Dissertation von

Alexandra Terwey

aus Köln

2019

Tag der Einreichung: 21.03.2019

Tag der mündlichen Prüfung: 09.07.2019

Referent: Prof. Dr. Heiko Wende (Universität Duisburg-Essen)

Korreferent: Prof. Dr. Andreas Hütten (Universität Bielefeld)

DuEPublico

Duisburg-Essen Publications online

UNIVERSITÄT
DUISBURG
ESSEN

Offen im Denken

ub | universitäts
bibliothek

Diese Dissertation wird über DuEPublico, dem Dokumenten- und Publikationsserver der Universität Duisburg-Essen, zur Verfügung gestellt und liegt auch als Print-Version vor.

DOI: 10.17185/duepublico/70612

URN: urn:nbn:de:hbz:464-20191017-150743-8

Alle Rechte vorbehalten.

Abstract

This thesis focuses on the element-specific contributions to the magnetocaloric effect in La(Fe,Si)₁₃-based compounds in dependence on Mn doping and interstitial hydrogenation. By utilizing nuclear resonant inelastic X-ray scattering (NRIXS), the local Fe-partial vibrational (phonon) density of states and thermodynamics were evaluated across the metamagnetic phase transition, which is the source of the magnetocaloric effect in this material class. The change in the vibrational entropy cooperatively contributes to the overall entropy change across the first order phase transition, which is rooted in strong electron-phonon coupling. An anomalous lattice softening by heating through the transition from the ferro- to paramagnetic state is present. The experimental data is then compared to first-principles calculations. The introduction of Mn results in a strong suppression of the entropy increase upon heating from the ferro- to paramagnetic phase. Combining X-ray magnetic circular dichroism (XMCD) measurements at the Fe K- and La L_{2,3}-edges with ⁵⁷Fe Mössbauer spectroscopy made it possible to identify the local element-specific magnetism of the Fe and La atoms in the compound depending on temperature and Mn content. An induced La magnetic moment, coupled antiparallel to the iron magnetic moment and a significant reduction in the Fe moment by increasing Mn doping is found due to hybridization between the Fe 3*d* and Mn 3*d*-states, altering the electronic structure. With rising Mn content, the spin frustration in the system drastically increases, partaking in the reduction of the Fe magnetic moment through increasing antiferromagnetic coupling between Fe and Mn. Due to strong hybridization between Fe and Mn, as well as through increase in temperature, the spectral shape of the X-ray absorption edges are strongly altered. Measuring the extended X-ray absorption fine structure (EXAFS) with rising Mn content indicates changes in the local geometry and electronic structure at the La L₃- and the Fe K-edges. Due to an isostructural volume decrease upon the phase transition upon heating from the ferro- to paramagnetic state, EXAFS revealed contractions of the next neighbor distances. An increase in Mn content results in a rising static part of the relative mean square atomic displacement which contributes to the reduction of the Fe moment and an alteration of the long range order. Hydrogenation affects the short range order, expanding the next neighbor distances. EXAFS, modeled by *ab-initio* multiple scattering calculations are compared to the experiments. The combined approach of element-specific characterization methods reveals a strong interplay between the various microscopic degrees of freedom in the system, which contribute to the thermodynamic behavior of La(Fe,Si)₁₃-based compounds.

Kurzfassung

Der Fokus dieser Arbeit liegt auf den element-spezifischen Beiträgen zum magnetokalorischen Effekt in $\text{La}(\text{Fe},\text{Si})_{13}$ Legierungen in Abhängigkeit von Mangan und Wasserstoffbeladung. Mithilfe von kernresonanter inelastischer Röntgenstreuung wurden die lokalen, von Fe getragenen Phononen-Zustandsdichten und thermodynamischen Eigenschaften über den metamagnetischen Phasenübergang hinweg untersucht, welcher die Ursache für den magnetokalorischen Effekt in diesen Materialien ist. Die Änderung der Vibrationsentropie trägt kooperativ zur gesamten Entropieänderung am Phasenübergang erster Ordnung bei und basiert auf starker Elektron-Phonon Kopplung. Eine anomale Gitteraufweichung beim Heizen von ferro- zu paramagnetischer Phase wird beobachtet. Die experimentellen Ergebnisse werden hierbei mit Ergebnissen aus der Dichtefunktionaltheorie verglichen. Das Einbringen von Mn in das System reduziert den Anstieg der Entropie beim Heizen von der para- zur ferromagnetischen Phase drastisch. Mithilfe der Kombination aus Röntgenzirkulardichroismus-Messungen an den Fe K- und La $L_{2,3}$ -Kanten und ^{57}Fe Mössbauer-Spektroskopie kann der lokale element-spezifische Magnetismus in den Fe und La Atomen in den Legierungen in Abhängigkeit von steigendem Gehalt an Mn quantifiziert werden. Ein induziertes La Moment, welches sich antiparallel zu dem Fe-Moment ausrichtet und eine starke Reduktion im Fe Moment ist sichtbar durch steigende Mn-Dotierung, welche durch die Änderung der elektronischen Struktur durch Hybridisierung der Fe und Mn $3d$ -Zustände hervorgeht. Mit steigendem Mn Gehalt erhöht sich die Spin-Frustration in dem Probensystem, welche zur Reduktion des Fe Momentes durch antiferromagnetische Kopplung zwischen Fe und Mn beiträgt. Durch die starke Hybridisierung zwischen Fe und Mn und durch Temperaturänderung, wird die spektrale Form der Röntgenabsorptionskanten stark verändert. Messungen der kantenfernen Röntgenabsorptionsfeinstruktur als Funktion des Mn-Gehaltes geben Aufschluss über die lokale Geometrie und elektronische Struktur an der La L_3 - und der Fe K-Kante. Aus der isostrukturellen Volumenreduktion beim Aufheizen durch den Phasenübergang vom ferromagnetischen zu paramagnetischem Zustand können nächste Nachbarabstände extrahiert werden. Erhöhung der Mn-Dotierung verursacht eine Erhöhung in der relativen statischen mittleren quadratischen Verschiebung der Atome, welche zur Reduktion des magnetischen Momentes an Fe beiträgt und eine Beeinflussung der Fernordnung hervorruft. Wasserstoffbeladung verändert die Nahordnung und vergrößert die nächsten Nachbarabstände. Ergänzende *ab-initio* Berechnungen der Feinstruktur werden mit den experimentellen Ergebnissen verglichen. Die Kombination aus diversen element-spezifischen Messmethoden zeigt eine starke Korrelation der mikroskopischen Freiheitsgrade, welche gemeinsam zum thermodynamischen Verhalten in $\text{La}(\text{Fe},\text{Si})_{13}$ Legierungen beitragen.

Contents

1. Introduction	7
2. Fundamentals and Theory	9
2.1. The Magnetocaloric Effect and the Thermodynamic Fundamentals	9
2.2. Magnetic Interactions	14
2.3. Sample System $\text{La}(\text{Fe},\text{Si})_{13}$	15
2.4. Interaction of X-rays and Matter	18
2.4.1. X-ray Magnetic Circular Dichroism	20
2.4.2. Extended X-ray Absorption Fine Structure	23
2.5. The Mössbauer Effect	25
2.6. Nuclear Resonant Inelastic X-ray Scattering	30
3. Experimental Methods	35
3.1. Synchrotron Radiation	35
3.2. X-ray Absorption Spectroscopy	37
3.2.1. X-ray Magnetic Circular Dichroism	37
3.2.2. Extended X-ray Absorption Near Edge Structure	38
3.3. Nuclear Resonant Inelastic X-ray Scattering	39
3.4. Mössbauer Spectroscopy	40
4. Sample Preparation and Characterization	43
5. Experimental Results and Discussion	51
5.1. ^{57}Fe NRIXS on Hydrogenated and Mn Doped $\text{La}(\text{Fe},\text{Si})_{13}$	51
5.1.1. Impact of Hydrogenation and Mn Addition on the VDOS and Thermodynamics in $\text{La}(\text{Fe},\text{Si})_{13}$	51
5.1.2. Effect of Hydrogenation - Comparison with DFT Calculations	69
5.1.3. Conclusion	75
5.2. Local Magnetism in Mn Doped $\text{La}(\text{Fe},\text{Si})_{13}$ -compounds	77
5.2.1. Temperature Dependence of the XMCD of $\text{La}(\text{Fe},\text{Si})_{13}$	77
5.2.2. Influence of Mn Doping on the XMCD of $\text{La}(\text{Fe},\text{Si},\text{Mn})_{13}$	82
5.2.3. Local Magnetism of La Probed at the $L_{2,3}$ -edges	87

5.2.4. Conclusion	100
5.3. Changes in Local Geometry by Mn Doping and Hydrogenation	101
5.3.1. EXAFS and Fourier Transform of $\text{LaFe}_{11.6-x}\text{Si}_{1.4}\text{Mn}_x$	103
5.3.2. Effect of Temperature on the Local Geometry	105
5.3.3. Element-specific Changes through Mn Doping	108
5.3.4. Element-specific Changes through Hydrogenation	111
5.3.5. Theoretical Modeling by FEFF	112
5.3.6. Data Fits and Local Geometry	118
5.3.7. Conclusion	131
5.4. Mössbauer Spectroscopy on $\text{La}(\text{Fe},\text{Si},\text{Mn})_{13}$	133
5.4.1. Magnetic Phase Transitions	133
5.4.2. Changes in Fe Local Magnetic Moment	136
5.4.3. Evolution of Spin Frustration	145
5.5. Conclusion	149
6. Conclusion and Outlook	151
A. Appendix	155
A.1. Magnetometry	155
A.2. Determination of the α -Fe Content	155
A.3. Correction of the α -Fe Content at the Fe K-edge EXAFS	156
A.4. NRIXS - Data Evaluation	157
A.5. Thermodynamic Properties in Hydrogenated and Mn Doped $\text{La}(\text{Fe},\text{Si})_{13}$	160
A.6. XMCD Background Correction	165
A.7. Sum Rule Analysis of High Field XMCD	165
A.8. Canting Angle	168
A.9. Center Line Shift and Quadrupole Splitting	171
A.10.FEFF Code	172
Bibliography	173
List of Figures	185
List of Tables	189
Acknowledgements	193

1. Introduction

With rising global temperatures as a result of global warming, the demand for cooling constantly increases. In 2016, 14 % of the worldwide energy consumption was accounted for cooling applications and extrapolation predicted the worldwide energy demand to rise significantly within the next 30 years [1, 2]. Especially refrigeration and air conditioning are two of the main applications, which are correlated with increasing numbers in population and fast growing economies. To accommodate as many people as possible with refrigeration and cooling, it is a necessity to find environmentally friendly alternatives to conventional gas-vapor compression techniques. Cooling is not only a commodity but needed for the maintenance of life quality, pharmaceutical storage and food safety [3]. Solid state refrigeration concepts provide new perspectives in terms of cooling, which are less hazardous, more ecologically friendly and potentially more energy efficient than conventionally used gas-vapour compression techniques [4, 5]. As potential new candidates for solid state refrigeration, air conditioning and thermomagnetic energy conversion, magnetocaloric materials have been found to be a useful class of materials [6–15]. Especially the possibility of upscaling production processes provides a broad range of opportunities for magnetocaloric materials. Until today a broad variety of materials have been found that possess a magnetocaloric effect and can potentially be used for applications.

The requirements for these materials are

- high adiabatic temperature change
- large change in the isothermal entropy
- low Debye temperature and specific heat
- working at room temperature
- small hysteresis
- easy to process, mechanically stable under cycling
- non toxic and not environmentally hazardous
- high abundance, cost effective

First observed in 1917 by Weiss and Piccard [16], the magnetocaloric effect has since then been found and studied in a broad range of materials. The use of the paramagnetic salt $\text{Gd}_2(\text{SO}_4)_3 \cdot 8\text{H}_2\text{O}$ made it possible to reach sub K temperatures by Giauque et al. [17, 18], resulting in the Nobel prize for chemistry in 1949. Since then, magnetocaloric materials have been a broad field of research and their potential user application has put many novel materials into the focus of current research. From functioning demonstrators to novel consumer applications [19], magnetocaloric materials already have their application and are commercially available [20]. Within this class of materials, especially $\text{LaFe}_{13-x}\text{Si}_x$ -based compounds stand out. These materials achieve a large magnetocaloric effect and offer the ability to be tailored specifically to temperature ranges as needed, such as functioning at room temperature, which makes it a perfect candidate to be utilized for possible user applications [21–27].

Within this thesis the effect of hydrogenation on the lattice dynamics and thermodynamic properties of $\text{LaFe}_{13-x}\text{Si}_x$ -based compounds will be illustrated by means of temperature dependent ^{57}Fe nuclear resonant inelastic X-ray scattering (NRIXS) and compared to corresponding first principles calculations. Additionally, also the effect of small amounts of Mn doping on the lattice dynamics will be discussed. The second part of the thesis will deal with the effect of Mn doping on the local magnetic properties. This has been studied by means of X-ray magnetic circular dichroism (XMCD) for varying Mn concentrations. The structural and geometric changes across the phase transition through Mn addition and hydrogenation, viewed from a local perspective, have been investigated using extended X-ray absorption fine structure measurements (EXAFS). Furthermore, the local magnetic properties have been studied by means of Mössbauer spectroscopy, the results of which were then cross-correlated with the results from the XMCD measurements. In the end a conclusion will be given.

2. Fundamentals and Theory

2.1. The Magnetocaloric Effect and the Thermodynamic Fundamentals

Magnetocaloric materials are usually characterized by a significant adiabatic temperature change $|\Delta T_{\text{ad}}|$ induced by magnetic fields and a large isothermal entropy change $|\Delta S_{\text{iso}}|$. At the phase transition temperature, T_{tr} , a structural first-order phase transition is accompanied by a drastic volume change, which is associated with a change in the magnetic state [4, 9, 26–28]. Figure 2.1 shows the schematic representation of a magnetocaloric cooling cycle. The magnetocaloric material starts at an ambient temperature T in a magnetically disordered paramagnetic state. The application of a magnetic field, still under adiabatic conditions, aligns the magnetic subsystem through the field and increases the temperature. This consequently results in a reduction of the magnetic entropy as the total entropy must stay constant. The reduction in the magnetic entropy is accompanied by an increase in the lattice entropy, the phonon subsystem, which results in heating of the material. If the material is surrounded by an exchange fluid, the heat can be transported away from the material until the initial temperature is reached again. Removal of the magnetic field now increases the magnetic entropy as the magnetic moments are not aligned anymore and magnetic disorder is introduced again. This leads to a subsequent cooling of the material as the lattice entropy compensates the increase of the magnetic entropy. An exchange fluid can be now used to absorb heat and the magnetocaloric material reaches the initial temperature again, starting another cooling cycle as described before.

This reversible temperature change in a material is called the magnetocaloric effect (MCE). To explain this effect, one has to have a look at the temperature dependent behavior of magnetic materials. The transition of a ferromagnetic material from its magnetically ordered ferromagnetic to the paramagnetic state, where the magnetic moments are randomly ordered, takes place at the Curie Temperature. This temperature dependent demagnetization can be described as a pure magnetic second order phase transition, which makes every magnetic material intrinsically magnetocaloric. To understand this

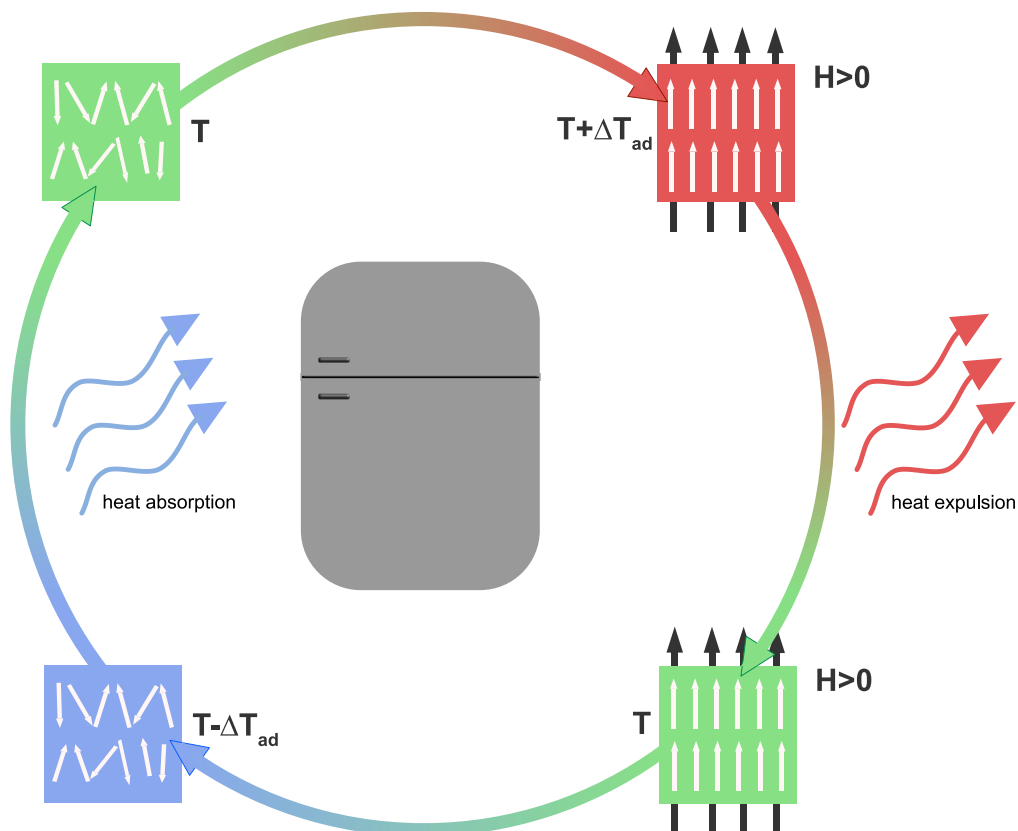


Figure 2.1.: Schematic depiction of a magnetocaloric cooling cycle under adiabatic conditions. The cycle starts at the top left at an ambient temperature T (green) without applied field. Refrigeration scheme adapted from [29].

effect it is important to have a look at the underlying thermodynamic principles.

The magnetocaloric effect has its fundamentals in the inner energy U . In a simple picture, the MCE can be described as the absorption and emission of heat when a magnetocaloric material is under the influence of an external magnetic field. Applying an external magnetic field, $\mu_0 H$, results in heating of the material. Removal of the field leads to cooling. The inner energy U is hereby dependent on the entropy S , the volume V and the magnetization M , or a magnetic field H , respectively. From this relation, the adiabatic temperature change and the change in the isothermal energy can be directly derived from the Gibbs free energy G . In a magnetic material G has the form

$$G = U - TS + pV - M\mu_0 H. \quad (2.1)$$

It is dependent on the intensive variables of the temperature T , the magnetic field H and

the pressure p . By differentiating the total free energy term, the entropy can be derived

$$dG = V dp - S dT - M \mu_0 dH. \quad (2.2)$$

In case of constant pressure, the total entropy can now be written as

$$S(T, H) = - \left(\frac{\partial G}{\partial T} \right)_H. \quad (2.3)$$

For the magnetic moment, which is the partial derivative of the free energy term under isothermal conditions and a constant magnetic field, we get the following expression

$$\mu_0 M(T, H) = - \left(\frac{\partial G}{\partial H} \right)_T. \quad (2.4)$$

With these equations, the Maxwell relations can be constructed as follows

$$\left(\frac{\partial S}{\partial H} \right)_T = \mu_0 \left(\frac{\partial M}{\partial T} \right)_H, \quad (2.5)$$

$$\Delta S_T(T, H) = \mu_0 \int_0^H \left(\frac{\partial M}{\partial T} \right)_H dH. \quad (2.6)$$

In a thermodynamic adiabatic system, the material changes its temperature by application of an external magnetic field. The change can be calculated from the entropy relation in Equation 2.6 with the specific heat capacity C_p

$$\Delta T_{ad}(T, H) = \mu_0 \int_0^H \frac{T}{C_p} \left(\frac{\partial M}{\partial T} \right)_H dH. \quad (2.7)$$

The relations above describe the thermodynamic principles, which are needed to explain the phase transition and are described in detail elsewhere [26]. Figure 2.2 (a) depicts a regular second order phase transition (SOPT). Heating of a magnetic material results in a stronger decrease of the magnetization when no magnetic field is applied. Below the critical temperature, the Curie temperature T_C , the magnetization decreases with increasing temperature until the Curie temperature is reached and $M(T)$ shows, according to mean-field theory, Brillouin-like behavior [30]. When $T = T_C$, the magnetic order breaks down and the sample is in a paramagnetic state. Above T_C , the magnetic susceptibility will follow the Curie-Weiss law, $\chi = \frac{M}{H} = \frac{C}{T-T_C}$. By application of an external field, the moments in the material are partially aligned, which leads to a slight stabilization of the ferromagnetic phase. The partial alignment results in a broadening of the transition which spans over a larger temperature range and the Curie temperature is shifted to a higher temperature. As the application of an external magnetic field stabilizes the magnetic

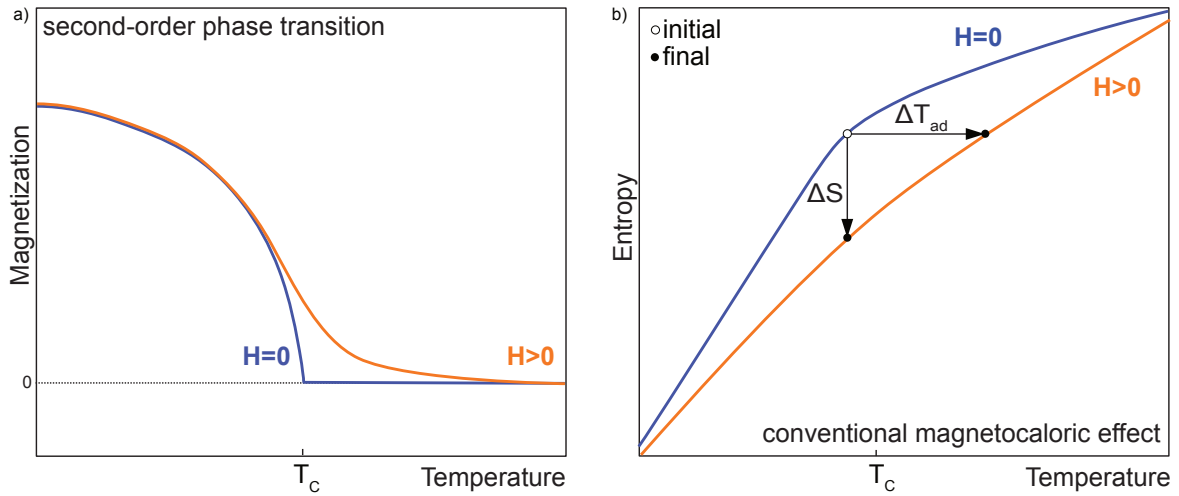


Figure 2.2.: Schematic sketch of a second order phase transition as found in magnetic materials. Depicted are (a) the temperature dependent evolution of the magnetization, with (orange line) and without (blue line) an applied magnetic field and (b) the entropy over temperature. Figure adapted from [32].

order, it consequently reduces the magnetic entropy in the material. In an isothermal system, the magnetic entropy can be changed through application of an external magnetic field as depicted in Figure 2.2 (b). Under adiabatic conditions, where the entropy is kept constant, the field application results in the adiabatic temperature change, as the lattice entropy has to counteract the decrease in magnetic entropy [26, 31]. Many magnetocaloric materials show a first order phase transition (FOPT). The temperature dependence of such a phase transition as a function of temperature is shown in Figure 2.3 for the magnetization (a) and the entropy (b). In materials that inhibit a conventional magnetocaloric effect, the magnetism breaks down abruptly when the material is heated up, due to a structural phase transition, where the lattice structure changes upon heating. By application of a magnetic field, the ferromagnetic phase (at low temperatures) is stabilized. The applied field shifts the structural first order phase transition to a higher transition temperature. Consequently, the change in the adiabatic temperature and entropy is analogous to the second order phase transition as shown before, but, the effect observed is in a broader range with sharp transitions, which makes it possible to switch abruptly between the states by field application and inducing a temperature change, or vice versa.

The magnetocaloric effect relies on a large change of the total entropy S_{tot} . Usually, three different contributions can be distinguished. The magnetic entropy S_{mag} , the electronic

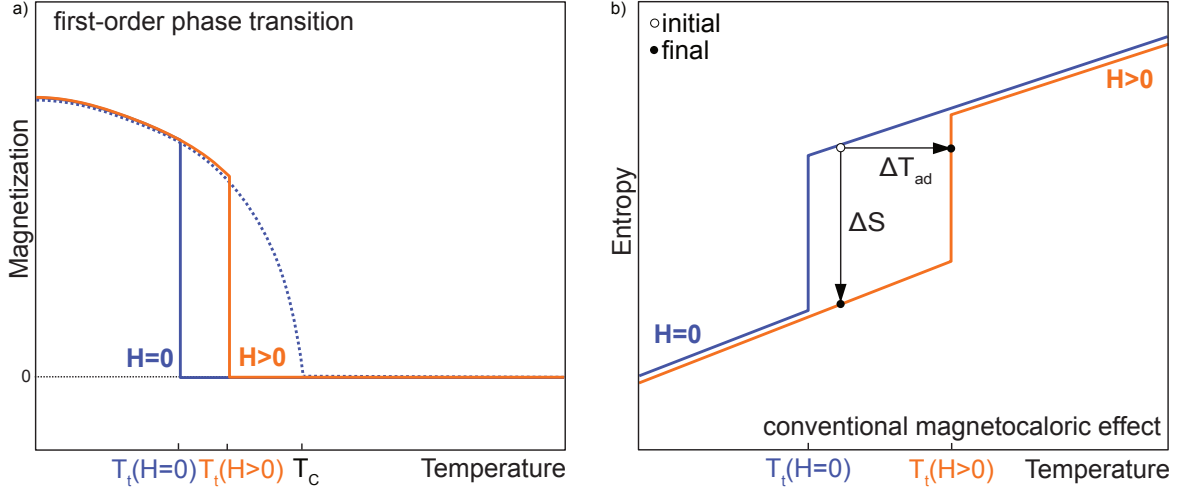


Figure 2.3.: Schematic sketch of a first order phase transition as found in magnetocaloric materials. Depicted are (a) the temperature dependent evolution of the magnetization, with (orange line) and without (blue line) an applied magnetic field accompanied by a structural phase transition at the phase transition temperature T_{tr} and (b) the entropy over temperature. Figure adapted from [32].

contribution S_{el} and the vibrational part of the entropy, S_{lat} [26, 33]:

$$S_{tot}(T, H) = S_{mag}(T, H) + S_{el}(T, H) + S_{lat}(T, H). \quad (2.8)$$

The different contributions to the entropy are described as follows. First, the magnetic entropy, relying on the alignment of the magnetic moments to each other in the mean field approximation [26]

$$S_{mag} = N_{mag} k_B \left[\ln \left(4\pi \frac{\sinh(x)}{x} \right) - x \coth(x) + 1 \right], \quad (2.9)$$

with

$$x = \frac{\mu_0 m_0 [\rho \eta_W M(T) + H]}{k_B T}, \quad (2.10)$$

which includes the number of magnetic degrees of freedom N_{mag} , m_0 , which is the effective magnetic moment per degree of freedom, the material density ρ and the molecular field constant η_W .

Secondly, the electronic entropy, including the electronic density of states $D(E)$ and Fermi-

Dirac distribution $f(E, T)$

$$S_{\text{el}} = -k_{\text{B}} \int_{-\infty}^{\infty} D(E) [1 - f(E, T) \ln(1 - f(E, T)) + f(E, T) \ln(f(E, T))] dE, \quad (2.11)$$

and last, the lattice entropy arising from the phonon subsystem, including the vibrational density of states $g(E)$ with Bose statistics $n(E, T)$

$$S_{\text{lat}} = -k_{\text{B}} \int_{-\infty}^{\infty} g(E) [(1 + n(E, T)) \ln(1 + n(E, T)) - n(E, T) \ln(n(E, T))] dE. \quad (2.12)$$

The distinction into these three contributions is not completely accurate, as the delocalized electrons in ferromagnetic $3d$ transition metals partake in the magnetism of the material. Thus, cross coupling terms between the three contributions have to be taken into account [26, 34, 35] as described later in this thesis.

Different measurement techniques provide access to the different entropy contributions. The electronic entropy is accessible by density functional theory (DFT) [34, 36, 37], photo emission spectroscopy [38] or X-ray spectroscopy [39–42]. The lattice entropy can be inferred from inelastic neutron scattering [43, 44] and via nuclear resonant inelastic X-ray scattering [34, 45–47].

Within this work different element-specific characterization methods have been utilized to detangle the vibrational and magnetic interactions and the local structural changes and their effect on the thermodynamic and magnetic behavior of $\text{La}(\text{Fe}, \text{Si})_{13}$ -based compounds with different dopants such as H or Mn.

2.2. Magnetic Interactions

To understand the intrinsic magnetic interactions at play in the discussed sample system, a short theoretical overview over the different magnetic coupling phenomena is given. If magnetic moments are uncompensated they either align parallel (ferromagnetically) or antiparallel (antiferromagnetically) to each other. Quantum mechanically this behavior can be explained by the exchange interaction \mathcal{H}_{ex} , with

$$\mathcal{H}_{\text{ex}} = -2 \sum_{i \neq j}^N J_{ij} \vec{S}_i \cdot \vec{S}_j \quad (2.13)$$

and the exchange integral given as J_{ij} . The exchange integral with $J_{ij}=J_{ji}$ is given as follows [30]

$$J_{ij} = \int \int \Psi_i(\vec{r}_1) \Psi_j(\vec{r}_2) \frac{e^2}{4\pi\epsilon_0 r_{12}} \Psi_i^*(\vec{r}_2) \Psi_j^*(\vec{r}_1) d\vec{r}_1 d\vec{r}_2. \quad (2.14)$$

It is effective between two adjacent molecular orbitals i and j with the spins \vec{S}_i and \vec{S}_j resulting from Coulomb interaction and the Pauli exclusion principle [48]. The complete wave function for fermions therefore has to be antisymmetric and consists of the spin $\chi(\vec{s}_1, \vec{s}_2)$ and the spatial wave function $\Phi(\vec{r}_1, \vec{r}_2)$

$$\Psi(\vec{r}_1, \vec{r}_2, \vec{s}_1, \vec{s}_2) = \Phi(\vec{r}_1, \vec{r}_2) \cdot \chi(\vec{s}_1, \vec{s}_2). \quad (2.15)$$

In a ferromagnetic material, $J_{ij} > 0$, the minimum energy is achieved with a parallel spin orientation. If $J_{ij} < 0$, then the magnetic moments couple antiparallel to each other.

2.3. Sample System La(Fe,Si)₁₃

The material systems investigated in this work are LaFe_{13-x}Si_x-based compounds. These intermetallic compounds form in a stable pseudo-binary La(M, M')₁₃ 1:13 phase (M = Fe, Ni and M' = Al, Si) [49–51]. Pure LaFe₁₃ does not exist due to positive heat formation at alloying [50]. LaFe_{13-x}Si_x crystallizes in stoichiometries of $1.2 \leq x \leq 2.5$ in a cubic NaZn₁₃ ($Fm\bar{3}c$) structure. Its unit cell consists of 112 atoms and has two non-equivalent Fe-sites. Figure 2.4 shows the whole cell and Figure 2.5 an ordered cell consisting of only 28 atoms with a nominal stoichiometry of LaFe_{11.5}Si_{1.5}. La is positioned on the 8a positions. Fe is located on two distinctly different sites, which, together, form an icosahedron with an Fe_I atom in its center (see inset 2.5). Fe_{II} occupies the 96-fold (96i)-sites, which exhibit a lower local symmetry, while Fe_I occupies the highly symmetrical eightfold (8b) Wyckoff positions. It is widely assumed that Si occupies the (96i)-sites randomly, shared with Fe_{II} as inferred from Mössbauer and neutron diffraction experiments [52–54].

Upon changing the temperature, LaFe_{13-x}Si_x-based compounds undergo a magneto-structural phase transition at T_{tr} . This transition is accompanied by a large isostructural

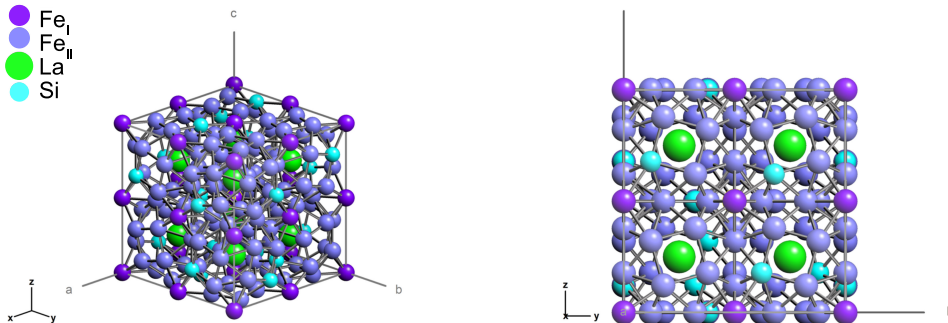


Figure 2.4.: Depiction of the whole ordered unit cell with 112 atoms of La(Fe, Si)₁₃ with the respective lattice sites. Fe_I on (8b) (dark purple) and Fe_{II} on (96i) (light purple), shared with Si (cyan) and La on (8a) (green).

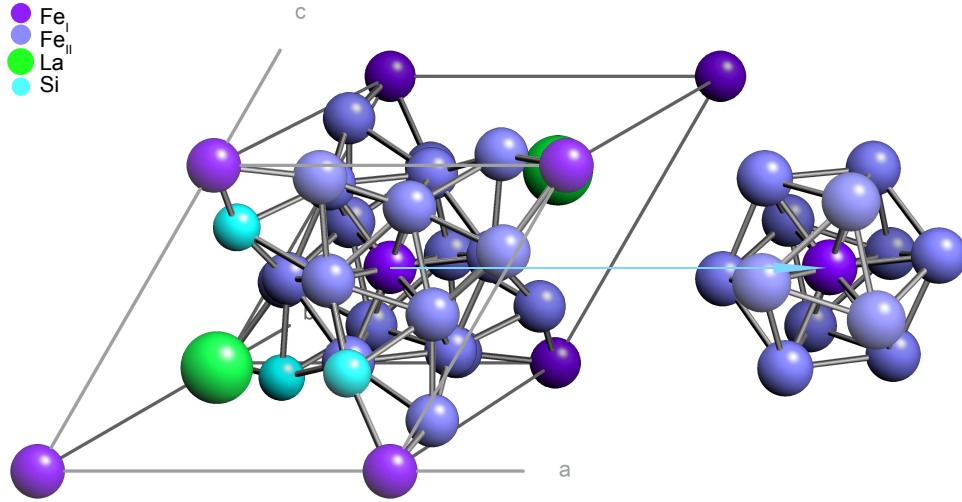


Figure 2.5.: Reduced cell of $\text{La}(\text{Fe}, \text{Si})_{13}$ consisting of 28 atoms on a fcc basis. The right-hand side depicts the surrounding of the highly symmetrical Fe_I site in an icosahedral cage of Fe_{II} -atoms. Figure adapted from [34, 35].

diffusion-less volume decrease upon heating, with a narrow thermal hysteresis [24, 55–57]. At low temperatures $\text{LaFe}_{13-x}\text{Si}_x$ is ferromagnetic with a collinear spin structure [35, 58, 59] and becomes paramagnetic after the magneto-structural phase transition. The addition of higher concentrations of Si into the compound gradually reduces the magnetization with increasing Si content, as it substitutes the Fe-sites, but results in a stabilization of the ferromagnetic phase, and is shifting the phase transition from the ferromagnetic to the paramagnetic state to higher temperatures. As a critical content of Si surpasses the threshold of $x = 1.8$ the phase transition changes from first to second order with a reduction in both $|\Delta T_{ad}|$ and $|\Delta S_{iso}|$ [50, 60, 61]. The first order character of the compound with low Si contents is connected to the itinerant nature of the electron metamagnetism [28, 36, 56]. From DFT calculations it was concluded that the reduction in the Fe moment is the result of hybridization between the Fe- d and Si- p -states [37, 62]. To overcome this behavior, it is possible to tailor the functionalities of $\text{LaFe}_{13-x}\text{Si}_x$ -based compounds and incorporate other atoms on the interstitial lattice sites, 24d, such as C, N, or H [36, 63–68]. In the unit cell, 24 interstitial sites can be occupied with hydrogen, which significantly increases the lattice parameter [67, 69, 70]. It has been shown that the lattice site for hydrogen is slightly displaced and the atoms rather reside on (48f) [53]. The lattice expansion through hydrogenation consequently results in a shift of the isostructural phase transition to higher temperatures as hydrogenation stabilizes the ferromagnetic phase of the compound due to stronger exchange coupling of the Fe sub-lattices.

As already depicted in Figure 2.6, full hydrogenation would lead to a hydrogen content of $y = 3$ with equal occupation of hydrogen on all 24 H_I and H_{II} -sites in the unit cell. It

has been shown in absorption experiments that the unit cell is not fully loaded and the hydrogenation will not significantly exceed a hydrogen content of $y \approx 1.8$ per formula unit [71–73], depending mainly on the composition and Si content. The fact that the unit cell cannot take up 24 hydrogen atoms is a result of the repulsive interactions between the partially filled p shell in Si on (96i) and H [74]. Additionally the next neighbor distance between two (48f)-sites is smaller than 2.1 \AA , which results in a not fully loaded unit cell as two hydrogen atoms can not simultaneously occupy two next neighbor (48f)-sites [53, 75]. This combination of effects consequently leads to a depression of the hydrogenation kinetics [71, 76]. This is in accordance with Hai et al. [76] who show that an increase in Si content yields a decrease in the hydrogen absorption kinetics. This is backed by first principle calculations [77] which indicate that the immediate Si surrounding is energetically less favorable by $310 - 320 \text{ meV}$ for hydrogen occupation, leading to an occupation of the H_I lattice sites first, before the H_{II} -sites are filled up and the hydrogenation process slows down drastically. Hydrogen preferentially fills the sites most distant from Si first. In this thesis, the samples with hydrogenation do not exceed a hydrogen content of $y = 1.6$. As the lattice expansion due to incorporation of interstitial atoms is the source for the increase of the shift in the transition temperature, these compounds are promising materials to use in room temperature applications. Hydrogenated compounds retain their first order phase transition [36, 68, 78] while shifting the itinerant electron metamagnetic transition significantly. Additional doping of Mn into the compounds can provide a first

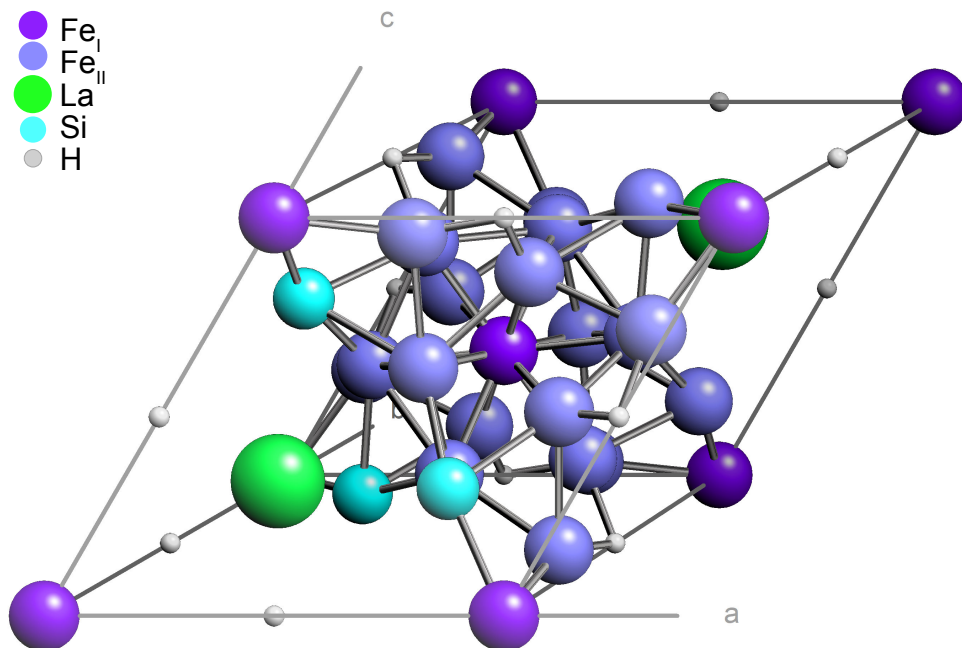


Figure 2.6.: Reduced cell with hydrogenation on the interstitial (24d)-sites of $\text{LaFe}_{11.5}\text{Si}_{1.5}\text{H}_{1.5}$. Figure adapted from [34, 35].

order phase transition while retaining good magnetocaloric performance and maintaining $|\Delta T_{\text{ad}}|$ and $|\Delta S_{\text{iso}}|$ [64, 68]. Mn also occupies the (96i)-sites randomly and consequently substitutes Fe. This gives the opportunity to specifically tailor the transition to temperatures as needed, covering a broad range (135 – 345 K) without changing the lattice symmetry [68, 79]. The Mn substitution prevents hydrogen from segregating and shifts the transition to lower temperatures [64, 80]. Balancing out the Mn and H contents in a thought out manner offers the possibility for specifically tailoring the transition.

2.4. Interaction of X-rays and Matter

X-ray based characterization methods give the possibility to determine local and element-specific electronic and geometric structure, and provide information on the chemical surrounding, and the local magnetic properties of an atom. To properly describe the different experimental methods used in this work, first the interaction of X-rays and matter has to be taken into account. When X-ray radiation interacts with matter it follows the Beer-Lambert law. The incident photon intensity I_0 is attenuated in the material of the thickness x with an attenuation coefficient $\tilde{\mu}$

$$I(E, x) = I_0 \cdot e^{-\tilde{\mu}(E) \cdot x}. \quad (2.16)$$

The effective absorption cross section $\sigma(E)$ is given by the transition probability T_{if} from the initial state $|i\rangle$ to the final state $\langle f|$, and the photon flux f_{ph} . This cross section $\sigma(E)$ can be estimated to be proportional to the absorption coefficient μ ,

$$\mu(E) \propto \sigma(E) = \frac{T_{if}}{f_{ph}}, \quad (2.17)$$



Figure 2.7.: Schematic depiction of X-ray attenuation with an incident intensity of I_0 passing through a material with the thickness x . Depicted are also the possible detection schemes.

as the photo effect dominates in the hard X-ray energy regime (> 5 keV) used within this work and losses through elastic Rayleigh and inelastic Compton scattering can be neglected [81]. Figure 2.7 depicts a schematic of the attenuation of X-rays through an absorbing medium of the thickness x with an incident photon intensity I_0 . The detection possibilities are given as well, with TY as the transmission yield, TEY as the total electron yield and FY as fluorescence yield. The transmission yield directly measures the transmitted X-ray intensity and, therefore, is only suitable for thin samples. The total electron yield and fluorescence yield are indirect detection measurements. The TEY measures the current of the excited electrons and the fluorescence yield the emitted photoelectrons generated through the excitation process.

The ionization energy to excite an electron from its core level into the continuum is specific for each absorbing atom and makes X-ray absorption spectroscopy (XAS) element-specific. If the incident X-ray energy is high enough, and the binding energy is overcome, the X-ray absorption coefficient has an abrupt increase, which results in the so-called absorption edge. The transition probability per unit time for the excitation of an electron is given by Fermi's golden rule with the initial state $|i\rangle$ and the final state $\langle f|$ and the corresponding energies ϵ_i and ϵ_f . $\rho(\epsilon_f)$ describes the density of the final states and \mathcal{H}_{int} is the Hamiltonian which describes the time dependent perturbation through the incident electromagnetic wave, see Equation 2.18.

$$T_{if} = \frac{2\pi}{\hbar} |\langle f | \mathcal{H}_{\text{int}} | i \rangle|^2 \delta(\epsilon_i - \epsilon_f) \rho(\epsilon_f). \quad (2.18)$$

The transitions between two electronic states ϵ_i and ϵ_f are given as the matrix element within

$$\mathcal{M} = \langle f | \mathbf{p} \cdot \boldsymbol{\epsilon} e^{i\mathbf{k}\mathbf{r}} | i \rangle. \quad (2.19)$$

The Hamiltonian in dipole approximation is given as the product of the momentum operator $\mathbf{p} = i\hbar\vec{\nabla}$ and the vector potential \mathbf{A} [30]

$$\mathcal{H}_e^{\text{int}} = \frac{e}{2m_e} \mathbf{p} \cdot \mathbf{A}, \quad (2.20)$$

describing the time dependent perturbation of the Hamiltonian \mathcal{H}_0 of the atom. The incident electromagnetic wave with given photon polarization $\vec{\epsilon}$ can be described by the vector potential \mathbf{A} , and the field is then defined as $\vec{A}(\mathbf{r}, t) = \vec{\epsilon} A_0 e^{i\vec{k}\vec{r}}$. For electric dipole transitions (E1) the relation $e^{i\mathbf{k}\mathbf{r}} \cong 1$ can be approximated. According to equation (2.19) this leads to the so called dipole selection rules, which determine all the allowed transitions between the two particle states $|i\rangle$ to $\langle f|$ with the form $|n, l, m_l, m_s\rangle$

$$\Delta l = \pm 1; \Delta m_l = 0, \pm 1; \Delta s = 0; \Delta m_s = 0. \quad (2.21)$$

where $q\hbar$ is the angular momentum of the incident X-ray [30]. According to these rules there are only transitions from the s to p -states allowed in case of the the K-edges. For the $L_{2,3}$ -edges, transitions are only allowed from the p to the d -states. When the dipole approximation, which assumes the vector potential to be spatially bigger than the physical system, is not valid, possible multipole effects have to be taken into account and the selection rules must be expanded. Quadrupolar excitations come into play for example, when hybridization effects are present between p and d -states or excitations from p into $4f$ -states are possible.

2.4.1. X-ray Magnetic Circular Dichroism

The effect used in this work to probe the local spin and orbital momentum is called X-ray magnetic circular dichroism. After its first theoretical prediction in 1975 [82] it was experimentally proven in 1987 by Schütz et al. [83]. The XMCD effect can be described in a two step model [30, 42]. Figure 2.8 depicts the 2-step model at the L-edges for a $3d$ -transition metal (here with Fe as an example). First, a circularly polarized X-ray photon is absorbed by a $2p$ core state. Due to spin orbit coupling ($\mathbf{j} = \mathbf{l} + \mathbf{s}$), the $2p$ levels are split into two states, $2p_{1/2}$ (L_2 -edge) and $2p_{3/2}$ (L_3 -edge). The absorption of light with its helicity vector μ^+ (μ^-) parallel (antiparallel) to the $2p$ orbital moments preferentially leads to excitation of electrons with spin up (down) direction. In the second step, the unoccupied $3d$ valence band acts as a spin detector as the excited polarized photo electrons are excited above the Fermi energy into the unoccupied spin polarized states. According to the Stoner model for a ferromagnetic material, with its origin in exchange interaction and Pauli exclusion principle, the spin up and down states are not equivalently occupied and the dichroism is a direct result of the spin orbit difference of the valence band. Therefore, in case of $L_{2,3}$ excitation from p -states, the magnetic moment can be probed as the dichroism reflects the imbalance of the differently filled valence states. The probing of the $L_{2,3}$ -edges results from electric dipole transitions (E1). In case of K-shell excitation from the $1s$ core shell no spin orbit coupling is present. As the s level is not spin orbit split, the angular momentum of the incident X-ray photon is completely transferred to the generated photoelectron. The information from K-edge measurements only provides information on the orbital polarization of the valence states. The main contribution of the excitation at the Fe K-edge results from $1s \rightarrow 4p$ transitions into delocalized $4p$ -states, from electric dipole transitions. The polarization of the $4p$ -states is a result of the hybridization with the surrounding $3d$ -states [84]. But, for the K-

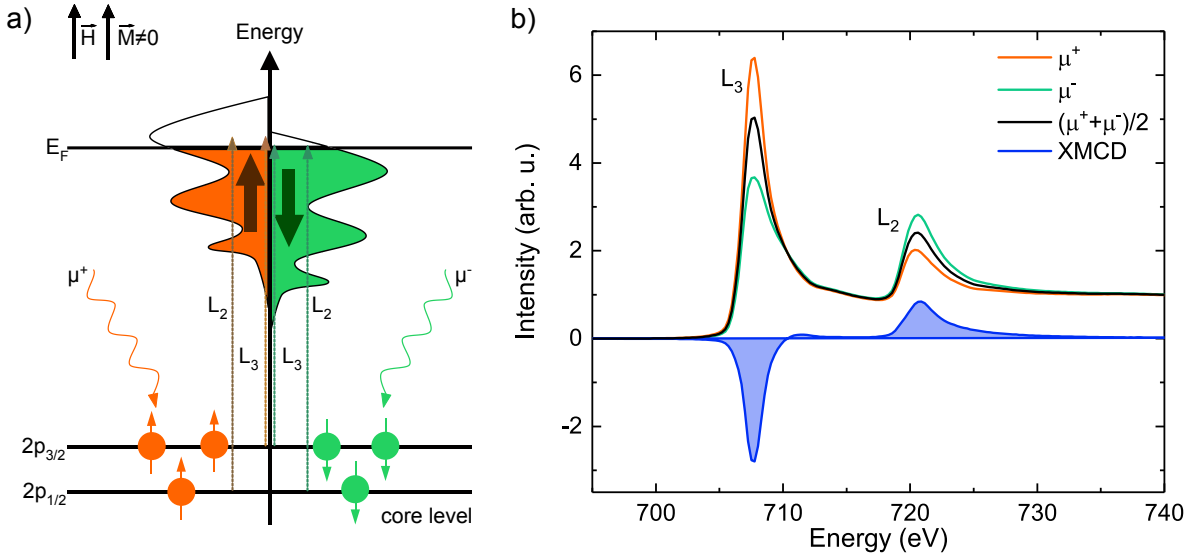


Figure 2.8.: XMCD effect for Fe L_{2,3}-edges a) Density of states for spin up and down states with the transitions for X-ray polarization in μ^+ and μ^- . The spin down states are nearly fully filled, spin up partially due to a magnetization in up direction. b) XAS of the L-edges for each light polarization and their difference, the XMCD. Figure adapted from [42].

edge analysis in transition metals, additionally electric quadrupolar transitions (E2) may have to be considered. Here, a core electron from the $1s$ state can be excited into the $3d$ -states [39, 85]. The transitions occur closely around the absorption edge and alter the pre-edge features of the XANES [86–89]. Therefore, for further analysis, we have to take into account that the transitions as reflected in the XANES might be enhanced due to quadrupolar transitions or hybridization between the p and d -states. Quadrupolar transitions at the L_{2,3}-edges are generally possible for excitations from the p -states into empty $4f$ -states, as observed for rare earth compounds [90–92].

Magneto-optical Sum Rules

The extraction of the spin and orbital moment from the X-ray absorption spectra can be done using the so called magneto-optical sum rules [93, 94]. Using only the dipole transitions at the L_{2,3}-edges (transitions from $2p \rightarrow 3d$ -states) [95] the orientation averaged sum rules are as follows (after Ref. [30, 96]): The charge sum rule is directly connecting the averaged X-ray absorption resonance intensity $\langle I \rangle$ of a transition from a core to a free valence state represented by the number of holes N_h . In case of the L_{2,3}-edges it is the spectral intensity for both edges,

$$\langle I \rangle = CN_h, \quad (2.22)$$

with $\langle I \rangle = \langle I_{L_3} + I_{L_2} \rangle$ as the integrated whiteline intensities at both absorption edges, which correspond to the empty states, the proportionality constant $C = \mathcal{A}\mathcal{R}^2 \frac{L}{3(2L+1)}$, with $\mathcal{A} = \frac{4\pi^2\hbar\omega}{137}$, and the radial matrix element \mathcal{R} , which describes the transitions from a core to a valence state. The sum rules rely on the integrated XMCD signal and the expected value for the ground state of the orbital magnetic moment. The spin sum rule (for the $L_{2,3}$ -edges) is defined as follows and can quantify the spin magnetic moment μ_s with the following relation

$$\langle -A + 2B \rangle = \frac{C}{\mu_B} \mu_s, \quad (2.23)$$

with C as given above. A refers to the integrated XMCD at the L_3 -edge, B at the L_2 -edge as seen in Figure 2.9 (a). The orbital moment μ_l can be extracted as follows

$$-\langle A + B \rangle = \frac{3C}{2\mu_B} \mu_l, \quad (2.24)$$

using the same relation for C as in case of the spin sum rule. As the spin asphericity expected in a cubic crystal field is small, the expectation value of the intra-atomic magnetic dipole operator $\langle T_Z \rangle$ is neglected here [30, 97]. As we measured La $L_{2,3}$ -edges, and only the unoccupied $5d$ -states are probed, the sum rules might not reflect the extracted values accurately. They have been used in this work to qualitatively quantify the evolution of the orbital and spin moment.

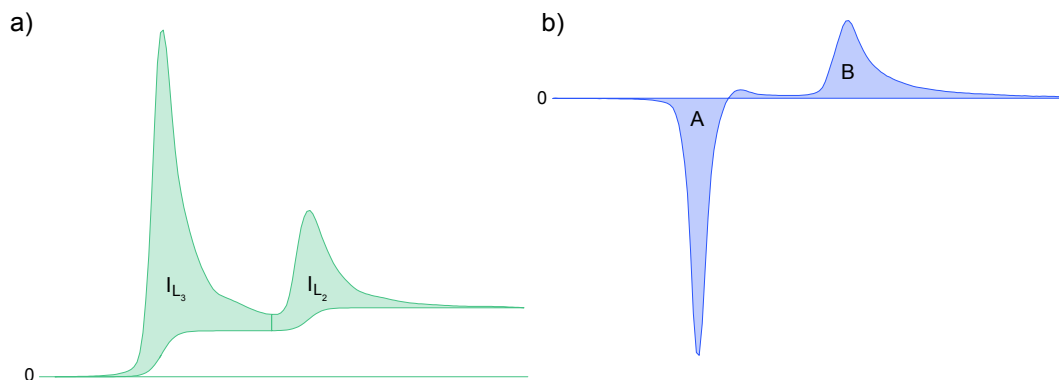


Figure 2.9.: Schematic view of the integrated area of the (a) whiteline intensity, which gives the number of empty states and (b) the integrated area of the XMCD, both shown exemplary for Fe $L_{2,3}$ -edges.

2.4.2. Extended X-ray Absorption Fine Structure

Extended X-ray absorption fine structure (EXAFS) measurements provide access to the local structural surrounding of an absorbing atom. The basic principle of EXAFS is the absorption of an incident X-ray photon, which then generates a photoelectron. The excited photoelectron leaves a core hole behind and is perturbed by the charge densities of the core electrons of the neighboring atoms. This scattering process then results in a modulation of the absorption coefficient $\mu(E)$. The generated photoelectron interferes with itself, which then leads to the characteristic EXAFS oscillations. This screening or modulation of the fine structure is described by EXAFS, which is normalized to the bare atom background μ_0 :

$$\chi(E) = \frac{\mu(E) - \mu_0(E)}{\mu_0(E)}. \quad (2.25)$$

By using the wave transformation

$$k = \sqrt{\frac{2m}{\hbar^2} \cdot (E - E_0)}, \quad (2.26)$$

the EXAFS $\chi(E)$ can be then transformed into k -space [81]. Figure 2.10 describes the absorption process of an atom in presence of a neighboring atom. The photoelectron of the absorbing atom scatters from the atom next to it. The left part shows the propagation of the photoelectron with the interference of itself with its neighbor. The right-hand part shows the modulation in the absorption coefficient $\mu_0(E)$ of the absorbing (bare) atom and the scattering atom.

X-ray absorption fine structure (XAFS) spectra generally consist of two parts. The near-edge spectra (XANES) energetically ranging up to ~ 30 eV past the main absorption edge and the EXAFS, which continues up to an energy range of a few keV past the absorption edge.

As described in section 2.4, the transition probability from an initial state to a final state is described by Fermi's golden rule and the absorption $\mu(E)$ can therefore be described as follows:

$$\mu(E) \propto |\langle i | \mathcal{H} | f \rangle|^2. \quad (2.27)$$

The final state f hereby is the combination of the absorbing (bare $|f_0\rangle$) atom and the neighboring atom ($|\Delta f\rangle$), leading the fine structure χ to be proportional to $|\Delta f\rangle$:

$$\chi(E) \propto |\langle i | \mathcal{H} | \Delta f \rangle|. \quad (2.28)$$

The change of the final state is the wave function of the scattered photo-electron in the

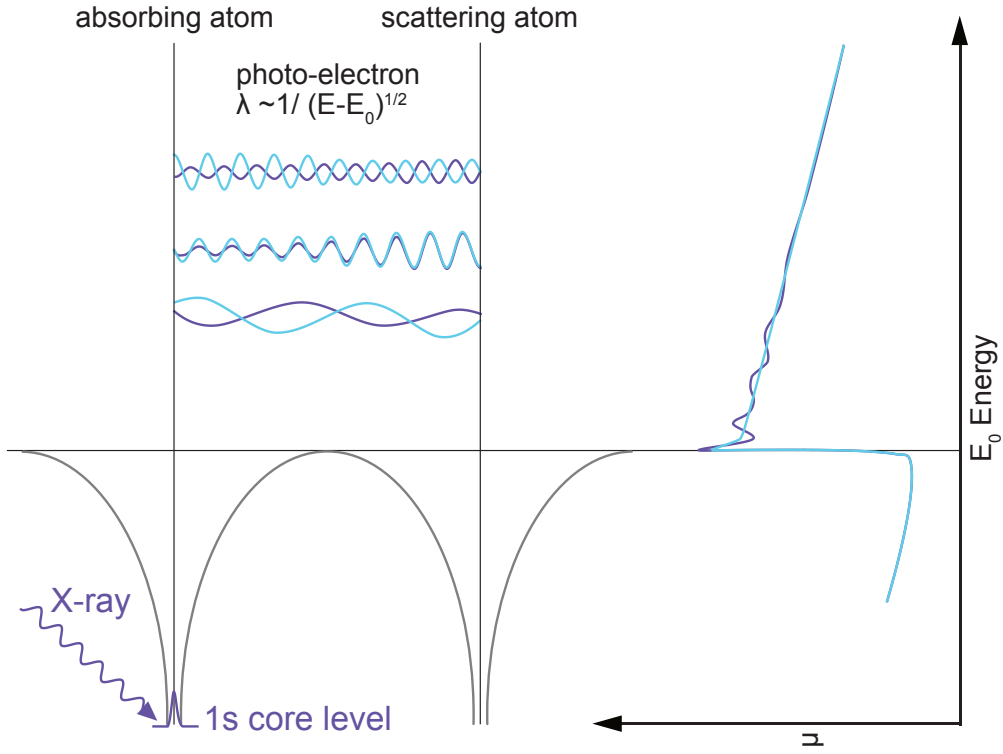


Figure 2.10.: Amplitude modulation of the X-ray absorption coefficient through scattering due to presence of a neighboring atom. The bare atom background refers to the purple line, the blue line is the backscattering amplitude. Adapted from [98].

distance r [98]:

$$\chi(E) \propto \int dr \delta(r) e^{ikr} \psi_{\text{scatter}}(r) = \psi_{\text{scatter}}(0). \quad (2.29)$$

With the assumption of a spherical wave for the outgoing photo-electron wave function, $\psi(k, r) = \frac{e^{ikr}}{kr}$, traveling to the scatterer and back to the absorbing atom results in

$$\chi(k) = \frac{f(k)}{kR^2} \sin[2kR + \delta(k)]. \quad (2.30)$$

Expanding this picture to more than two atoms while including intrinsic losses, the mean free path of the scattering atom and disorder, leads to the EXAFS equation $\chi(k)$:

$$\chi(k) = \sum_j \frac{S_0^2 N_j f_j(k) e^{-\frac{2R_j}{\lambda(k)}} e^{-2k^2 \sigma_j^2}}{k R_j^2} \sin(2kR_j + \delta_j(k)). \quad (2.31)$$

This equation consists of the backscattering amplitude $f_j(k)$ from each neighboring atom j , its number N_j and their distance R_j and the phase shifts $\delta_j(k)$, resulting from the

scattering of the photoelectron. The disorder in the system is described by σ_j^2 . It consists of a static and dynamic part, $\sigma_j^2 = \sigma_{\text{static}}^2 + \sigma_{\text{vib}}^2$. The vibrational part includes the temperature dependent Debye-Waller factor, which takes the lattice dynamic into account, whilst the static part describes the static disorder in the crystal. High static and dynamic disorder leads to stronger amplitude reductions for higher k -values. The disorder can be modeled with a pair distribution function of the absorbing atom with its surrounding neighbors, which gives rise to the exponential damping in $e^{-2k^2\sigma_j^2}$. In the pair distribution function, the first cumulant describes the average distance of the absorbing atom to its scatterer, while the second cumulant is the Debye Waller factor. Higher order cumulants include the thermal expansion and anharmonic losses [39, 98]. The inelastic losses in the scattering process are described by the first exponential term. The amplitude reduction due to many body effects (multi-electron excitations) are described by the amplitude reduction factor S_0^2 , which can be explained as the losses due to excess energy in the photo ionization process, which do not contribute to the EXAFS when a weakly bound electron is excited either into a higher energetic state (shake up) or into the continuum (shake off) [81].

2.5. The Mössbauer Effect

Mössbauer Spectroscopy is a useful tool to gain information on the local magnetic and electronic environment of Mössbauer nuclei. It is non destructive and highly sensitive. In this work only ^{57}Fe has been used due to its suitability for studies on magnetic properties, but there are many more isotopes, which can be utilized [99]. The Mössbauer effect can be understood as the recoilless nuclear resonant emission and absorption of a γ -photon [100].

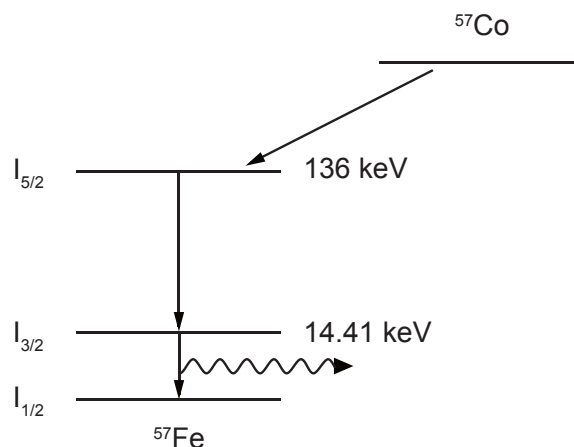


Figure 2.11.: Schematic of the decay of ^{57}Co to ^{57}Fe with emission of 14.41 keV γ -photons.

It provides insight into the fine structure of the nuclear levels by resonant gamma-ray absorption.

The source used to produce γ -photons with the resonant energy of ^{57}Fe is radioactive ^{57}Co embedded in a Rh matrix. It decays to an excited ^{57}Fe $I_{5/2}$ level via electron capture, which then either leads to a direct transition into the ground state with an energy of 136 keV or a decay to the $I_{3/2}$ state, with a natural linewidth of $\Gamma = 4.66$ neV, with its origin in the Heisenberg uncertainty principle, $\Gamma\tau = \hbar$, and a given lifetime τ of the excited $I_{3/2}$ state. The subsequent decay into the ground state leads to the emission of a γ -photon with an energy of 14.41 keV. Considering classical mechanics and the case of a free atom, in a nuclear transition caused by an incident γ -photon, the nucleus has a recoil energy E_R due to momentum conservation and the energy E_0 of the incident γ -photon is reduced by the recoil energy E_R .

$$E_R = \frac{\hbar^2 k^2}{2m} \quad (2.32)$$

For the Mössbauer effect to work, the incident gamma-ray must compensate the momentum. The recoil energy can be written as follows with the gamma photon momentum $\mathbf{p}_\gamma = -\hbar\mathbf{k}$. Figure 2.12 depicts the relative absorption probability of a γ transition. The lattice vibrations manifest as sidebands next to the Mössbauer absorption line [101].

If the atom is embedded in a crystal, its ability to recoil during the absorption and emission of a γ -photon is limited and the momentum of the recoil energy is transferred to the lattice through phonons (quantized lattice vibrations). If the mass in the recoil energy

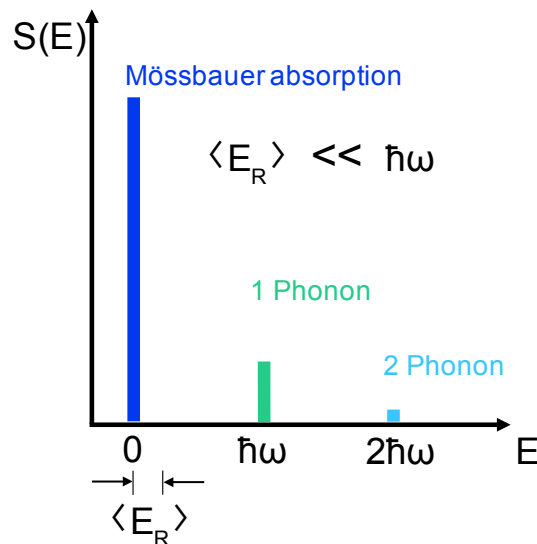


Figure 2.12.: Schematic depiction of the relative absorption probability of a γ -photon transition under presence of phonon transitions for a very small average recoil energy $\langle E_R \rangle$ [102]. Figure adapted from [103].

equation is that of the whole crystal, which is significantly higher than that of a single atom, this leads to the recoil energy being negligibly small. This process is called the recoil-free nuclear resonance absorption and leads to elastic emission processes without phonon creation [99, 103], the Mössbauer absorption. Figure 2.12 schematically depicts the relative absorption probability of a γ -transition for a very small recoil energy of 2 meV for ^{57}Fe . Considering the Debye model, the fraction of the γ -photons which are absorbed recoil-free is described by the Lamb-Mössbauer factor (or Debye-Waller factor in X-ray scattering) [103]

$$f_{\text{LM}} = \exp \left(-\frac{3E_{\text{R}}}{2k_{\text{B}}\Theta_{\text{D}}} \left[1 + 4 \left(\frac{T}{\Theta_{\text{D}}} \right)^2 \int_0^{\frac{\Theta_{\text{D}}}{T}} \frac{x dx}{e^x - 1} \right] \right), \quad (2.33)$$

with the Debye temperature Θ_{D} and $x = \frac{\hbar\omega}{k_{\text{B}}T}$. In the thin absorber approximation the Lamb-Mössbauer factor is directly proportional to the resonant absorption area in the Mössbauer spectrum.

As the natural linewidth of the Mössbauer lines is very small, 4.66 neV for ^{57}Fe , hyperfine interactions can be observed and analyzed. Figure 2.11 depicts the different interactions for the ^{57}Fe nucleus of an absorber material with its electronic environment regarding the energy difference of the resulting fine structure.

The isomer shift, denoted in Figure 2.13 as electric monopole interaction, is a result of the Coulomb interaction of the nuclear charge and mainly the charge density of the electrons at the nucleus, the s -electrons. A shift δ_{abs} results directly from a change in the charge density of the s -electrons in the absorber material relative to the source material. A decrease of the shift is a sign of an increase in s -electron charge density at the absorbing nucleus. Another electric hyperfine interaction is the nuclear quadrupole interaction, which leads to a splitting (2ε) of the excited state. Electric quadrupole interaction arises from asymmetrically distributed charges around the absorbing nuclei, which give a rise to the electric field gradient (EFG). The asymmetry can be caused by electron polarization due to crystal field effects or non-spherical charge distributions [99]. In a magnetic surrounding, the nuclear levels are split into six resonant lines due to the nuclear Zeeman effect (magnetic dipole interaction), the ground state $I_{1/2}$ is split into two sub levels, the excited state $I_{3/2}$ is divided into 4 sub levels. The energy for each level is given as

$$E_m = -\mu B m_I \frac{1}{I} = -g\mu_n B m_I, \quad (2.34)$$

with $\mathcal{H}_m = -\boldsymbol{\mu} \cdot \mathbf{B} = -g\mu_n \mathbf{I} \cdot \mathbf{B}$. B is the hyperfine magnetic field at the nucleus. μ_n is the nuclear magnetic moment, m_I the magnetic quantum number, I is the nuclear spin and g the nuclear g-factor. For the ^{57}Fe -isotope only transitions between $\Delta m_I = 0, \pm 1$ are

allowed (dipole selection rules). From the relative line intensities of the Mössbauer spectra it is possible to extract the relative spin orientation, the canting angle θ and the magnetic structure of the material studied. The relative intensities of the lines are proportional to the squared Clebsch-Gordan coefficients $C = \langle I_g m_g L m | I_e m_e \rangle$. The relative probability $P(\theta)$ for a resonant absorption process from the ground state $|I_g m_g\rangle$ to the excited state $|I_e m_e\rangle$ is given as [105, 106]:

$$P(\theta) = |C\chi_L^m(\theta)|^2 \quad (2.35)$$

with $|\chi_L^m\rangle$ as the quantum state of the incident γ -photon. The angular dependence of the transition probability is given in χ_L^m for M1 magnetic dipole transitions.

The intensity ratio between the lines 2 and 3 as well as 4 and 5, respectively can then be given as:

$$A_{23} = \frac{I_2}{I_3} = \frac{4 \sin^2 \theta}{1 + \cos^2 \theta}, \quad \theta = \arccos \sqrt{\frac{4 - A_{23}}{4 + A_{23}}}, \quad (2.36)$$

with the average canting angle θ . Figure 2.14 depicts the relative line intensities for the three extreme cases. In the first case, the lines 2 and 5 vanish and the lines have a ratio 3:0:1:1:0:3. In this case, the γ -photon is parallel to the spin and the hyperfine magnetic

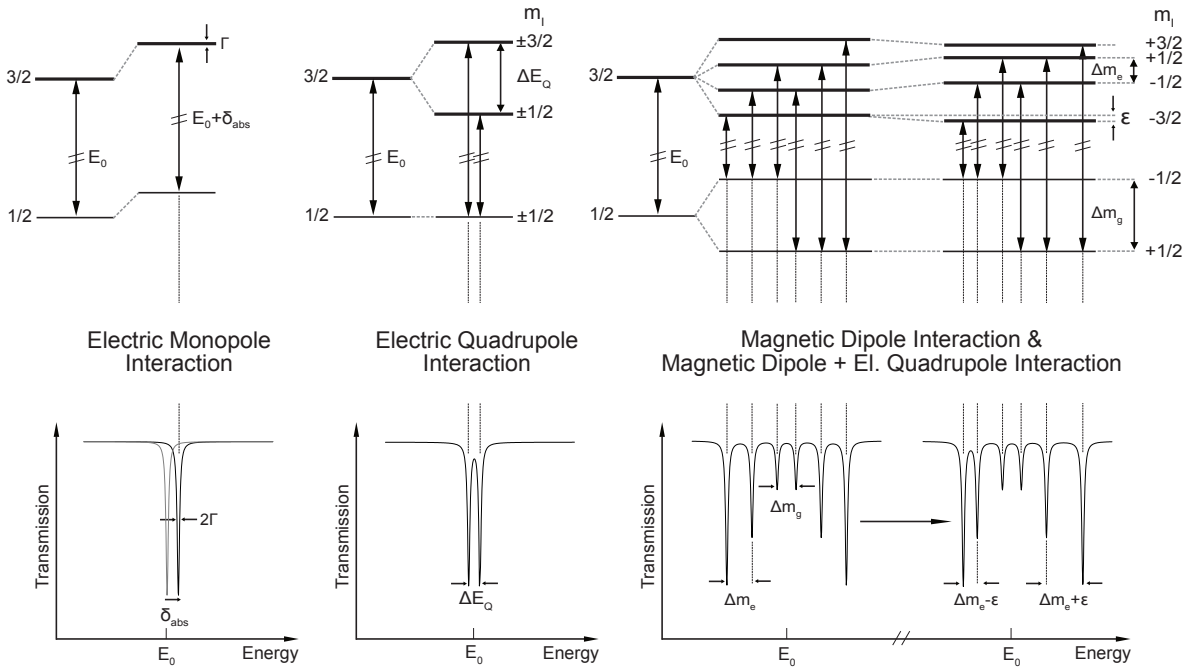


Figure 2.13.: Influence of different hyperfine interactions on ^{57}Fe Mössbauer spectra by Coulomb interaction (isomer shift, left), quadrupole interaction (middle) and magnetic dipole interaction (Zeeman splitting) and a combination of the latter (right). The arrows depict the allowed transitions according the dipole selection rules. The bottom graphs depict the effect on the absorption spectra in transmission. Adapted from [103, 104].

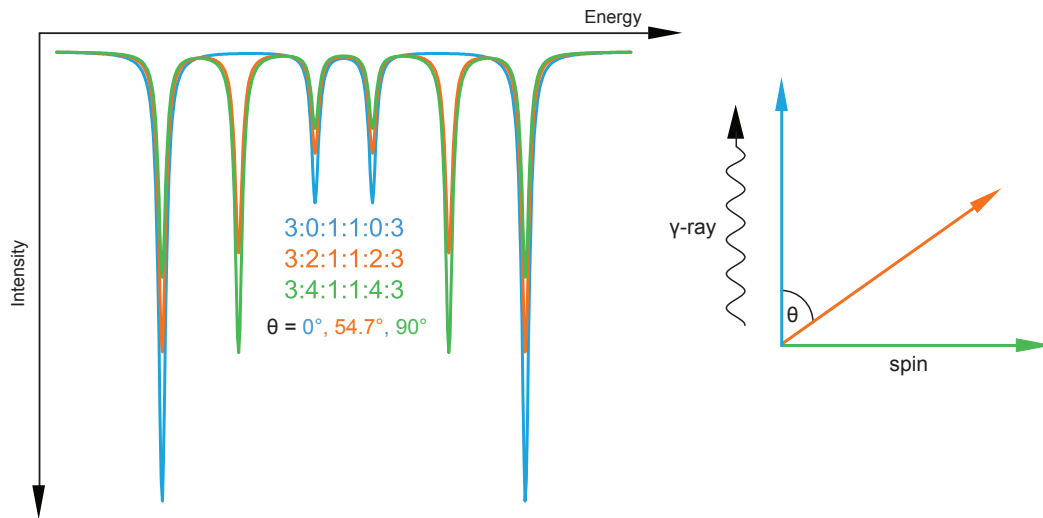


Figure 2.14.: Schematic of the intensities of the relative absorption, the A_{23} ratio, for three extreme case, the incident γ -photon parallel to the hyperfine magnetic field B , or the spin, respectively ($\theta = 0^\circ$) (blue line), at $\theta = 54.7^\circ$ (purple line) and at $\theta = 90^\circ$ (green line). Figure adapted from [104].

field B ($\theta = 0^\circ$). The Fe magnetic moment μ_{Fe} is antiparallel to the hyperfine magnetic field B . The second case is a line ratio of 3:2:1:1:2:3. This is the case, for the "magic angle" ($\theta = 54.7^\circ$), which also coincides with a random spin orientation in a 3D sample, for example, a powder sample, without the application of an external magnetic field. The third case is an intensity ratio of 3:4:1:1:4:3 where the incident γ -photon is perpendicular to the spin, the Fe magnetic moment or the hyperfine magnetic field B .

Angle dependent probabilities of transitions between Zeeman-split energy levels							
Line	Transition	Δm	C^2	$P(\theta)$	$P(0)$	$P(90)$	P
1 (6)	$\pm\frac{1}{2} \rightarrow \pm\frac{3}{2}$	± 1	1	$\frac{3}{4}(1 + \cos^2\theta)$	3/2	3/4	1
2 (5)	$\pm\frac{1}{2} \rightarrow \pm\frac{1}{2}$	0	1/3	$\sin^2\theta$	0	1	2/3
3 (4)	$\pm\frac{1}{2} \rightarrow \mp\frac{1}{2}$	∓ 1	2/3	$\frac{1}{4}(1 + \cos^2\theta)$	1/2	1/4	1/3

Table 2.1.: Mössbauer transition probabilities and intensity ratio according to magnetic quantum numbers.

2.6. Nuclear Resonant Inelastic X-ray Scattering

The method of Nuclear Resonant Inelastic X-ray Scattering (NRIXS) directly provides access to the lattice dynamics and the phonon (vibrational) density of states, the VDOS [45, 107, 108]. Experiments can be performed on crystalline or non crystalline materials, as it is an atomistic method and only sensitive to the element probed, which has to be a Mössbauer sensitive nucleus, thus limiting the accessible materials. As the investigated sample system, $\text{La}(\text{Fe}, \text{Si})_{13}$ -based compounds, mainly consist of iron, this experimental method gives access to a sufficiently large contribution to the thermodynamic lattice behavior of $\text{La}(\text{Fe}, \text{Si})_{13}$, by probing ^{57}Fe . The energetic width of the excited nuclear state, the natural line width Γ , amounts to only 4.66 neV for ^{57}Fe as described in section 2.5. The lifetime of the vibrational excitations broadens the resonance line and reduces their intensity by 6-7 orders of magnitude in comparison to the elastic peak from the Mössbauer absorption. This makes it necessary to use synchrotron radiation for excitation of the vibrational sidebands due to the need of a high spectral intensity in order to excite a nuclear state with small energy resolution [109]. NRIXS can be described as so called phonon assisted nuclear resonance absorption. The incident X-ray photon energy is tuned relative to the nuclear resonance of the absorbing atom. In a simple Einstein model, when an X-ray photon is absorbed, it exhibits a simultaneous change of the nuclear state and the vibrational quantum state. The combination of these creates new energy levels, which can be occupied (see Figure 2.15).

If the nucleus is hypothetically fixed and isolated and experiences no recoil from the X-ray absorption process, only X-ray photons, which have the 14.41 keV nuclear resonance energy E_0 are created. If $E_0 \neq E$, the probability to excite the nucleus via phonon assistance with an X-ray photon in the energy range $[E, E + dE]$ is given by $S(E)dE$. As the nucleus is not isolated and lattice excitation is considered (see Figure 2.15 righthand side), new energy levels are created from the combinations of nuclear and vibrational quantum states by off resonance excitation [45]. The excitation probability density $S(E)$ contains all possible phonon energies. The simplified picture of the Einstein solid does not hold in real materials as many phonons exist with different energies. The sidebands in the excitation probability broaden, and show a continuous phonon spectrum. The distinction into one phonon and multi-phonon contribution on the other hand is still applicable. The solid lines refer to phonon creation, and the dashed sidebands refer to the phonon annihilation processes. If the incident X-ray energy is not sufficient to excite the nuclear resonance ($E < E_0$), phonons must be annihilated, and if the energy is exceeding the nuclear resonance ($E > E_0$), phonons are created. The Boltzmann factor provides the

ratio of the probability that this process happens.

$$S(E) = \exp(\beta \cdot E) S(-E) \quad (2.37)$$

with $\beta = \frac{1}{k_B T}$. After the excitation process, the decay of the nucleus back into the ground state will result in emission of an X-ray photon with the energy of 14.4125 keV or by transfer of the energy to the electron system. This creates a conversion electron with an energy of 7.3 keV from the K-shell of Fe (highest probability). The hole created is filled by electrons and fluorescent conversion X-rays with a characteristic energy of 6.3 keV are emitted, which provide the measured signal [109]. The recoil energy [110],

$$\langle E \rangle = \int E \cdot S(E) dE = \frac{\hbar^2 k^2}{2M} = E_R, \quad (2.38)$$

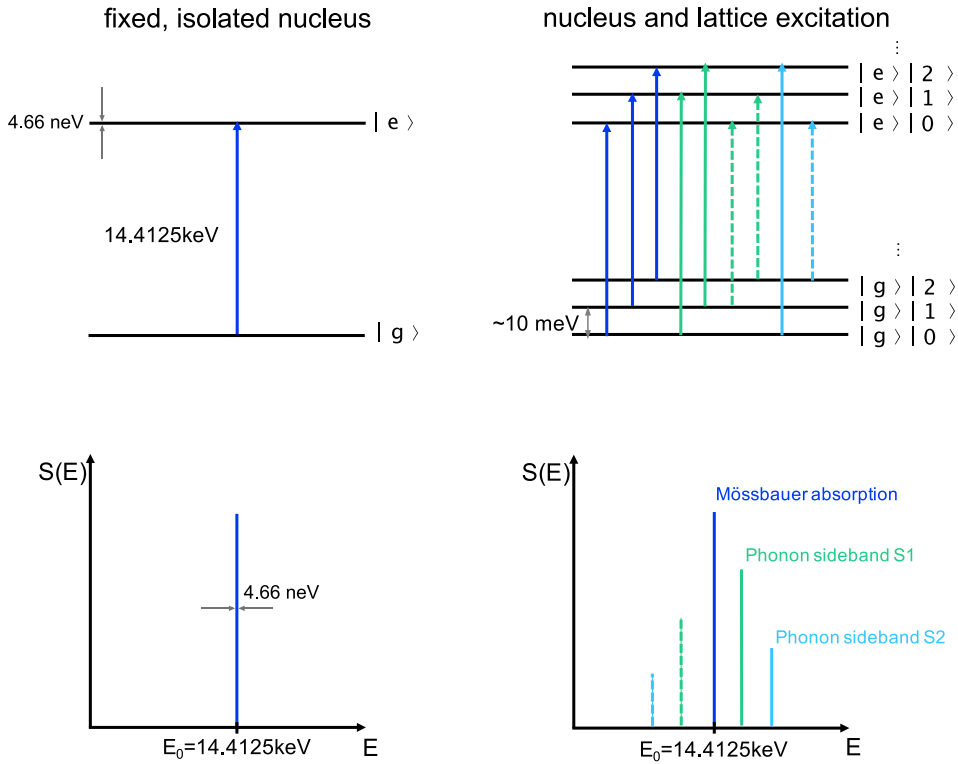


Figure 2.15.: Energy level scheme of a hypothetically fixed nucleus (left) and a nucleus in an Einstein solid (right). The energy levels created through X-ray absorption are shown at the top. g denotes the ground state, e the excited states with the respective number of phonons present. Next to the elastic peak (Mössbauer absorption line) the dashed and solid lines represent the phonon side bands. They indicate transitions, which represent phonon annihilation and creation. Figure adapted from [45].

given by Equation 2.38, together with $E_R = 2$ meV for ^{57}Fe , leads to the normalization of the excitation probability $S(E)$. Equation 2.38 is known as Lipkin's sum rule [110]. The one phonon excitation probability (in the harmonic approximation [111]) is as follows

$$S_1 = \frac{E_R}{E - (1 - \exp(\beta E))} g(E). \quad (2.39)$$

From the measured and normalized excitation probability, the one-phonon contribution S_1 can be extracted [111]. NRIXS is only sensitive to the lattice dynamics [107, 111–113]. The measurement of the phonon excitation probability therefore provides direct access to the ^{57}Fe -partial vibrational density of states, $g(E)$, as it is directly proportional to the parameter S_1 [107, 111–113]:

$$g(E) = \begin{cases} \frac{E}{E_R} \tanh(x) (S_1(E) + S_1(-E)) & \text{if } E > 0 \\ 0 & \text{if } E < 0. \end{cases} \quad (2.40)$$

With the knowledge about $g(E)$, reflecting the lattice dynamics of the Fe sub-lattices, a number of thermodynamic properties such as the vibrational entropy S_{lat} and specific heat C_V , as well as the Lamb Mössbauer factor f_{LM} and the Fe contribution to the Debye temperature Θ_D can be extracted [34, 47].

$$S_{\text{lat}} = 3k_B \int_0^\infty (x \coth x - \ln(2 \sinh x)) g(E) dE, \quad (2.41)$$

with $x = \frac{\beta E}{2}$ and $\beta = (k_B T)^{-1}$,

$$C_{\text{lat}} = 3k_B \int_0^\infty x^2 \cdot \text{csch}(x) g(E) dE, \quad (2.42)$$

$$f_{\text{LM}} = \exp\left(-E_R \int \frac{g(E)}{E} \cdot \coth(x) dE\right). \quad (2.43)$$

In order to find a suitable Debye temperature, the entropy Debye temperature Θ_D as well as the specific heat Debye temperature can be directly calculated from the moments ϵ_n of $g(E)$ [114–116]. In the high temperature limit the logarithmic moment provides the entropy Debye temperature:

$$\ln(\epsilon_0) = \frac{\int_0^\infty \ln(E) g(E) dE}{\int_0^\infty g(E) dE} \quad (2.44)$$

and

$$k_B \Theta_D(0) = \exp\left(\frac{1}{3}\right) \epsilon_0. \quad (2.45)$$

The second moment of $g(E)$

$$\epsilon_2 = \frac{\int_0^\infty E^2 g(E) dE}{\int_0^\infty g(E) dE} \quad (2.46)$$

provides the specific heat Debye temperature, which is defined as

$$k_B \Theta_D(2) = \left(\left(\frac{2}{3} + 1 \right) \epsilon_2 \right)^{\frac{1}{2}}. \quad (2.47)$$

Furthermore, the Debye temperature can also be obtained via the Lamb-Mössbauer factor f_{LM} by using Equation 2.33. One has to bear in mind that these Debye temperatures only show the Fe contribution to the total Debye temperature, but yield very good results as the sample system mainly consists of Fe. The assumption to use this approximation is in a good agreement with the experiments performed around the phase transition at elevated temperatures and consistent with DFT calculations (as described in subsection 5.1.1). Further details about NRIXS and its data evaluation can be found in section A.4.

3. Experimental Methods

In the following chapter an overview over the used experimental setups will be given. To gain knowledge on element-specific properties, it was necessary to utilize photons with specific energies to excite core electrons of given elements. Except for the Mössbauer experiments where radioactive sources have been used to produce gamma-photons, all experiments have been performed using highly brilliant (high photon flux in small angle and short period of time) synchrotron radiation at different synchrotron light sources. This gave the possibility to tune the incident excitation energies and photon polarization as needed. All experiments in this work have been done either at the European Synchrotron Radiation Facility **ESRF** in Grenoble, France (for the case of X-ray absorption experiments, XMCD and EXAFS) or at the Advanced Photon Source **APS** at the Argonne National Laboratory, Argonne, USA, for the NRIXS experiments, both using hard X-ray radiation.

3.1. Synchrotron Radiation

Synchrotron radiation is produced by the acceleration of electrons up to nearly the speed of light, which are fed into a storage ring, where they are kept on a circular orbit. The electrons are forced onto a circular trajectory and are accelerated. According to classical electrodynamics, accelerated charges emit electromagnetic radiation due to Lorentz forces [97]. A synchrotron radiation facility usually consists of four elemental parts. An electron source, where free electrons are usually emitted thermally, a linear accelerator (LINAC) or micron, the synchrotron, or booster ring, and the storage ring. A schematic overview over the setup of a synchrotron facility can be seen in Fig 3.1. The free electrons are focussed into a small beam and then fed into a pre-accelerator, usually a LINAC. Here the electrons are pre-accelerated up to a few MeV by utilizing alternating electric fields. From the LINAC, the electrons are injected in packets, so called bunches, into the booster ring. Here, the electrons can be accelerated up to values of a few GeV (6-7 GeV in case of the ESRF and APS [117, 118]). The electron bunches are then injected into the storage ring, where the beam is kept on a circular orbit using high magnetic fields. As an electron bunch is radially accelerated in this magnetic field (either in bending magnets or in so

called insertion devices, like wigglers and undulators), synchrotron radiation is produced. To maintain the high acceleration energy, the electron bunches are coupled into radio frequency cavity resonators to not suffer losses from the emission of synchrotron radiation. Due to the high velocity of the circulating electron bunches close to the speed of light, relativistic effects need to be taken into account leading the beam to suffer from frequency losses due to the relativistic Doppler effect and Lorentz contractions. In order to provide a stable orbit, the beam is focussed with quadrupole or sextuple magnets. The beam lines are built out tangentially from the ring. As mentioned before, the synchrotron radiation enters the experimental end stations after bending magnets or insertion devices. Bending magnets are dipole magnets, which first polarize the synchrotron radiation linearly in a vertical plane and the electrical field parallel to the plane of orbit [97]. Moving away from the plane of orbit the linear polarization tends to decrease while the circular contributions increase. To increase the brilliance and to control the polarization of the synchrotron beam, undulators are used. Undulators are arrays of dipole magnets, which are oriented with their fields opposite to each other [30]. Due to Lorentz force, the electrons from the storage beam are forced onto a wiggled path. Depending on the periodical arrangement of the magnetic arrays, radiation can be produced to interfere for specific wavelengths. As the gap between the undulators can be adjusted, their magnetic field strength is controllable. Planar undulators are used to produce linearly polarized light, while helical undulators are used for the production of elliptically or circularly polarized light. Behind the bending magnet or the insertion device, single crystal monochromators are used to focus and monochromatize the synchrotron radiation to the desired energy.

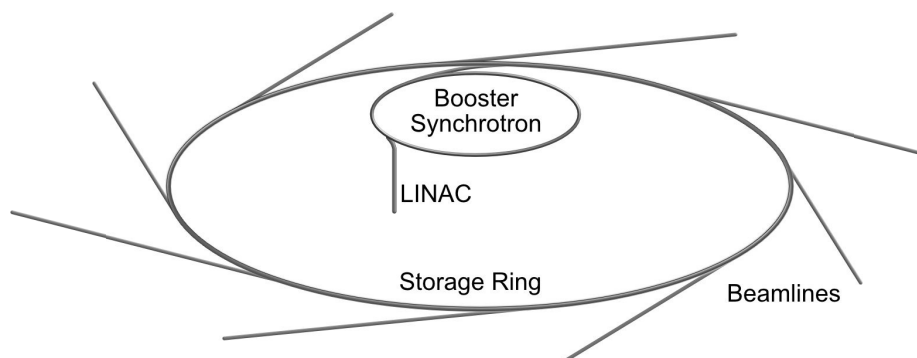


Figure 3.1.: Schematic aerial view of a synchrotron radiation facility.

3.2. X-ray Absorption Spectroscopy

3.2.1. X-ray Magnetic Circular Dichroism

ESRF ID12

All XMCD measurements in this work have been performed at the circular polarization beam line ID12 at the ESRF. Here it is possible to measure with linearly or circularly polarized light in an energy range of 2-15 keV [119], at low temperatures and in high magnetic fields. The beam line has 3 undulators, which are optimized for the different energy ranges. The XMCD measurements have been performed in a high field superconducting solenoid with the possibility to apply a magnetic field up to 17 T [120]. The direction of the magnetic field is parallel to the incident X-ray beam and temperature in the setup can be regulated from 2.2 K to 325 K [41]. The XMCD measurements have been performed on powder samples with signal detection using the fluorescence yield. The signal was detected by a photo diode, the incoming beam flux I_0 is measured by a Ti foil and serves as reference for the detected X-ray absorption signal. Figure 3.2 depicts the schematic setup of the ID12.

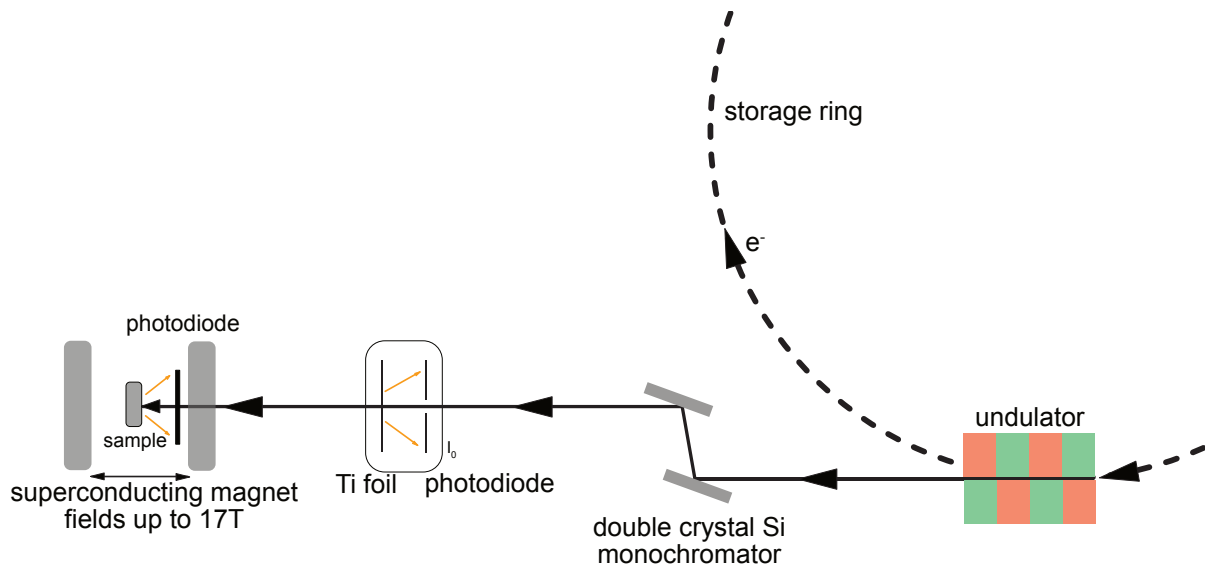


Figure 3.2.: Experimental setup in fluorescence mode of beam line ID12 at the ESRF, Grenoble. The sample temperature can be varied in a range of 2 – 325 K and magnetic fields up to 17 T can be applied.

3.2.2. Extended X-ray Absorption Near Edge Structure

ESRF BM30b

EXAFS measurements have been performed at the beam line BM30b of the ESRF, Grenoble. The X-rays are fed into the experimental end station with a bending magnet. They first pass 3 sets of micrometric slits and a mirror before passing through a monochromator consisting of two Si crystals. Here the energy of the incident beam can be tuned in a range of 4 – 40 keV. The mirrors are used for the vertical and horizontal beam divergence. The beam can be focussed down to $100 \times 300 \mu\text{m}$. After passing another mirror, the incident beam current I_0 is measured. For our experiments the samples are ground into a fine powder and mixed with cellulose before being pressed into a pellet of 5 mm diameter and mounted in a helium cryostat with a temperature range from 20 – 300 K. The experiments have been performed in fluorescence mode under an incident angle of 45° . To capture the emitted fluorescence signal, a liquid nitrogen cooled Canberra Germanium detector with an array of 30 energy selective elements and an energy resolution of 300 eV was used [121]. From the fluorescence, the absorption signal $\mu(E)$ can be calculated by dividing it by the initial photocurrent I_0 .

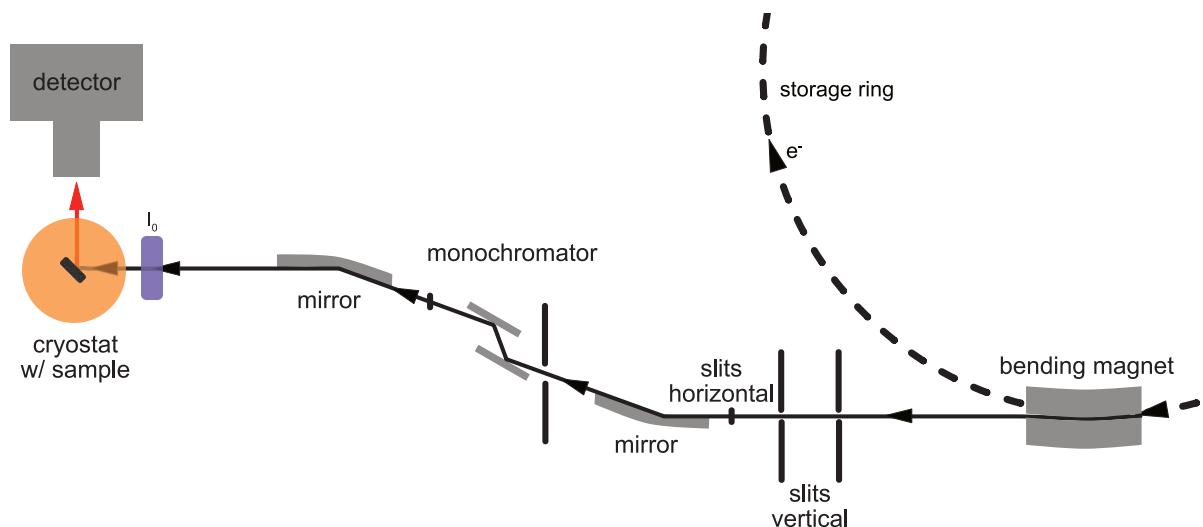


Figure 3.3.: Schematic view of the experimental setup in fluorescence mode of beam line BM30b at the ESRF, Grenoble. The sample temperature can be varied in a range of 20 – 300 K. Adapted from [121].

3.3. Nuclear Resonant Inelastic X-ray Scattering

APS 3ID

^{57}Fe nuclear resonant inelastic X-ray scattering experiments (NRIXS) have been performed at the Sector 3-ID (beam lines 3-ID B and D) at the Advanced Photon Source, Argonne National Laboratory to investigate the lattice dynamics and to obtain the VDOS [107, 108, 112, 113, 122].

For these experiments a very narrow energetic bandwidth of the incident X-ray beam is necessary. The energy of the incoming beam needs to be precisely tuned to an X-ray energy around the nuclear resonance energy of $E_0 = 14.412\text{ keV}$ of ^{57}Fe . After passing an undulator, the linearly polarized X-ray beam needs to be reduced in energetic bandwidth. In order to obtain that small energetic bandwidth, the X-ray beam first passes through a high heat-load monochromator consisting of two water-cooled diamonds, which reduces the energetic bandwidth of the incident X-ray down to 1 eV . Then it passes a high res-

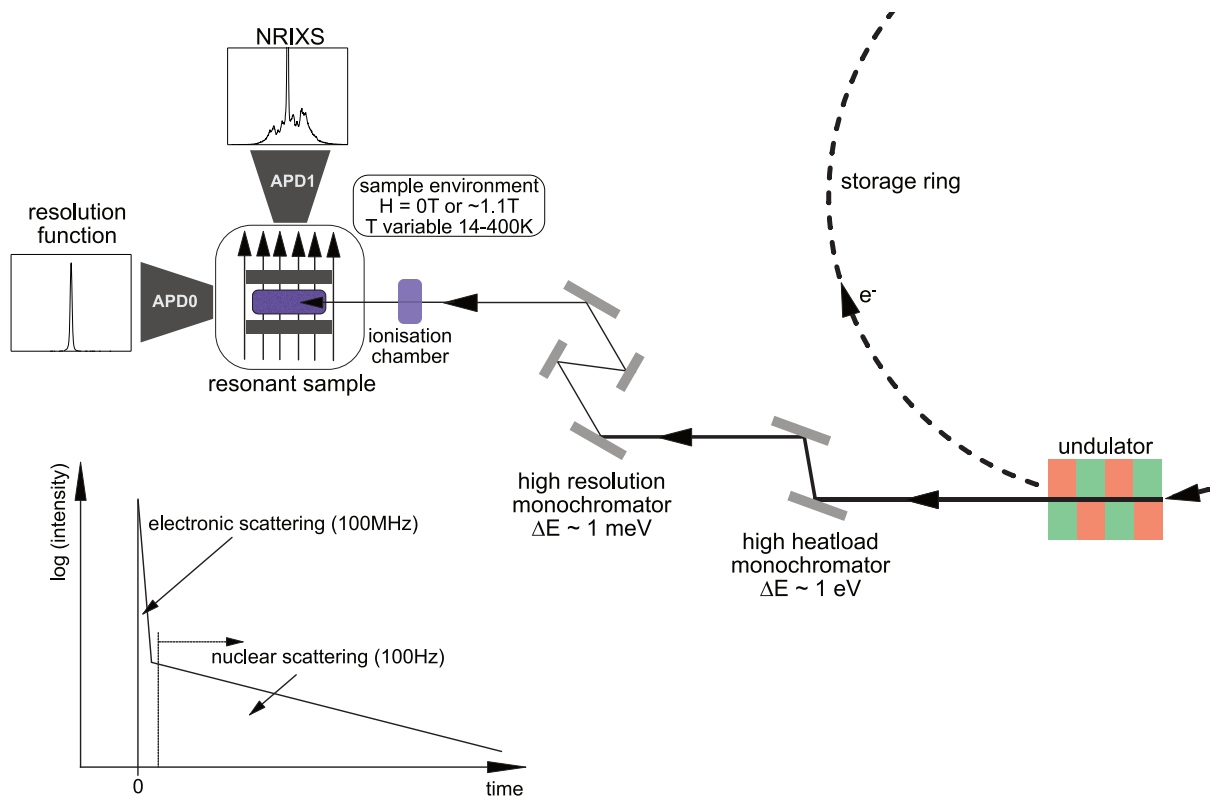


Figure 3.4.: Schematic view of the experimental setup of beam line 3-ID at the APS, Argonne. The incident X-ray beam is tuned down to a narrow energetic bandwidth and focused on the sample in grazing incidence. The sample environment can be adjusted in terms of temperature and a magnetic field can be applied. The inset depicts the time delay to omit non resonant scattering events (adapted from [45]).

olution silicon crystal monochromator. The bandwidth is cut down here to 1 meV [123]. In the next step, the beam passes through a toroidal mirror and the collimated beam is focussed onto the sample at grazing incidence relative to the sample surface in an experimental setup with or without applied field. In the experimental setup, two diodes are used to collect the data. An avalanche photo diode (APD0) measures the resolution function, the incident beam shape, which has to be subtracted from the signal before evaluation. The second avalanche photo diode (APD1) is used as a detector to register predominantly the 6.3 keV fluorescence X-ray signal emitted only from the nuclear resonant scattering events. To omit scattering processes like electronic scattering, which happen much faster than the nuclear scattering (3 orders of magnitude), the detector is connected to a timing circuit, introducing an electronic time delay in the operation of the detector [45], thus omitting the fast electronic scattering events. The samples were measured in two different setups. For the low temperature measurements up to 300 K, the samples were placed in setup using a closed cycle cryostat and were mounted under a dome shaped Be window. Above room temperature, the samples were placed on a custom built heater setup operating under atmospheric pressure with an applied magnetic field of 1.1 T, or without. The samples used in the NRIXS experiments were prepared as powder with grain sizes $< 100 \mu\text{m}$ and embedded in epoxy resin on a Cu plate to provide good thermal contact of the heater to the sample. In order to heat the sample throughout the experiments, a LakeShore 340 temperature controller with a silicon diode temperature sensor and PID regulation was used. This setup provided the experiment with a temperature accuracy of 0.1 K.

3.4. Mössbauer Spectroscopy

To obtain information on the local magnetism under the influence of rising Mn content ^{57}Fe Mössbauer experiments have been done. The experiments were performed in transmission geometry as schematically shown in Figure 3.5. The source, ^{57}Co in a Rh matrix, which produces the γ -rays with an energy of 14.41 keV, is mounted on an electromechanical Mössbauer drive. Behind the sample a detector (here a proportional counter) collects the transmitted signal. The Mössbauer drive is moving with a triangular velocity function in constant acceleration mode and the energy modulation of the γ -ray is produced due to the Doppler effect. The resulting spectrum captured by the detector will have negative intensities (absorption lines) as the incident γ -rays will be partially absorbed by the sample at specific energies. For low temperature measurements, the sample can be cooled down to liquid helium temperature in a liquid nitrogen/helium bath cryostat. The measurement setup used for high field measurements, in order to obtain information on

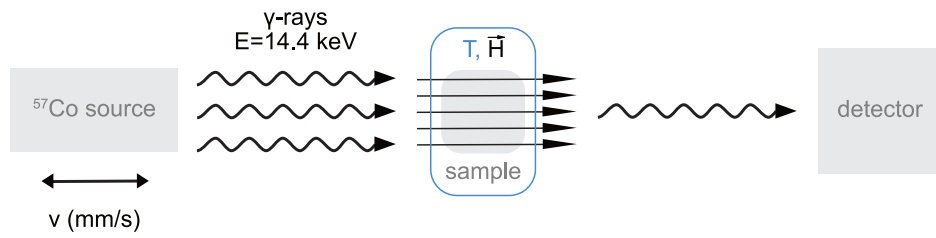


Figure 3.5.: Experimental setup of the transmission Mössbauer experiments. The drive moves with constant acceleration. The sample environment can be cooled down to 4.3 K and a magnetic field of 5 T can be applied.

the spin structures in the sample, utilizes a magnet cryostat with superconducting coils in split-pair (Helmholtz) geometry, making it possible to measure in magnetic fields up to 5 T with the γ -ray direction either parallel (longitudinal geometry) or perpendicular (transverse geometry) to the magnetic field direction.

4. Sample Preparation and Characterization

All the samples used throughout this work were prepared by the Functional Materials Group of Prof. Dr. Oliver Gutfleisch at the TU Darmstadt. The samples were produced by melting in Ar atmosphere. After melting the samples were subsequently annealed at a temperature of 1373 K for 7 days in an Ar-filled quartz tube to provide a pure 1:13 phase. The annealing process was followed by quenching in water. For the hydrogenated samples the (experimentally) full hydrogenation (see section 2.3) was obtained by heating the sample in a furnace at 0.9 bar H_2 atmosphere at 723 K for one hour. All sample preparation followed the methods according to the procedures described in [68, 124]. A full listing of all samples used within this work is given in Table 4.1, with transition temperature and the measurement techniques performed in each sample.

As Mn doping and hydrogenation strongly influences the transition temperature (as described in section 2.3), the samples used throughout this work have been magnetically pre-characterized via temperature dependent vibrating sample magnetometry, using a Quantum Design PPMS DynaCool to precisely determine the transition temperatures and the thermal hystereses of the compounds. Furthermore $M(H)$ protocols have been used to determine the residual α -Fe content of the samples, which have to be taken into account for further evaluations, shown later on. First, the transition temperatures of the samples have been evaluated with regard to their Mn content. Figure 4.1 depicts the $M(T)$ measurements of the $LaFe_{1.6-x}Si_{1.4}Mn_x$ series with increasing Mn content ranging from $x = 0 \dots 1$. The magnetization curves have been taken in a temperature range from 50 – 250 K for $x < 0.5$ and from 4 – 200 K for $x > 0.5$ in an external magnetic field of $\mu_0 H = 10$ mT. The samples have been measured using a zero field cooled / field cooled (ZFC-FC) protocol, where the sample is cooled down without the application of an external magnetic field, then heated with an applied magnetic field, and then cooled down again, while the magnetization is measured as a function of temperature. Depicted are the temperature dependent magnetization curves, which are normalized to the maximum of the magnetization at low temperatures at the field cooled branch.

Undoped $LaFe_{1.6}Si_{1.4}$ has a transition temperature of $T_{tr} \sim 190$ K (see Table 4.1). The

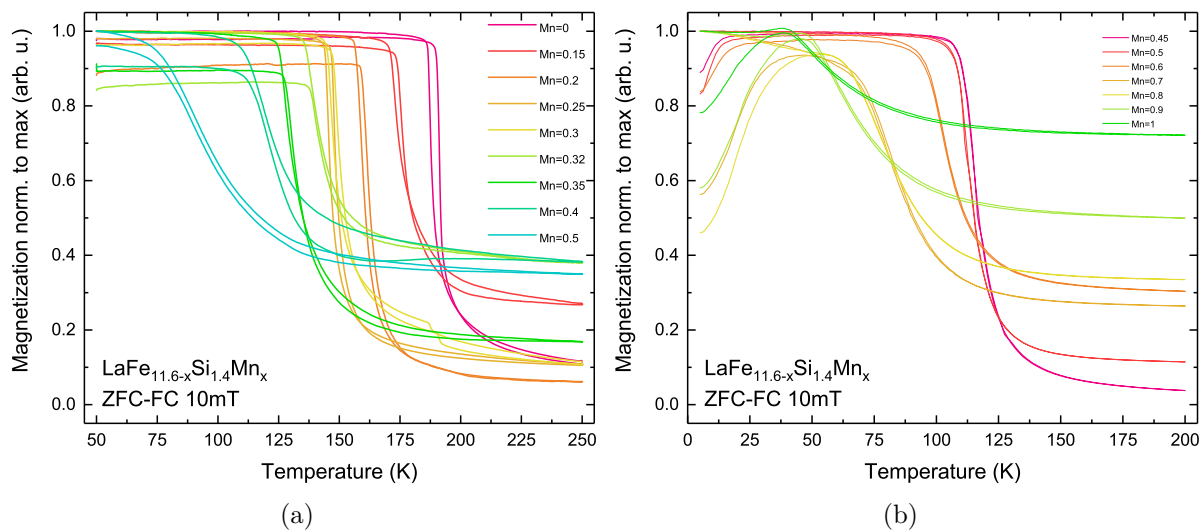


Figure 4.1.: Temperature dependent magnetization measurement of the whole LaFe_{1.6-x}Si_{1.4}Mn_x sample series using a ZFC-FC protocol, measured in an applied external magnetic field of $\mu_0 H = 10$ mT. The color gradient depicts the rising Mn content from red (low Mn content) to blue (high Mn content). (a) Mn contents between $x = 0 \dots 0.5$ (b) $x = 0.45 \dots 1$.

addition of Mn in the LaFe_{1.6-x}Si_{1.4}Mn_x sample series results in a reduction of the transition temperature with rising Mn content, which covers a broad temperature range from a transition of $T_{tr} \sim 190$ K at a Mn content of $x = 0$ down to $T_{tr} \sim 60$ K at a concentration of $x = 1$. This behavior is consistent with the assumption that Mn replaces the Fe_{II}-sites, and due to the reduction in the magnetic moment, shifts the temperature to lower values (see Figure 4.2) [68]. To determine an estimate of the transition temperature, the $M(T)$ curves have been normalized to their minimum and maximum value and the transition temperature refers to the temperature in the middle of the hysteresis. Furthermore, the shape of the transition changes from a sharp first order phase transition at low Mn concentrations to a broader transition, increasing the difficulty to determine a precise transition temperature. The increase in dopant concentration slowly changes the shape of the transition, widening the transition region and progressing towards second order. Figure 4.1 (b) depicts Mn concentrations from $x = 0.45$ to $x = 1$. From the magnetization curves we can deduce spin glass behavior for high Mn concentrations as indicated by the ZFC branch, at temperatures below 50 K. This behavior is in accordance with results from Wang et al. [125] and has also been observed in iron rich amorphous Fe-La alloys [126]. All samples show the first order FM to PM phase transition, as well as an FM to spin glass transition. For Mn concentrations up to $x = 0.6$, it takes place at ~ 10 K, while for higher Mn content, this FM-SG transition is shifted up to ~ 25 K.

Through the Mn doping and replacement of Fe, the magnetization also is strongly af-

Sample list			
Composition	T_{tr} [K]	Hysteresis [K]	Characterization Method
LaFe _{11.6} Si _{1.4}	190	3.2	XMCD, EXAFS, Mössbauer
LaFe _{11.45} Si _{1.4} Mn _{0.15}	176.6	1.3	XMCD, EXAFS, Mössbauer
LaFe _{11.4} Si _{1.4} Mn _{0.2}	161.5	2	Mössbauer
LaFe _{11.35} Si _{1.4} Mn _{0.25}	148	2.4	XMCD, EXAFS, Mössbauer
LaFe _{11.3} Si _{1.4} Mn _{0.3}	151.4	2	XMCD, EXAFS, Mössbauer
LaFe _{11.28} Si _{1.4} Mn _{0.32}	142.7	0.9	Mössbauer
LaFe _{11.25} Si _{1.4} Mn _{0.35}	132.7	0.7	Mössbauer
LaFe _{11.2} Si _{1.4} Mn _{0.4}	122.6	2.3	Mössbauer
LaFe _{11.1} Si _{1.4} Mn _{0.5}	96.6	2.1	XMCD, EXAFS, Mössbauer
LaFe _{11.15} Si _{1.4} Mn _{0.45}	116.6	0.4	Mössbauer
LaFe _{11.1} Si _{1.4} Mn _{0.5}	114.3	0.2	Mössbauer
LaFe ₁₁ Si _{1.4} Mn _{0.6}	105	0.5	Mössbauer
LaFe _{10.9} Si _{1.4} Mn _{0.7}	83	1	Mössbauer
LaFe _{10.8} Si _{1.4} Mn _{0.8}	81	0	Mössbauer
LaFe _{10.7} Si _{1.4} Mn _{0.9}	69.6	0.8	Mössbauer
LaFe _{10.6} Si _{1.4} Mn ₁	63.3	1.4	Mössbauer
LaFe _{11.4} Si _{1.5} Mn _{0.1}	178	4	NRIXS
LaFe _{11.4} Si _{1.6} H _y	330	4	NRIXS
LaFe _{11.4} Si _{1.5} Mn _{0.1} H _y	320	4	NRIXS

Table 4.1.: List of all the samples used within this work with their nominal stoichiometry, their transition temperatures T_{tr} , with an error below 0.1 K, with respective hysteresis width and the experimental method applied to them. The transition temperature refers to the temperature taken at the middle of the hysteresis.

ected. Figure 4.3 depicts the field dependent magnetization curves for the samples in the LaFe_{11.6-x}Si_{1.4}Mn_x series, taken at low temperatures of 5 K (Mn content $x = 0 - 0.5$, Figure 4.3 (a)), and 4.3 K (Mn content $x = 0.45 - 1$, Figure 4.3 (b)). The measurements have been performed in an applied external magnetic field sweep of ± 9 T. From the magnetization curves it is clearly visible that the high field magnetization is drastically reduced by Mn substitution, which partially originates from the removal of Fe and the reduction in the Fe moment. This will be further discussed in subsection 5.4.2 and section 5.2.2. Furthermore, for Mn contents above a value of $x = 0.6$ the magnetization tends not to saturate in an applied external magnetic field of 9 T. We infer possible spin canting from this behavior, which will be thoroughly discussed in subsection 5.4.2. Additionally, all magnetization curves show that they do not reach zero magnetization at zero field in their PM phase. The residual magnetization indicates the presence of additional secondary phases in the samples.

As known from work previously performed on La(Fe,Si)₁₃-based compounds [34, 47, 127],

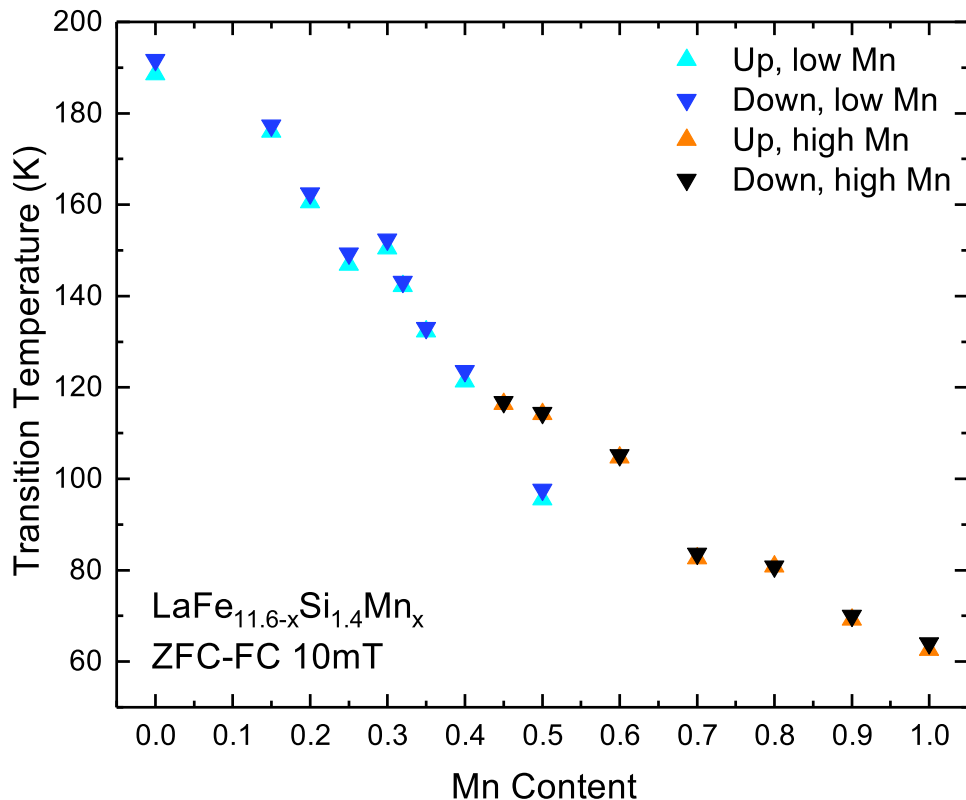


Figure 4.2.: Transition temperatures obtained from magnetization measurements using a ZFC-FC protocol, values taken approximately at the middle of the hysteresis (see Figure A.1 for exact position) for temperature up (upward pointing triangles) and down (downward pointing triangles) measurements. The blue and cyan triangles depict the concentrations between $x = 0 \dots 0.5$, the black and orange triangles the concentrations of $x = 0.45 \dots 1$. The error of the measurement is smaller than the symbols.

and HR-PXRD measurements, (see Figure 4.6, later in this chapter) α -Fe is always present in various contents in addition to the main 1:13 phase. This α -Fe content results in the residual magnetization in the PM phase as seen for all Mn contents. For further evaluations, the residual secondary phase contents of α -Fe have been subtracted from the data or accounted for, where local properties of Fe have been probed within this work. In order to obtain the secondary phase content, field dependent magnetometry has been performed up to an applied external magnetic field of $\mu_0 H = 9$ T in the paramagnetic phase of each sample, for the hydrogenated samples at a measurement temperature of 360 K, for the Mn-doped samples at 300 K. The residual α -Fe content was determined following the route as described in Ref. [127]. From the fit of the magnetization curve in the high field range (from 1 – 2 to 9 T) and the known value for the α -Fe magnetization at room temperature of $218 \frac{\text{emu}}{\text{g}}$ [128] it was possible to determine the secondary phase content. A more detailed description can be found in section A.2. On the sample system with

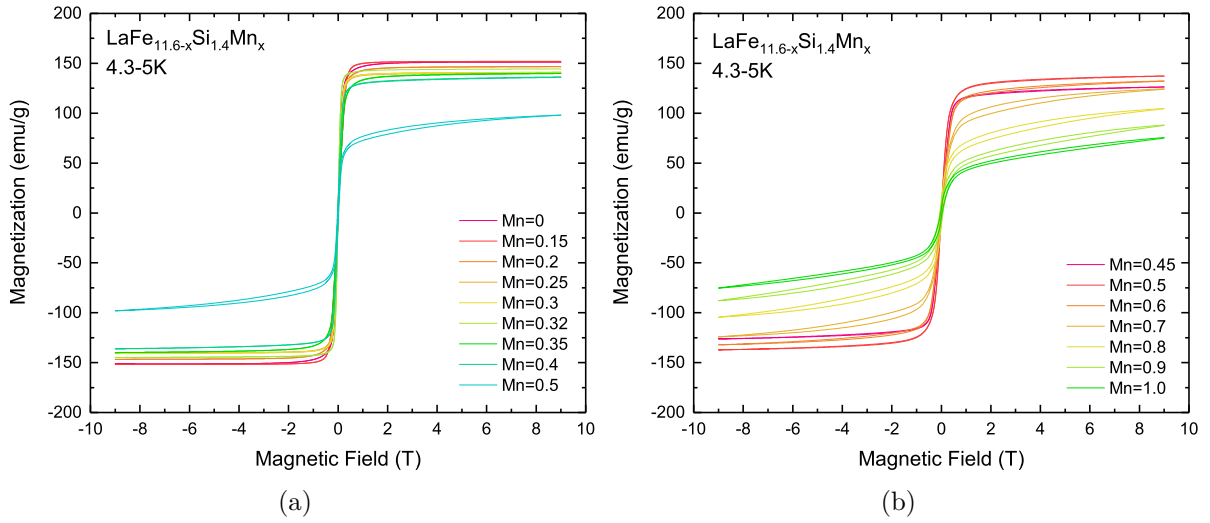


Figure 4.3.: Field dependent magnetometry in low temperature (4.3 – 5 K) for all Mn doped samples in the LaFe_{11.6-x}Si_{1.4}Mn_x series ranging from Mn contents of 0-0.5 (a) and 0.45 to 1 (b). Curves are shown without correction for residual secondary phase contents.

α -Fe content in the LaFe_{11.6-x}Si_{1.4}Mn_x series at EXAFS experiments

Stoichiometry	α -Fe content
LaFe _{11.6} Si _{1.4}	1.75 %
LaFe _{11.45} Si _{1.4} Mn _{0.15}	6.79 %
LaFe _{11.35} Si _{1.4} Mn _{0.25}	3.47 %
LaFe _{11.3} Si _{1.4} Mn _{0.3}	1.37 %
LaFe _{11.1} Si _{1.4} Mn _{0.5}	9.34 %

Table 4.2.: Sample list of LaFe_{11.6-x}Si_{1.4}Mn_x EXAFS samples.

Mn addition, XMCD, EXAFS, as well as Mössbauer experiments have been performed to gain a detailed picture of the interplay of structure and magnetism with respect to Mn concentration across the first order phase transition. For all experiments, the samples have been crushed and ground into a fine powder. For the XMCD experiments, the powder has been mixed with carbon and pressed into a pellet. EXAFS measurements have been performed on pellets pressed from a homogeneous mixture of sample powder and cellulose. The pellets used in EXAFS experiments have been magnetically characterized afterwards via field dependent magnetometry as described before in order to obtain the residual α -Fe secondary phase (see Table 4.2).

Furthermore, the samples prepared for use in the NRIXS experiments have been enriched with an amount of 30 % of the ⁵⁷Fe isotope during the preparation. This was done to

improve the data quality and shorten the acquisition time during the experiments. For all the experiments, the ingots were crushed and ground into a polycrystalline powder with a grain size $\leq 100 \mu\text{m}$. These samples had a nominal composition of $\text{LaFe}_{11.4}\text{Si}_{1.5}\text{Mn}_{0.1}$, $\text{LaFe}_{11.4}\text{Si}_{1.5}\text{Mn}_{0.1}\text{H}_y$ and $\text{LaFe}_{11.4}\text{Si}_{1.6}\text{H}_y$ with a hydrogen content of $y \sim 1.6$. Figure 4.4 (a) demonstrates the shift of the transition temperature due to the addition of a small Mn content. Even for additions as small as $x = 0.1$ the phase transition is reduced by approximately 12 – 16 K in comparison to pure $\text{LaFe}_{11.6}\text{Si}_{1.4}$. This shift can be reversed by hydrogenation. Figure 4.4 (b) shows the hysteresis obtained for Mn addition and full hydrogenation, $y = 1.6$, and an increase in the phase transition temperature by 142 K. Hydrogenation without any Mn addition (Figure 4.4 (b)) increases the transition temperature even more, approximately by 152 K with respect to the non hydrogenated references to transition temperatures around 320 – 330 K. Regardless of the shift of the temperatures, the thermal hysteresis in the Mn doped and hydrogenated compounds remains small, being as narrow as 3 K.

To determine the influence of a magnetic field on the transition temperature for the NRIXS experiments, temperature dependent magnetometry has been performed on the hydrogenated compound with the stoichiometry $\text{LaFe}_{11.4}\text{Si}_{1.6}\text{H}_{1.6}$ as a function of increasing magnetic fields. The field values varied from 0.25 – 3 T. According to the results of these $M(T)$ data, Figure 4.5 (a) shows the shift induced by increasing the magnetic fields.

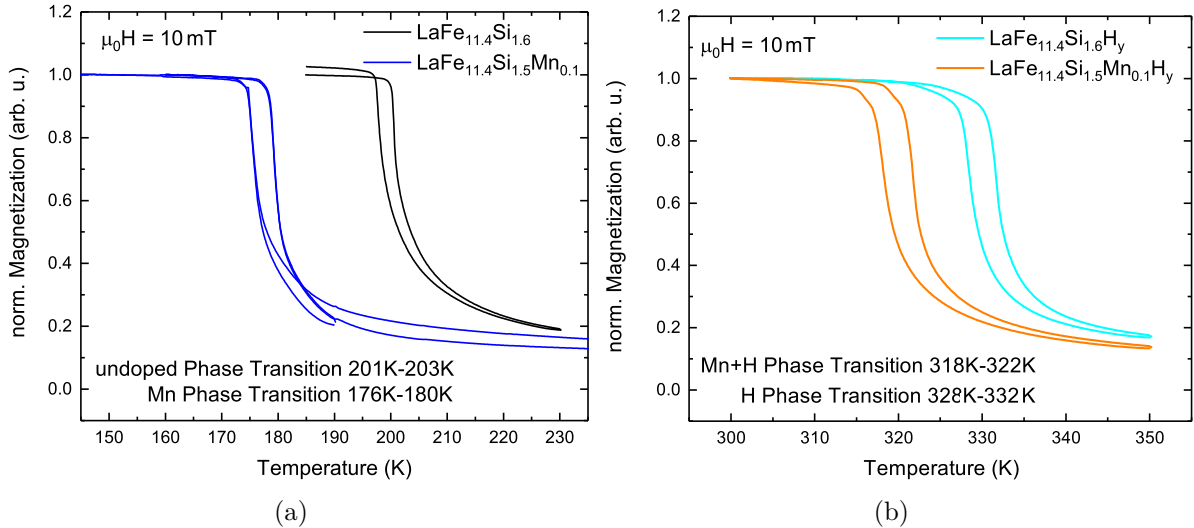


Figure 4.4.: Temperature dependent magnetization curves for the samples, enriched with 30 % of ^{57}Fe for the NRIXS experiments. (a) depicts the hystereses of $\text{LaFe}_{11.6}\text{Si}_{1.4}$ without Mn (black line) and of $\text{LaFe}_{11.4}\text{Si}_{1.5}\text{Mn}_{0.1}$ with small Mn addition (blue line), (b) shows the hystereses with the FOPT for the hydrogenated compounds $\text{LaFe}_{11.4}\text{Si}_{1.6}\text{H}_{1.6}$ (cyan line) and $\text{LaFe}_{11.4}\text{Si}_{1.5}\text{Mn}_{0.1}\text{H}_{1.6}$ (orange line).

From that graph it is clear that the change in the transition temperature amounts to $3.5 \frac{\text{K}}{\text{T}}$, thus shifting the transition temperature for the measured compound from $T_{\text{tr}} = 329 \text{ K}$ to $T_{\text{tr}} = 333 \text{ K}$ in a field of 1.1 T . Figure 4.5 (b) shows the direct comparison of hydrogenated $\text{LaFe}_{11.4}\text{Si}_{1.6}\text{H}_{1.6}$ in two different magnetic fields, which roughly correspond to the fields applied in the NRIXS measurements, which have been taken at zero external magnetic field and in a magnetic field of 1 T . From the graph the shift of the FOPT of $3.5 \frac{\text{K}}{\text{T}}$ is apparent and the phase coexistence region is broadened for an increased magnetic field.

As these samples were measured with ^{57}Fe -NRIXS to determine the vibrational thermodynamic properties, the residual α -Fe content of the powder prepared had to be accounted for and quantitatively estimated. The powder prepared for the beam time in 2016 had residual contents of $< 2\%$ for all samples (see Table 4.3). As this value only changes the VDOS within the error margin of the measurements, the Fe contents have not been subtracted from the VDOS. For a detailed description of the correction accounted for the secondary phase contents, see Appendix A.

In the 2017 beam time, the powder of the hydrogenated sample, which has been measured, had an α -Fe content of 4.47% . This value has been subtracted from the VDOS of the hydrogenated compound and the thermodynamic properties shown have been calculated from the α -Fe-corrected VDOS.

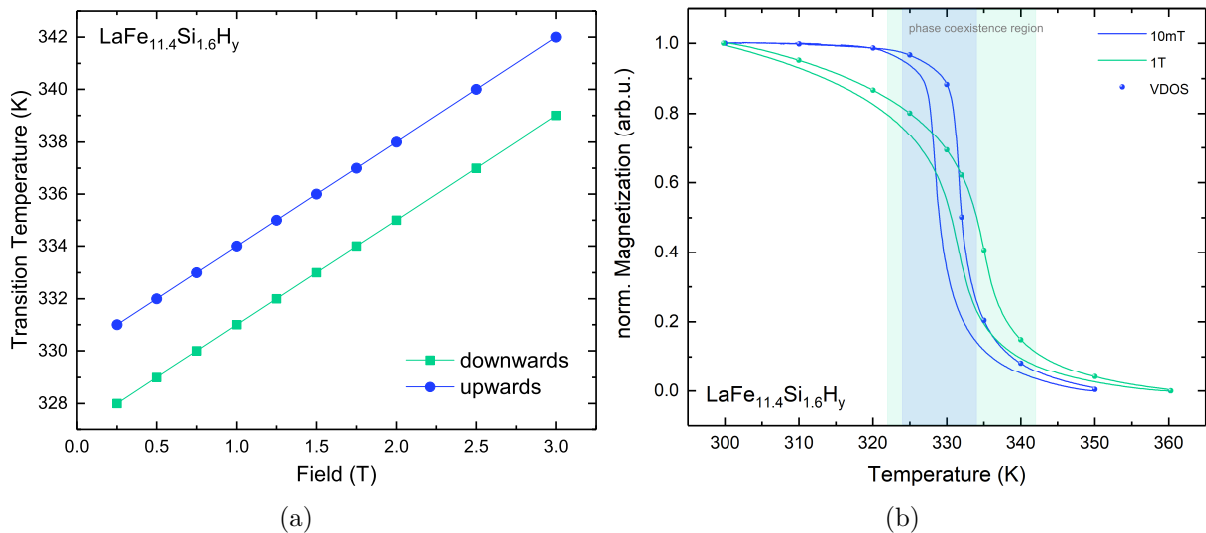


Figure 4.5.: (a) Change of the transition temperature, measured with increasing (blue) and decreasing (green) temperature (upwards and downwards) for magnetic fields up to 3 T . (b) Temperature dependent magnetization curves for hydrogenated $\text{LaFe}_{11.4}\text{Si}_{1.6}\text{H}_{1.6}$ in a low field 10 mT (blue curve) and in an applied magnetic field of 1 T (green curve), corresponding to the NRIXS measurements. The blue dots indicate the points, where NRIXS spectra have been taken. The shaded areas correspond to the phase transition region.

NRIXS samples		
Stoichiometry	α -Fe content	Beamtime
$\text{LaFe}_{11.4}\text{Si}_{1.5}\text{Mn}_{0.1}$	1.68 %	2016
$\text{LaFe}_{11.4}\text{Si}_{1.5}\text{Mn}_{0.1}\text{H}_{1.6}$	1.72 %	2016
$\text{LaFe}_{11.4}\text{Si}_{1.6}\text{H}_{1.6}$	1.91 %	2016
$\text{LaFe}_{11.4}\text{Si}_{1.6}\text{H}_{1.6}$	4.47 %	2017

Table 4.3.: Sample list of NRIXS samples.

To confirm the structural phase, high resolution powder X-ray diffraction (HR-PXRD) of ^{57}Fe enriched $\text{LaFe}_{11.4}\text{Si}_{1.6}\text{H}_{1.6}$ has been performed at the ESRF using X-rays with an energy of 31 keV. From the spectrum depicted in Figure 4.6 it is obvious that the sample is in its 1:13 majority phase. The orange line at 11.3° , 16° , 19.7° depict the fit of the secondary phase and mark the peaks of the residual secondary phase of α -Fe in the range depicted. The blue line is a fit of the 1:13 phase to the spectrum.

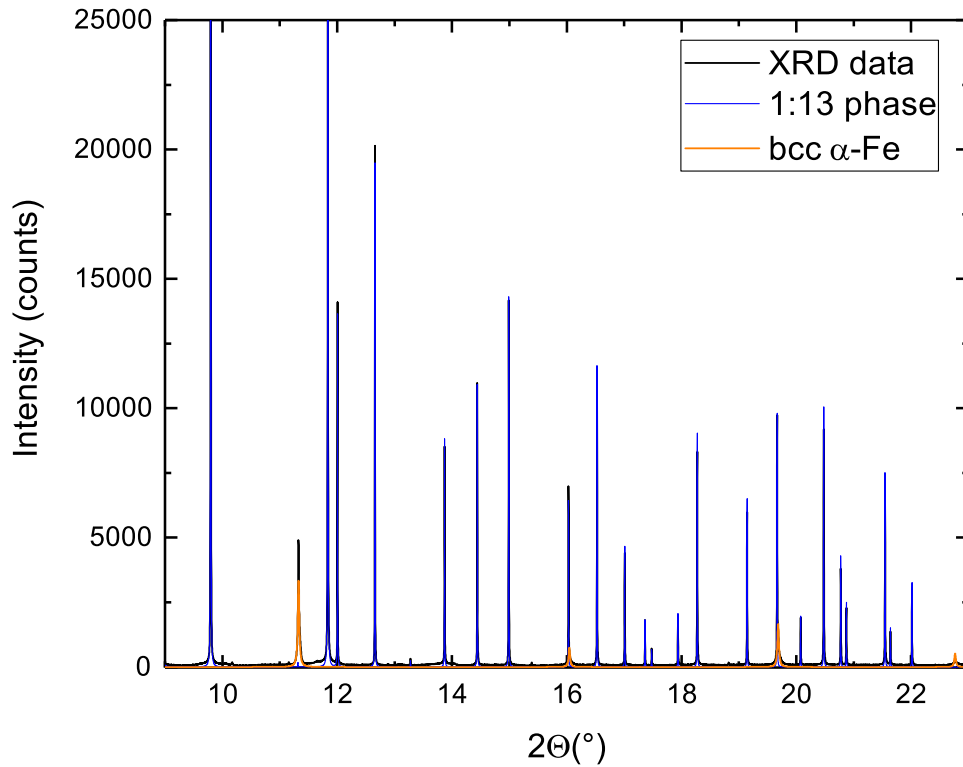


Figure 4.6.: High resolution powder X-ray diffraction (HR-PXRD) on powder of the ^{57}Fe enriched $\text{LaFe}_{11.4}\text{Si}_{1.6}\text{H}_{1.6}$ sample ($E = 31$ keV) at 310 K. The orange line marks the fit of the secondary phase of α -Fe to the spectrum (black line). The other peaks can be attributed to the 1:13 majority phase (fit of 1:13 phase in blue). HR-PXRD data have been provided by C. Giacobbe, ESRF.

5. Experimental Results and Discussion

5.1. Fe-partial Thermodynamics and Phonon Density of States in Hydrogenated and Mn doped $\text{La}(\text{Fe},\text{Si})_{13}$ obtained via ^{57}Fe NRIXS

In this chapter the vibrational contributions of the Fe-sub-lattices to the vibrational density of states (VDOS) and their influence on the thermodynamic behavior of various $\text{LaFe}_{13-x}\text{Si}_x$ compounds with Mn and H addition in different compositions are discussed. Different thermodynamic properties such as the lattice entropy S_{lat} , lattice specific heat C_{lat} and Debye temperature Θ_{D} have been extracted and compared. The VDOS can be experimentally obtained by utilizing ^{57}Fe NRIXS (see section 2.6). All NRIXS experiments in this work have been performed at the sector 3-ID at the APS, Argonne.

5.1.1. Impact of Hydrogenation and Mn Addition on the VDOS and Thermodynamics in $\text{La}(\text{Fe},\text{Si})_{13}$

To investigate the influence of interstitial atoms and dopants on the lattice contribution to the thermodynamic properties, 3 different samples have been measured across the metamagnetic phase transition and in their ferromagnetic and paramagnetic state, respectively. Figure 5.1 shows the ^{57}Fe -partial vibrational density of states of a reference sample with a nominal stoichiometry of $\text{LaFe}_{11.6}\text{Si}_{1.4}$ (orange line) in its ferromagnetic state. This sample has been selected as a comparison to the other studied compounds, which are close to this reference in the contents of Fe and Si. The data for the reference specimen is taken from [34] and is consistent with the studies in [47]. The samples prepared for the beamtime in 2016 all had a residual α -Fe content of $< 2\%$ (see chapter 4), which has not been subtracted for the discussion of the VDOS as the effect is smaller than the error of the measurements. The undoped compound has been compared to a sample with only a small Mn addition ($\text{LaFe}_{11.4}\text{Si}_{1.5}\text{Mn}_{0.1}$, green line), pure H addition ($\text{LaFe}_{11.4}\text{Si}_{1.6}\text{H}_{1.6}$,

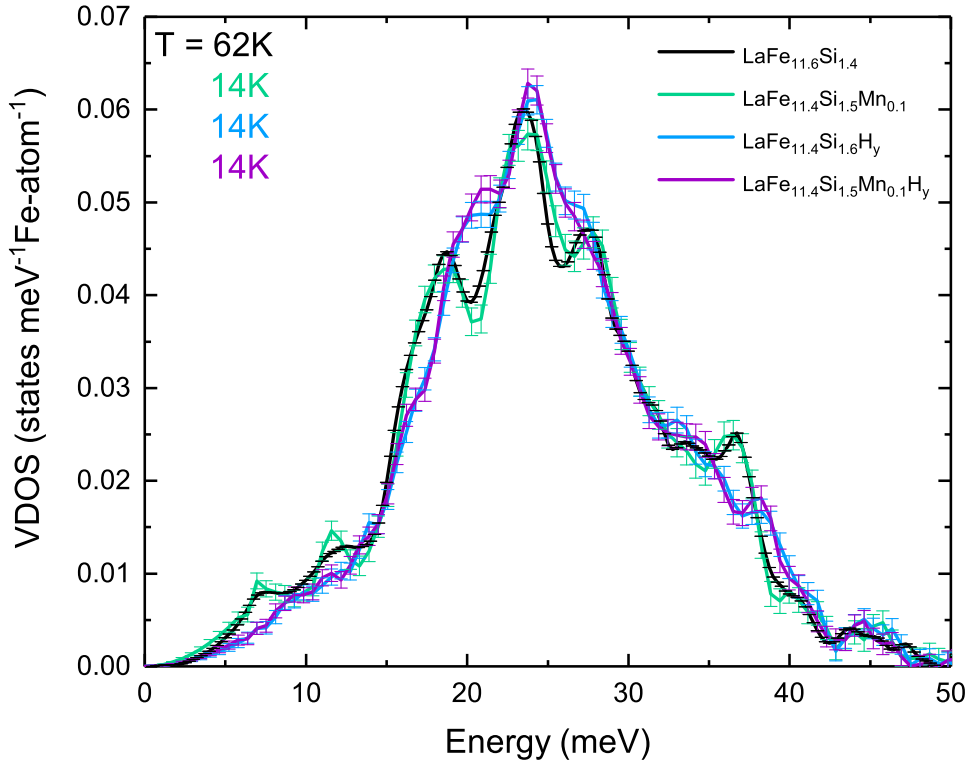


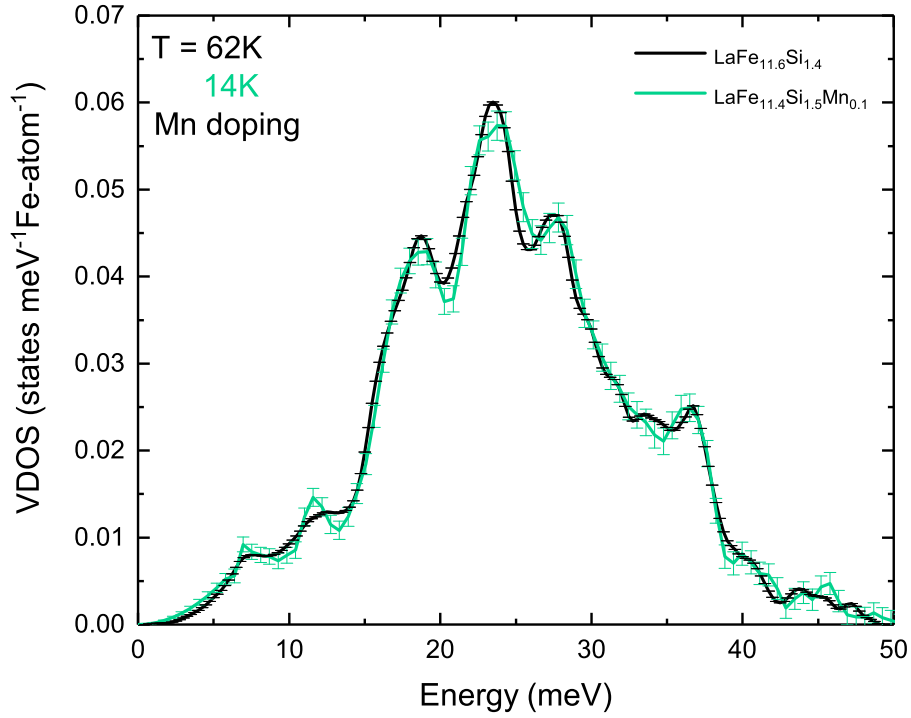
Figure 5.1.: Comparison of the Fe-partial VDOS of $\text{LaFe}_{11.6}\text{Si}_{1.4}$ (undoped reference sample, black line), Mn-doped $\text{LaFe}_{11.4}\text{Si}_{1.5}\text{Mn}_{0.1}$ (green line), hydrogenated $\text{LaFe}_{11.4}\text{Si}_{1.6}\text{H}_{1.6}$ (blue line) and Mn-doped and hydrogenated $\text{LaFe}_{11.4}\text{Si}_{1.5}\text{Mn}_{0.1}\text{H}_{1.6}$ (purple line). All spectra are taken in the FM phase.

blue line), and a combination of both ($\text{LaFe}_{11.4}\text{Si}_{1.5}\text{Mn}_{0.1}\text{H}_{1.6}$, pink line), all at low temperatures to be in a definite FM state. In the structure of the VDOS there are striking differences observable in between the different samples, especially hydrogenation results in strong changes of the structure of the VDOS. The single contributions and elements will be discussed in the following by comparing the undoped reference sample to the sample with a small Mn addition and with the purely hydrogenated compound. Furthermore, a closer evaluation of the effect of hydrogenation onto the structure of the (partial) VDOS and its resulting thermodynamic properties will be given in detail. These results will then be compared to first principle calculations, which have been performed for the case of a (experimentally) fully hydrogenated compound, following the discussion in Ref. [129].

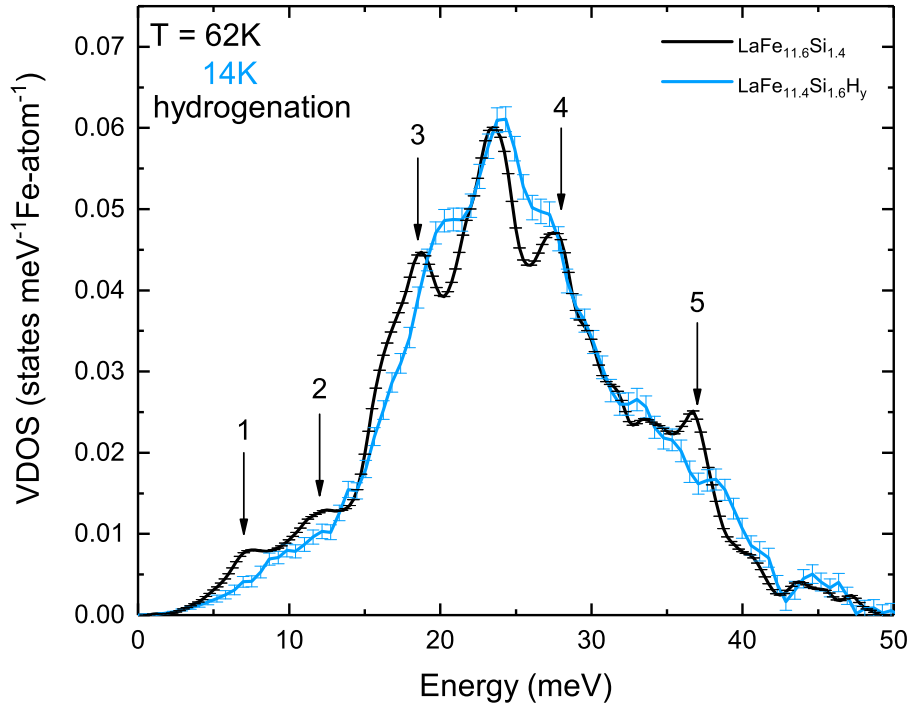
Figure 5.2 (a) depicts the low temperature VDOS obtained at 62 K and 14 K, respectively for the undoped reference sample (black line) and the sample with little Mn doping ($\text{LaFe}_{11.4}\text{Si}_{1.5}\text{Mn}_{0.1}$, green line). From the spectra shown in Figure 5.2 (a) it is apparent that the addition of Mn in concentrations as low as $x = 0.1$ does not significantly affect the VDOS, and thus the phonon excitations. Both low temperature VDOS show basically the same features at the same energetic positions. There are 6 peaks clearly

visible in both spectra. The shape and structure of the phonon spectrum is comparable to the undoped reference sample. The phonon peaks remain at the same energetic values with three weak peaks at 7, 12 and 37 meV, a main peak at 23 meV with two satellite peaks at 18 meV and 28 meV. To investigate the impact of hydrogenation alone, a sample without any Mn addition, but with full hydrogenation (meaning approximately half of the available (24d)-sites occupied as discussed in section 2.3) has been compared to the reference. Taking a closer look at the difference between the hydrogenated sample and the undoped and non-hydrogenated sample reveals an apparent impact of hydrogenation on the VDOS. Figure 5.2 (b) shows the phonon spectra taken at low temperatures in their ferromagnetic (FM) phase, for the hydrogenated sample at $T = 14$ K ($\text{LaFe}_{11.4}\text{Si}_{1.6}\text{H}_{1.6}$) and for the reference sample at $T = 62$ K ($\text{LaFe}_{11.6}\text{Si}_{1.4}$), respectively. All temperatures are low enough to neglect a redshift, and the VDOS can be assumed to be comparable to a 0 K spectrum. The low temperature (partial) VDOS of $\text{LaFe}_{11.6}\text{Si}_{1.4}$ exhibits a dominant peak at ~ 23.5 meV with weaker peaks No. 3 and 4 at ~ 18 and ~ 28 meV, respectively. At low phonon energies, there are only weak peaks near ~ 7 meV and ~ 12 meV (1 and 2). Furthermore, a weak high-energy peak can be seen at ~ 37 meV (No. 5). The differences to be seen are striking. Hydrogenation affects the shape of the partial VDOS drastically. The phonon peaks are broadened and smeared out. Pointed out with black arrows in Figure 5.2 (b) are the significant phonon features, which show strong changes after hydrogenation. They are at energetic values of 7, 12, 18.5, 28 and 37 meV. These peaks reduce their amplitude. The peaks, numbered 1 and 2 at energies of 7 and 12 meV are reduced to a low amplitude, i.e. they are smoothed by hydrogenation. The phonon peaks number 3-5 at 18.5 meV, 28 meV and 37 meV, respectively, on the other hand are reduced to broad shoulders and are energetically redistributed, thus the features slightly shift in energy, with peak number 3 and 5 shifting to slightly higher and peak number 4 to slightly lower energies. This smoothing of the VDOS implies that most phonon modes are strongly broadened and damped due to hydrogenation.

As the metamagnetic phase transition plays a key role in these magnetocaloric compounds and the thermodynamic performance relies on the first order phase transition, the NRIXS measurements have been performed on all samples in both magnetic phases, ferromagnetic and paramagnetic, and compared to each other. The effect of the phase transition onto the vibrational density of states is clearly visible by direct comparison of the spectra in Figure 5.3 taken at 14 K (FM, blue line) and 360 K (PM, pink line) on hydrogenated $\text{LaFe}_{11.4}\text{Si}_{1.6}\text{H}_{1.6}$. The residual, broadened and slightly shifted phonon peaks (the shoulders mentioned above in Figure 5.2 (b), here also numbered 3-5) at the energies at 20, 27 and 38 meV change after the sample undergoes the phase transition. Peaks 3 and 5 vanish nearly completely in the paramagnetic state. Especially phonon mode No. 4



(a)



(b)

Figure 5.2.: Direct comparison of the Fe-partial VDOS of $\text{LaFe}_{11.6}\text{Si}_{1.4}$ (undoped reference sample, black line data taken from [34]) and Mn doped $\text{LaFe}_{11.4}\text{Si}_{1.5}\text{Mn}_{0.1}$ (green line) (a) as well as (b) hydrogenated $\text{LaFe}_{11.4}\text{Si}_{1.6}\text{H}_{1.6}$ (blue line). The VDOS were derived from corresponding NRIXS spectra taken at low temperatures, i.e. at 62 K for $\text{LaFe}_{11.6}\text{Si}_{1.4}$ and at 14 K for $\text{LaFe}_{11.4}\text{Si}_{1.6}\text{H}_{1.6}$ and $\text{LaFe}_{11.4}\text{Si}_{1.5}\text{Mn}_{0.1}$, in the FM phase. The black arrows in (b), labeled with numbers 1-5 at phonon energies E of 7, 12, 18, 28 and 37 meV depict the energetic positions, where significant changes occur due to hydrogenation [129].

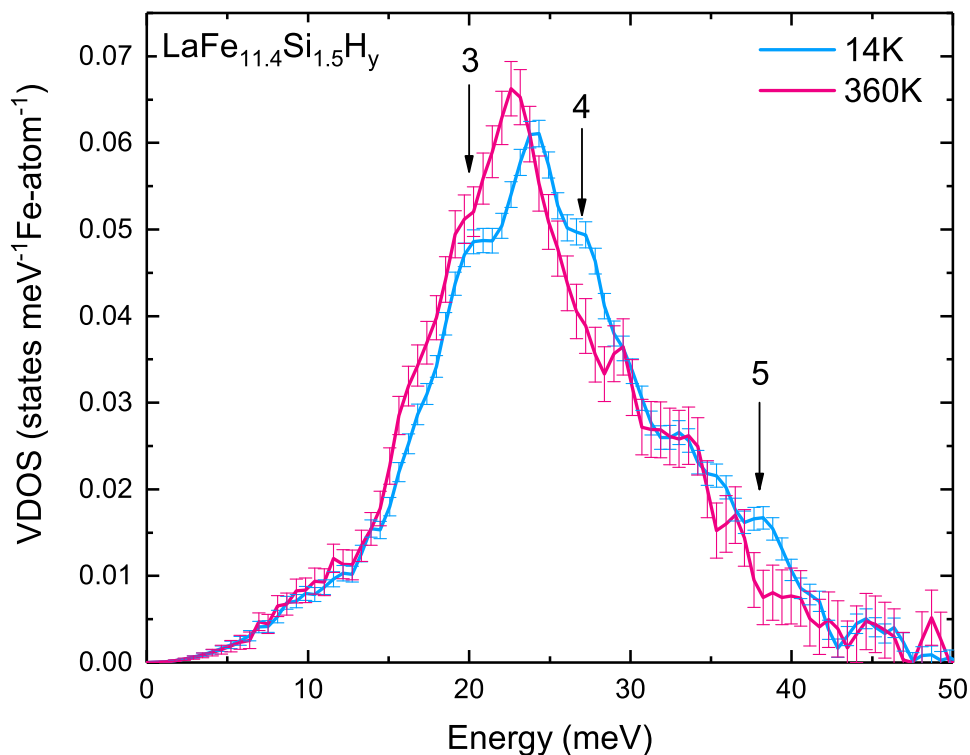


Figure 5.3.: Comparison of the Fe-partial (partial) VDOS of the $\text{LaFe}_{11.4}\text{Si}_{1.6}\text{H}_{1.6}$ sample in its FM phase at 14 K (blue line) and in its PM phase at 360 K (pink line). The black arrows depict the changes in the VDOS, which occurs after undergoing the metamagnetic phase transition at $T_{\text{tr}} = 329$ K, at energetic values of about 20, 27 and 38 meV [129].

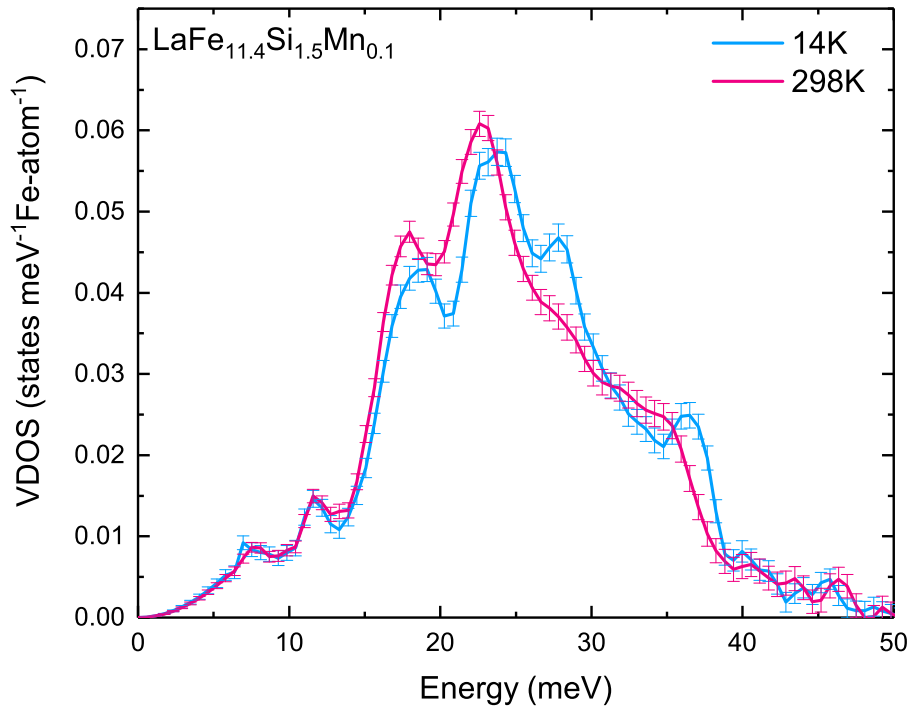
near 28 meV is suppressed drastically and completely smoothed out, no residual feature remains visible.

This smoothing can be explained as a microscopic signature of strong magneto-elastic (spin-phonon) coupling of the Fe magnetic moments in the hydrogenated ferromagnetic compound. This behavior is similar to studies previously done on the undoped and non hydrogenated reference sample $\text{LaFe}_{13-x}\text{Si}_x$ [34, 47]. As compared to the results by Gruner et al. [34], the peak reduction to be seen in hydrogenated $\text{LaFe}_{13-x}\text{Si}_x$ upon the FM to PM transition is weaker than in the non hydrogenated compounds, but the phonon peak near 28 meV is still completely quenched and vanishes upon entering the paramagnetic, magnetically disordered phase, when heated through the phase transition with a transition temperature of $T_{\text{tr}} = 329$ K.

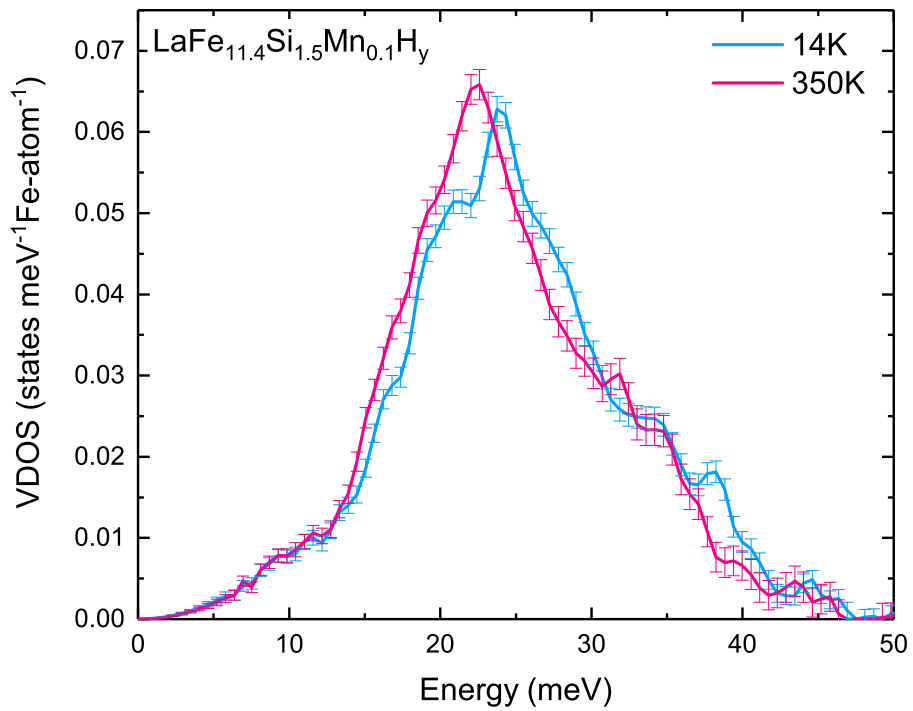
Another difference between the magnetically ordered, ferromagnetic, and the disordered, paramagnetic, state is a uniform shift of the phonon modes to lower phonon energies (redshift), which is visible in the direct comparison of both VDOS in Figure 5.3. The energetic redshift implies an overall increase of the vibrational entropy as discussed later. This redshift occurs, contradictory to expectations as the sample undergoes a large vol-

ume decrease of $\sim 1\%$ upon heating through the isostructural transition. The expected behavior would be an energetic blueshift in the phonon energy E ($\frac{\Delta E}{E} > 0$) from Grüneisen theory [48], and not a redshift ($\frac{\Delta E}{E} < 0$). The Grüneisen relation $\frac{\Delta E}{E} = -\gamma(\frac{\Delta V}{V})$, where $\gamma > 0$ is the average Grüneisen constant, and $\frac{\Delta V}{V} < 0$ is the relative volume contraction at the isostructural FM-to-PM transition at T_{tr} for $\text{LaFe}_{11.4}\text{Si}_{1.6}\text{H}_{1.6}$, would indicate a blueshift of the VDOS. The shift to lower phonon energies now implies a softening of the lattice in the PM phase. This behavior has already been observed in the undoped and non hydrogenated reference $\text{LaFe}_{13-x}\text{Si}_x$ -compounds [34]. The low energy phonon modes exhibit such a weak intensity that possible changes are not visible in the VDOS.

Figure 5.4 (a) depicts the direct comparison of the VDOS for the FM and PM phases of Mn-doped $\text{LaFe}_{11.4}\text{Si}_{1.5}\text{Mn}_{0.1}$ ($T_{\text{tr}} \sim 180$ K). The distinct differences in the VDOS described above, such as the strong suppression of the ~ 27 meV phonon mode and the strong redshift, are also visible in Figure 5.4 (a). The most apparent impact of the magnetostructural phase transition is the energetic redshift, which has been already discussed above, as well as the disappearance of the phonon mode at about 27 meV. The sample with low Mn concentration thus behaves in the same way as the reference sample, showing strong lattice softening upon undergoing the phase transition, implying strong spin-phonon coupling. Despite the addition of Mn, further hydrogenation in the sample $\text{LaFe}_{11.4}\text{Si}_{1.5}\text{Mn}_{0.1}\text{H}_{1.6}$ leads to the behavior of the material as described in the purely hydrogenated compound (see Figure 5.4 (b)). The phonon modes get broadened and energetically redistributed, and the ~ 28 meV shoulder of the main peak, which is reminiscent of the strong spin-phonon coupling, vanishes upon heating above the phase transition. When comparing the VDOS of $\text{LaFe}_{11.4}\text{Si}_{1.5}\text{Mn}_{0.1}$ and $\text{LaFe}_{11.4}\text{Si}_{1.5}\text{Mn}_{0.1}\text{H}_{1.6}$ in Figure 5.4 (a) and (b), the mean energy $\langle \hbar\omega \rangle$ is reduced by -3.1% in the hydrogenated sample across the phase transition from $T_{\text{FM}} = 14$ K to $T_{\text{PM}} = 298$ K and 350 K, respectively while the main peak at ~ 24 meV shifts by -2.7% . Mn addition reduces the redshift, as $\langle \hbar\omega \rangle$ is reduced by -2.3% in case of pure Mn doping and by -2.5% for Mn doping and hydrogenation. While the undoped reference sample has an energetic redshift of $\frac{\Delta E}{E} = -1.5\%$ [47], hydrogenation reduces the shift by $\frac{\Delta E}{E} = -3.1\%$. As will be shown later, the hydrogenated sample shows that the energetic redshift has a big impact on the change in the entropy, the enhancement of the entropy increase at T_{tr} is smaller than in comparison to the reference sample. In Figure 5.5 the temperature evolution of the hydrogenated sample $\text{LaFe}_{11.4}\text{Si}_{1.6}\text{H}_{1.6}$ is shown at five temperature points below and two above the phase transition. From the spectra it is obvious that the VDOS changes closely above and below the transition temperature of $T_{\text{tr}} = 329$ K, showing that the main contribution to the energetic redshift occurs around the phase transition temperature. The phonon modes near the energies 20 and 27 meV decay upon heating and the whole VDOS



(a)



(b)

Figure 5.4.: Fe-partial VDOS measured in the FM state at 14 K (blue line) and in the PM state at 298 K and 360 K, respectively (pink line). Shown are the VDOS of two samples, (a) $\text{LaFe}_{11.4}\text{Si}_{1.5}\text{Mn}_{0.1}$ ($T_{\text{tr}} \sim 180$ K) and (b) $\text{LaFe}_{11.4}\text{Si}_{1.5}\text{Mn}_{0.1}\text{H}_{1.6}$ with $T_{\text{tr}} \sim 320$ K.

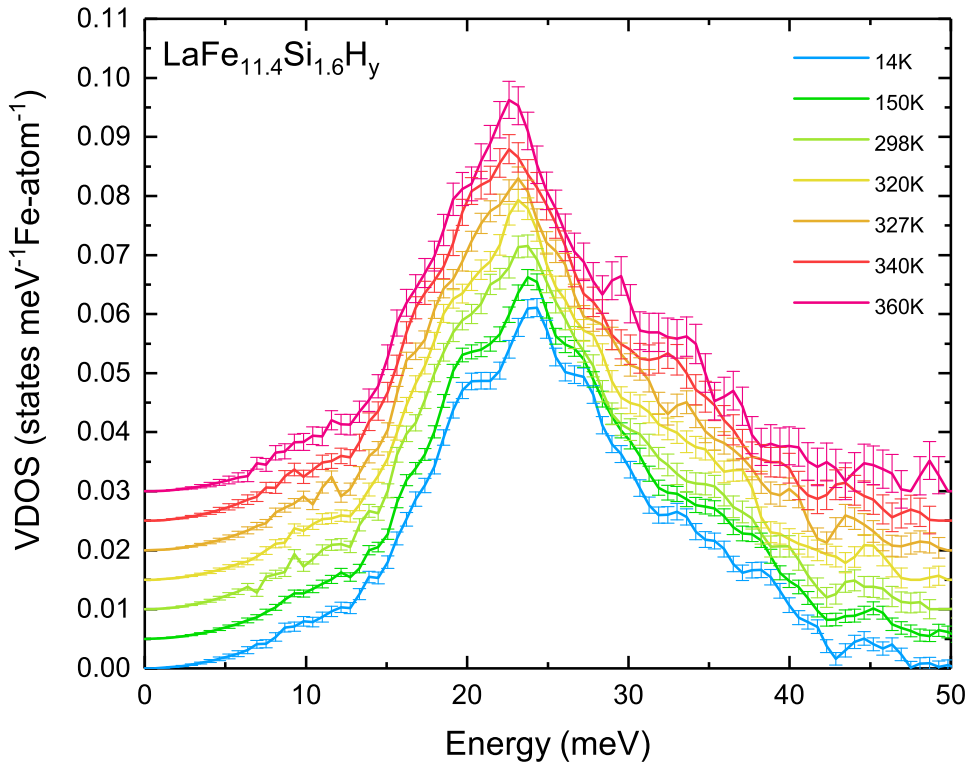
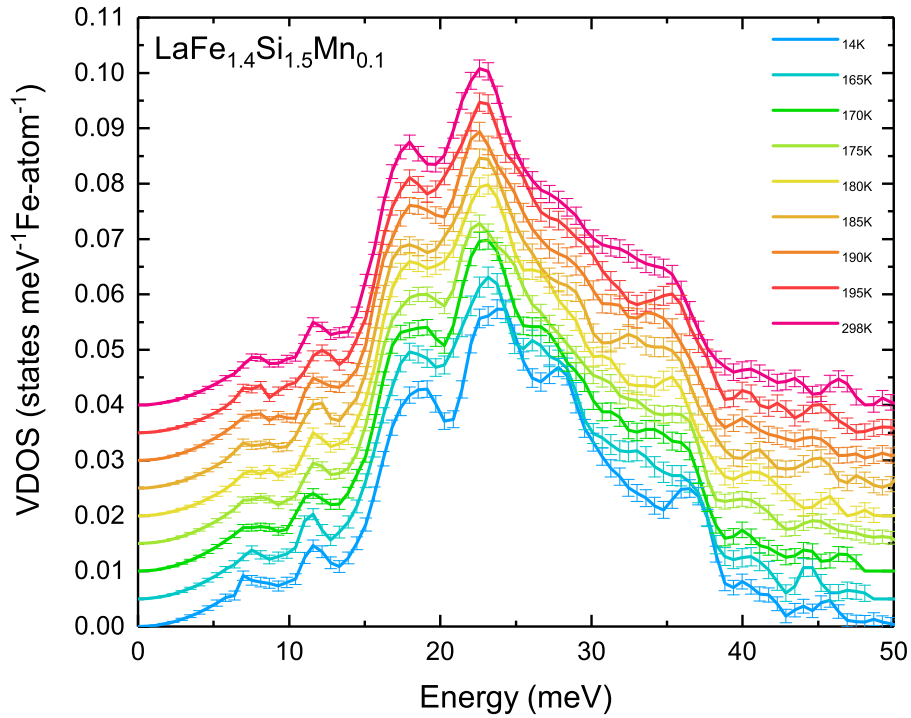


Figure 5.5.: Fe-partial VDOS of $\text{LaFe}_{11.4}\text{Si}_{1.6}\text{H}_{1.6}$ measured across the phase transition obtained by NRIXS at different temperature points, from 14 K (bottom line, blue) to 360 K (top line, pink) following a color gradient ($T_{\text{tr}} \sim 329$ K). The sample depicted has an α -Fe content of only 1.91 % and has not been corrected for the residual secondary phase content. For better visualization the curves are vertically shifted by $0.005 \text{ states (meV)}^{-1}(\text{Fe} - \text{atom})^{-1}$.

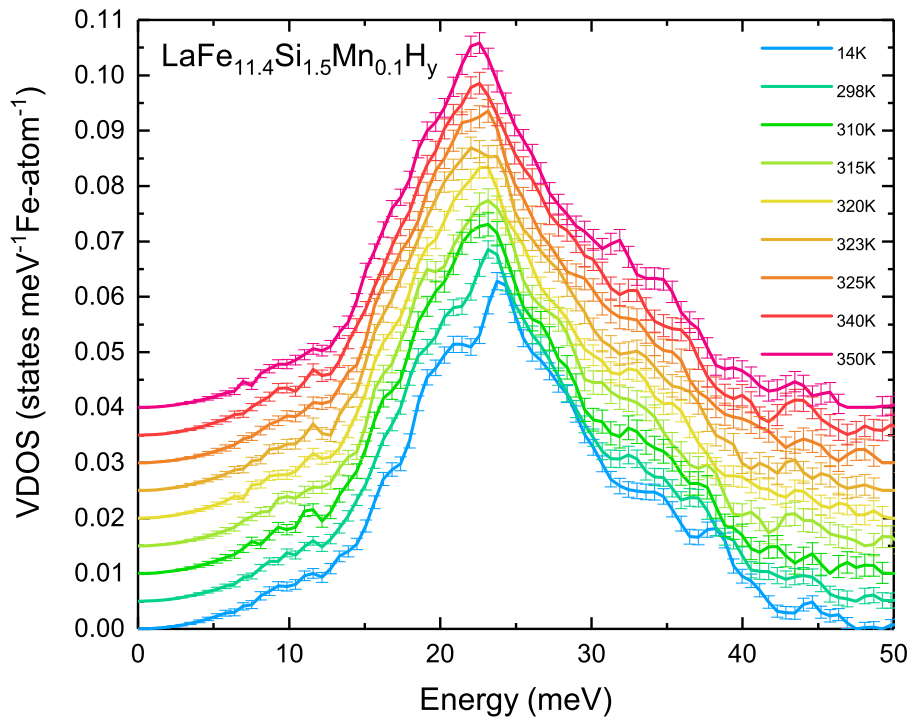
is shifted to lower energies as a result of the contradictory lattice softening with increasing temperature, despite lattice contraction.

Taking a closer look at the VDOS of the sample with pure Mn addition, $\text{LaFe}_{11.4}\text{Si}_{1.5}\text{Mn}_{0.1}$, in small concentrations as depicted in Figure 5.6 (a), reveals the same behavior as in the non hydrogenated compounds of the reference sample. The whole VDOS energetically shifts to lower phonon energies after undergoing the phase transition at $T_{\text{tr}} = 180$ K. Furthermore, the phonon mode at 27 meV is completely quenched. Figure 5.6 (b) basically shows the same behavior for the Mn doped and hydrogenated sample $\text{LaFe}_{11.4}\text{Si}_{1.5}\text{Mn}_{0.1}\text{H}_{1.6}$ as seen in the purely hydrogenated compound, which already has been described above and seen in Figure 5.3.

To determine the impact of Mn as a dopant and of the interstitial hydrogenation, a thorough investigation of the vibrational thermodynamic properties has been done. As the VDOS provides direct access to the partial Fe contribution to the thermodynamic properties, the lattice entropy S_{lat} , the lattice specific heat C_{lat} and the Fe contribution to the Debye temperatures have been extracted for all the samples described above by



(a)



(b)

Figure 5.6.: Fe-partial VDOS measured across the phase transition and obtained by NRIXS at different temperature points, from 14 K (bottom line, blue) to 298 K and 360 K, respectively (top line, pink) following a color gradient. For better visualization the curves are vertically shifted by $0.005 \text{ states (meV)}^{-1} (\text{Fe-atom})^{-1}$. (a) $\text{LaFe}_{11.4}\text{Si}_{1.5}\text{Mn}_{0.1}$ ($T_{\text{tr}} \sim 180 \text{ K}$) and (b) $\text{LaFe}_{11.4}\text{Si}_{1.5}\text{Mn}_{0.1}\text{H}_{1.6}$ ($T_{\text{tr}} \sim 320 \text{ K}$).

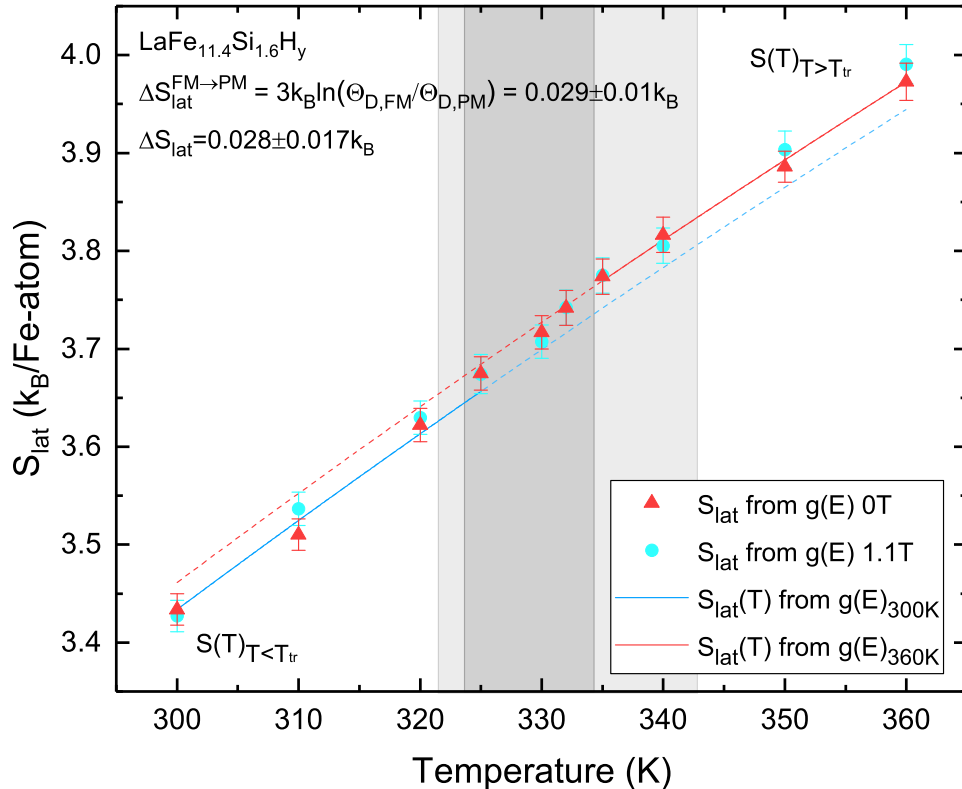


Figure 5.7.: Vibrational (lattice) entropy S_{lat} of $\text{LaFe}_{11.4}\text{Si}_{1.6}\text{H}_{1.6}$, calculated via Equation 2.41 from the Fe-partial experimental VDOS, $g(E)$, at several temperature points across the phase transition. $\text{LaFe}_{11.4}\text{Si}_{1.6}\text{H}_{1.6}$ exhibits an increase in S_{lat} at the FM-to-PM transition by $\Delta S_{\text{lat}} = 0.028 \pm 0.017 k_B/\text{Fe-atom}$. The blue line depicts the calculated $S_{\text{lat}}(T)$ for the FM and the red line for the PM phase, using the experimentally determined $g(E)$ at the given measurement temperatures, and fitted to the given entropy points in the FM region and PM region, respectively. The VDOS of the measured sample has been corrected for the residual α -Fe content of 4.47 % [129]. The grey shaded areas indicate the phase coexistence regions without (dark grey) and with an applied magnetic field of 1.1 T (grey).

using the known thermodynamic relations as described in section 2.6.

All the extracted thermodynamic properties show the contribution of the Fe sub-lattice to the total isothermal properties. Figure 5.7 depicts the vibrational Fe-partial lattice entropy S_{lat} per Fe atom of hydrogenated $\text{LaFe}_{11.4}\text{Si}_{1.6}\text{H}_{1.6}$, calculated via Equation 2.41 from the Fe-partial experimental VDOS, $g(E)$. The data points have been acquired at various measurement temperatures across the first order metamagnetic phase transition. Measurements have been done with increasing temperature in an applied field of 1.1 T as well as in zero field. To determine a change in the lattice entropy across the transition, the temperature dependence of the lattice entropy $S_{\text{lat}}(T)$ has been calculated from the experimentally determined VDOS $g(E)$ in zero magnetic field for a temperature point

in the sample's defined ferromagnetic phase at 300 K (shown as the blue line) and in the defined paramagnetic state at 360 K (red line). For the temperature evolution the temperatures have been chosen to be as close to the transition as possible, but to be mainly outside of the hysteresis region to exclude a possible mixing and starting of phase coexistence, to prevent using temperature points, which lie within a possibly magnetically mixed phase. The lattice entropy has been extracted using the thermodynamic relation given in section 2.6, using Equation 2.41.

From Figure 5.7 it is clearly visible that the entropy $S_{\text{lat}}(T)$ shows an offset across the transition. The transition region in case of zero magnetic field and at 1.1 T is indicated by the grey areas, respectively. This enhancement in entropy, which is directly related to the redshift in the VDOS at T_{tr} , as discussed earlier has a value ΔS_{lat} of $0.028 \pm 0.017 \text{ k}_B/\text{Fe-atom}$ in case of the hydrogenated sample. This value per Fe atom corresponds to a change of $\Delta S_{\text{lat}} = 3.2 \pm 1.9 \frac{\text{J}}{\text{kgK}}$. The jump in S_{lat} occurs at the phase transition region in between 325 – 335 K, in agreement with a transition temperature of $T_{\text{tr}} = 329 \text{ K}$ as deduced from magnetometry. From the extracted entropy values it can be seen that there is no significant difference between the measurement in zero field and in a field of 1.1 T within the error margin. The enhancement of the entropy across the phase transition has been estimated by calculating the temperature dependent entropy function $S_{\text{lat}}(T)$ from the VDOS at zero field at 300 K in the defined FM state and in the PM state at 360 K. The curves in Figure 5.7 correspond to the calculated thermodynamic functions according to Equation 2.41. The entropy jump has been taken as the difference between these two functions directly at the transition temperature of 329 K. Comparison of the obtained values with those of the non-hydrogenated reference sample $\text{LaFe}_{11.6}\text{Si}_{1.4}$ shows a strong impact of hydrogenation on the sample system. The value for the change in lattice entropy ΔS_{lat} in hydrogen free $\text{La}(\text{Fe},\text{Si})_{13}$ is $0.060 \pm 0.023 \text{ k}_B/\text{Fe-atom}$, or $6.9 \pm 2.6 \frac{\text{J}}{\text{kgK}}$ [34, 47]. The lattice entropy change ΔS_{lat} from the Fe subsystem for the hydrogenated compound shown here is found to be reduced by 50 % in comparison to the reference sample. Measurements of the isothermal entropy on the hydrogenated sample via $M(T, H)$ measurements show a total increase $|\Delta S_{\text{iso}}|$ of $9.11 \pm 0.01 \frac{\text{J}}{\text{kgK}}$ near the transition temperature in an applied magnetic field of $\mu_0 H = 1.1 \text{ T}$ (see entropy measurements in Appendix A and Figure A.7). The value for the change in lattice entropy ΔS_{lat} obtained for the hydrogenated compound $\text{LaFe}_{11.4}\text{Si}_{1.6}\text{H}_{1.6}$ of $0.028 \pm 0.017 \text{ k}_B/\text{Fe-atom}$ or $3.2 \pm 1.9 \frac{\text{J}}{\text{kgK}}$ for just the vibrational contribution of the Fe sub-lattices therefore contributes approximately with $\sim 35 \%$ to the total isothermal entropy change $|\Delta S_{\text{iso}}|$, which is a significant contribution of the Fe lattice.

Figure 5.8 shows the vibrational specific heat obtained via Equation 2.42 from the Fe-partial experimental VDOS, $g(E)$ for the hydrogenated compound. Here, a similar behavior is expected as in the lattice entropy across the phase transition. As the sample

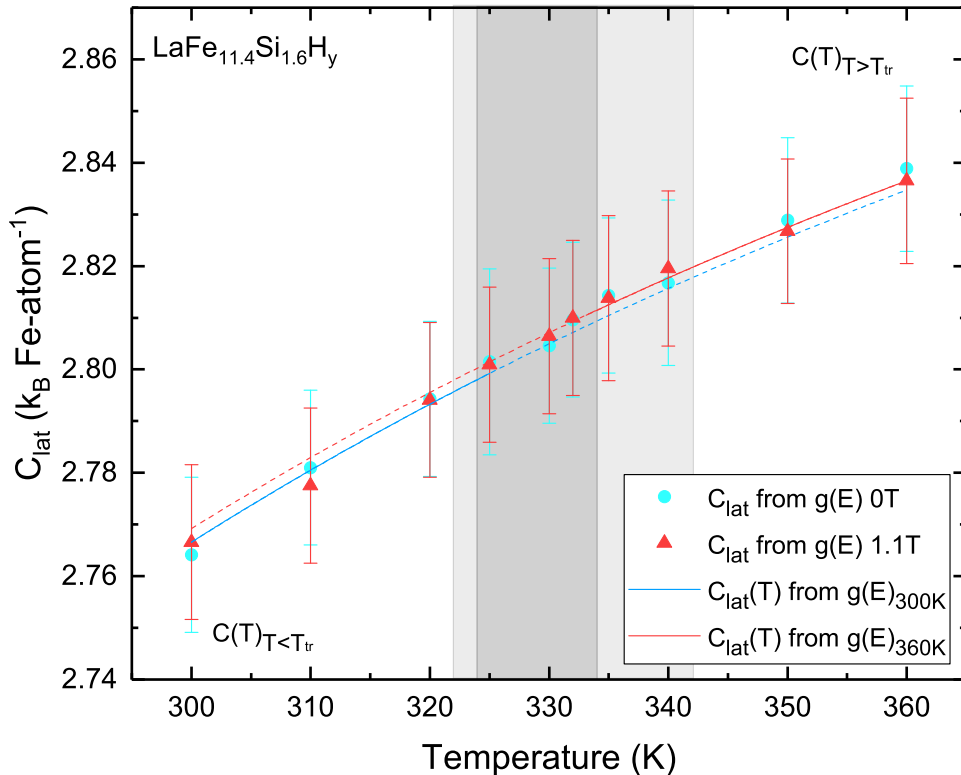


Figure 5.8.: Vibrational (lattice) specific heat C_{lat} , calculated via Equation 2.42 from the Fe-partial experimental VDOS, $g(E)$, at several temperature points across the phase transition in $\text{LaFe}_{11.4}\text{Si}_{1.6}\text{H}_{1.6}$. The grey shaded areas indicate the phase coexistence regions without (dark grey) and with an applied magnetic field of 1.1 T (grey).

undergoes the metamagnetic phase transition and the structural change upon heating, the specific heat shows a weak, but jump-like behavior. The red triangles correspond to the measurements done without an applied magnetic field, while the blue circles depict the in field (1.1 T) measurements. It can be seen that C_{lat} changes for both cases in the same fashion. The increase in specific heat across the transition only amounts to $0.002 \pm 0.015 k_B/\text{Fe-atom}$ and has been taken from the difference of the extrapolated thermodynamic functions $C_{\text{lat}}(T)$, calculated from Equation 2.42, at 300 K and 360 K in the FM and PM state, respectively. In order to find a useful description for the Debye temperatures Θ_D , the entropy Debye temperatures have been extracted from the logarithmic moment of the VDOS, $g(E)$ [114–116], as described in section 2.6, following the same evaluation route as in Ref. [34]. Furthermore, the Debye temperature was also extracted via Equation 2.33 from the Lamb-Mössbauer factor. Figure 5.10 (a) depicts the comparison of the temperature dependence of the extracted Debye temperatures via both evaluation routes for the hydrogenated sample $\text{LaFe}_{11.4}\text{Si}_{1.6}\text{H}_{1.6}$ with no external magnetic field applied. Figure 5.10 (b) shows the evolution of the Lamb-Mössbauer fac-

Thermodynamic properties of $\text{LaFe}_{11.4}\text{Si}_{1.6}\text{H}_{1.6}$			
T [K]	$S_{\text{lat}} [\frac{k_{\text{B}}}{\text{Fe-atom}}]$	$C_{\text{lat}} [\frac{k_{\text{B}}}{\text{Fe-atom}}]$	f_{LM}
300	3.43 ± 0.02	2.77 ± 0.02	0.742 ± 0.001
310	3.51 ± 0.02	2.78 ± 0.02	0.739 ± 0.001
320	3.62 ± 0.02	2.79 ± 0.02	0.728 ± 0.001
325	3.67 ± 0.02	2.80 ± 0.02	0.722 ± 0.001
330	3.72 ± 0.02	2.81 ± 0.02	0.720 ± 0.001
332	3.74 ± 0.02	2.81 ± 0.02	0.719 ± 0.001
335	3.77 ± 0.02	2.81 ± 0.02	0.714 ± 0.001
340	3.82 ± 0.02	2.82 ± 0.02	0.712 ± 0.001
350	3.89 ± 0.02	2.83 ± 0.01	0.706 ± 0.001
360	3.97 ± 0.02	2.84 ± 0.02	0.698 ± 0.001

Table 5.1.: Lattice contributions to the thermodynamics extracted from the Fe-partial VDOS $g(E)$, without application of a magnetic field.

tor across the phase transition. From the Debye temperatures, we can deduce that both models provide a consistent description of the Fe-partial Debye temperatures in the system. Across the FM-to-PM phase transition, a reduction in the Debye temperature is seen for both methods. Recalculating the lattice entropy via the entropy Debye temperature shows that the obtained values for the entropies match well with the directly extracted lattice entropies from the VDOS, and the results are directly comparable, as depicted in Figure 5.9. The deviation between both methods of calculating the entropy is in a range of only 5%. This shows that in the temperature range we performed our experiments, the Debye approximation yields reasonable results and serves as a useful model in order to describe the sample system with the extracted entropy Debye temperatures at the measured temperatures properly. The evolution of the entropy Debye temperature calculated according to this procedure (as listed in Table 5.2) clearly shows a change through the phase transition. From the ferromagnetic low temperature phase to the paramagnetic high temperature phase, the entropy Debye temperature shows a decrease as depicted in Figure 5.10 (a) (black dots). Here the entropy Debye temperature has also been compared with the Debye temperature extracted from the Lamb-Mössbauer factor (blue triangles). The hydrogenated sample shows a reduction of 13 K in the entropy Debye temperature with values of $\Theta_{14\text{K}}^{\text{Fe}} = 386 \pm 7 \text{ K}$ for the FM phase and a value of $\Theta_{360\text{K}}^{\text{Fe}} = 374 \pm 1 \text{ K}$ in the PM phase.

The same behavior can be seen for the specific heat Debye temperature, here the decrease is $\Theta_{\text{D}} = 396 \pm 2 \text{ K}$ for the FM phase and a value of $\Theta_{\text{D}} = 385 \pm 2 \text{ K}$ in the PM phase. These values are $\sim 15 \text{ K}$ higher than the temperatures extracted for the H-free reference

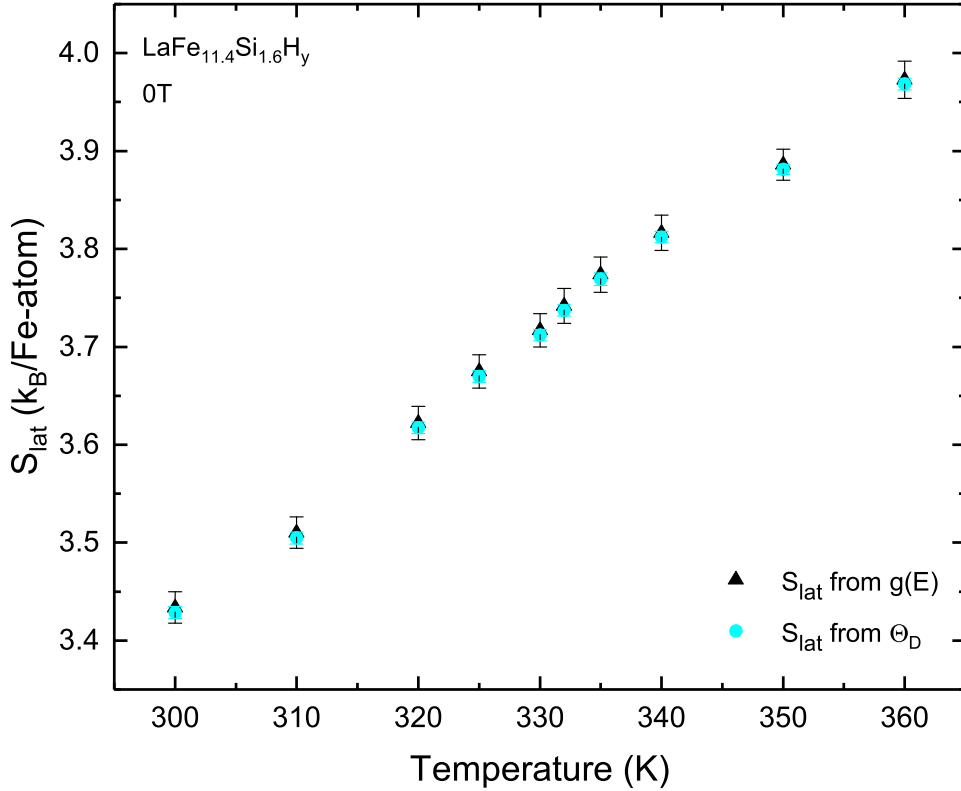


Figure 5.9.: Vibrational (lattice) entropy S_{lat} of $\text{LaFe}_{11.4}\text{Si}_{1.6}\text{H}_y$, calculated via Equation 2.41 from the Fe-partial experimental VDOS, $g(E)$ (black triangles), at several temperature points across the phase transition and calculated from the extracted entropy Debye temperatures (cyan dots) in 0 T. The VDOS of the sample measured has been corrected for the residual α -Fe content of 4.47 %.

sample [34]. The increase of approximately 4 % in the Fe contribution to the entropy Debye temperature upon hydrogenation in comparison to the non hydrogenated reference sample is in agreement with the trend seen in the total Debye temperature as observed from measurements of the low temperature specific heat by Lovell et al. [130]. This finding is in accordance with our experimental results from NRIXS measurements when considering that the Fe contribution to the total Debye temperature plays a significant and large role. Furthermore, we obtained consistent data from first principles DFT calculations (see Table 5.2), which agree with the trend in the increase of the Fe contribution to the Debye temperatures as well as the trend observed in other works [130]. Despite the increase in the Fe-partial Debye temperature compared to non hydrogenated compounds, this does not indicate a lattice stiffening, as hydrogenation just shifts the cut off energy in $g(E)$ to higher values compared to the hydrogen free system. The behavior of the Lamb-Mössbauer factor, which is directly related to the mean square atomic displacement in the sample is shown in Figure 5.10 (b). Here, the evolution of the Lamb-Mössbauer factor

is given with increasing temperature. The lines refer to the extrapolated thermodynamic curves for the factors calculated in the distinct FM (blue line) and PM (red line) phase. Across the phase transition at around 329 K, a decrease is visible, which is in accordance with the anomalous lattice softening also observed in the VDOS for the given sample. As the extracted lattice entropies for the sample with interstitial hydrogen show that hydrogenation results in a strong reduction of the entropy change of about 50 % upon the metamagnetic phase transition relative to the undoped reference sample, a closer evaluation has been done for samples with pure Mn addition as well as with a combination of both, Mn doping and hydrogenation. Figure 5.11 depicts the lattice entropy per Fe-atom of the Fe subsystem of $\text{LaFe}_{1.4}\text{Si}_{1.5}\text{Mn}_{0.1}$ across the phase transition for the Mn doped sample, taken in zero applied magnetic field with increasing temperatures. The phase transition is in a temperature range between 176 – 180 K. The extracted increase in the Fe-partial vibrational entropy, which is to be expected due to the apparent redshift in the VDOS, as seen and discussed in Figure 5.4, seems to be drastically reduced in comparison to the reference sample as well as to the hydrogenated compound discussed above. Mn addition obviously strongly affects the entropy jump across the transition. From the energetic redshift, which was evident in Figure 5.4 (a) it is to be expected that the lattice entropy increases during the magnetostructural phase transition. Surprisingly, what can be observed from the data of the lattice entropy across the phase transition is that there is seemingly no entropy jump within the error, despite the apparent redshift

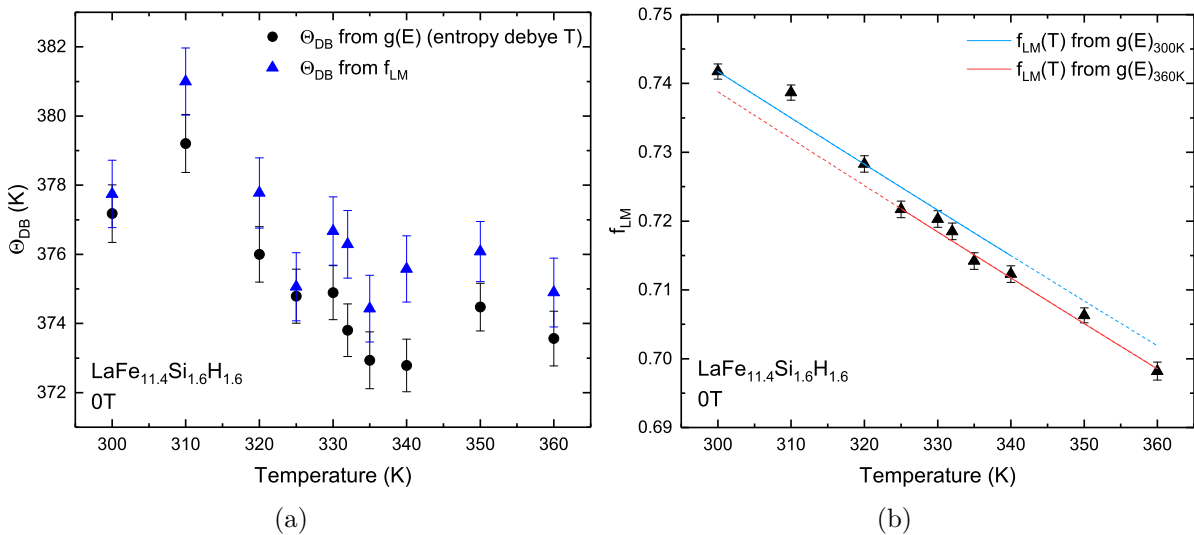


Figure 5.10.: (a) Calculated entropy Debye temperatures of hydrogenated $\text{LaFe}_{11.4}\text{Si}_{1.6}\text{H}_{1.6}$ calculated from $g(E)$ (black dots) and from the Lamb Mössbauer factor f_{LM} (blue triangles). (b) Temperature evolution of f_{LM} with extrapolated curve for the FM (blue) and PM (red) phase as calculated from $g(E)$ after Equation 2.43.

Entropy and specific heat Debye temperatures of $\text{LaFe}_{1.4}\text{Si}_{1.6}\text{H}_y$ in 0 T				
Temperature [K]	$\Theta^{\text{Fe}}(0)$ [K]	$\Theta^{\text{Fe}}(2)$ [K]	$\Theta_{f_{LM}}^{\text{Fe}}$ [K]	Θ^{tot} [K]
14	386.2 ± 7.5	395.7 ± 2	384.5 ± 2.5	
300	377.2 ± 0.8	386.6 ± 2.2	377.7 ± 1.0	
310	379.2 ± 0.8	389.6 ± 2.3	381.0 ± 1.0	
320	376 ± 0.8	385.9 ± 2.2	377.8 ± 1.0	
325	374.8 ± 0.8	385.1 ± 2.2	375.1 ± 1.0	
330	374.9 ± 0.8	385.3 ± 2.3	376.7 ± 1.0	
332	373.8 ± 0.8	383.8 ± 2.2	376.3 ± 1.0	
335	372.9 ± 0.8	383.2 ± 2.5	374.4 ± 1.0	
340	372.8 ± 0.8	382.5 ± 2.2	375.6 ± 1.0	
350	374.5 ± 0.7	385.6 ± 2.1	376.1 ± 0.9	
360	373.6 ± 0.8	384.7 ± 2.4	374.9 ± 1.0	
DFT-FM	391 K			436 K
DFT-PM	369 K			420 K

Table 5.2.: Experimentally extracted Debye temperatures of hydrogenated $\text{LaFe}_{1.4}\text{Si}_{1.6}\text{H}_{1.6}$ calculated from the logarithmic moment $\Theta^{\text{Fe}}(0)$, the 2nd moment $\Theta^{\text{Fe}}(2)$ and via the Lamb-Mössbauer f_{LM}^{Fe} factor in comparison with first-principles calculations.

when directly comparing the FM and PM phase of the Mn doped sample. The change in entropy only amounts to $\Delta S_{\text{lat}} = 0.005 \pm 0.01 k_B$ or $0.57 \pm 1.15 \frac{\text{J}}{\text{kgK}}$, which is smaller than the error of the measurement.

Comparing the experimental results for the sample with low Mn doping and the reference sample, the change in entropy is reduced to only about $\sim 9\%$ of the undoped sample despite the negligible change in the shape of the VDOS. There are only two possible origins for a change in the entropy from the experimentally obtained VDOS. First, a change in the shape of the VDOS, and second, an energetic shift of the VDOS to different energies, as the phase transition is rather sharp and the transition region quite narrow. As already discussed, an increase in the lattice entropy can be expected when a redshift occurs in the system as more states are occupied at a given temperature for lower energies. From that point of view, we expect an increase in the lattice entropy as the mean energy of the phonon density of states shifts approximately in a similar range, $\Delta\langle\hbar\omega\rangle = -2.3\%$ as the hydrogenated sample (-3.1%), yet the effect seems to be drastically reduced. Therefore a closer look at the direct changes of the VDOS in comparison to the undoped reference sample has been done. Figure 5.12 shows the evolution of the Mn doped sample in comparison to the reference. Figure 5.12 (a) depicts the purely ferromagnetic phase, (b) shows the VDOS of the Mn doped sample approximately 20 K below the transition,

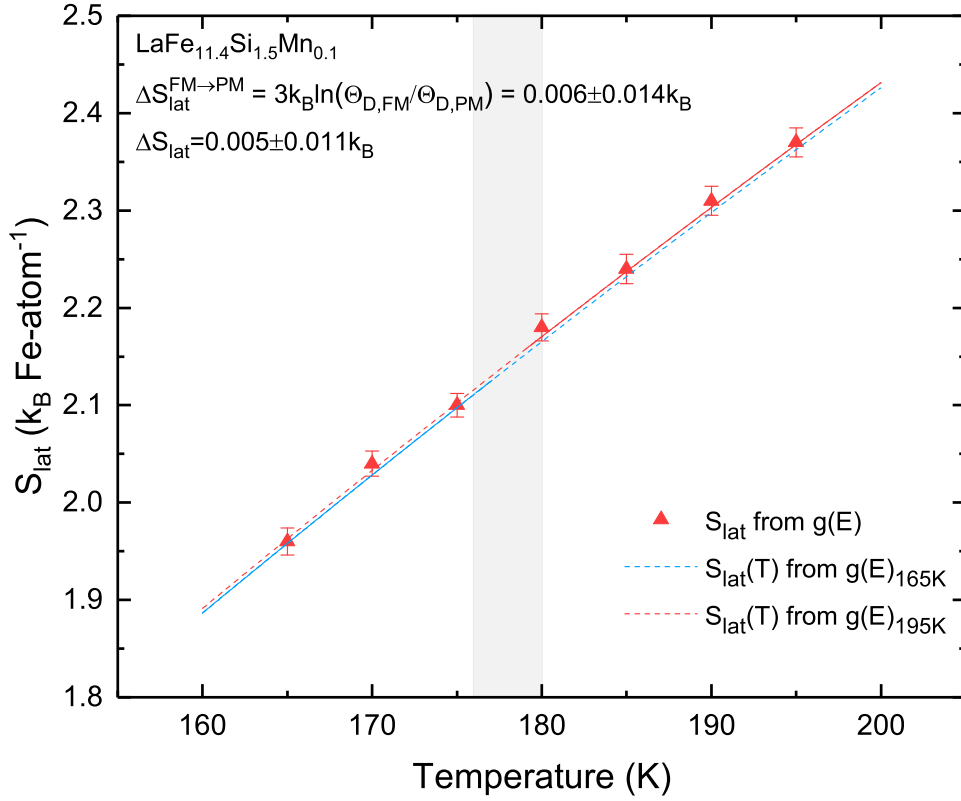


Figure 5.11.: Vibrational (lattice) entropy S_{lat} , calculated via Equation 2.41 from the Fe-partial experimental VDOS, $g(E)$, in $\text{LaFe}_{1.4}\text{Si}_{1.5}\text{Mn}_{0.1}$ at several temperature points across the phase transition.

(c) shows the VDOS 20 K above the phase transition and (d) shows the VDOS of the fully transformed sample in the paramagnetic state at room temperature.

From the direct comparison it can be seen that in the same magnetic state, the undoped sample shows a slightly increased redshift as compared to the Mn doped sample. Furthermore, the structure of the VDOS, differs strongly between the undoped reference and the Mn doped specimen just before the phase transition starts. This is the case despite a very strong similarity of the VDOS in the low temperature FM state and high temperature PM state. The increase in the lattice entropy seems to be strongly suppressed in the Mn doped sample, as a result of the shape of the VDOS: This behavior results from phonon modes, which are now differently distributed in energies in contrast to the reference sample. From the VDOS, the entropy Debye temperatures were also calculated. The evolution of the entropy Debye temperature in the two distinct magnetic states showed a decrease of the value, as already seen in the hydrogenated compound. Yet, the absolute values are lower and decrease from $\Theta_{14\text{K}}^{\text{Fe}} = 374 \pm 8 \text{ K}$ in the ferromagnetic phase down to $\Theta_{298\text{K}}^{\text{Fe}} = 366 \pm 1 \text{ K}$ in the paramagnetic state. This decrease is only about 2% across the phase transition and is a smaller decrease than that which was observed in $\text{LaFe}_{1.4}\text{Si}_{1.6}\text{H}_{1.6}$. The values

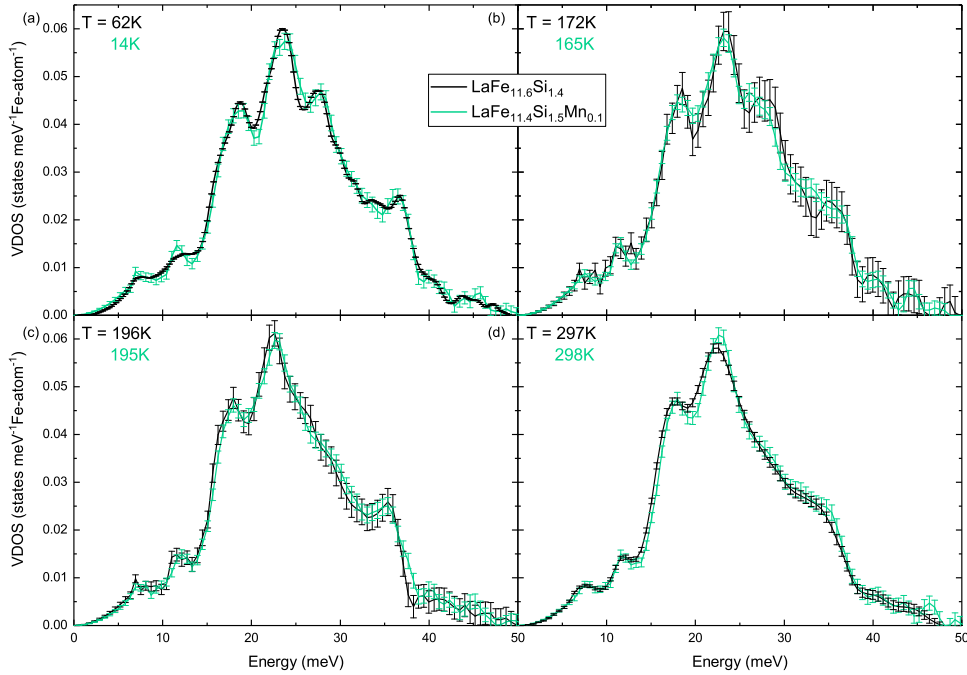


Figure 5.12.: Comparison of the Fe-partial VDOS of the undoped reference (black curve) and Mn doped LaFe_{11.4}Si_{1.5}Mn_{0.1} (green curve) from the FM (a) to the PM (d) state with two intermediate temperatures closely below (b) and above (c) the transition.

for the Mn doped specimen agree with data obtained from specific heat measurements by Lovell et al. [130].

Interestingly, when more closely evaluating the compound, which is hydrogenated and has a very small Mn addition, it shows a different behavior in the evolution of the entropy across the phase transition. Here the reduction of the lattice entropy of the subsystem is bigger than in the Mn doped sample, yet it is still reduced compared to the hydrogenated compound. Figure 5.13 shows the lattice entropy calculated from the $g(E)$ and the logarithmic moment of the VDOS of LaFe_{1.4}Si_{1.5}Mn_{0.1}H_y, again measured with increasing temperature. The transition takes place around 318 – 322 K. The entropy shows a step like behavior with increasing temperature. Yet, the extracted value for the change of the lattice entropy ΔS_{lat} , obtained again from the difference of the temperature dependent $S_{\text{lat}}(T)$ evolution of the lattice entropies calculated at a temperature point in the FM and a PM phase (here taken at 310 K and 350 K), taken at the phase transition, only has a value of $\Delta S_{\text{lat}} = 0.009 \pm 0.026 k_{\text{B}}$ or $1.03 \pm 2.98 \frac{\text{J}}{\text{kgK}}$. This value is reduced by 70 % in comparison to the purely hydrogenated compound and even reduced by 85 % in comparison to the undoped reference sample. This behavior might be attributed to the lattice expansion caused by the interstitial hydrogen atoms, allowing different phonon

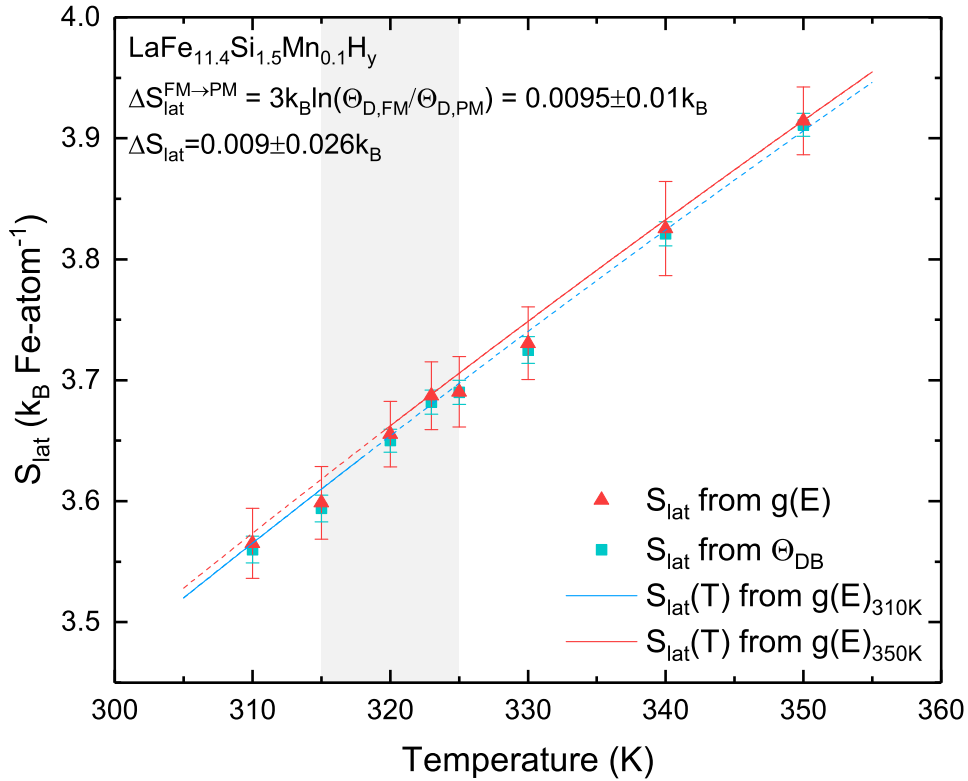


Figure 5.13.: Vibrational (lattice) entropy S_{lat} , calculated via Eq. (2.41) from the Fe-partial experimental VDOS, $g(E)$, (red triangles) and calculated from the entropy Debye temperature Θ_{D} (green squares) in $\text{LaFe}_{1.4}\text{Si}_{1.5}\text{Mn}_{0.1}\text{H}_y$ at several temperature points across the phase transition.

modes to be excited in the system, which are possibly suppressed in a structure with a smaller lattice parameter as is the case for the Mn doped sample. We observe a strong moment volume coupling in these sample systems, which links the magnetic behavior to the unit cell volume [35] and this behavior can be observed as an imprint in the VDOS, and therefore a change in the lattice entropy.

5.1.2. Effect of Hydrogenation - Comparison with DFT Calculations

Corresponding to the experimental data of the hydrogenated compound with a stoichiometry of $\text{LaFe}_{11.4}\text{Si}_{1.6}\text{H}_{1.6}$, first principle DFT calculations have been performed by P.D. Dr. M. E. Gruner (University of Duisburg-Essen) within the framework of the project in order to understand the effect of hydrogenation on the $\text{La}(\text{Fe},\text{Si})_{13}$ -based compounds. This chapter will give a closer insight into the electronic structure and its effect on the phonon subsystem, closely following the discussion in Ref. [129]. The direct comparison of the calculated site resolved VDOS and the Fe-partial experimental VDOS is shown in Figure 5.14 (a). The Fe-partial VDOS for the two distinct magnetic phases, low temperature

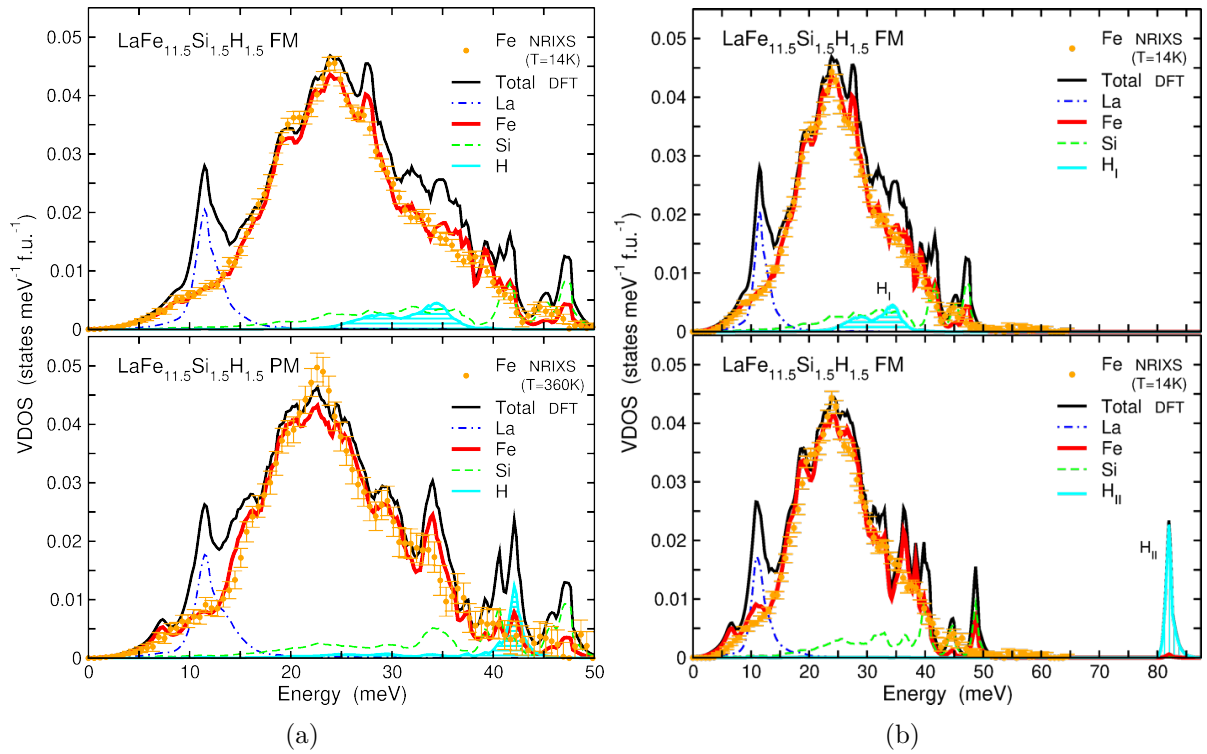


Figure 5.14.: Element-resolved vibrational density of states $g(E)$ of hydrogenated $\text{LaFe}_{11.5}\text{Si}_{1.5}\text{H}_{1.5}$ in the (a) FM (top) and PM (bottom) phase obtained from DFT [129] and (b) in the FM phase for the the distinct H-sites, H_I and H_{II} (Calculations by M. E. Gruner). Figure (a) taken from [129].

FM and high temperature PM phase, agree well with the experimental data measured at $T = 14\text{K}$ and at $T = 360\text{K} > T_{\text{tr}}$. The calculated VDOS reproduces the features of the experimentally obtained data including the redshift of the entire phonon spectrum to lower phonon energies, as well as the particular broadening of the spectral features at energies of 18 and 28 meV, respectively, which are closely located around the central maximum of the VDOS and well pronounced in the hydrogen free and undoped reference sample as well as the purely Mn doped compound. The change of the spectral features mentioned can be interpreted analogously to the hydrogen free case, where this change indicates a strong magneto-elastic coupling [34, 47]. Even though hydrogen is a light element, one third of the phonon modes can be found in the spectrum at low energies, despite the expectation of high frequency modes for light elements in the vibrational spectrum [131]. In the calculations presented, the lowest modes ascribed to hydrogen are in between 15 – 50 meV, which is an indication of shallow direction on the binding surface, where hydrogen atoms can move freely. The low energy modes are in agreement with calculations done on equiatomic LaFeSiH , where a fraction of the H modes are found at rather low energies around 10 meV [132].

In both magnetic phases the partial Fe VDOS obtained by DFT calculations fits the experimental data very well and the significant features visible in the VDOS are reproduced. Especially the broadening of the phonon modes, which were clearly visible as distinct peaks in the non hydrogenated reference samples, can also be seen in the calculation. Furthermore, the hydrogenation shows a site preference in terms of the site occupation. Figure 5.14 (b) depicts the element resolved VDOS for occupation of the H_I (upper viewgraph) and the H_II -sites (lower viewgraph). The comparison of DFT calculations of the site and element-specific VDOS yields a better agreement for the H_I -sites, than for occupation of the H_II -sites. From the direct comparison of the Fe-partial VDOS to the calculated site dependent VDOS, it can be deduced that hydrogen predominantly occupies the H_I first, leading to a very good agreement with the experimental results. This behavior is in accordance with the energetically less favorable H_II -sites, which will be occupied slower than the H_I -sites. An experimentally full hydrogenation, mainly consists of occupied H_I -sites, as already discussed in section 2.3. The smoothing of the spectral features in the VDOS can be attributed to electron-phonon coupling. Additionally, there are other reasons, which can result in broadening and damping of phonon modes. Damping can be a result of perturbations due to anharmonic interatomic potentials. This anharmonicity leads to rapid energy transfer from one phonon state to another, which then, again, leads to the broadening in the phonon modes in the VDOS. This phonon-phonon coupling reduces the phonon lifetimes as it increases the phonon scattering and thus results in broadening. Temperature dependent positional and chemical disorder also has an effect on phonon-phonon coupling, which can change the structure in the VDOS. Another possible effect leading to broadened phonon modes are mass differences inside a crystal lattice [133]. Furthermore, significant electron-phonon coupling is a source for phonon broadening. The electron-phonon coupling in the system can be deduced from the calculations of the element-resolved electronic DOS, as depicted in Figure 5.15 for both magnetic states, FM and PM. The results from the DFT calculations are in agreement with calculations presented by Gercsi et al [37]. From the element-resolved DOS we can infer a hybridization of the H- and Fe states at an energy around -7.5 eV , which energetically lies below the d -band edge for Fe as compared to a hydrogen free compound and explains the stability in hydrogenated $\text{La}(\text{Fe},\text{Si})_{13}$ as it corresponds to a gain in the formation energy from hydrogenation. Around the Fermi level E_F , the DOS of H can be neglected. The main contribution here is predominantly from the Fe-sites in both magnetic phases, and thus, analogous to the hydrogen free case as discussed in Ref. [34]. In the FM state, the DOS exhibits a minimum in the minority spin channel at E_F , as indicated by the arrow in the upper viewgraph of Figure 5.15. This feature is the origin of the stabilization of the high moment of Fe in the system, which can be amounted to

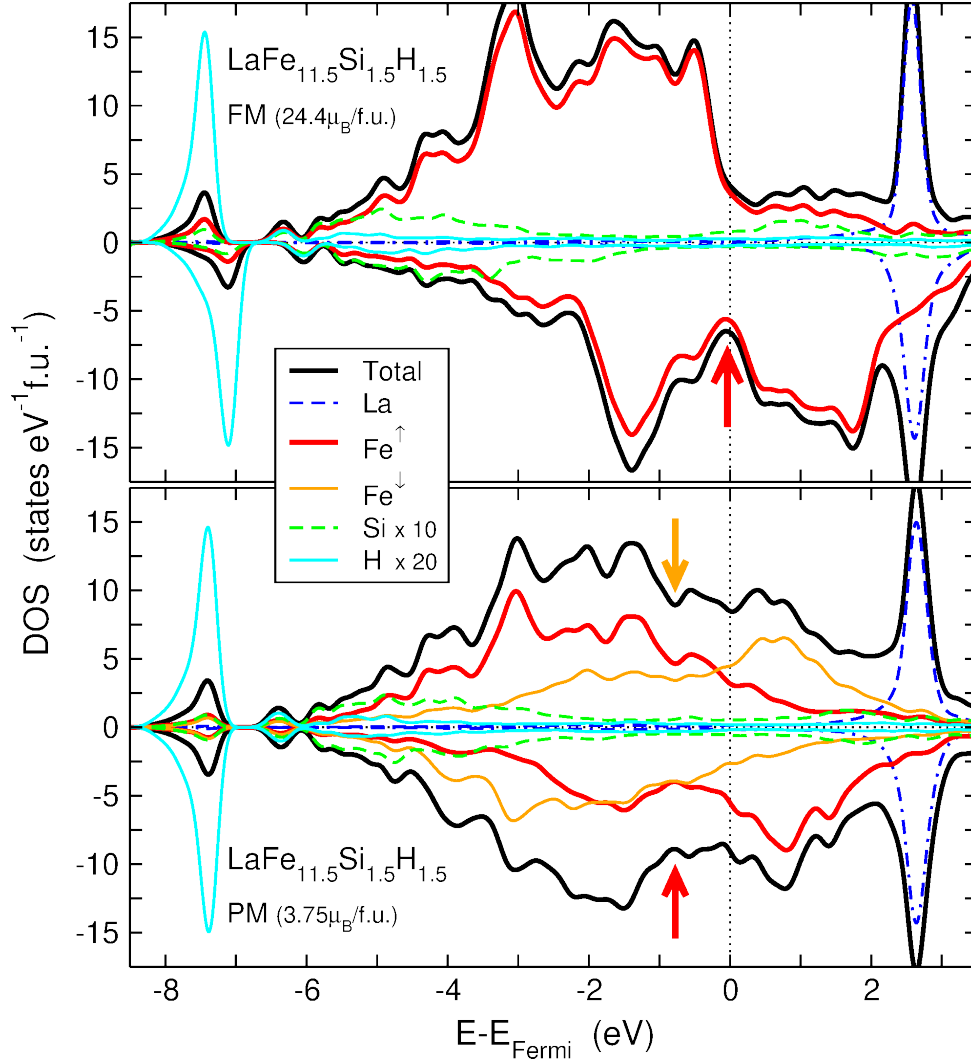


Figure 5.15.: Spin-, element- and site-resolved electronic density of states $D(E)$ of $\text{LaFe}_{11.5}\text{Si}_{1.5}\text{H}_{1.5}$ in the FM (top) and PM (bottom) phase from DFT. The black lines represent the total DOS of each spin channel, blue (dash-dotted) and red (solid) lines show the partial DOS of La and Fe^\uparrow . In the PM state part of the Fe atoms have an opposite magnetic orientation (Fe^\downarrow) (orange line). The partial Si and H contributions (green dashed lines and cyan solid lines) are enlarged by a factor of 10 and 20, respectively. The vertical red arrow depicts the minority spin minimum at the Fermi energy E_{Fermi} in the FM state. The shift of the minimum in the minority spin channel of the respective site-projected Fe-DOS (Fe^\uparrow and Fe^\downarrow) is indicated by the red and orange arrows in the bottom panel (Calculations by M. E. Gruner). Figure taken from [129].

$2.2\mu_{\text{B}}$ and is also apparent in the hydrogen free compound. The high Fe moment has been validated through Mössbauer experiments and will be further described in detail in subsection 5.4.2. The calculation for the paramagnetic phase in $\text{LaFe}_{11.5}\text{Si}_{1.5}\text{H}_{1.5}$ has been done analogously to the methods in Ref. [34, 35] for a hydrogen free case. The

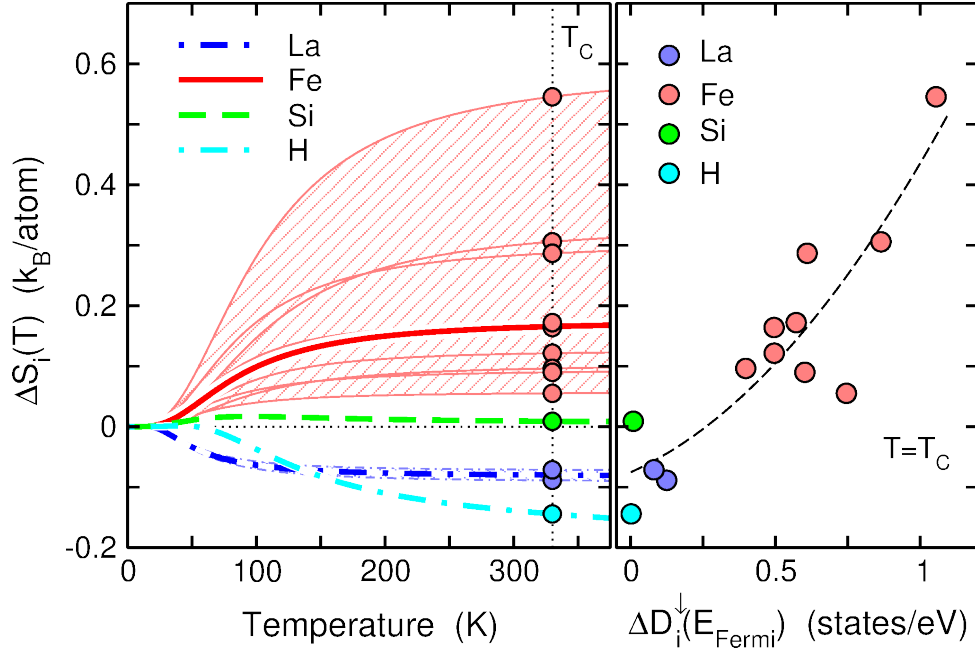


Figure 5.16.: Difference in entropy $\Delta S_i = S_i(\text{PM}) - S_i(\text{FM})$ per lattice site i as a function of T (left panel), calculated from the element- and site-resolved FM- and PM-VDOS obtained by DFT. The thick lines show the element-specific averages. In the left panel, the site-resolved entropy change (circles) at $T_{tr} = 329$ K is plotted against the change in the site-projected minority spin DOS at the Fermi level $\Delta D_i^\downarrow(E_{\text{Fermi}})$. The dashed line serves as a guide to the eye for the correlation between both quantities. We interpret this as a consequence of the adiabatic electron-phonon coupling in hydrogenated La-Fe-Si (Calculations by M. E. Gruner). Figure taken from [129].

obtained DOS shows similar characteristics also to be found in the hydrogen free system. Figure 5.15 shows in the lower panel the DOS in the PM phase. Around the Fermi level, the minimum in the minority spin channel is broadened visibly as a result from the hybridization of the minority and majority Fe d -states with reversed magnetic orientation. This effect goes along with a reduction in the local magnetic moment of Fe to $1.8 \mu_B$ due to moment volume coupling [35]. The minimum is shifted by $0.5 - 1$ eV (red arrow in lower viewgraph of Figure 5.15) below the Fermi level as a result from a decrease in the exchange splitting. Thermal disorder strongly changes the electronic structure, leading to the closing of the narrow gap.

The electronic DOS is filled up at the Fermi level in the magnetically disordered PM phase, which increases the anomalous softening of the vibrational modes as a result of adiabatic electron-phonon coupling [34, 134–136] rather than the generally expected increase of the phonon frequencies upon lattice contraction. This behavior is in agreement with temperature-dependent measurements of the thermopower [137], which is sensitive to the structure of the electronic DOS closely around the Fermi energy, where a similar change in

the characteristic shapes has been observed across the phase transition for hydrogenated and hydrogen free compounds.

Additionally to the DOS, the site resolved minority spin density has also been compared to the computed lattice entropy change across the metamagnetic phase transition, as depicted in Figure 5.16. The left panel depicts the temperature dependent entropy change as calculated from the respective site-dependent VDOS via Equation 2.41 for the FM and PM state in Figure 5.15. The thin lines correspond to the sites, the solid thick lines to the elemental averages. The Fe-sites (red) contribute cooperatively (positively) to the entropy change at the FM-PM transition. Whilst the contribution from Si is rather small and can thus be neglected, La and H show the opposite behavior than Fe and decrease the entropy across the transition. This behavior is in accordance with the lattice contraction and smaller volume in the PM phase. The overall contribution per site from H and La is small, in contrast to the effect of the Fe-sites and does neither affect the lattice entropy change ΔS_{lat} or the electronic entropy change ΔS_{el} significantly at the transition temperature. This effect can be explained by the fact that in the energetic range around -6 eV , where H could hybridize with the Fe d -states, which are sensitive to magnetic order, the H-states have a low DOS. From the experiment a value for the entropy of the Fe-specific increase ΔS_{lat} of $0.028 \pm 0.017 k_{\text{B}}/\text{Fe-atom}$ across the FM to PM transition was obtained. The absolute values for the Fe-partial entropy change from DFT calculations is with a value of $0.16 k_{\text{B}}/\text{Fe}$ significantly larger than the experimentally deduced value. This might be attributed to the idealized model for the magnetic phases used in the DFT calculations, which neglect excitations at finite temperature of the magnetic system as well as thermal expansion in the FM phase, while the experimental data was obtained closely to the phase transition with possibly residual FM order in the PM phase close to T_{tr} . The discrepancy and the overestimation of the calculated entropy value has already been discussed in Ref. [34, 47].

Comparing the relative change of the lattice entropy across the phase transition in the calculation, we find a reduction of the entropy enhancement by about 50% through hydrogenation in comparison with the non-hydrogenated case. This finding is consistent with the experimental data, which also shows a decrease of the entropy enhancement across the transition as compared to the hydrogen free compounds. This finding is in agreement with recent studies by Gercsi et al. [37] who concluded that hydrogenation leads to a decrease of electron-phonon coupling. S_{lat} reflects the elastic properties of the lattice. The site-resolved entropy corresponds to the occupation of the respective ion in phase space and thus, as the ion vibrates, more space can be occupied when moving into a softer potential. Adiabatic electron-phonon coupling directly correlates the free states at the Fermi level to the vibrational properties in the system [134–136] and has been

identified as the source of the anomalous lattice softening in hydrogen free $\text{La}(\text{Fe},\text{Si})_{13}$ [34, 35, 47]. Thus, we expect the same behavior of the disappearance of the minority spin minimum in the electronic DOS at the Fermi level, which leads to a softer lattice. This lattice softening is then reflected in an entropy enhancement across the phase transition. The righthand panel of Figure 5.15 (b) shows that this correlation is effective, when the inequivalent lattice sites i are compared at the transition temperature with the change in the local site-resolved minority spin DOS at the Fermi level as depicted in Figure 5.15 (a).

5.1.3. Conclusion

In this section, the Fe-partial vibrational (phonon) density of states (VDOS) of hydrogenated $\text{LaFe}_{11.4}\text{Si}_{1.6}\text{H}_{1.6}$, Mn doped $\text{LaFe}_{11.4}\text{Si}_{1.5}\text{Mn}_{0.1}$ and the hydrogenated and Mn doped compound $\text{LaFe}_{11.4}\text{Si}_{1.5}\text{Mn}_{0.1}\text{H}_{1.6}$ has been determined by means of ^{57}Fe NRIXS measurements in zero external field as well as in an applied magnetic field of 1.1 T. Comparing these samples with an undoped reference revealed characteristic differences in the shape of the VDOS for hydrogenated compounds in comparison to the non-hydrogenated ones. These results are confirmed by first-principles calculations with the element-resolved VDOS within the framework of density functional theory (DFT). It was found that Mn addition does not affect the structure of the VDOS significantly, but strongly suppresses the enhancement in the lattice entropy ΔS_{lat} across the phase transition.

The temperature evolution of the VDOS across the isostructural phase transition for hydrogenated $\text{LaFe}_{11.4}\text{Si}_{1.6}\text{H}_{1.6}$ shows the same trend as observed in non-hydrogenated compounds. This observation can also be applied towards the hydrogenated and Mn doped sample, as well as the purely Mn doped compound. For all samples an overall energetic redshift of the VDOS near T_{tr} can be observed despite the strong lattice contraction, when undergoing the isostructural first-order phase transition from the low temperature FM phase to the high temperature PM phase.

The DFT calculations show that this anomalous redshift is attributed to adiabatic electron-phonon coupling, as already observed in non-hydrogenated $\text{LaFe}_{11.6}\text{Si}_{1.4}$ [34, 35, 47]. The electron-phonon coupling is the cause of the lattice softening upon the phase transition. Its origin lies in the site resolved minority spin density of states, where a characteristic minimum in the minority spin density can be observed in the FM state at the Fermi level. This minimum shifts and broadens upon the introduction of magnetic disorder in the PM state. Furthermore, in the hydrogenated samples a strong reduction of the phonon peak at ~ 27 meV is observed, it is reduced to a shoulder. The addition of hydrogen results in a strong alteration of the phonon peaks. While the phase transition from FM to PM does not affect most of the peaks considerably, the peak at ~ 27 meV vanishes in all

compounds measured. This effect can be explained as a microscopic manifestation of the strong magneto-elastic coupling present in $\text{La}(\text{Fe},\text{Si})_{13}$ -based compounds.

In addition to the changes in the structure of the VDOS, the temperature dependent behavior of some thermodynamic properties has been extracted. The vibrational (lattice) entropy S_{lat} has been extracted across the magnetostructural phase transition. For $\text{LaFe}_{11.4}\text{Si}_{1.6}\text{H}_{1.6}$ the vibrational entropy S_{lat} , directly obtained from the VDOS, $g(E)$, shows an increase by $0.028 \pm 0.017 k_{\text{B}}/\text{Fe-atom}$ (or $3.2 \pm 1.9 \frac{\text{J}}{\text{kgK}}$) upon heating through the phase transition from the FM to the PM state. This value is found to be just half of the value observed in the non hydrogenated and undoped compound [47]. The trend of the increase of ΔS_{lat} upon the phase transition is in agreement with the trend from the DFT calculations. It contributes additively with $\sim 35\%$ to the overall isothermal entropy change ΔS_{iso} at T_{tr} . Rather surprisingly, the addition of Mn drastically reduces this effect and the entropy enhancement is suppressed strongly. In this case the entropy change only amounts to $\Delta S_{\text{lat}} = 0.005 \pm 0.01 k_{\text{B}}$ or $0.57 \pm 1.15 \frac{\text{J}}{\text{kgK}}$. This can be explained by stronger changes in the structure of the VDOS. Additional incorporation of hydrogen together with Mn seems to reverse the suppression and leads to a pronounced entropy enhancement around the transition of $\Delta S_{\text{lat}} = 0.009 \pm 0.026 k_{\text{B}}$ or $1.03 \pm 2.98 \frac{\text{J}}{\text{kgK}}$, which is still smaller than in the purely hydrogenated compound. The extracted values for the Debye temperatures of the Fe subsystem $\Theta_{\text{D}}^{\text{Fe}}$ in the hydrogenated samples are approximately 4% larger than in the hydrogen-free case. The entropy Debye temperature in the Mn doped sample is within the range of the undoped compound. In both cases, $\Theta_{\text{D}}^{\text{Fe}}$ is decreasing from the FM to the PM state.

5.2. Local Magnetism in Mn Doped La(Fe,Si)₁₃-compounds

With La(FeSi)₁₃ having a rather complex crystal structure with two inequivalent Fe sub-lattices, the local magnetism of the material was of particular interest. To investigate the local magnetic interactions, we performed X-ray magnetic circular dichroism (XMCD) measurements. A study of a sample series of LaFe_{11.6-x}Si_{1.4}Mn_x with different Mn concentrations ranging from $x = 0 \dots 0.5$ has been done. By also taking the temperature dependence of the FM-PM phase transition into account, it was possible to investigate the effect of Mn and its magnetic coupling to the Fe sub-lattices across the first order phase transition. The Fe K-edges, as well as the La L_{2,3}-edges have been probed in the different magnetic states. As Mn substitutes the Fe_{II}-sites (96i), randomly as predicted from theory, a change in the XMCD signal of the Fe K-edge with rising Mn concentration as an imprint of the change in the local magnetic moments of iron is expected. EXAFS measurements have been performed on 5 samples with varying Mn content. This has been done in order to determine the local lattice parameters precisely and investigate the effects of increasing Mn contents on the local structural surrounding. EXAFS spectra have been taken at the Fe K-edge as well as the La L₂-edge in both magnetic phases, at the low temperature FM and the high temperature PM phase, respectively.

5.2.1. Temperature Dependence of the XMCD of La(Fe,Si)₁₃

Fe K-edge - Temperature Dependence

For the purpose of investigating the structural change from a local magnetic point of view, undoped La(Fe, Si)₁₃ with a nominal stoichiometry of LaFe_{11.6}Si_{1.4} has been investigated utilizing X-ray absorption measurements at the Fe K-edge across the metamagnetic phase transition. Here, we measured the temperature dependence of the X-ray Absorption Near Edge Structure (XANES) as well as the X-ray magnetic circular dichroism (XMCD) across the phase transition. The transition temperature of the measured specimen is at $T_{tr} = 193$ K in an applied magnetic field of $B = 50$ mT. The width of the thermal hysteresis is narrow with a value of only 1 K. The XANES spectra have been taken at five temperature points across the phase transition from the ferromagnetic (FM) to paramagnetic state (PM), two points below the transition, and three above at values of $T = 150, 190, 200, 210$ and 300 K, respectively. The XANES spectra were taken in an applied magnetic field of $B = -1$ T. In order to obtain the corresponding XMCD, the spin dependent absorption spectra have been taken with circularly polarized incident X-rays of negative and positive helicity corresponding to parallel and antiparallel orientation

of the incident photon helicity to the applied magnetic field.

Figure 5.17 (top) depicts the normalized XANES at the Fe K-edge in an energy range of 7100 – 7135 eV with a zoom into the pre-edge feature at ~ 7114 eV corresponding to the second maximum in the XMCD (denoted as energy 3). The spectrum predominantly reflects dipolar transitions from the $1s$ to empty $4p$ -states. In the XANES, the pre-edge feature at ~ 7114 eV can be ascribed to possible quadrupolar enhanced transitions from $1s$ to empty $3d$ -states. This pre-edge structure starts in the FM phase as a weakly defined step-shaped feature. With increasing temperature, the shape of the pre-edge changes and becomes more pronounced and peak-like as the phase transition is induced in the sample system by continuous temperature increase, assuming an increase in quadrupolar transitions by an increase in the temperature. The changes arising from driving the system through the isostructural phase transition, therefore, can be directly screened by measuring the XANES as the pre-edge feature is very sensitive to the changes of the local atomic surrounding. The compression of the crystal, and thus the decrease of the lattice parameter influences the electronic surrounding of the Fe atoms. The orbital overlap is increased by reduction of the lattice parameter, resulting in a reduction of the electronic density of states close to the Fermi level through d -band broadening and consequent reduction in the magnetic moment as a result of the Stoner criterion [138]. With rising temperature, the first order phase transition is induced and the isostructural compression leads to the introduction of the PM state.

This is directly observable by comparing the XMCD spectra whilst increasing the temperature. Here a strong change in the magnetic behavior of the measured sample is visible. The K-edge XMCD itself has a derivative-like shape. From the spectrum it can be inferred that there is an existing finite magnetic moment at the two temperature points taken at the temperatures below the phase transition as to be expected for the sample being in the ferromagnetic state. Upon heating above the transition temperature, the XMCD signal shows significant reduction, indicating the transition into the paramagnetic state. This shows that the magnetism of the compounds is mainly driven by the Fe sub-lattices whose magnetic moment abruptly reduces upon the phase transition. The first strongly pronounced feature appears at the energetic position denoted as 1 in Figure 5.17.

The significant feature in between 7112 – 7113 eV (denoted as 1) in the XMCD can possibly be attributed to the quadrupolar enhanced transitions [85–88, 139–141], which are a common feature in the X-ray Absorption Spectrum (XAS) of transition metal K-edges, due to the hybridization of the p and d -states, which lead to the possibility of more empty states to be occupied. This first sharp and narrow feature in the XMCD decreases with rising temperature. This is a possible effect of the changes in the crystal field through the phase transition, altering the local electronic structure of the absorbing Fe atom, as the

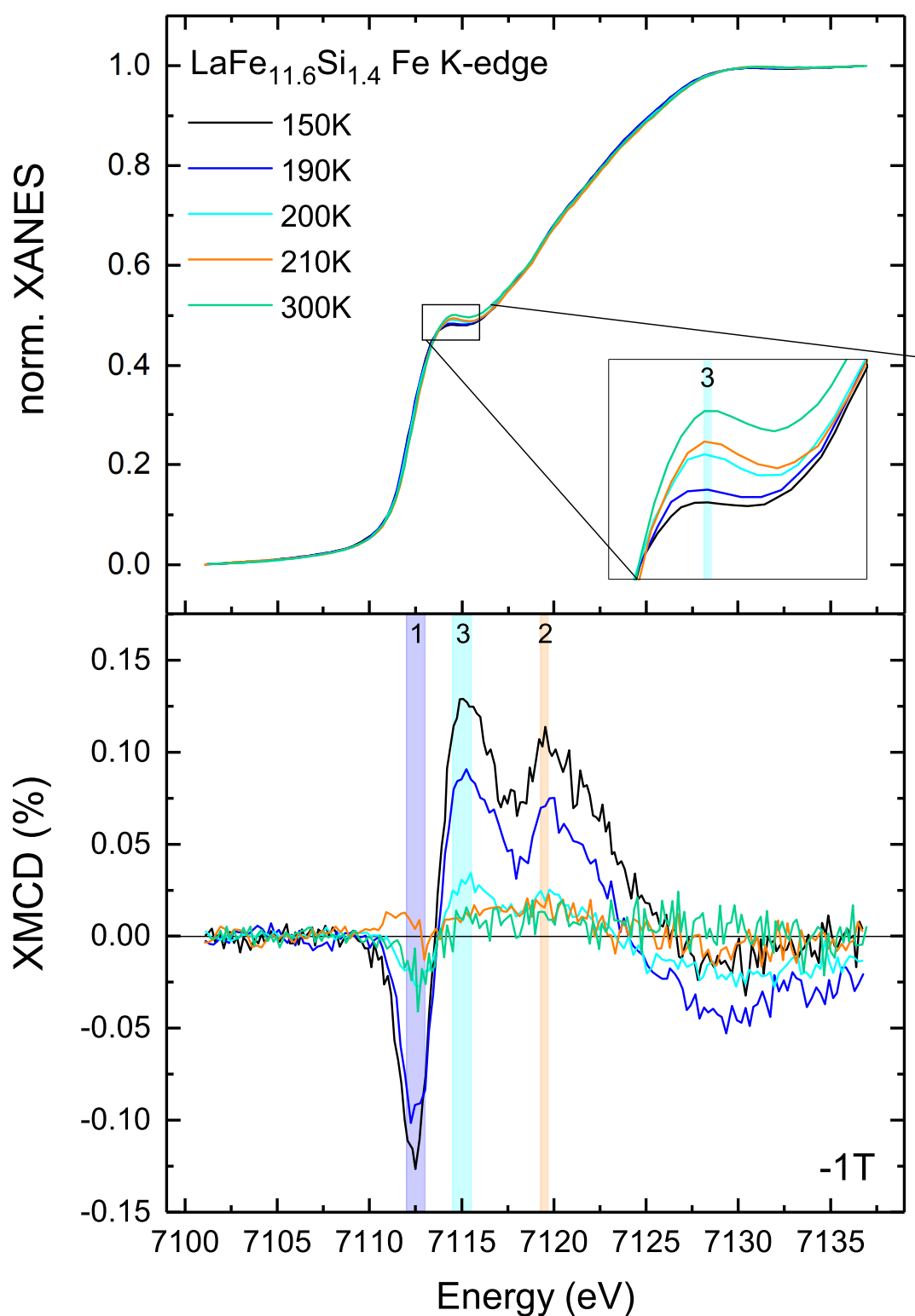


Figure 5.17.: Temperature dependence of the normalized XANES (top view graph) and XMCD (bottom view graph) at the Fe K-edge of $\text{LaFe}_{11.6}\text{Si}_{1.4}$. Spectra taken at experimental temperatures from the FM phase at 150 K (black line) to the PM phase at 300 K (green line). The inset in the top view graph shows a zoom at the energy of ~ 7114.5 eV.

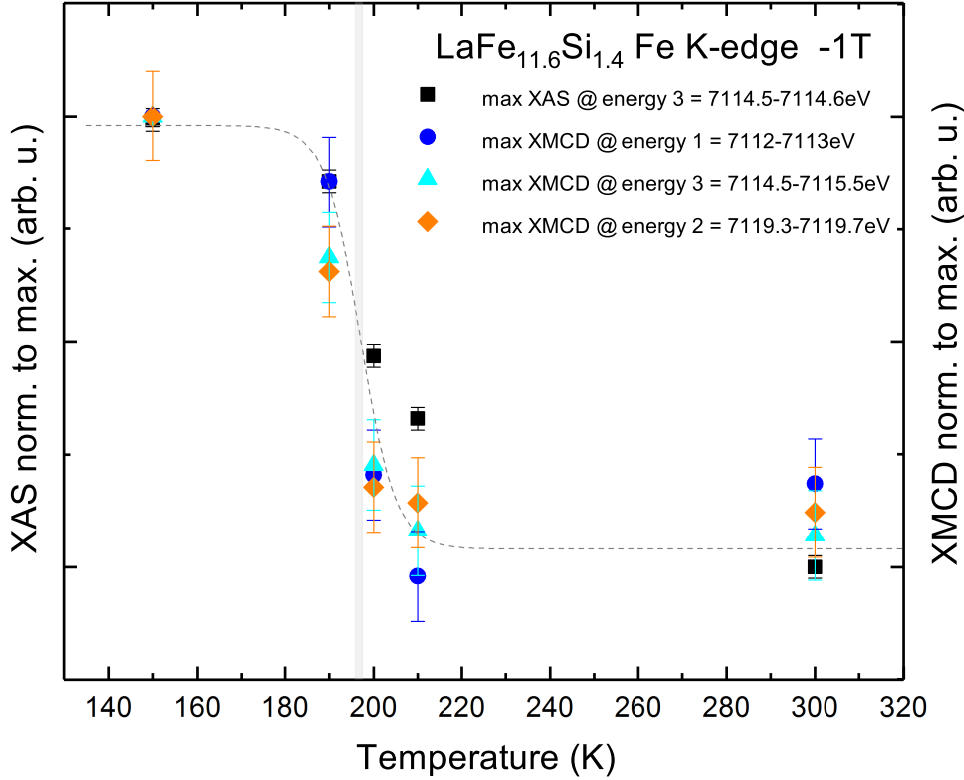


Figure 5.18.: Temperature dependence of the XAS at the pre-edge position of ~ 7114.5 eV and the values of the maximum XMCD of LaFe_{11.4}Si_{1.6} at the energies denoted as energies 1-3. The grey shaded area refers to the approximate position of the first order phase transition in 1 T in the system around 196 K as obtained from magnetization measurements. The dashed line serves as a guide to the eye.

crystal reduces its lattice constant upon heating through the phase transition. Comparing the evolution of the pre-edge feature with the maxima of the obtained XMCD at the three different energy positions (as indicated by the shaded areas 1-3 in Figure 5.17) shows a strong correlation to the magnetic signal obtained from the XMCD. As the XAS increases through the phase transition, from the FM to PM state, the magnetic moment reduces, and the XMCD decreases. From Figure 5.17 (bottom), which depicts the evolution of the XMCD signal across the metamagnetic phase transition, it is clear that the magnitude of the XMCD signal rapidly decreases as the first order phase transition is induced. While the transition was determined to be at around 193 K in an applied magnetic field of 50 mT, an applied field of 1 T shifts the transition to slightly higher temperatures, approximately to 196 K (according to the field dependent $M(T)$ experiments performed on a similar sample, see chapter 4). While the measurements at 150 K and 190 K are still in the FM phase, the drop of the magnetic signal to only a very small residual moment at 200 K nicely reflects the sharp first order phase transition.

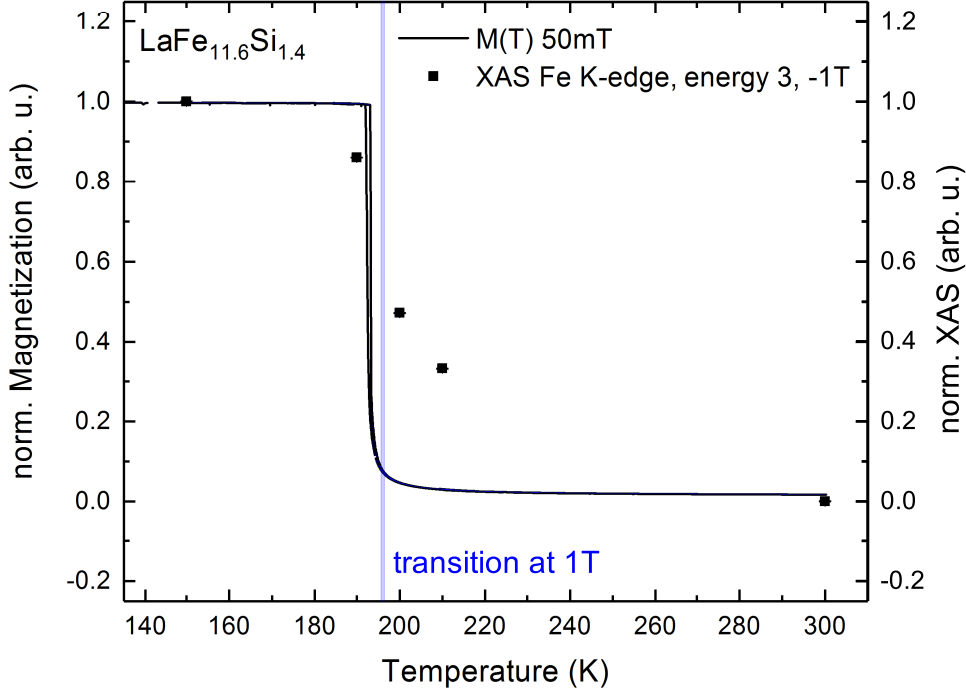


Figure 5.19.: Temperature dependence of the XAS at the pre-edge position around ~ 7114.5 eV in -1 T and the temperature dependent magnetization curve, depicting the first order phase transition of $\text{LaFe}_{11.4}\text{Si}_{1.6}$ at 50 mT. The blue shaded area refers to the approximate position of the first order phase transition in the system around 196 K which is expected to be shifted by the external field of -1 T.

A direct comparison of the temperature dependence of the maximum XAS in the pre-edge region and the maximum XMCD signals is depicted in Figure 5.18. Here the evolution of the XMCD at different energetic positions is shown as a function of temperature. The phase transition takes place at 196 K. The thermal hysteresis of the sample in zero field is as small as 1 K and has been marked by the grey shaded area. From the evolution of both XMCD as well as the XAS, it can be seen that the transition is slightly broadened, compared to the sharp transition region. The dashed line refers to the proposed transition in the given magnetic field. In Figure 5.19, the magnetostructural phase transition obtained via temperature dependent magnetometry measurements at 50 mT is compared to the change of the intensity of the XAS at the pre-edge at an energy of ~ 7114.5 eV, to show the broadening of the phase transition in 1 T. From the changes of the pre-edge feature with rising temperatures it can be deduced that the structural change, precisely the lattice contraction, is imprinted on the shape of the XAS, as described above. From the comparison of the magnetometry measurement with the marked position of the rather sharp phase transition in zero field it can be seen that the structural change stretches over a broader temperature range, due to the applied magnetic field.

5.2.2. Influence of Mn Doping on the XMCD of La(Fe,Si,Mn)₁₃

Changes of XMCD and XANES at Fe K-edge

As already seen in the temperature dependent XMCD measurements, the pre-edge holds a strong sensitivity to small changes in the local surrounding of the absorbing atom. By measuring the XANES and the XMCD of the Fe K-edge with rising Mn content, consequently a change in the pre-edge feature is expected. The sample series with a nominal stoichiometry of LaFe_{11.6-x}Si_{1.4}Mn_x has been measured below the metamagnetic phase transition in applied magnetic fields of ± 2 T at a temperature of 3 K in the ferromagnetic state and at an elevated temperatures in the paramagnetic state at 300 K with positive and negative X-ray helicity to obtain the XMCD. Figure 5.20 (top) depicts the XANES at the Fe K-edge in the magnetically ordered ferromagnetic state with increasing Mn content. The pre-edge feature at the rising edge clearly shows an imprint of rising Mn content in the XAS. The spectral shape of the absorption edge is strongly altered with increasing Mn content. This behavior can be explained by a change in the 3*d* band of the compound through substitution of the Fe-sites with Mn atoms. The substitution of the Fe atoms results in changing hybridization between the delocalized 4*p*-states and the 3*d*-states in the compound and consequent changes in the quadrupolar transitions which are reflected in the shape of the pre-edge structure as the Fe and Mn 3*d*-states hybridize. The direct comparison of the intensity of the XAS at the pre-edge feature to the Mn content shows that the XAS is generally reduced by an increase in Mn doping (Figure 5.20 (top)). The spectral shape at the pre-edge flattens out with higher Mn content. With the assumption of rising disorder in the compound through increase in Mn content the flattening of the pre-edge feature can be explained. A change in the XMCD with respect to the rising Mn content can be observed as well.

Mn doped sample series LaFe _{11.6-x} Si _{1.4} Mn _x		
Stoichiometry	Transition temperature [K]	Edges measured
LaFe _{11.6} Si _{1.4}	190	Fe K, La L _{2,3}
LaFe _{11.45} Si _{1.4} Mn _{0.15}	177	Fe K, La L _{2,3}
LaFe _{11.35} Si _{1.4} Mn _{0.25}	148	Fe K, La L _{2,3}
LaFe _{11.3} Si _{1.4} Mn _{0.3}	151	Fe K, La L _{2,3}
LaFe _{11.1} Si _{1.4} Mn _{0.5}	97	Fe K, La L ₃

Table 5.3.: Sample list of the Mn-doped series with given nominal stoichiometry, transition temperature in 50 mT and the corresponding absorption edges at which spectra were taken.

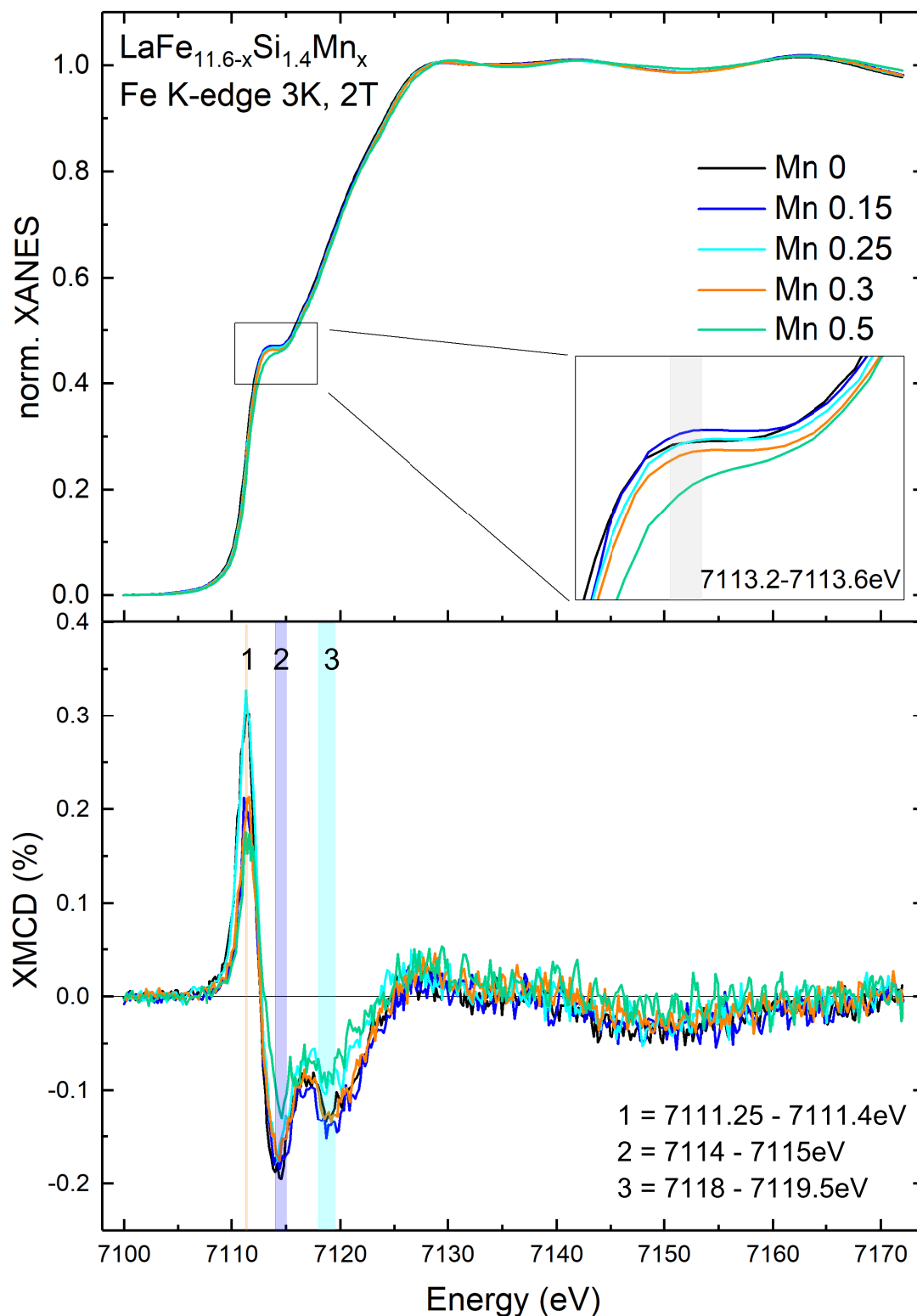


Figure 5.20.: Dependence of the normalized XANES (top view graph) and XMCD (bottom view graph) at the Fe K-edge of $\text{LaFe}_{11.6-x}\text{Si}_{1.4}\text{Mn}_x$, taken in the FM phase at 3 K at 2 T. Shown is the evolution regarding the Mn content from $x = 0$ (black line) to the $x = 0.5$ (green line). The inset in the top view graph shows a zoom at the energy of ~ 7113.5 eV.

Figure 5.20 (bottom) shows the obtained XMCD spectra of $\text{LaFe}_{11.6-x}\text{Si}_{1.4}\text{Mn}_x$ with the Mn concentrations in the range of $x = 0 \dots 0.5$. First it can be noted that all samples carry a magnetic signal at the Fe K-edge, which correlates with the low temperature ferromagnetic state of $\text{LaFe}_{11.6-x}\text{Si}_{1.4}\text{Mn}_x$ -based compounds.

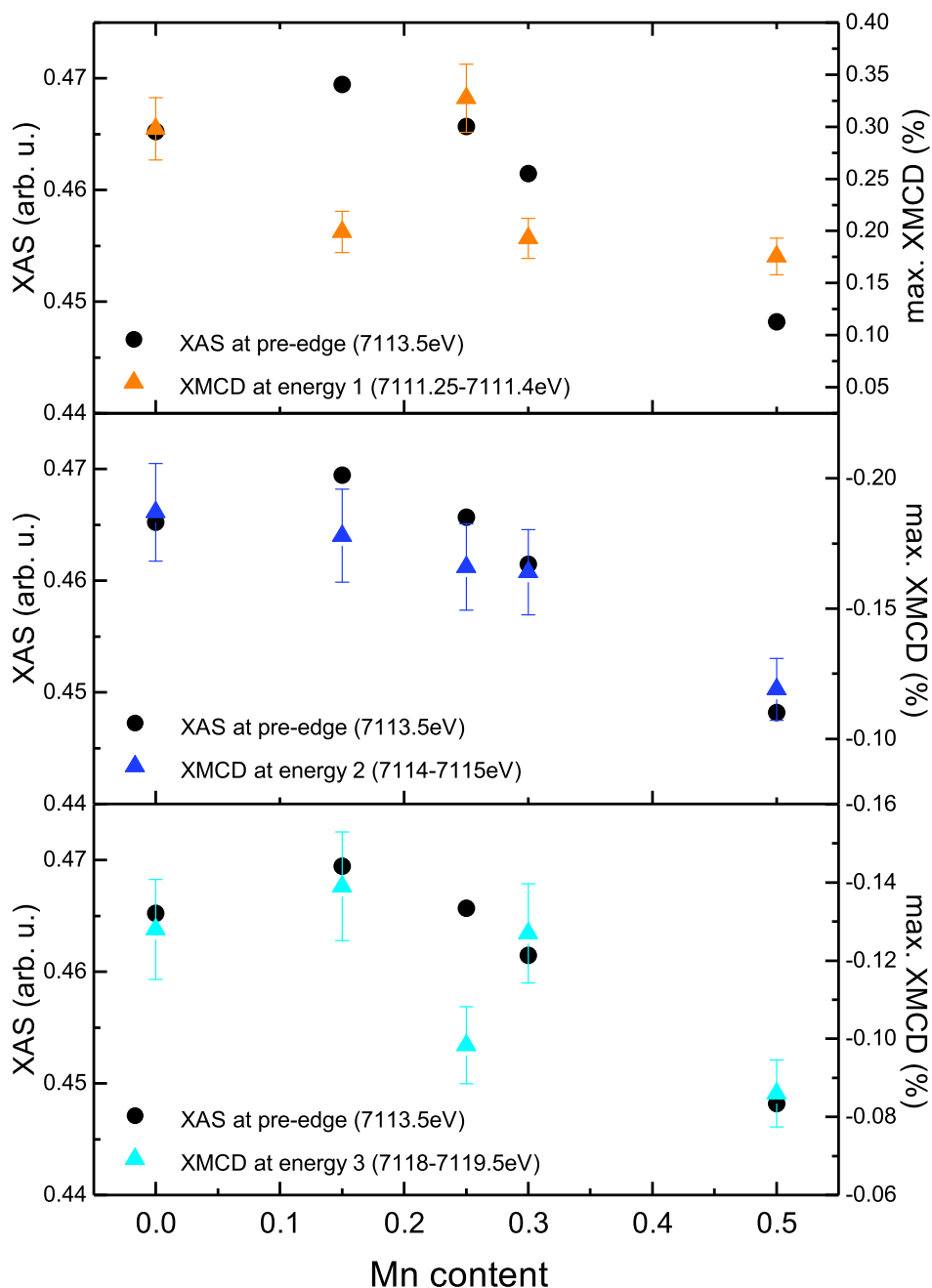


Figure 5.21.: Dependence of the pre-edge feature in the XAS at $\sim 7113.5\text{eV}$ and the maximum value of the XMCD at given energies 1 at $\sim 7111.3\text{eV}$, 2 at $\sim 7114.5\text{eV}$ and 3 at $\sim 7118.8\text{eV}$ with rising Mn content at the Fe K-edge. The error in the XAS is smaller than the symbols. The data follow from Figure 5.20.

Furthermore, it can be seen that the XMCD signal at all energetic positions decreases with increasing Mn content. To correlate the structural changes imprinted on the pre-edge with the magnetism in the sample system, Figure 5.21 compares the maximum XAS at the pre-edge position with the maximum of the XMCD at three different energy positions marked 1-3 in the graph. While the XMCD at the energetic positions before (energy 1) the pre-edge feature at 7113.5 eV does not show any correlation with the XAS, the XMCD at energy position 2 and 3 seems to correlate with the value of the XAS at the pre-edge feature. While the XAS is reduced for all Mn contents it can be inferred that the pre-edge is most sensitive to the local changes through Mn substitution. As the XAS at the pre-edge reduces from a Mn content of $x = 0$ to $x = 0.5$, the XMCD also shows a decrease for the energy positions 2 and 3. Due to this reduction a direct correlation between the Mn content and the magnetic moment of Fe is seen. The Fe moment decreases by increasing the Mn content. This behavior is in agreement with the macroscopic magnetometry measurements (see chapter 4, Figure 4.3 (a)). The absolute value of the maximum XMCD reduces by 36.4% at the energetic position 3 just after the pre-edge feature. The reduction in the moment is in accordance with the theoretical prediction that the Fe moment is reduced by Mn doping due to higher disorder, stronger spin frustration and non collinear alignment with rising Mn content [77] and can be correlated with the local structural changes, which will be described in section 5.3 and correlated to Mössbauer experiments in subsection 5.4.2 and subsection 5.4.3.

Effect of Field Induced Phase Transition on XMCD at the Fe K-edge

In order to investigate the impact of the phase transition, the XMCD has been taken at the Fe K-edge whilst driving the transition with an applied magnetic field. Here we compare the undoped sample with a nominal stoichiometry of $\text{LaFe}_{11.6}\text{Si}_{1.4}$ and a sample with a Mn content of 0.3 ($\text{LaFe}_{11.3}\text{Si}_{1.4}\text{Mn}_{0.3}$). The undoped sample has a transition temperature of $T_{\text{tr}} = 190$ K, while the sample with $x = 0.3$ has a transition at 151 K (in 10 mT). Figure 5.22 depicts the XANES and the corresponding XMCD for both samples in their initial ferromagnetic state at 3 K in 2 T (black lines). Here we can see that the pre-edge feature has a step-like shape and both samples show a strong XMCD signal. In the paramagnetic state above the transition temperature at 220 K, and in 2 T, the pre-edge feature turns into a peak like structure (see inset Figure 5.22 top viewgraph) as described in section 5.2.2. The shape of the pre-edge feature has been ascribed to quadrupolar transitions. From the temperature dependent measurement of the Fe K-edge an alteration of the spectral shape of the pre-edge is found with increasing temperature. The more compressed the lattice and, thus, higher the temperature, the more enhanced the peak-like structure, the kink, which emerges at the pre-edge. This observation is in

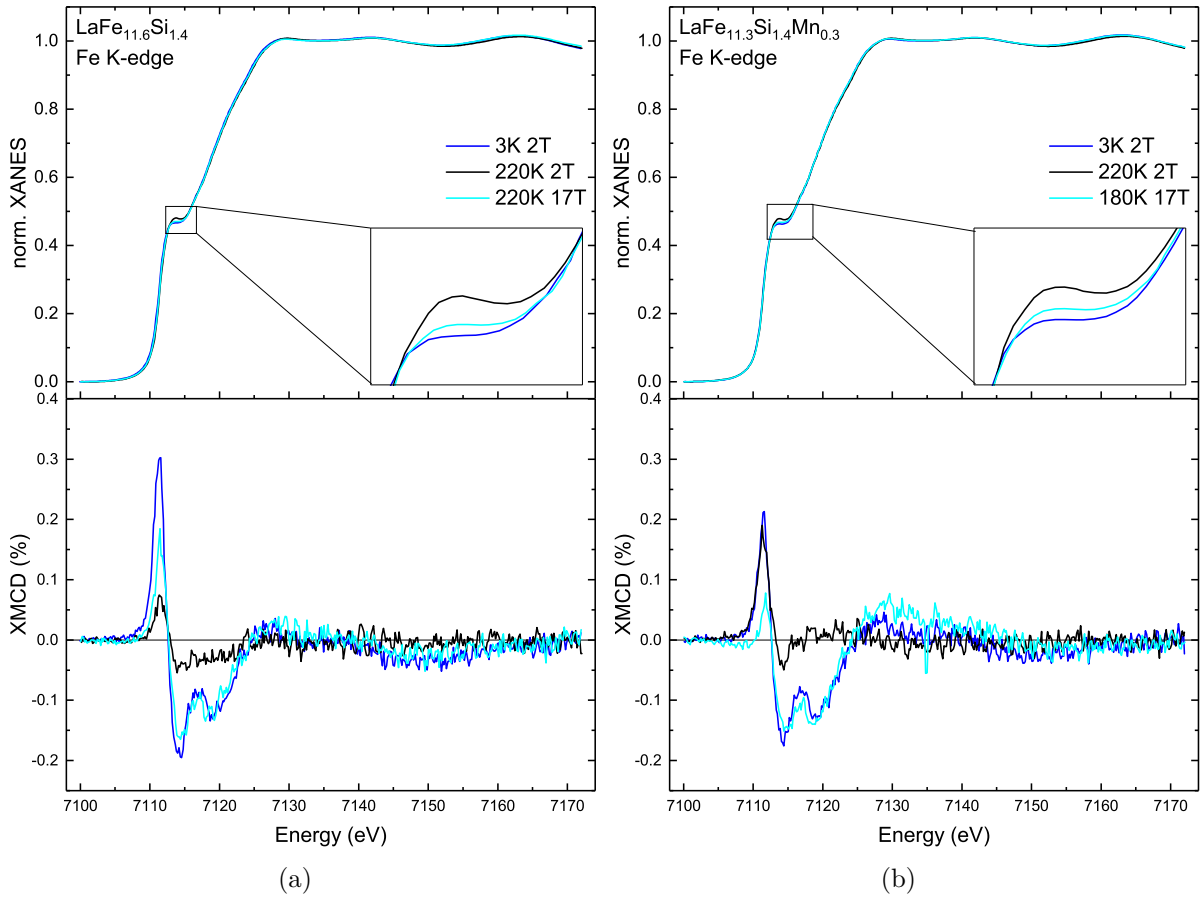


Figure 5.22.: XANES and XMCD for two samples with different Mn content in their ferromagnetic low temperature phase at 3 K and 2 T (blue line), the paramagnetic high temperature phase at 220 K in 2 T (black line) and in the FM phase at elevated temperatures 220 K and 180 K in 17 T (cyan line), respectively for Mn contents of $x = 0$ (a) and $x = 0.3$ (b).

agreement with studies on pressure induced transition from *bcc*-Fe to *hcp*-Fe [138], where the pre-edge feature changed in the same way as observed in our compound through lattice compression. On the other hand, with higher Mn content, the feature flattened, which can possibly be attributed to either fewer available states in the *3d* band and thus, fewer quadrupolar transitions or the rising disorder in the Mn doped compound. The enlarged pre-edge region in the top graph of Figure 5.22, therefore, directly reflects the structural phase of the sample. For the FM state at 3 K and in 2 T, the feature is step-shaped, whereas in the PM phase at 220 K in 2 T a peak slowly emerges, as observed in the temperature dependent XANES described above.

Stabilization through the application of a magnetic field of 17 T at 220 K, and consequently shifting the temperature of the first order phase transition by approximately ~ 60 K reduces the pre-edge feature back to a step like feature, with little deviation from the

initial low temperature FM state. The XMCD (Figure 5.22 bottom viewgraph) is in accordance with the magnetic state inferred from the pre-edge structure. Between 3 K and 220 K at 2 T the value of the XMCD drastically reduces. In the PM state only a residual signal remains with a feature at ~ 7111 eV, which has nearly its initial intensity in case of the sample with a Mn content of $x = 0.3$, while the undoped sample shows a strong reduction in the XMCD at this energetic position. It has to be noted that the XMCD in the sample with a Mn content of $x = 0.3$ overall is reduced in comparison to the undoped sample, which is in agreement with the observation of a reduction in the XMCD signal at the Fe K-edge by increasing Mn content. By applying high fields of 17 T, and shifting the transition temperature for both samples by ~ 60 K, the XMCD at 220 K (for an Mn content of 0) and 180 K (for an Mn content of $x = 0.3$) (cyan lines), is in a high temperature FM state. Both samples show a prominent XMCD signal with an intensity as large as in the initial low temperature FM phase. It has to be noted that the sharp positive peak in the XMCD does not rise to its initial intensity through the field driven transition. However, this peak is similar to that of elemental iron, where it is ascribed to the free $3d$ -states [138], and is reduced by decrease of the lattice parameter. This leads to the assumption that in the FM high temperature phase the lattice parameter may already be reduced, which could be attributed to the broadening of the phase transition through high magnetic fields, as discussed in chapter 4, or an effect of the high magnetic field, which affects the hybridization.

5.2.3. Local Magnetism of La Probed at the $L_{2,3}$ -edges

To determine the influence of the magnetic surrounding on the La atoms in the Mn doped $\text{LaFe}_{11.6-x}\text{Si}_{1.4}\text{Mn}_x$ compounds with respect to the Mn content, the XMCD has been taken at the La $L_{2,3}$ -edges, reflecting the transitions from the $2p$ - to $5d$ -states. The spectra were measured in the low temperature FM state at 3 K with an applied magnetic field of $\mu_0 H = 2$ T. Figure 5.23 depicts the XANES and corresponding XMCD spectra for the four different Mn contents $x = 0, 0.15, 0.25$ and 0.3 . The intensity of the XMCD signal is slightly above 2% for all Mn contents. Even though La has empty $4f$ -states and it has been shown that quadrupolar transitions (E2) from the $2p$ to $4f$ -states are possible in rare earth atoms [90, 142], we can derive from the shape of the XMCD that this is not the case for La, as electric quadrupolar transitions are typically reflected in a derivative like structure in the XMCD at energetic positions before the Fermi energy E_0 .

From the spectra it is apparent that La has an induced magnetic moment. The polarization of the La $5d$ -states arises from the surrounding magnetic matrix of the transition metal ions Fe and Mn and hybridization of the La $5d$ -states with the spin-polarized $3d$ -states of Fe and Mn. From the XMCD signal we can conclude that the induced magnetic

moment of La is oriented antiparallel to that of the Fe sub-lattices in the compound. Antiferromagnetic coupling is expected according to the Bethe-Slater curve, which gives the ratio of the interatomic distances as a function of the radii of the incompletely filled d -shells. By filling up the d -states, the sign of the exchange integral J changes from negative (AFM coupling) to positive (FM coupling). As the $5d$ -state in La only has one electron and the shell is less than half filled, AFM coupling is to be expected. The antiparallel $3d$ - $5d$ coupling is present between Fe and La when when the $3d$ band splitting is larger than the $5d$ band splitting [143]. The hybridization results in a change of the relative position of minority and majority bands with respect to the Fermi energy, reducing the hybridization for the spin up states. The opposite effect is the case for the spin down states and therefore the $5d$ moment is coupled antiparallel to the Fe $3d$ states [144, 145].

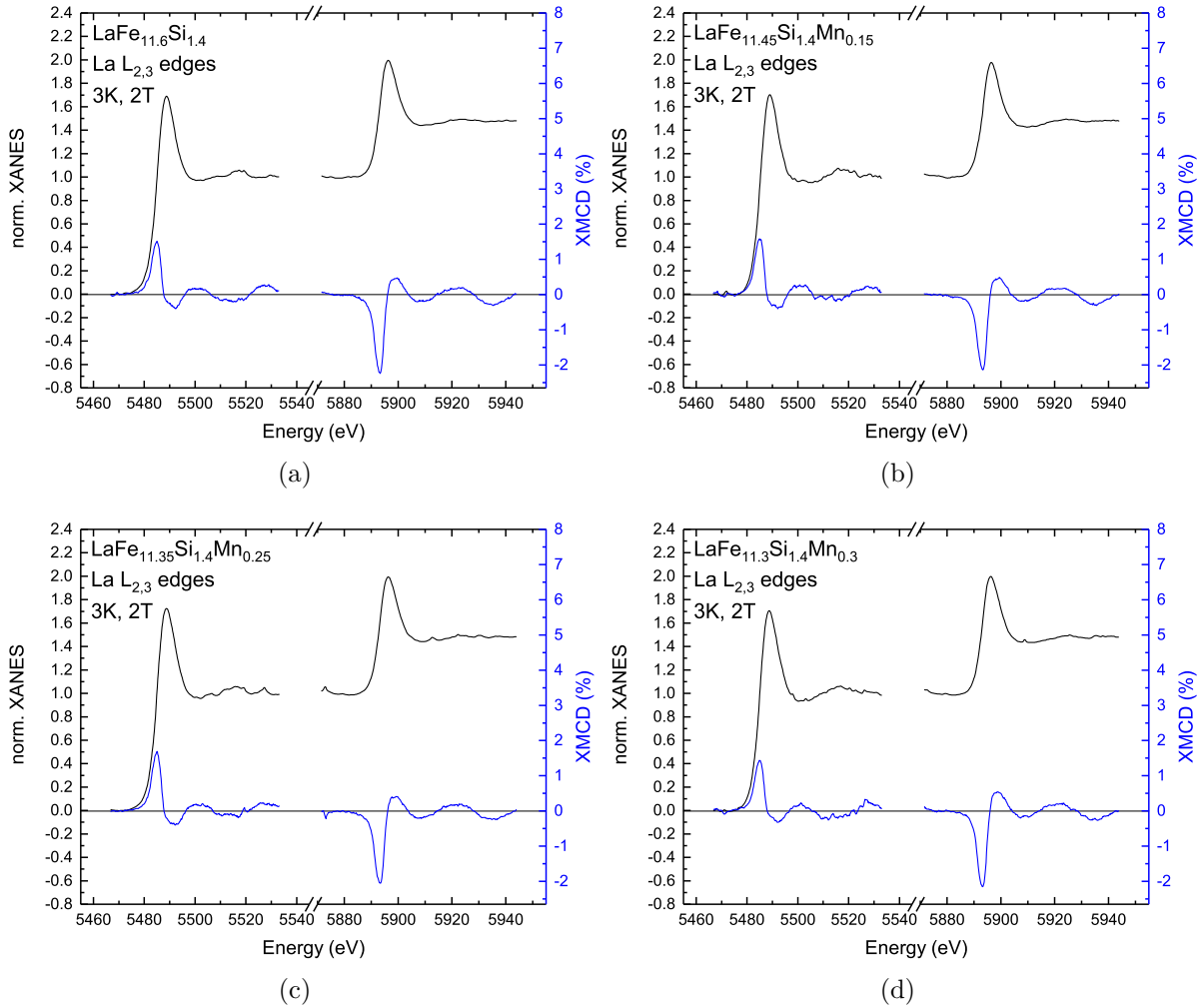
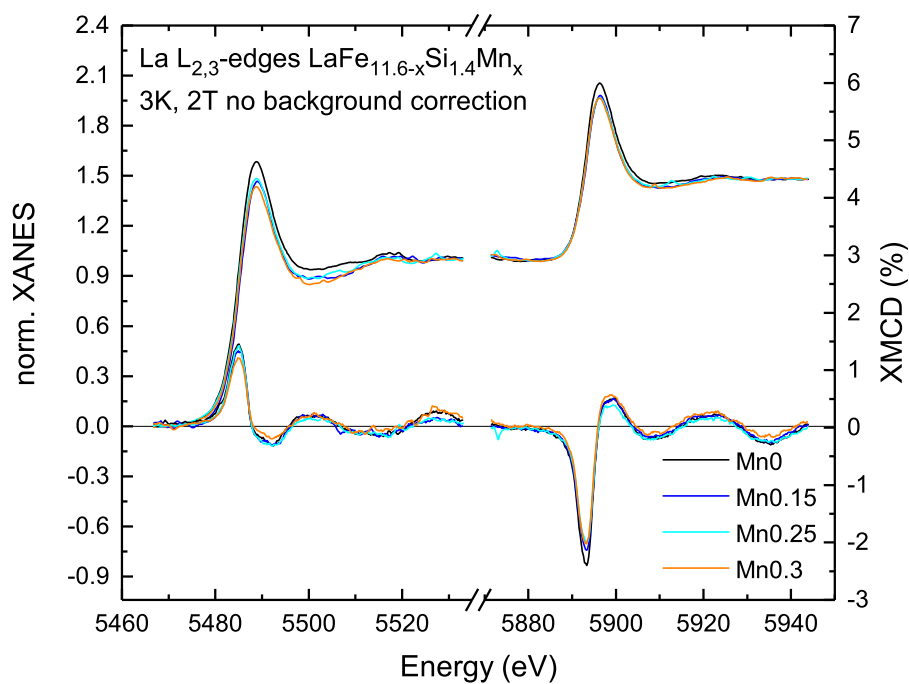


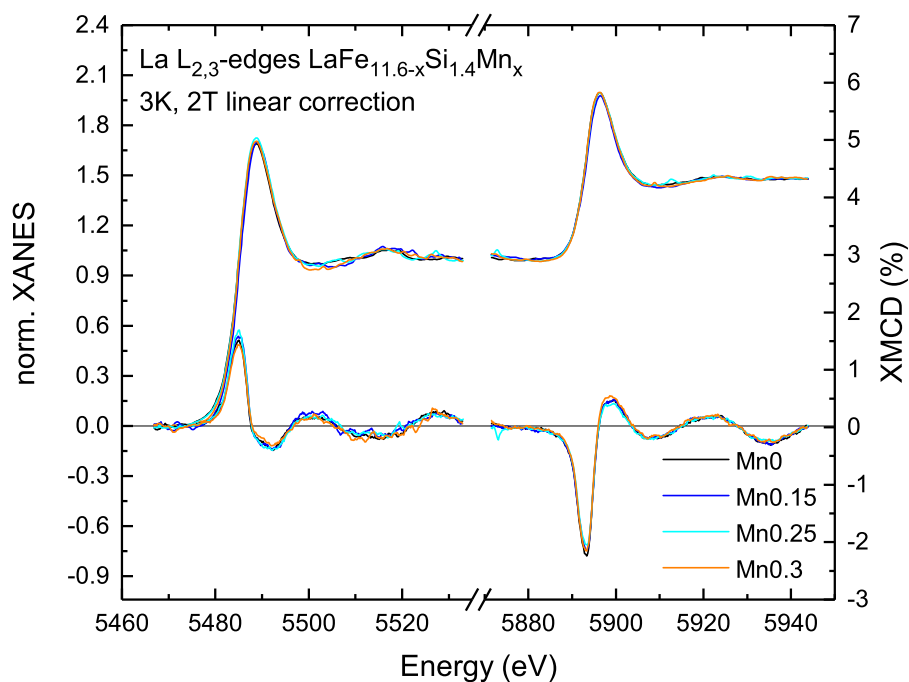
Figure 5.23.: XANES (black line) and XMCD (blue line) of the Mn doped series of $\text{LaFe}_{11.6-x}\text{Si}_{1.6}\text{Mn}_x$ at the La $L_{2,3}$ -edges with Mn contents from 0 (a), 0.15 (b), 0.25 (c) and 0.3 (d).

The alteration of the electronic surrounding is of importance, as the thermodynamic properties in $\text{La}(\text{Fe},\text{Si})_{13}$ -based compounds are affected strongly by coupling of the electronic and phonon subsystem. The changes at the Fermi level strongly contribute to the entropy change across the phase transition (see subsection 5.1.1). Antiparallel coupling has also been observed in La/Fe thin film heterostructures, where, due to strong $3d$ to $5d$ hybridization effects at the interfaces, La was polarized by the Fe layer. Also, this effect was observed in Fe-rich intermetallic compounds where an induced moment in Lutetium (Lu), which has the same number of empty d -states as La, was found to be antiparallel to the magnetic moment of Fe [146–149]. It is expected that the orbital moment is quenched in the $5d$ states due to crystal field effects [93], but from the integrals of the XMCD at the La $L_{2,3}$ -edges it can be seen that a residual orbital moment remains, as will be described later on.

Figure 5.24 depicts the normalized and uncorrected XANES for the sample series with increasing Mn content. It is directly clear that the whiteline intensity seems to be affected by Mn addition. Figure 5.25 (a) shows the evolution of the maximum intensity in the XANES at the La $L_{2,3}$ -edges with respect to the Mn content. At both absorption edges, the whiteline intensity decreases with a rise in Mn content. This effect might be attributed to hybridization effects between Fe $3d$ and Mn $3d$ -states which polarize the La $5d$ -states, leading to fewer available states to occupy, and thus, a reduction in the whiteline intensity. While a change of the free $5d$ -states in La intuitively is not expected, Shao et al. [150] proposed that electron transfer and changes in the local environment affect the La L_3 -edge when changing the Fe content or including interstitial hydrogen. It has to be noted that this effect strongly relies on whether or not a background removal has been performed and how the data has been normalized, as the post processing of the data can artificially remove or increase the effect. The effect of hydrogenation on the oscillatory fine structure in $\text{La}(\text{Fe},\text{Si})_{13}$ will be shown in section 5.3. In order to clarify the changes in the free Fe $3d$ -states a study of the XAS of the Fe $L_{2,3}$ -edges on differently Mn doped samples in the soft x-ray regime could answer how the Mn doping influences the whiteline intensity of Fe at these edges. In Figure 5.25 (b), the uncorrected XMCD is shown as a function of rising Mn content at both La absorption edges. From the XMCD, it can be seen that La carries a finite induced magnetic moment. Despite the value of the maximum XMCD at the L_3 -edge at a Mn content of 0.25, a correlation between the Mn content and the absolute value of the XMCD is visible. With increasing Mn content, the absolute value of the XMCD, and consequently the value of the La magnetic moment, decreases at both edges. In order to quantify this observation, a sum rule analysis has been applied to the $L_{2,3}$ -edges to extract the values for the magnetic spin and orbital moments of La.



(a)



(b)

Figure 5.24.: Normalized XANES and XMCD of the Mn doped sample series $\text{LaFe}_{11.6-x}\text{Si}_{1.4}\text{Mn}_x$ (a) without background correction and (b) with linear background correction.

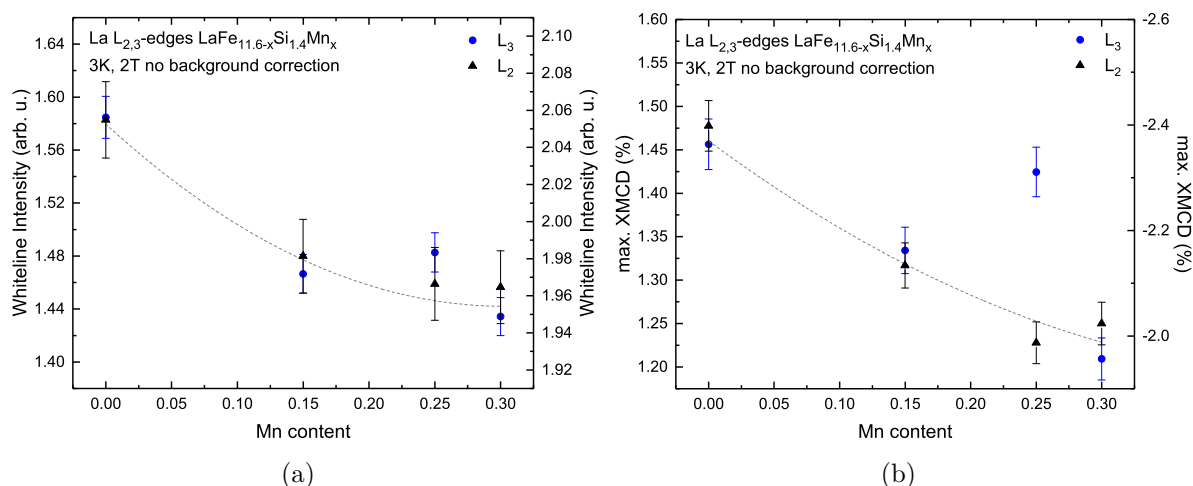


Figure 5.25.: Evolution of (a) the whiteline intensity (maximum value of the XAS) and (b) the maximum value of the XMCD at the La $L_{2,3}$ -edges with respect to the Mn content of the normalized XANES without any background correction. The dashed lines serve as a guide to the eye.

Sum Rule Analysis at the $L_{2,3}$ -edges

From the measurements at the La $L_{2,3}$ -edges, it was possible to evaluate whether the Mn content has an influence on the induced magnetic moment in $\text{LaFe}_{11.6-x}\text{Si}_{1.4}\text{Mn}_x$. By application of the sum rules it was possible to quantify the moments with regard to the Mn content in the respective sample. The analysis has been done in the ferromagnetic state.

For the sum rule analysis of the La $L_{2,3}$ -edges a few assumptions had to be made. For evaluation of the integrals the magneto-optical sum rules as described in section 2.4.1 have been used. For a background correction only a linear background subtraction has been done for the XANES as well as the XMCD. For the normalization process, the pre-edge and post-edge have been corrected to be parallel to each other as depicted in Figure 5.24 (b). From the discussion of the uncorrected spectra and the change in whiteline intensity in dependence on the Mn content, the sum rule analysis might not actually reflect the real values for the induced magnetic moments in the system. As the spectra were taken in fluorescence yield, the spectral shape might also not accurately reflect the absorption cross section due to saturation effects and decay inside the sample. The sum rule analysis therefore only gives qualitative answers and cannot be trusted in terms of the actual values as systematic deviations will be introduced [151]. The spectra have not been corrected for self absorption effects as the spectra were taken at normal incidence and the self absorption scales with increase in grazing angle [152]. In order to determine a trend in the induced magnetic spin and orbital moments and consequent sum rule analysis, it was important

to use a branching ratio which properly reflects the system. Due to the possible multiplet effects [153], which can change the expected branching of the p to d -states between the L_3 to L_2 -ratio of $\frac{2}{3}$, an experimentally determined branching ratio for the La $L_{2,3}$ -edges was used. From the spectra taken as seen in Figure 5.26 the branching ratio was estimated to be $\frac{1}{1.48}$. This branching ratio has been used throughout the whole evaluation of the magnetic moments of La, meaning that the L_3 -edge is normalized to 1, and the L_2 -edge is normalized between 1 and 1.48. The empty states N_h have been fixed to 9 as La only has one electron in the $5d$ shell. The step of the step functions used to extract the occupied states in the sample were fixed at three different positions to evaluate how the choice of the step function affects the calculated moment. First, the step was set to the edge jump, the energy E_0 (maximum of the derivative of the XANES). The second position was setting the step to the energetic position of the maximum whiteline intensity. The third evaluation was done by choosing the step at the minimum of the derivative of the XANES, which means integrating over the whole whiteline intensity.

Figure 5.27 exemplarily shows a normalized whiteline intensity with all three different step functions and the equivalent energetic positions. Once in the maximum of the XAS (cyan line), at the edge jump E_0 (blue line), which has been defined at the energetic position where the derivative of the white line is in its maximum and over the whole

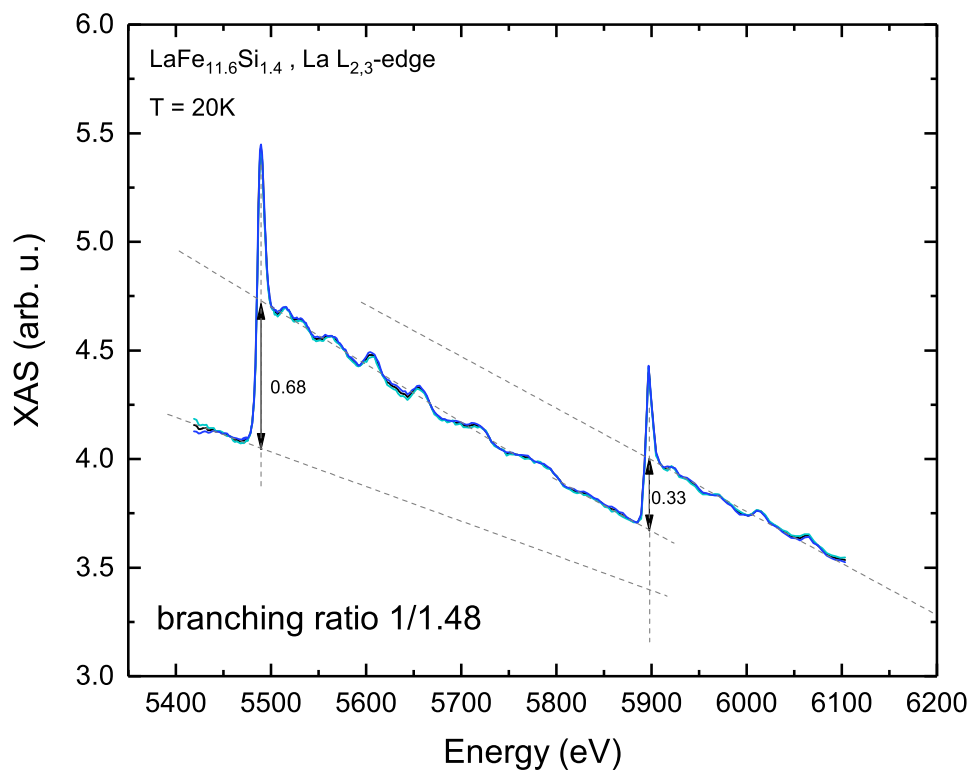


Figure 5.26.: Experimentally obtained branching ratio for the La $L_{2,3}$ -edges, measured in transmission mode without application of an external magnetic field.

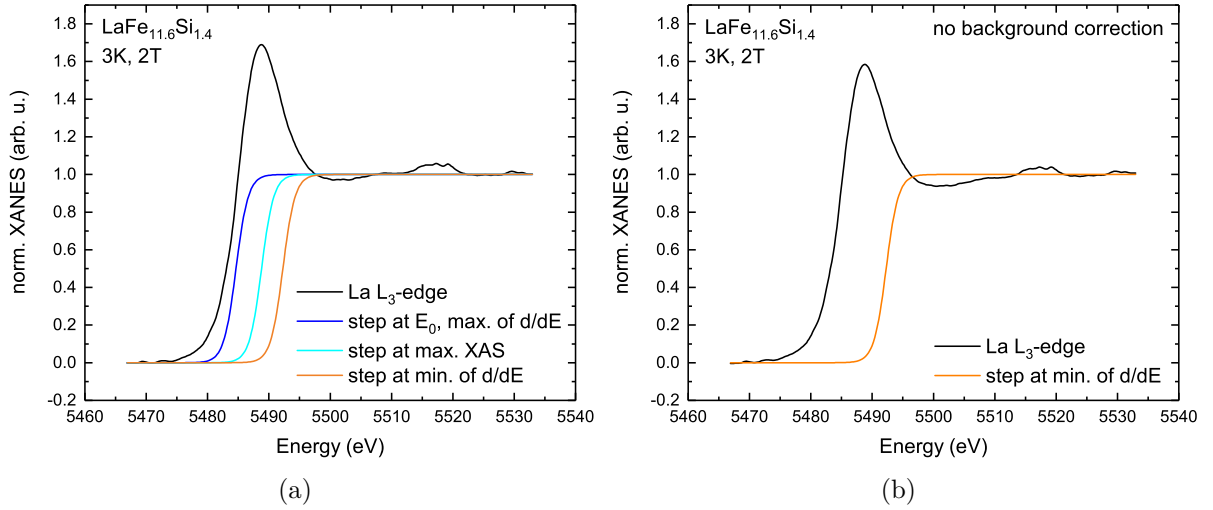


Figure 5.27.: Example of the step functions used for the sum rule analysis, depicted for $\text{LaFe}_{11.4}\text{Si}_{1.6}$ at the L_3 -edge. (a) The black line depicts the normalized XANES, the blue line the step function with the step at the maximum value of the XAS, the cyan line with the step at E_0 (maximum of derivative of the XAS) and the orange line depicts the step function at the minimum of the derivative of the XAS. (b) Uncorrected XANES with the step function used, which covers the whole whiteness intensity and corresponds to the step at the minimum of the XAS derivative.

whiteline intensity with the step at the energetic position where the derivative of the XAS is in its minimum. Furthermore, the sum rule analysis has been applied to the uncorrected spectra with integration over the whole whiteness intensity as well, as the whiteness showed a strong dependence on the Mn content. All routes used for sum rule evaluation of the orbital and the spin moment show the same trends with increasing Mn content, despite a slight difference in the absolute value. While the step function chosen seems to be unphysical, it was set to go through the median of the oscillations which are present in the post edge region. Figure 5.28 (a) depicts the extracted values of the magnetic spin moment μ_s for various Mn contents from $x = 0 \dots 0.3$. From the sum rule analysis we find that the magnetic spin moment μ_s seems to slightly decrease with increasing Mn content, which is in accordance with the magnetometry measurements (see chapter 4) and the expected decrease in the Fe magnetic moment, which will be further discussed in subsection 5.4.2. The evaluation with the step functions as described above with the step at E_0 and the consequent integrals of the XMCD yields values for the spin moment, which are in the range of those values calculated via DFT, i.e. around $-0.2 \mu_B$ [77] (see Figure 5.28 (a) dark blue circles). The values calculated with the step function with the step at E_0 will be used in this work to be compared to the results from Mössbauer experiments as they are closest to the magnetic moments obtained by

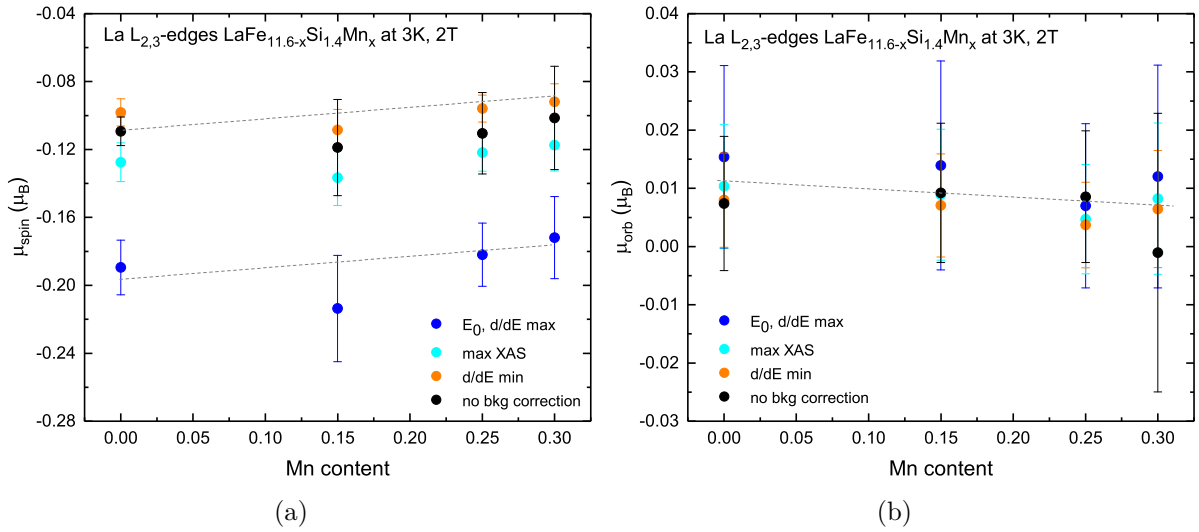


Figure 5.28.: Calculated magnetic spin (a) and orbital moments (b) for all three evaluation routes, with the step function at E_0 , the maximum XAS (middle) and at the minimum of the derivative of the XAS (bottom). All values have been calculated with a branching ratio of $\frac{1}{1.48}$. The dashed lines serve as a guide to the eye.

the DFT calculations. Within the error margin it is questionable to deduce a definite decrease of the spin magnetic moment in La with rising Mn content. To validate the sum rule analysis with a background correction, the extracted values have also been compared to the values calculated from the uncorrected XANES and corresponding XMCD. We find that the values of the sum rule analysis for the uncorrected XANES and XMCD lie in between the values with the step function at the maximum of the XAS intensity and the values obtained by using the step function with its edge step at the second derivative of the XAS. As the whiteline intensity seems to be sensitive to the local surrounding, as described before, and shows a dependence on the Mn content it might be not adequate to correct the spectra. The undoped sample with a stoichiometry of $\text{LaFe}_{11.6}\text{Si}_{1.4}$ shows a value of $\mu_s = -0.19 \pm 0.02 \mu_B$ (using the step function with the step at E_0). This value decreases to $\mu_s = -0.17 \pm 0.02 \mu_B$ at a Mn content of $x = 0.3$. Figure 5.28 (b) depicts the calculated magnetic orbital moments μ_{orb} for increasing Mn contents. The induced orbital moment is positive. With increasing Mn content the orbital magnetic moment also seems to decrease, but within the margin of error a definite dependence on the Mn content can not be proven. The induced magnetic moment of La just slightly decreases with rising Mn content, and the atomic arrangement surrounding the La atoms is not strongly affected by Mn substitution up to a Mn content of $x = 0.3$.

Taking into account the fact that at a Mn content of $x = 0.5$ only 1 Fe atom is replaced by a Mn atom within two formula units, it can be understood that the effect on La is

Induced magnetic moments in La of LaFe _{11.6-x} Si _{1.4} Mn _x			
edge step at maximum XAS			
Mn _x	$\mu_{\text{La,s}} [\mu_{\text{B}}]$	$\mu_{\text{La,l}} [\mu_{\text{B}}]$	$\mu_{\text{La,tot}} [\mu_{\text{B}}]$
0	-0.13 ± 0.01	0.010 ± 0.011	-0.12 ± 0.02
0.15	-0.14 ± 0.02	0.009 ± 0.011	-0.13 ± 0.03
0.25	-0.12 ± 0.01	0.005 ± 0.009	-0.13 ± 0.02
0.3	-0.12 ± 0.02	0.008 ± 0.013	-0.11 ± 0.03
edge step at E_0			
Mn _x	$\mu_{\text{La,s}} [\mu_{\text{B}}]$	$\mu_{\text{La,l}} [\mu_{\text{B}}]$	$\mu_{\text{La,tot}} [\mu_{\text{B}}]$
0	-0.19 ± 0.02	0.015 ± 0.016	-0.17 ± 0.03
0.15	-0.22 ± 0.03	0.014 ± 0.018	-0.20 ± 0.04
0.25	-0.18 ± 0.02	0.007 ± 0.014	-0.17 ± 0.03
0.3	-0.17 ± 0.02	0.012 ± 0.019	-0.16 ± 0.04
edge step at minimum of XAS derivative			
Mn _x	$\mu_{\text{La,s}} [\mu_{\text{B}}]$	$\mu_{\text{La,l}} [\mu_{\text{B}}]$	$\mu_{\text{La,tot}} [\mu_{\text{B}}]$
0	-0.10 ± 0.01	0.008 ± 0.008	-0.09 ± 0.02
0.15	-0.11 ± 0.01	0.007 ± 0.009	-0.10 ± 0.02
0.25	-0.10 ± 0.01	0.004 ± 0.007	-0.09 ± 0.02
0.3	-0.10 ± 0.01	0.006 ± 0.010	-0.09 ± 0.02
edge step at minimum of XAS derivative, no background correction			
Mn _x	$\mu_{\text{La,s}} [\mu_{\text{B}}]$	$\mu_{\text{La,l}} [\mu_{\text{B}}]$	$\mu_{\text{La,tot}} [\mu_{\text{B}}]$
0	-0.11 ± 0.01	0.007 ± 0.012	-0.10 ± 0.02
0.15	-0.12 ± 0.03	0.009 ± 0.012	-0.11 ± 0.04
0.25	-0.11 ± 0.02	0.009 ± 0.011	-0.10 ± 0.04
0.3	-0.10 ± 0.03	-0.001 ± 0.024	-0.10 ± 0.05

Table 5.4.: Magnetic spin and orbital moments of La, extracted via sum rule analysis for the Mn doped sample series with a branching ratio of $\frac{1}{1.48}$.

very small. The induced total magnetic moment approximately lies between a value of $-0.17 \mu_{\text{B}}$ and $-0.1 \mu_{\text{B}}$, according to the different evaluation methods.

The changes and influence of Mn content on the local magnetic moment of Fe will additionally be discussed in subsection 5.4.2. From the XMCD at the Fe K-edge we deduced a reduction of the orbital Fe moment by subsequent Mn addition, where the XMCD signal reduced upon Mn doping in the FM state (see section 5.2.2). The sum rule analysis shows that La indeed carries an induced magnetic moment, which is caused by the surrounding

Fe sub-lattices, but yet is not sensitive to the Mn contents in small concentrations. The orbital moment, depicted in Figure 5.28 (b) shows that the whole sample series has a small finite magnetic orbital moment, with the opposite sign to that of the magnetic spin moment. The orbital moment is above zero for all Mn contents and lies, regardless of evaluation method and choice of step function, at approximately $0.01 \mu_B$. An increase in the orbital momentum can be expected by ligand field effects, which give rise to the orbital anisotropy and thus, a magnetic orbital moment. Within the error it is unclear whether the slight decrease in the orbital moment through Mn doping is a definite effect. As obtained from DFT calculations, La has a small orbital moment [77], which agrees with the results from the sum rule analysis. Table 5.4 lists all the calculated values of the magnetic spin and orbital moments of La in the Mn doped sample series for all three step functions used and a branching ratio of $\frac{1}{1.48}$.

The extracted induced magnetic moments of La from the sum rule analysis are shown in Figure 5.29 (a), while the comparison to the evolution of the maximum XMCD at the energetic position E2, 7114 – 7115 eV, which showed a strong correlation with rising Mn content, is given in Figure 5.29 (b). Here it is directly visible that the La magnetic moment is proportional to the value of the XMCD of the Fe K-edge. Both slightly decrease with rising Mn content.

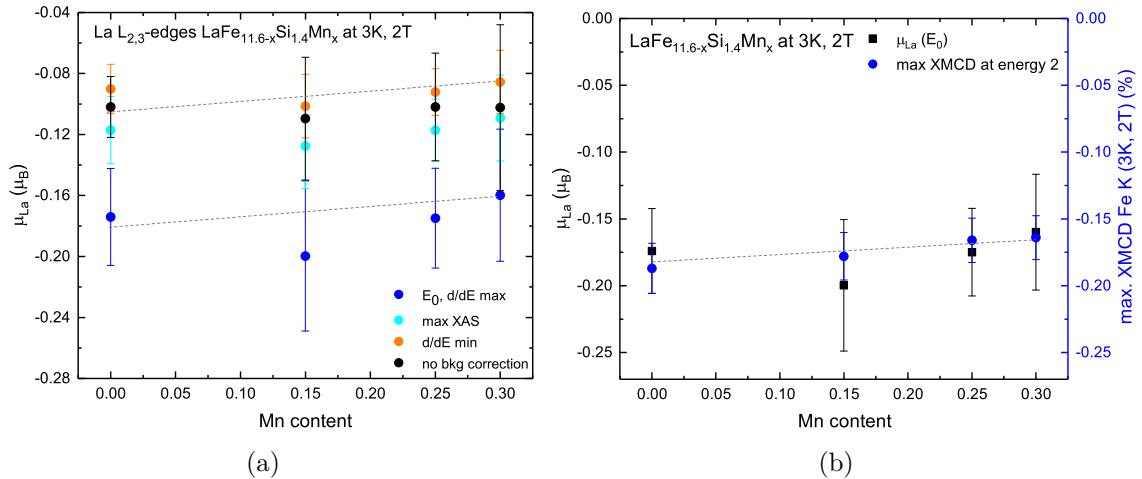


Figure 5.29.: (a) Comparison of the total magnetic moment of La μ_{La} in dependence of the Mn content using all three step functions. (b) Comparison of the extracted magnetic moment of La using the analysis with the step function at E_0 and the maximum value of the XMCD at the Fe K-edge at the energetic position 2, 7114 – 7115 eV. The dashed lines serve as a guide to the eye.

Effect of the Field Induced Transition on XMCD at La L_{2,3}-edges

The effect of external magnetic fields on the local induced La moment in LaFe_{11.6}Si_{1.4} and LaFe_{11.3}Si_{1.4}Mn_{0.3} has been studied by recording the XANES and respective XMCD at a temperature, which lies above the phase transition in an applied external magnetic field of 2 T. The samples were measured at a temperature of $T_{\text{exp}} = 220$ K with applied fields of 2 T, 8 T as well as 17 T in case of LaFe_{11.3}Si_{1.4}Mn_{0.3}. From the direct comparison between the uncorrected XANES in the FM (black line) and PM phase (orange line) in undoped LaFe_{11.6}Si_{1.4} as depicted in Figure 5.30 at an applied field of 2 T, one can infer a dependence of the spectral shape of the absorption edge with regard to the magnetic state of the sample. The comparison of the XMCD in the FM and PM state shows that La still holds a residual induced magnetic moment even in the PM phase. The second effect, next to the change in the whiteline intensity is the change of the XMCD by field application. It is increased for both samples with increasing magnetic fields. Figure 5.31 shows the normalized XANES and XMCD of (a) LaFe_{11.6}Si_{1.4} and (b) LaFe_{11.3}Si_{1.4}Mn_{0.3}. The first effect to notice in the XANES is a change in the whiteline intensity with regard to an applied magnetic field. Furthermore, higher magnetic fields strongly affect the shape of the whiteline. The application of a magnetic field of 8 T reduces the whiteline intensity in

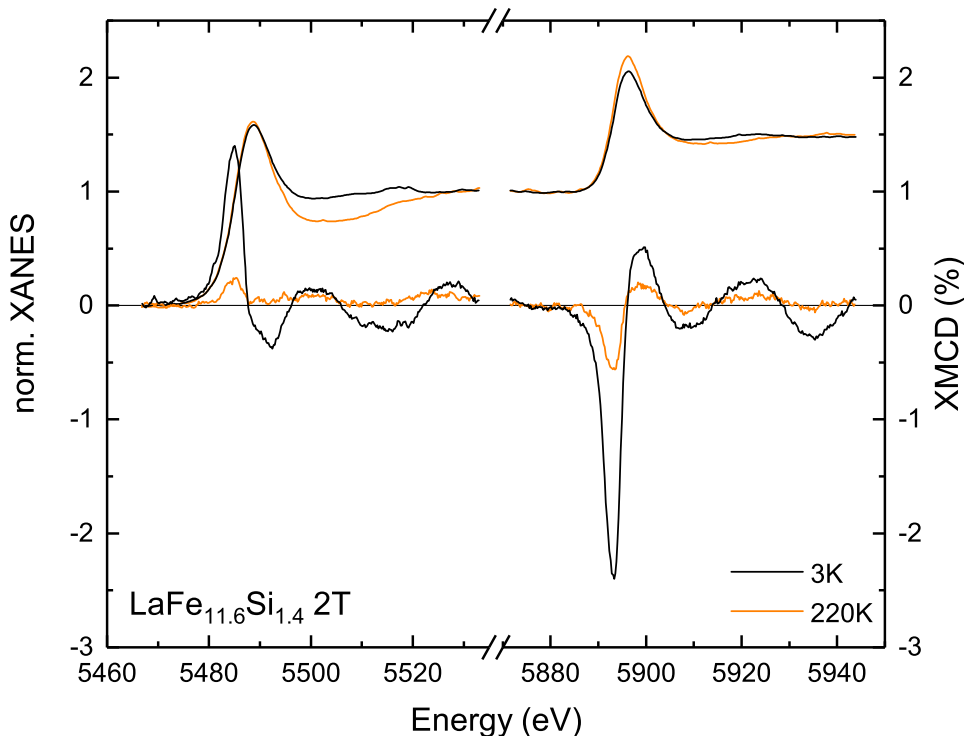
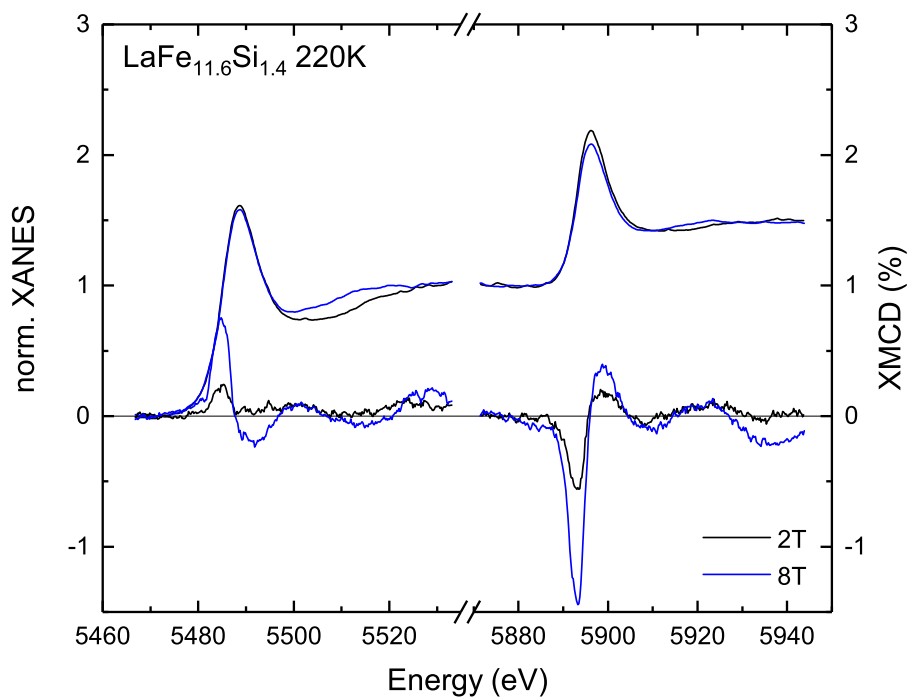


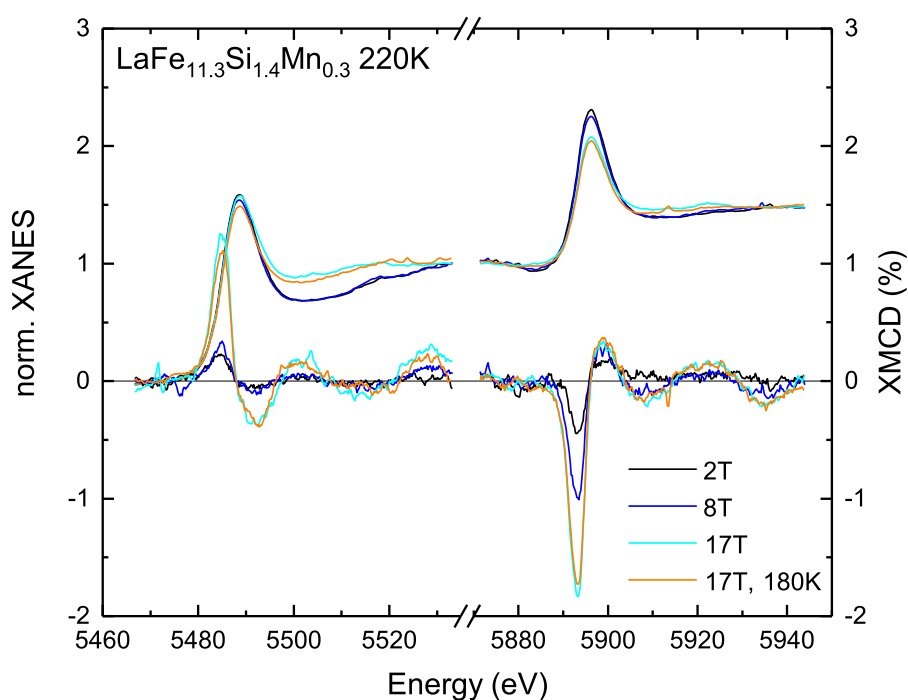
Figure 5.30.: Comparison of the normalized XMCD and XANES without background correction at the La L_{2,3}-edges in LaFe_{11.6}Si_{1.4} at 2 T in their magnetic ordered FM state at 3 K and in the magnetically disordered PM state at 220 K.

comparison to 2 T. This effect is even more pronounced for a significantly higher magnetic field of 17 T. It has to be noted, though that through the distortion of the spectral shape, the intensity of the maximum in the whiteness intensity is strongly sensitive to the chosen point for normalization as well as possible background corrections. As background correction resulted in unphysical large white line intensities, the XAS shown have not been corrected for the background. An example of the effect of background correction can be found in section A.6. From the XMCD, a linear background has been subtracted and scaled to the normalized XAS.

A reduction in the intensity and compression of the spectral shape can be connected to the measurement of the fluorescence yield and could possibly result from saturation effects [42, 151, 154]. By high field application, the ferromagnetic phase is stabilized despite being above the low field transition temperature and a magnetic signal can be observed. The strong applied magnetic fields increase the exchange splitting in the $3d$ band of the Fe atoms, which are the source of the induced magnetic signal of La. Hence, the magnetically saturated sample shows a bigger XMCD signal. In Figure 5.31 the uncorrected and normalized spectra are shown for the undoped sample (a) and the sample with a Mn content of $x = 0.3$ (b). As the spectral shape at both edges is strongly distorted with regard to the applied magnetic field, it is questionable whether background correction and consequent sum rule analysis yields physically correct information about the system. Furthermore, underlying broad Bragg peaks originating from bigger crystallites within the sample might distort the spectral shape of the XAS, making it difficult to differentiate between a real, or an effect due to the experimental conditions. This indicates that in this sample system, the spectral shape at the La $L_{2,3}$ -edges has to be discussed with caution. An evaluation with background correction and applied sum rule analysis can be found in section A.7. As temperature dependent magnetometry has been done on the sample system, it was possible to determine the approximate temperature shift in the transition temperature of $3.5 \frac{\text{K}}{\text{T}}$ (see chapter 4). For the undoped compound with a transition at ~ 190 K, the application of a magnetic field of $\mu_0 H = 8$ T results in a shift of 28 K, and shifting the first order phase transition from 190 K to 218 K. At the experimental temperature of 220 K we can assume that the sample most likely already is in the transition from the FM to PM state. The hysteresis is drastically stretched by high field application, which leads to only a very small reduction of the magnetic moment in comparison to the FM state. The sample with a Mn content of $x = 0.3$ has a phase transition temperature of ~ 150 K. Applying 8 T leads to an increase in the transition temperature to 178 K. At the experimental temperature of 220 K, the sample is in its PM state. A further increase in the field up to 17 T shifts the transition temperature by ~ 60 K. Then, the sample is in the ferromagnetic phase at 220 K, as well as at 180 K.



(a)



(b)

Figure 5.31.: Normalized XANES and XMCD of (a) $\text{LaFe}_{11.6}\text{Si}_{1.4}$ and (b) $\text{LaFe}_{11.3}\text{Si}_{1.4}\text{Mn}_{0.3}$ without background correction of the XANES at the La $L_{2,3}$ -edges. The measurements were taken at 220 K in 2 T and 8 T, respectively (a) and in 2 T, 8 T, 17 T and at 180 K in 17 T, respectively.

This can be deduced by the intensity of the XMCD, which has nearly the same amplitude for both temperatures.

5.2.4. Conclusion

In this section it was found that the spectral shape of the Fe K-edge is sensitive to the structural state and to the Mn content in $\text{La}(\text{Fe},\text{Si},\text{Mn})_{13}$, detecting slight changes in the electronic surrounding. Based on the evolution of the kink in the pre-edge feature it was possible to see a dependence on the reduction in the lattice parameter introduced by heating the sample through the phase transition as well as an influence through Mn doping.

While Fe holds a finite magnetic moment as seen from the XMCD at the K-edges, it was gradually reduced by substituting Mn, which is in agreement with the reduction of the magnetization seen in magnetometry measurements in chapter 4. The first order phase transition could be stabilized through the application of high external magnetic fields while heating above the transition temperature. It has been found from the XANES and XMCD at the La $L_{2,3}$ -edges that La holds an induced magnetic moment, coupled antiparallel to that of Fe. The induced moment is a direct consequence of the hybridization of the Fe and Mn $3d$ -states and the La $5d$ states, changing the electronic structure significantly.

At the La $L_{2,3}$ -edges the spectral shape, more precisely the whiteline intensities, of the uncorrected spectra showed a strong dependence on the rising Mn content. With increase in the Mn concentration, the whiteline intensity reduced. The corresponding XMCD showed a reduction in its intensity with regard to the increase in Mn. While the change in the whiteline intensity here in this system and with these experimental data can not conclusively be attributed to a physical effect inside the sample system, the XMCD showed a reduction regarding the Mn content.

To quantify the magnitude of the induced La moment, consequent sum rule analysis via different evaluation routes showed only little effect on the total magnetic moment of La with rising Mn doping. It slightly decreases with rising Mn content. The induced orbital magnetic moment in the system remains positive, meaning it seems to be not completely quenched in the crystal structure. The uncertainty of the sum rule analysis lies within the strong alteration of the structural shape of the XAS through magnetic fields and Bragg peaks. From measurements of the field induced transition at the La $L_{2,3}$ -edges it was concluded that the spectral shape is strongly affected by the high magnetic fields and the magnetic state, which possibly hints towards other hybridization effects as a consequence of the structural compression across the first order phase transition and the magnetic polarization induced as an effect of the external magnetic fields.

5.3. Changes in Local Geometric Structure by Mn Doping and Hydrogenation

EXAFS measurements have been performed in order to determine the local geometric structure and disorder in Mn-doped $\text{La}(\text{Fe},\text{Si})_{13}$ compounds. Furthermore, the influence of hydrogenation has been evaluated in the samples the NRIXS experiments have been performed on. The measurements on the Mn doped compounds have been done in the two distinct magnetic states of $\text{La}(\text{Fe},\text{Si},\text{Mn})_{13}$ in both magnetic phases with different Mn contents. In order to predict the degree of disorder and compare the assumed structures before evaluating the local geometry, *ab-initio* multi-scattering calculations via *FEFF* [155] have been done to be compared with the experimental data. The effect of hydrogenation on the local structure only has been investigated at the low temperature FM state. EXAFS spectra have been taken at the Fe K-edge, the La L_3 -edge as well as the Mn K-edge at 20 K in the FM, and at 300 K, the PM phase. This has been done in order to precisely evaluate the changes in the local geometric structure around the absorbing atom across the phase transition with respect to the Mn doping. The absorption spectra were taken in fluorescence mode as described in subsection 3.2.2. The measurements, taken at the Fe K-edge, have all been corrected for the residual α -Fe content. The α -Fe secondary phase content has been calculated from subsequent magnetometry measurements on the pressed powder samples used for the experiments following the procedure described in chapter 4. The correction of the absorption spectra has been done using a reference spectrum of iron foil at 60 K and at 300 K (see section A.2), which has been weighted with the according secondary phase contents as obtained by magnetometry as listed in Table 4.2. To extract the EXAFS, $\chi(k)$, the obtained energy dependent absorption spectra, $\mu(E)$, had to be normalized and corrected for residual backgrounds. The correction and normalization has been performed using *Athena* from the *Demeter* software package [156, 157], where the edge step $\mu_0(E)$ is estimated and the background is subtracted. For the background a spline function has been used, which resembles the bare atom background. The spline function has been adjusted such that it runs through the EXAFS oscillations without artificially amplifying any oscillations. Figure 5.32 (a) depicts exemplary the absorption spectrum at the La L_3 -edge in $\text{LaFe}_{11.6}\text{Si}_{1.4}$ at 20 K with the spline function, which has been subtracted. The edge step is extracted from the difference at the energetic position E_0 after defining a pre- and post-edge region by adjusting a second order polynomial function to the spectrum. After normalization, the EXAFS $\chi(k)$ is calculated (according to Equation 2.31). The spectra shown in this work all have been k -weighted to amplify oscillations at higher energies, while damping low energy oscillations which do not hold information on the local geometry. Quadratic or

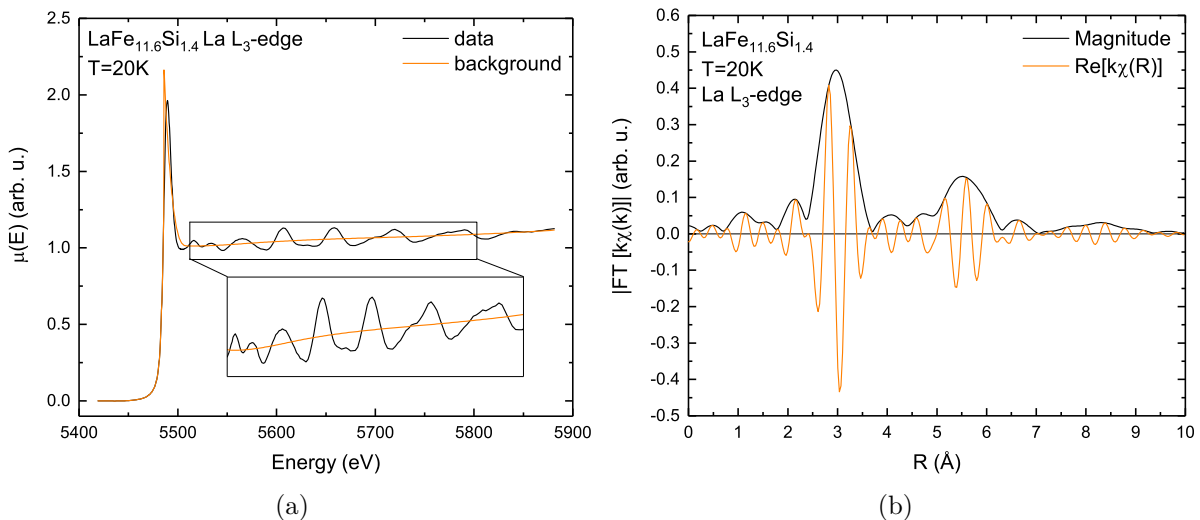


Figure 5.32.: (a) Absorption spectrum (black line) of $\text{LaFe}_{11.6}\text{Si}_{1.4}$ at 20 K at the La L_3 -edge with a spline function (orange) for the background (b) Fourier transform (black line) of the isolated EXAFS of (a) with real part (orange).

higher order k -weights lead to an exaggeration of the higher energy oscillations and might amplify noise rather than real oscillations. By using a forward Fourier transform (FFT) on the k -weighted EXAFS, the coordination shells can be extracted and transformed back from the momentum space [158]. Selecting an appropriate k -range for the transform yields the distance in real space $|\chi(R)|$, which reflects the coordination shells of the absorbing atom. This procedure gives the possibility to determine the radial distances between the absorbing and scattering atoms element-specifically. The first coordination shell usually includes the next neighbor scatterers and mainly single scattering paths. As a window function throughout this work Hanning functions have been used with $dk = 0.2$. The higher the energetic range in which $\mu(E)$ is taken, the more information is in the FFT. Figure 5.32 (b) shows the Fourier transform of the k -weighted EXAFS together with its real part. The absolute values of the peak maxima of the coordination shells are shifted from the true distance by a small factor α , which usually amounts to $\sim 0.2 - 0.5 \text{ \AA}$ with respect to the real distances in the compound due to the phase shift. This shift has to be taken into account when evaluating the local geometry [81, 98]. A backward transformation provides further information about the fine structure oscillations in EXAFS by, for example, only transforming the first shell, in order to see the effect of the second shell scattering in the EXAFS. Depending on the measured k -range for the different absorption edges, the resolution of the distinguishable distances varies. The resolution in radial distance ΔR is dependent on the selected k -range for the Fourier transform and is $\sim \frac{\pi}{2\Delta k}$. EXAFS measurements at the Fe K-edge, therefore, have a minimum resolution of 0.16 \AA for the distances, which can be distinguished in the measurements presented,

while the measurements at the Mn K-edge and the La L₃-edge only have a resolution of $\Delta R = 0.22 \text{ \AA}$ and 0.3 \AA , respectively, due to the comparably small k -range, which was measured. The resolution was limited due to the other absorption edges present in the sample. This leads to more structured coordination shells in the Fourier transform for the Fe K-edge, while the coordination shells at the Mn K- and La L₃-edges have a Gaussian shape due to lack of the structural resolution.

First a comparison of the whole Mn series and the two extreme cases, i.e. a comparison of the different magnetic states, and then a comparison for Mn contents of $x = 0$ to $x = 0.5$ will be shown. Furthermore, the effect through hydrogenation will be explained, before a consequent analysis of the different edges, using theoretical calculations by *FEFF* and fits by *Larch* [159] of all edges will be presented.

5.3.1. EXAFS and Fourier Transform of LaFe_{11.6-x}Si_{1.4}Mn_x

EXAFS oscillations at the Fe K-edge are depicted in Figure 5.33 (a) with the corresponding forward Fourier transform in (b). The EXAFS has been transformed in a range between $3.9 - 14 \text{ \AA}^{-1}$. Due to the noise in the data at high k -values, a slight ripple is added to the Fourier transform. In the EXAFS oscillations changes can be seen, which originate from the consequent substitution of Fe by Mn. All $k\chi(k)$ show the same features. At 6.5 \AA^{-1} a beating node is apparent, which changes the shape of the envelope function. At $4.5, 8.5$ and 9.8 \AA^{-1} the EXAFS has shoulders, which originate from the scattering of the second coordination shell. Increasing Mn content shows a slight shift in the oscillation towards higher k -values, which indicates a reduction in the lattice parameter, while the shoulders in the EXAFS at $6.5, 7.5$ and 8.5 \AA^{-1} again originate from the second coordination shell.

The shoulders in the EXAFS oscillations of the La L₃-edge also arise from the scattering of the second coordination shell. To obtain the radial distances, a forward Fourier transform of $k\chi(k)$ has been done in between $3.7 - 9.5 \text{ \AA}^{-1}$. The effect of Mn doping at the La L₃-edge only results in an amplitude reduction of the oscillation and the peaks in the Fourier transform. The fine structure remains nearly unchanged, meaning that La is less affected by the Mn doping than the Fe K-edge or the Mn K-edge. With rising Mn content a shift in the EXAFS is more apparent than at the Fe K-edge. At the Mn K-edge, the shape of $k\chi(k)$ does not change with rising Mn content in contrast to the Fe K-edge and the La L₃-edge. Here, also a beating node is seen, slightly suppressing the oscillation at 6.5 \AA^{-1} . This effect is present, if two coordination shells are very close to each other [81]. In the FT of $k\chi(k)$ in between $3.5 - 10.7 \text{ \AA}^{-1}$, it can be seen that the first and second coordination shell both slowly shift to smaller radial distances with rising Mn content. A decrease of the next neighbor distance upon increase of Mn doping is consistent with

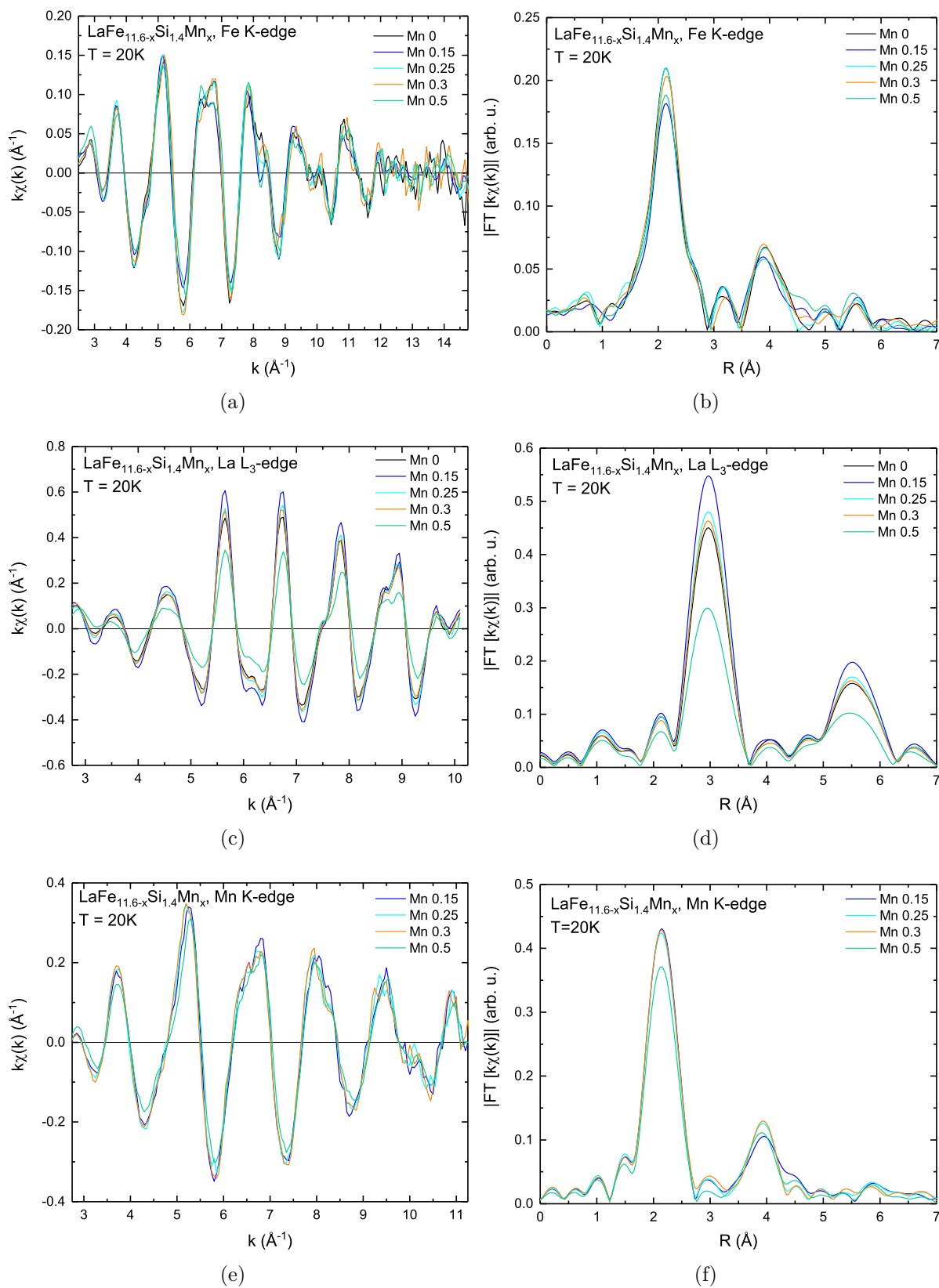


Figure 5.33.: Comparison of the EXAFS $\chi(k)$ (a,c,e) and the k -weighted Fourier transform $|\text{FT}[k\chi(k)]|$ (b,d,f) for $\text{LaFe}_{11.6-x}\text{Si}_{1.4}\text{Mn}_x$ taken in the FM state at 20 K at the Fe K-edge (a,b), the La L_3 -edge (c,d) and the Mn K-edge (e,f). Data are shown for Mn contents of $x = 0, 0.15, 0.25, 0.3$ and 0.5 , respectively.

literature [127]. Furthermore, it can be noted that the effect of the shift in radial distances seems to be more pronounced in the second coordination shell. Here, the shift seems to be strongly influenced by the disorder originating from Mn.

5.3.2. Effect of Temperature on the Local Geometry

The direct comparison of the oscillatory fine structure reveals distinct differences between samples of varying stoichiometries and temperatures. Figure 5.34 depicts the Fe K-edge measurement of the reference sample with a composition of $\text{LaFe}_{11.6}\text{Si}_{1.4}$ without Mn addition. Shown is the X-ray absorption $\mu(E)$, Figure 5.34 (a), for the two magnetic phases, i.e. for the low temperature ferromagnetic phase at 20 K, and the high temperature paramagnetic phase at 300 K. Figure 5.34 (b) depicts the extracted EXAFS $\chi(k)$. From the EXAFS, a shift in the oscillations to higher frequencies is visible from the FM (black) to the PM (orange) phase. The shift of the oscillatory fine structure can directly be attributed to the isostructural volume contraction upon heating through the metamagnetic phase transition, which takes place in the sample around 190 K. As the lattice parameter decreases from the FM to PM phase, the oscillations in momentum space are shifted to higher values, directly reflecting the magnetostructural phase transition. Due to a rise of the dynamic disorder σ_{dyn}^2 , which is increased by the thermal disorder, the amplitude of the EXAFS is drastically reduced in the PM phase. In the FM phase there are just zero point vibrations present, which do not damp the amplitude significantly. The temperature dependent damping in the EXAFS oscillations as well as the frequency shift is

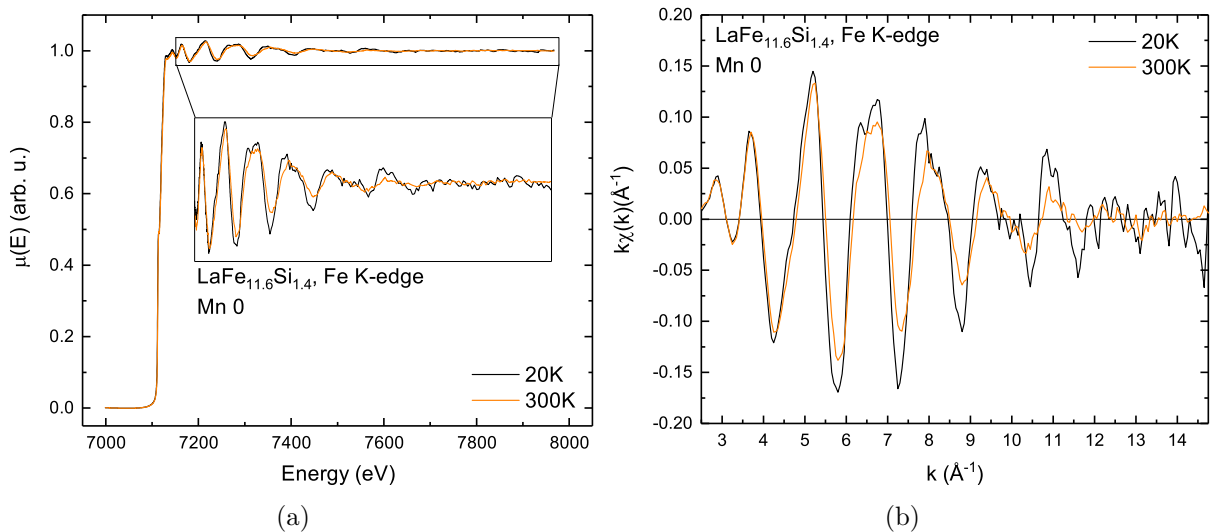


Figure 5.34.: (a) Normalized absorption spectrum for $\text{LaFe}_{11.6}\text{Si}_{1.6}$ in the FM (black) and PM (orange) phase with (b) corresponding k -weighted EXAFS $k\chi(k)$ in both magnetic phases.

consistent for all Mn contents and can be observed at all edges measured within this work. From the Fourier transform of the k -weighted EXAFS a shift of the main peaks of the coordination shells can be directly inferred. Figure 5.35 depicts the Fourier transform of the Fe K-edge (a,b), and the La L_3 -edge (b,c) in the FM and PM phase, respectively for Mn contents of $x = 0$ (a,c) and $x = 0.5$ (b,d). The error in the maximum peak position of the radial distances in the coordination shells can be approximated to be 0.01 \AA . The effect on the immediate surrounding of the Fe K-edge is with -0.015 \AA is very small. A shift due to the temperature change cannot be conclusively inferred from the data from the FM to the PM phase and will be discussed in the following chapters where the structure is fitted. For the La L_3 -edge the behavior is different. Here the radial distance of both coordination shells change visibly. A strong shift of the first and of the second coordination shell can be seen by changing the temperature and inducing the structural volume contraction. The main peak of the undoped compound shifts by 0.06 \AA from the FM to PM transition, the second peak even shifts by 0.16 \AA . From the Fourier transform of the Mn doped compound, Figure 5.35 (f), with $x = 0.5$ first of all a strong amplitude reduction is apparent, which can be attributed to increasing disorder through the Mn addition. Additionally, the main peak, corresponding to the first coordination shell is also shifted by 0.06 \AA to smaller distances, across the transition. For the second shell peak it is difficult to estimate a single position for the maximum, as the coordination shell is highly reduced in their amplitude. The Fe K-edge does not express a shift in the maximum of the first coordination shell at all. At the Mn K-edge, depicted in Figure 5.35 (e,f), the FT of the compound with $x = 0.15$ and $x = 0.5$ show that the second coordination shell has more structure in the PM phase than the comparable second shell at the Fe K-edge, despite the same expected surrounding, as Mn substitutes the Fe-sites and has the same next neighbor coordination as the Fe atoms. In the second shell, a double peak structure emerges, with one feature shifting towards lower and the other shifting to higher radial distances. This clearly points towards a distinct modification through Mn doping with influence of the transition on the structure, as the shell seems to separate these two different peaks. In the first coordination shell, a shift to lower distances is visible at a Mn content of $x = 0.15$. The main peak position of the first shell shifts by 0.06 \AA to smaller distances, the second shell by 0.06 \AA as well. The reduction is less pronounced in the sample with $x = 0.5$, here, no shift can be seen at the first coordination shell, which is the same behavior as observed at the first coordination shell of the Fe K-edge for a Mn content of $x = 0.5$. The fact that no shift is visible at the Fe and Mn K-edges for high Mn contents leads to the assumption that the high disorder in the system strongly affects the local surrounding of both Mn and Fe, as a reduction in the nearest coordination is still visible at the La L_3 -edge with a Mn content of $x = 0.5$. From the comparison of the

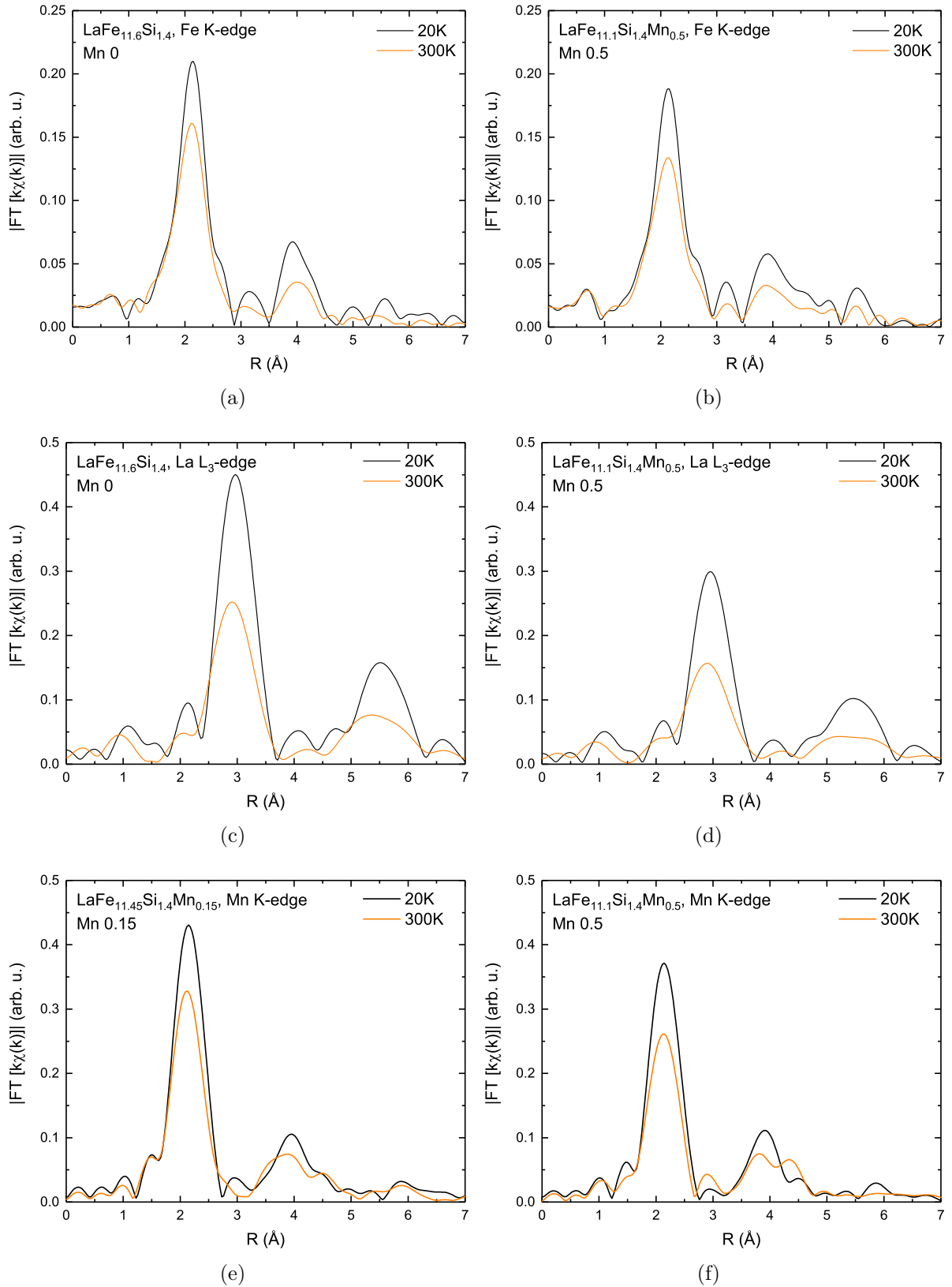


Figure 5.35.: Forward Fourier transform at the Fe K-edge (a,b), the La L_3 -edge (c,d) and the Mn K-edge (e,f) for Mn contents of 0 (a,c), 0.15 (e) and 0.5 (b,d,f) in the FM phase at $T_{exp} = 20$ K (black line) and in the PM phase at $T_{exp} = 300$ K (orange line).

different edges for no and high Mn doping it can be seen that the next neighbor distances do not shift uniformly. The main peak of the first coordination shell shifts the most at the La L₃-edge, while the immediate next neighbor distance of Fe seems not to be reduced at all. This observation leads to the assumption that the structural volume contraction of 1% upon the first order magnetostructural transition is not completely isostructural as the atomic distances do not change equally and little change is observed at the Fe K-edge, which holds the largest amount of structural information due to the k -range measured.

5.3.3. Element-specific Changes through Mn Doping

From the XAS and XMCD measurements at the Fe K-edge and the La L_{2,3}-edges, as described in subsection 5.2.3, the changes through Mn doping were significant. Here, first the absorption spectrum of LaFe_{11.6-x}Si_{1.4}Mn_x at the La L₃-edge is shown in the FM phase at $T_{\text{exp}} = 20$ K. Figure 5.36 depicts $\mu(E)$ of the whole series with all Mn contents measured. As discussed earlier in subsection 5.2.3, the uncorrected XAS of the La L_{2,3}-edges in LaFe_{11.6-x}Si_{1.4}Mn_x, showed a changing whiteline intensity with varying Mn content. While in the uncorrected spectra a trend could be inferred, which correlated the increase of the Mn content to the decrease in the whiteline intensity, here the corrected and normalized absorption spectra show a variation in the intensity of the whiteline, but no direct correlation to the Mn content.

To investigate the effects of high Mn doping, the undoped sample has been compared to the compound with a Mn content of $x = 0.5$ in the FM phase at 20 K. As depicted in Figure 5.37, the EXAFS shows a slight shift of the oscillations to higher k -values at all edges, which indicates a reduction in lattice constant with increasing Mn content. At the Fe and Mn K-edges, the amplitude of the oscillations between Mn $x = 0$ and $x = 0.5$ do not significantly change. In contrast to that behavior is that of the La L₃-edge, where we can see a damping in the EXAFS oscillation, as well as in the Fourier transform. As all the measurements are taken in the FM phase at 20 K, this effect can only result from the static disorder σ_{stat}^2 in the sample in the immediate surrounding of the La absorber. The Fourier transform at the Fe and Mn K-edge, again, show similarities with respect to Mn doping. The first coordination shell is not visibly affected by an increase in Mn content, whilst the second coordination shell shift to smaller values. In the Fourier transform, no changes in the radial distance is visible at the Fe K-edge, while at the La L₃-edge a reduction of 0.023 Å and 0.025 Å can be inferred in the first and shell in the second shell, respectively. At the Mn K-edge only a reduction is visible in the second coordination shell. Here the radial distance is reduced by 0.05 Å. Mn doping seems to affect the long range order strongly, which is most pronounced at the Fe K-edge.

In the EXAFS at the Fe K-edge a distinct modification can be seen in the oscillations

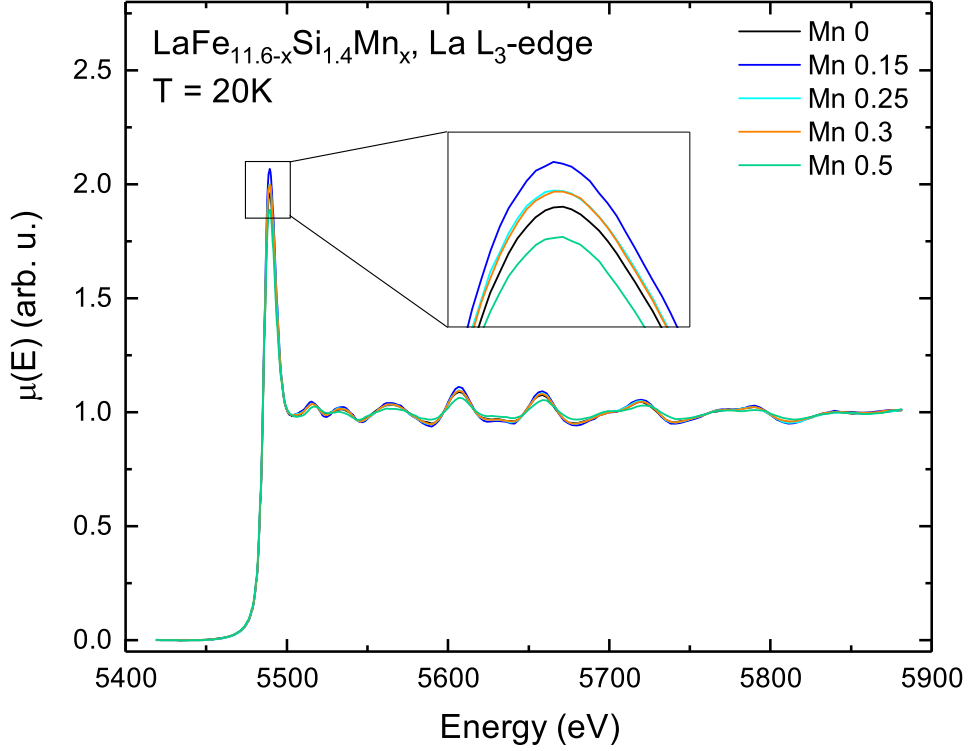


Figure 5.36.: Normalized absorption spectrum of $\text{LaFe}_{11.6-x}\text{Si}_{1.4}\text{Mn}_x$ in the FM phase at 20 K for various Mn contents x , ranging from 0 to 0.5.

at 8.5 \AA^{-1} . Here the oscillation shows a dip resulting from distinct modifications in the second coordination shell as seen in the Fourier transform in between a radial distance of $4 - 5 \text{ \AA}$. While the amplitude at the Fe K- and Mn K-edges in the EXAFS is not significantly affected by Mn doping, the opposite behavior is observed at the La L_3 -edge. Here, the EXAFS oscillations are strongly reduced through Mn doping, while the structure of the oscillations is not affected in the EXAFS. While the Mn doping only slightly reduces the next neighbor coordination in contrast to the temperature effect, the modification of the EXAFS is strongly pronounced. Both Fe K- and Mn K-edges show a beat node which results from multiple next neighbor distances very close to each other and thus, a dip in the envelope of the oscillation appears.

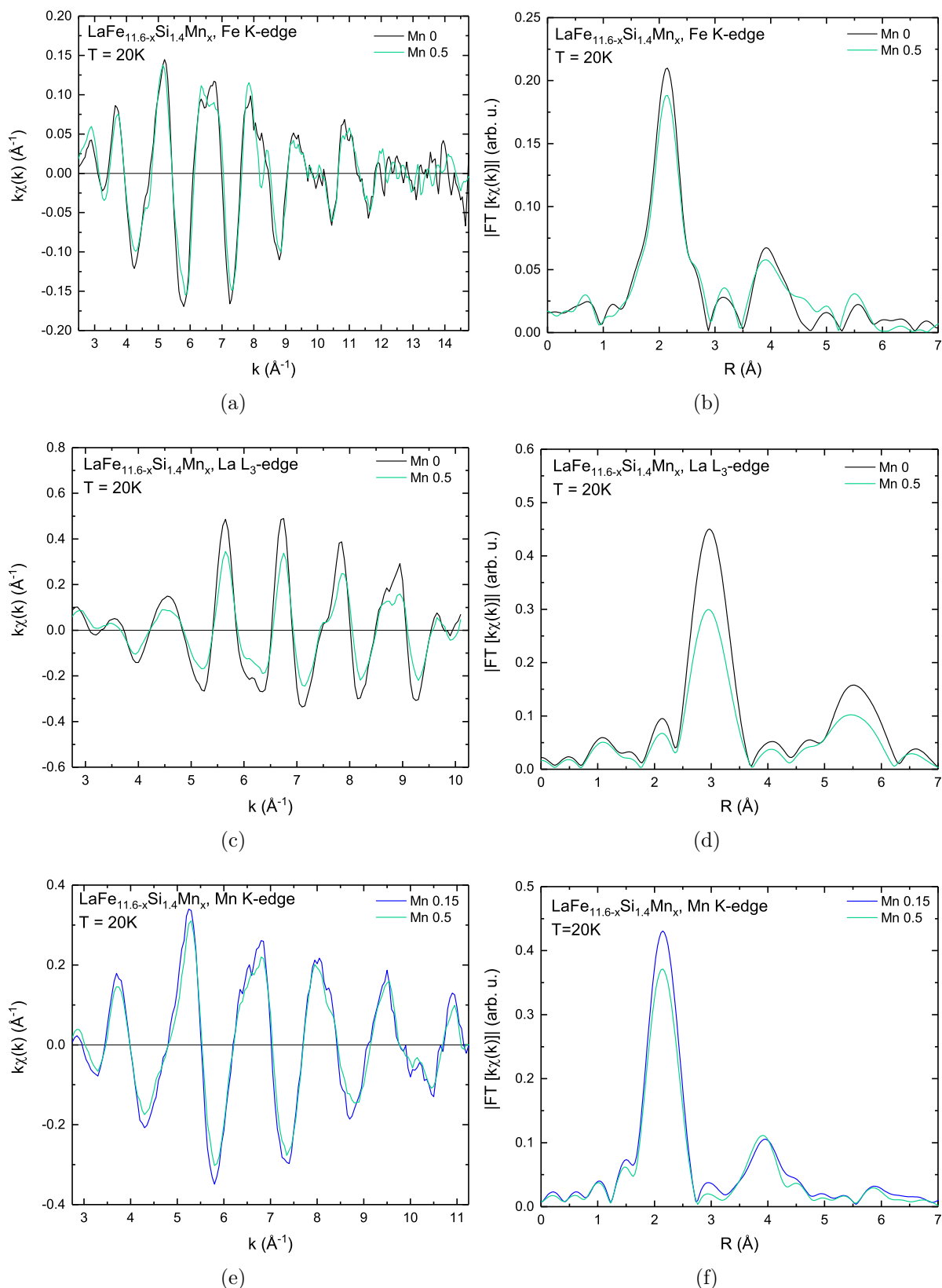


Figure 5.37.: Comparison of the EXAFS of $\chi(k)$ (a,c,e) and the k -weighted Fourier transform $|FT[k\chi(k)]|$ (b,d,f) for $\text{LaFe}_{11.6}\text{Si}_{1.4}$ (black line), $\text{LaFe}_{11.45}\text{Si}_{1.4}\text{Mn}_{0.15}$ (blue line) and $\text{LaFe}_{11.1}\text{Si}_{1.4}\text{Mn}_{0.5}$ (green line), taken in the FM state at 20 K at the Fe K-edge (a,b), the La L_3 -edge (c,d) and the Mn K-edge (e,f).

5.3.4. Element-specific Changes through Hydrogenation

As hydrogenation has a strong impact on the lattice parameter by increasing the lattice parameter significantly, the effect of experimentally full hydrogenation $y = 1.6$, has been evaluated by means of EXAFS. The samples used are the undoped reference with the nominal composition $\text{LaFe}_{1.4}\text{Si}_{1.6}$ and the hydrogenated sample $\text{LaFe}_{1.4}\text{Si}_{1.6}\text{H}_{1.6}$, which have been shown in subsection 5.1.1. In Figure 5.38, the absorption $\mu(E)$ is shown at the La L_3 -edge of $\text{LaFe}_{1.4}\text{Si}_{1.6}$ (black line) and $\text{LaFe}_{11.4}\text{Si}_{1.6}\text{H}_{1.6}$ (green line) at an experimental temperature of 20 K in the FM phase. Apart from an apparent change in the oscillations of the EXAFS region, the inset shows the enlarged maximum of the whiteline, which shows a change between the undoped and hydrogenated compound.

EXAFS measurements have been taken in the FM phase at $T_{\text{exp}} = 20 \text{ K}$ at the La L_3 - and the Fe K-edges. From the EXAFS as depicted in Figure 5.39 (a,c) a strong shift in the oscillations is visible to lower frequencies upon hydrogenation (green line) at both absorption edges. This indicates a significant lattice expansion caused by hydrogenation. In the Fourier transform, the increase of the next neighbor distances is nicely visible. The first shell peak at the Fe K-edge shifts the Fe-Fe next neighbor distance by 0.05 \AA , while the La-Fe distance at the La L_3 -edge also shifts by 0.05 \AA . At the second shell no shift is visible through hydrogenation at the La L_3 -edge. At the Fe K-edge on the other hand,

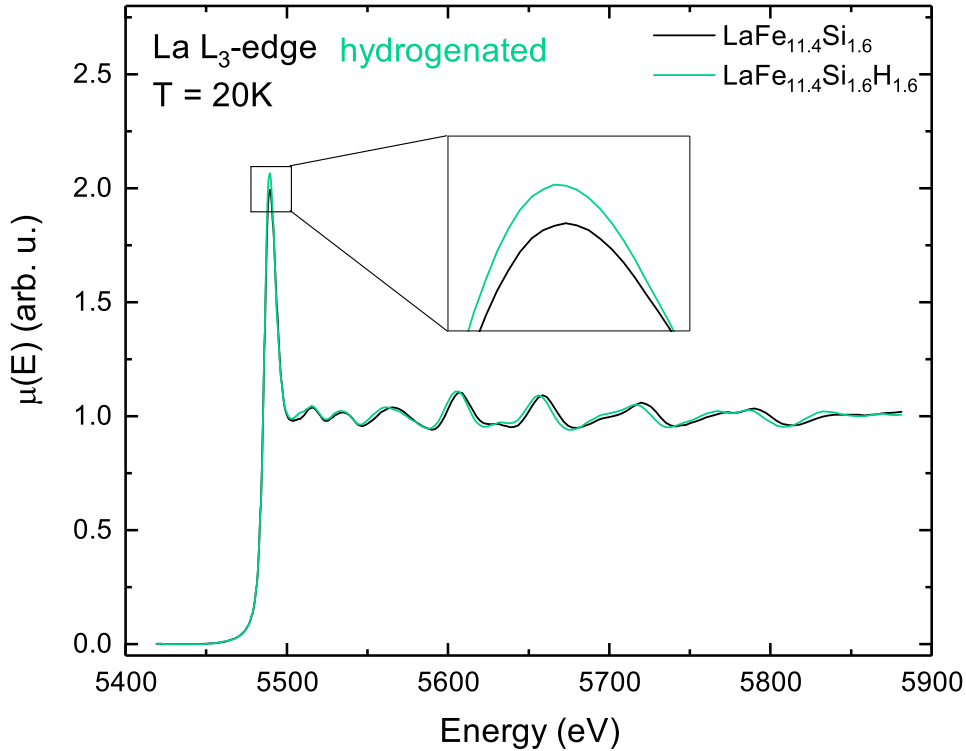


Figure 5.38.: Normalized absorption spectrum of $\text{LaFe}_{11.4}\text{Si}_{1.6}$ (black line) and $\text{LaFe}_{11.4}\text{Si}_{1.6}\text{H}_{1.6}$ (green line) in the FM phase at 20 K.

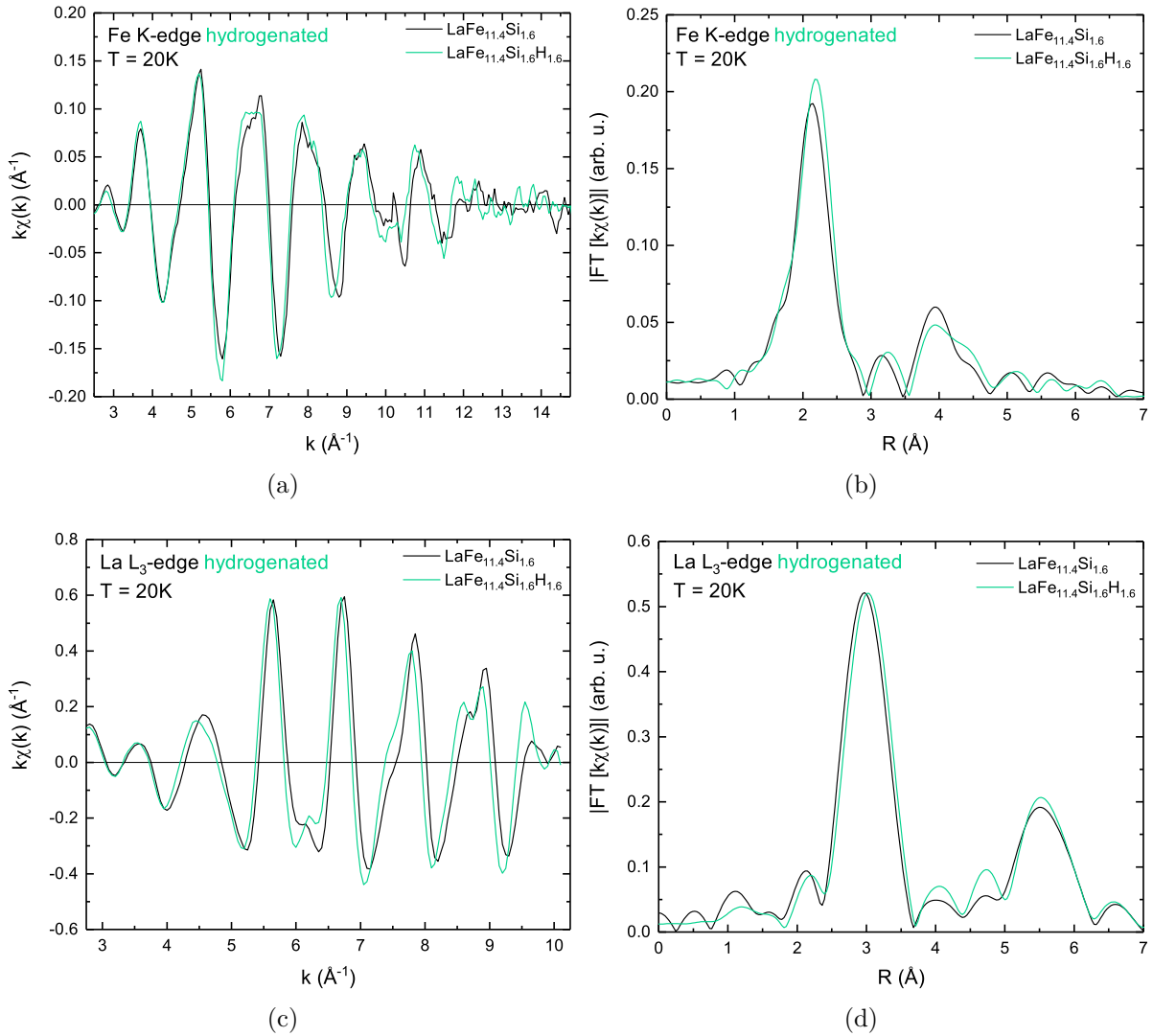


Figure 5.39.: Comparison of the EXAFS of $\chi(k)$ (a,c) and the k -weighted Fourier transform $|\text{FT}[k\chi(k)]|$ (b,d) for $\text{LaFe}_{11.4}\text{Si}_{1.6}$ (black line) and $\text{LaFe}_{11.4}\text{Si}_{1.6}\text{H}_{1.6}$ (green line), taken in the FM state at 20 K at the Fe K-edge (a,b), and the La L_3 -edge (c,d).

the main peak does not shift, but a another scattering contribution emerges at a higher R -value through hydrogenation.

5.3.5. Theoretical Modeling by FEFF

In order to find a correct model to fit the experimental data, calculations using the *FEFF* 9 code have been performed [155]. *FEFF* is an *ab-initio* code, which uses multiple scattering theory in order to calculate spectra for X-ray excitations and the electronic structure [160]. The *FEFF* code calculates the self consistent potentials for each scatterer in an atomic matrix on the basis of a crystallographic input using the EXAFS Equation 2.31. The

output consists of the summation of all scattering paths surrounding the absorbing atom within the radius chosen for the calculations. The *FEFF* calculations have been done for each individual atomic site at the Fe and Mn K-edge as well as the La L₃-edge. The results from each single calculation have been averaged over all sites in order to compare the calculations with the experimental data as the experiment reflects an averaged signal over all the sites. The smallest amount of Mn which can be simulated is a content of $x = 0.5$. The structure used for the calculations only consists of two formula units, which in total can only include one Mn atom for a Mn content of $x = 0.5$. This content serves as a reference for the spectra of the Mn doped samples. An example for a *FEFF* input can be found in section A.10. The input consists of the structural parameters and a listing of the atomic sites in the crystallographic model. As the experiment has been performed on powder samples, calculation has been set up to calculate a polarization averaged EXAFS. To calculate the potentials, the local exchange correlation potentials (Hedin-Lundqvist model [161]) have been used. The self consistent potentials have been set to a radius of the atomic cluster around the absorbing atom of 6 Å. The k -range for the EXAFS has been adjusted according to the k range measured in the experiment. The Fe K-edge has been calculated up to 15 Å⁻¹, the La L₃-edge to 12 Å⁻¹ and the Mn K-edge up to 10 Å⁻¹. The amplitude reduction factor S_0^2 , which has been kept at 0.85 for all calculations performed, accounts for the many body effects in the system. To model the disorder in the compound, a static and dynamic term has been assumed. The static disorder σ_{stat}^2 in the system has been kept low for the calculation of the La L₃-edge with around $\sigma_{\text{stat}}^2 = 0.002 \text{ \AA}^2$. As the disorder was expected to be higher on the Fe-sites, as these atomic positions are shared with Si as well as with Mn, the static disorder term has been increased for a better model of the EXAFS and lies for the models used in a range of 0.007 – 0.008 Å². As thermal disorder is another factor, which reduces the amplitude, the calculations include a correlated Debye model [162] with σ_{dyn}^2 including the experimentally extracted Debye temperatures of 370 K for the low temperature FM phase and 350 K for the room temperature measurements. The Debye temperatures used were taken from NRIXS experiments (see subsection 5.1.1). These values are in agreement with other studies and yield a very good agreement with the calculations in comparison to the experimental data [47, 130]. The volume contraction upon heating through the structural phase transition was modeled into the calculations using the R -multiplier, which has been adjusted to fit the EXAFS oscillations. The structural models used for the *FEFF* calculations have been provided by M. E. Gruner. The crystal structures used for the *ab-initio* calculations were energetically relaxed to minimize the intra-atomic forces. The *FEFF* input has been generated by using *Atoms* [163] and adjusted accordingly for disorder and lattice contraction or expansion parameters as described above. All *FEFF*

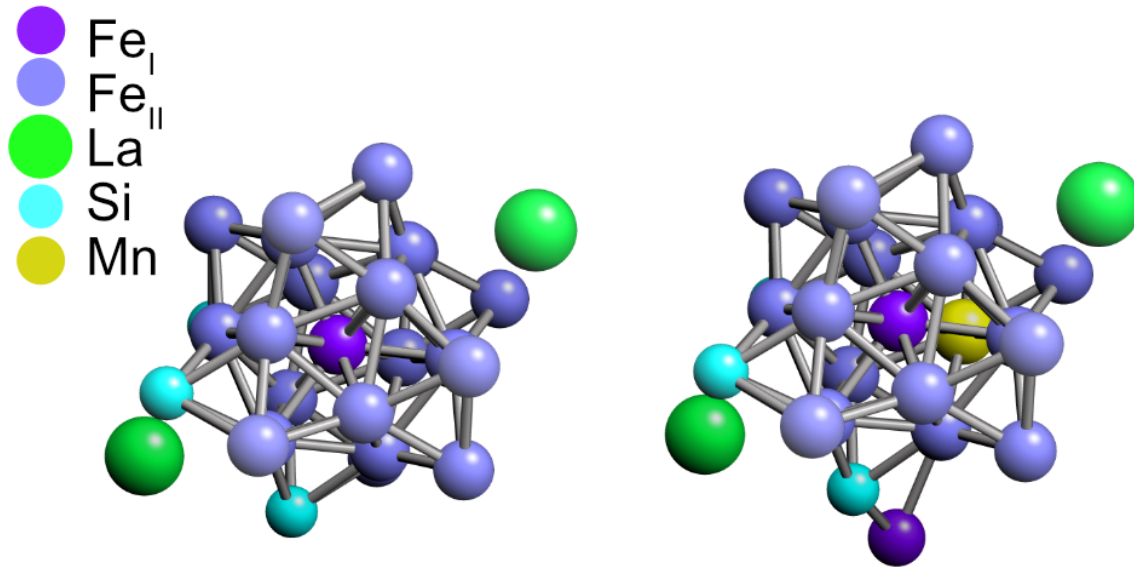


Figure 5.40.: Crystallographic models used for the *FEFF* calculations, without (left) and with Mn doping (right). The structural parameters were provided by M. E. Gruner.

calculations shown in this work are in the FM phase at 20 K and in the PM phase at 300 K. For the fits, adjusted models with corresponding correlated Debye models, adjusted for the decrease in lattice parameter, have been used. A more detailed description of the *FEFF* calculations in this sample system can be found in Ref. [164]. The structural models used for the calculations are depicted in Figure 5.40. The lefthand side depicts the model for the undoped compound, the righthand side the model used for a Mn content of $x = 0.5$, where Mn resides on an Fe_{II} atomic (96i)-site. For the *FEFF* calculations of the Mn K-edge and a Mn content of $x = 0.5$, a structural model has been used with Mn fixed on one Fe_{II} site in an energetically relaxed structure with the assumption of antiferromagnetic coupling of Mn to the Fe atoms. Figure 5.41 depicts the comparison of the experimentally obtained k -weighted EXAFS at the La L_3 -edge and the *FEFF* calculation for the k -weighted EXAFS $\chi(k)$ and the Fourier transform. From the *FEFF* 9 calculations, it was found that the first shell at the La L_3 -edge only consists of 24 single scattering paths of La-Fe and La-Si for the La1 site, as the crystallographic model assumed the Si atoms around La. The second coordination shell, on the other hand, consists mainly of multiple scattering contributions. First, La-Fe single scattering with a coordination of 24, 48 double scattering and 78 triangle scattering paths in between a radial distance of $5.88 - 5.89 \text{ \AA}$ occurs, making it difficult to fit the structure due to its complexity as will be described later on. The *FEFF* calculation at the La L_3 -edge and the experimental data are in very good agreement, despite a slight shift in the Fourier

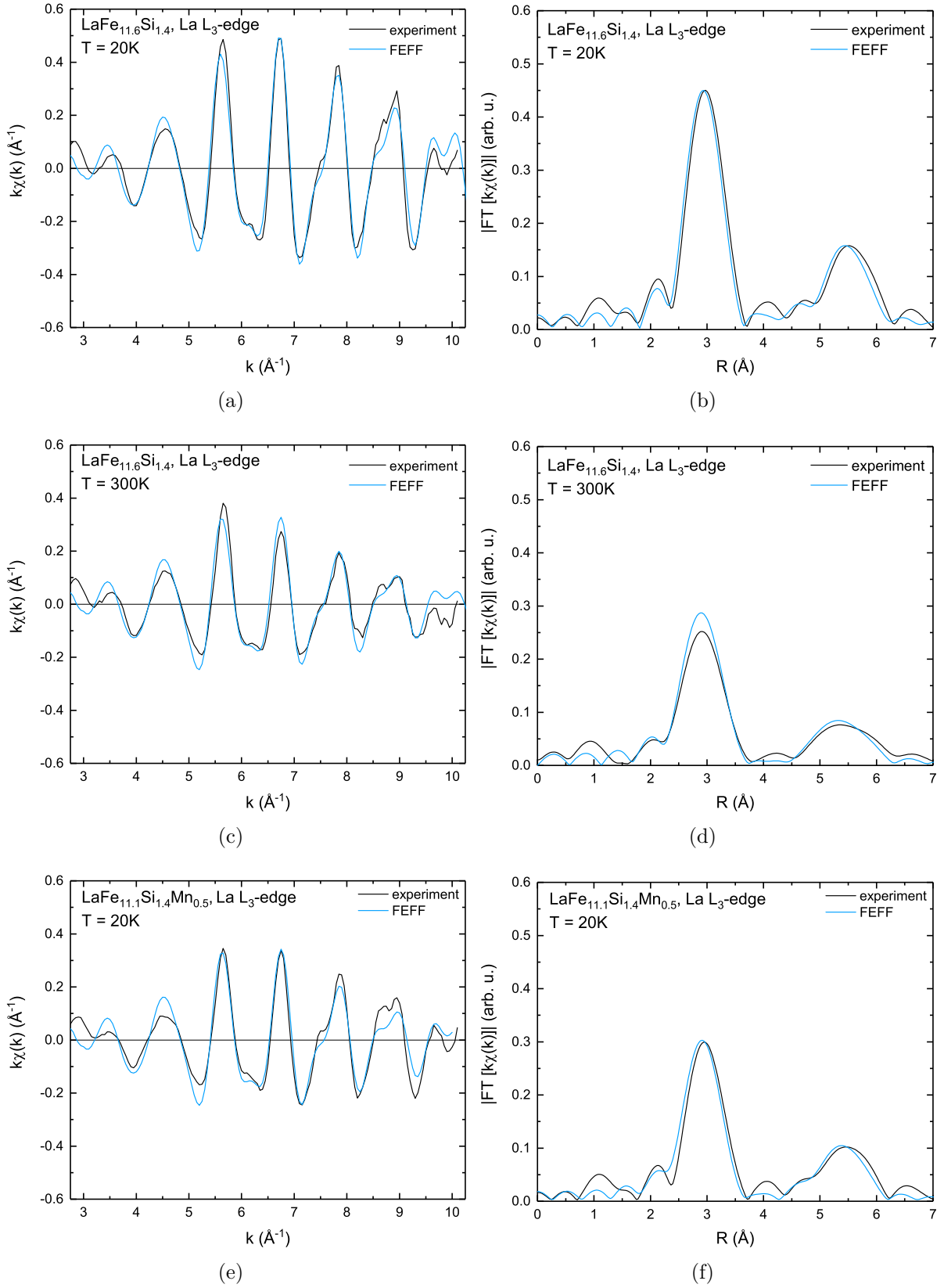


Figure 5.41.: Comparison of the *FEFF* 9 calculation (blue line) using the 28 atom cell to the experimental data (black) at 20 K (a, b) and 300 K (c, d) for the La L₃-edge. (a, c, e) The k -weighted EXAFS oscillation $k\chi(k)$ and (b, d, f) the corresponding Fourier transform $|\text{FT}[k\chi(k)]|$. Mn contents are 0 (a, b, c, d) and 0.5 (e, f).

transform to smaller radial distances. The calculated $k\chi(k)$ also have been transformed over the exact same k -range as in the experimental data for direct comparison.

The majority of the Fe-atoms are on the Fe_{II}-sites. They are surrounded by 9 Fe atoms with slightly varying next neighbor distances in between 2.4 – 2.6 Å according to the structural model. In the calculation of the EXAFS in Figure 5.42 (a), it can be seen that, while the overall frequency seems to match the oscillations, the model used leads to exaggerated amplitude at low k -oscillations. This might point towards contributions of scattering of lighter elements, which usually impacts low k -oscillations. Furthermore, as seen in Figure 5.42 (b), the structural model assumed next neighbor distances for the first coordination shell which vary more than the experimental data and are shifted to a smaller radial distance. In the experiment, the next neighbor distances of Fe do not vary as broadly as the distances in the structural model of the first shell. Furthermore, the next neighbor distances are a bit further away in the experiment at the first shell, while the second shell matches. The structural model used for the calculation, therefore, might be problematic as it does not recreate the next neighbor distances of Fe adequately. From the calculations at the Mn K-edge a similar effect is visible as at the Fe K-edge.

At low k -values, the oscillations are exaggerated, while the experimental signal is damped and the reverse effect is visible at higher k -values. The Fourier transform consequently reveals radial distances which are too small. The first coordination shell additionally is too broadly distributed, while the first coordination shell in the experiment is more narrow. Nevertheless, for both Fe K- and Mn K-edge, all features in the oscillatory fine structure are reproduced in the *FEFF* calculation, despite the shoulder at 4.5 Å⁻¹. The mismatch at the lower k -range is attributed to the broader distribution in the Fe-Fe distances assumed in the structural model for the first shell, compared to the experimental data.

<i>FEFF</i> parameters with $S_0^2 = 0.085$							
Edge	Mn _x	structural model	$\sigma_{\text{stat}}^2[\text{Å}^2]$	T [K]	$\Theta_{\text{DB}}[\text{K}]$	R _{mult}	k -range [Å ⁻¹]
La L ₃	0	small relaxed	0.002	20	370	1.003	12
	0	small relaxed	0.002	300	350	1	12
	0.5	small AF	0.0055	20	370	1.000	12
Fe K	0	small relaxed	0.008	20	370	1.000	15
	0	small relaxed	0.008	300	370	1.000	15
	0.5	small AF	0.007	20	370	1.000	15
Mn K	0.5	small AF	0.005	20	370	1.000	12

Table 5.5.: Parameters of the *FEFF* calculation

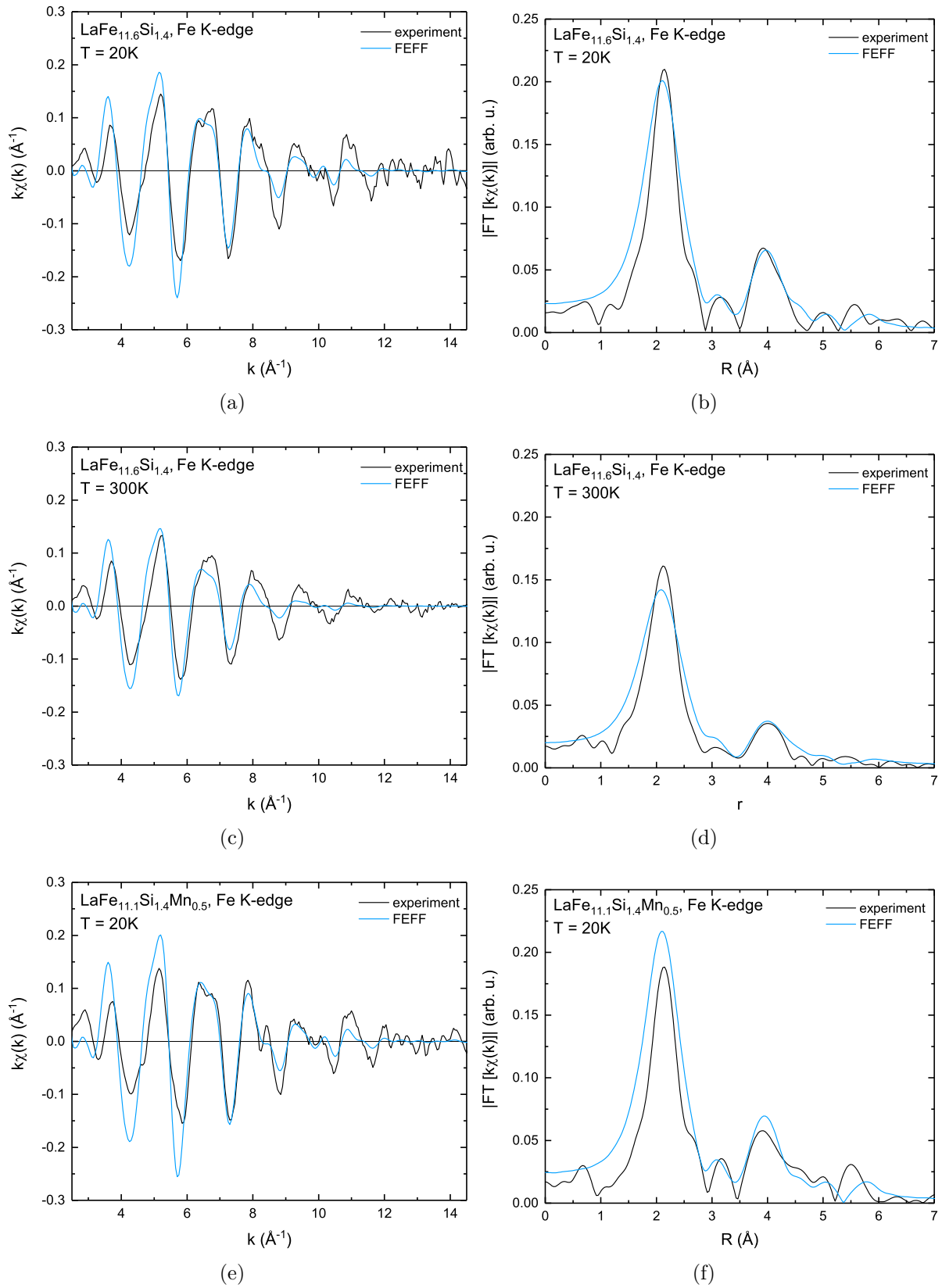


Figure 5.42.: Comparison of the *FEFF* 9 simulation (blue line) using the 28 atom cell to the experimental data (black) at 20 K (a, b) and 300 K (c, d) for the Fe K-edge. (a, c, e) The k -weighted EXAFS oscillation $k\chi(k)$ and (b, d, f) the corresponding Fourier transform $|\text{FT}[k\chi(k)]|$. Mn contents are 0 (a, b, c, d) and 0.5 (e, f).

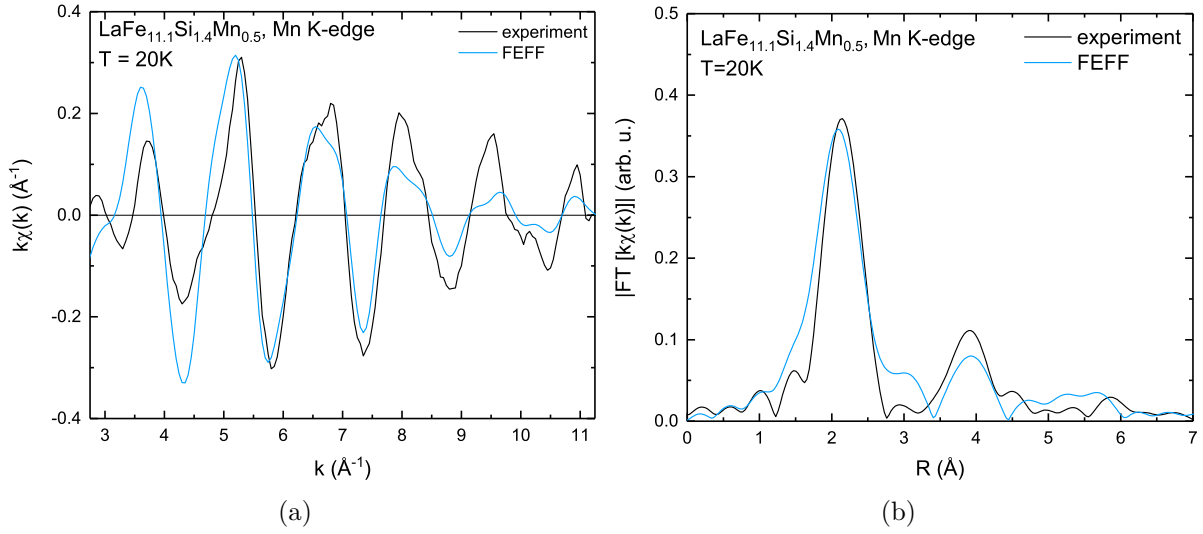


Figure 5.43.: Comparison of the *FEFF* 9 simulation (blue line) using the 28 atom cell to the experimental data (black) at 20 K for the Mn K-edge with $x = 0.5$. (a) The k -weighted EXAFS oscillation $k\chi(k)$ and (b) the corresponding Fourier transform $|\text{FT}[k\chi(k)]|$.

5.3.6. Data Fits and Local Geometry

For the analysis of the next neighbor distances, the EXAFS spectra were fitted using the *Larch* code [159, 165], which runs a least-squares fit to the experimental data on the basis of the paths which have been generated by a *FEFF* calculation. For each path the parameters can be adjusted individually in order to fit the experimental data and analyze the local structure. All fits in this work have been performed using *FEFF* calculations of the ordered cell containing 28 atoms in an energetically unrelaxed structure in order to simplify the fitting process in the rather complex crystallographic structure. The structure used had the nominal stoichiometry of LaFe_{11.5}Si_{1.5} consisting of two formula units (see Figure 2.5 in section 2.3). The La atom is surrounded by a polyhedral coordination of 24 Fe atoms of equal distance. While the structural model used in the *FEFF* calculation was an ordered cell, meaning that the La was symmetrically surrounded by 3 Si, while the real structure consists of high disorder of Si, which randomly occupies the Fe_{II}-sites. To account for the Mn content, the structural model has been adjusted with one Mn atom replacing one Fe_{II}-site and a stoichiometry of LaFe_{11.0}Si_{1.5}Mn_{0.5}.

To adequately perform a fit and correctly model the random distribution of Si inside the crystallographic structure, two different methods have been tested for a fit to the first coordination shell. First, the fit has been done only accounting for the 24 Fe atoms around the absorbing La atom. Secondly, in order to model with Si, the degeneracy of the single scattering of Si has been fitted by using the relation $24 - N_{\text{Fe}}$ for the path degeneracy

with 24 being the maximum amount of Fe atoms which possibly surround the absorbing La atom. Figure 5.44 (a) depicts the first shell fits with both models to the La L_3 -edge in the ferromagnetic state at 20 K to the data of the undoped compound $\text{LaFe}_{11.6}\text{Si}_{1.4}$. Both fits to the first coordination shell, with the assumption of a path degeneracy of $N_j=24$ for La-Fe single scattering only (blue line), as well as with the inclusion of Si (orange line), yield the same next neighbor distance within the margin of error as listed in Table 5.6. The additional inclusion of the La-Si paths is reflected in a stronger damping in the FT. To compare the two fit models to the fitted EXAFS oscillations, a backward Fourier transform has been done only over the first coordination shell of the experimental data. Figure 5.44 (b) depicts the comparison between both models used for the data fit. It can be seen that the effect of Si, reflected in the EXAFS oscillation, is a stronger damping of the oscillations at lower k -values. As there are no shifts in the radial distance in the FT, nor an frequency shift observable when Si is included in the EXAFS, for further evaluations, only the La-Fe single scattering paths have been fitted and the La-Si paths have been neglected.

After simplifying the model, the fit has been extended to the second shell. After fitting the first shell and obtaining a value for the static disorder, the second coordination shell can be modeled. In the fit the second shell was modeled using La-Fe single scattering (again, neglecting the potential La-Si paths), with a path degeneracy of 24, as well as La-Fe-Fe triangle scattering and a degeneracy of 48, also without accounting for La-Fe-Si

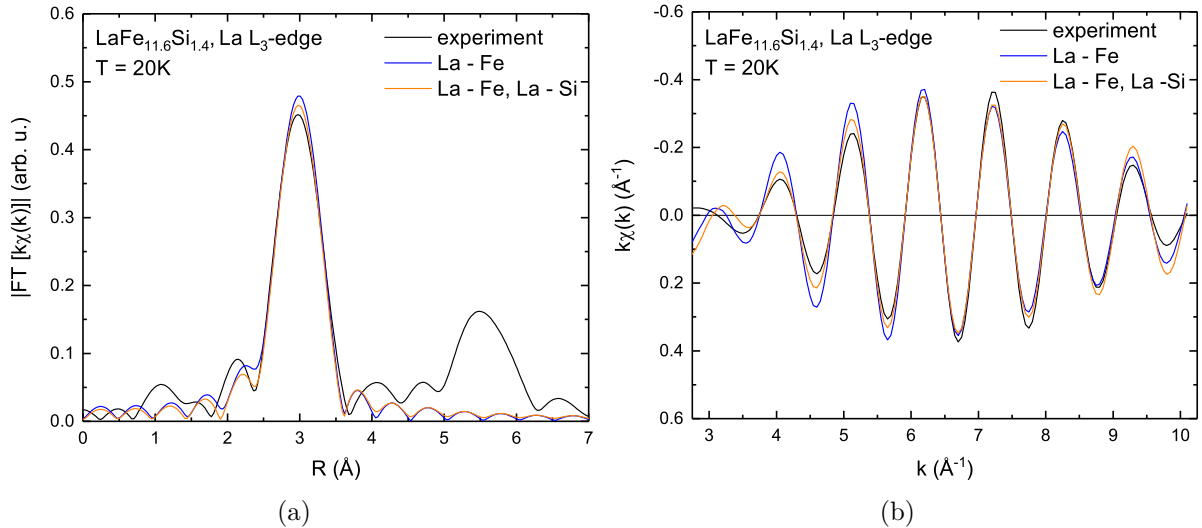


Figure 5.44.: (a) FT transformation of the first shell fit of the La L_3 -edge at 20 K in $\text{LaFe}_{11.6}\text{Si}_{1.4}$ using only La-Fe single scattering paths (blue) and including additional La-Si paths (orange) to the experimental data (black). (b) Backward Fourier transform over the first shell of the experimental data (black) in comparison to the oscillations for both fitting methods.

and La-Si-Fe paths. The potential scattering events which included Si have been added to the La-Fe-Fe path degeneracy. From the fit it was possible to obtain the next neighbor distances of La. In the FM phase at 20 K, La and Fe have a distance of $3.37 \pm 0.03 \text{ \AA}$. The additional fit of the Si distance showed a smaller effective distance of $3.32 \pm 0.05 \text{ \AA}$. Both values are the same within the uncertainty of the error of the fit, which makes it questionable to assume a real smaller distance for Si. Figure 5.45 depicts the fit for the first and second shell at the La L_3 -edge to the k -weighted EXAFS and the corresponding Fourier transform in both magnetic phases. The static disorder has been fixed for the single scattering contributions in both the first and second shell, after a fit to the first shell only with single scattering La-Fe paths. The static disorder was estimated to be $\sigma_{\text{stat}}^2 = 0.0038 \text{ \AA}^2$. The additional La-Fe-Fe path has been left open as a fit variable and resulted in a static disorder term, which is within the error the same as for the single scattering path, but consequently too small. This is possibly an effect originating from neglecting the La-Fe-Fe-Fe paths for the fit, which also contribute to the second coordination shell.

Despite the simplified approach used for the fit, the oscillatory fine structure is well reproduced in the fit, except for the dip in the oscillation at 6.3 \AA in the FM, as well as in the PM phase, which seems to be shaped inversely to that of the experimental data. The obtained values for the next neighbor distances are slightly too big for both coordination shells and the amplitude of the fit in the Fourier transform is too high, due to the lack of Si in the structure assumed for the fitting procedure. The reduction of the next neighbor distance across the phase transition at the La L_3 -edge is -0.03 \AA , but within the uncertainty of the fit not completely reliable. For a Mn content of $x = 0.5$, also a two shell fit has been performed under the same assumptions and simplifications as described above. Figure 5.45 (c) shows the EXAFS and (d) the corresponding Fourier transform in both magnetic phases, i.e. in the ferromagnetic state at 20 K and in the paramagnetic state at 300 K. For the structural model, Mn has been fixed on one single Fe_{II} -site. To investigate the influence of Mn on the structure, a simple first shell fit has been performed to the experimental data at the La L_3 -edge in the whole Mn doped sample series. Here, the concentrations ranged from $x = 0$ to $x = 0.5$. As smaller amounts of Mn were not possible to model in the 28 atom cell used for the fits, all the Mn doped samples have been fitted using the *FEFF* calculation of the unrelaxed structure with a Mn content of $x = 0.5$.

Figure 5.46 depicts the evolution of (a) R and (b) σ_{stat}^2 with rising Mn content. From the radial distance R we cannot infer a change in the next neighbor distance within the margin of error. Even though the fits consequently revealed a smaller next neighbor coordination distance in the PM state for all Mn contents, which is in agreement with the expectation

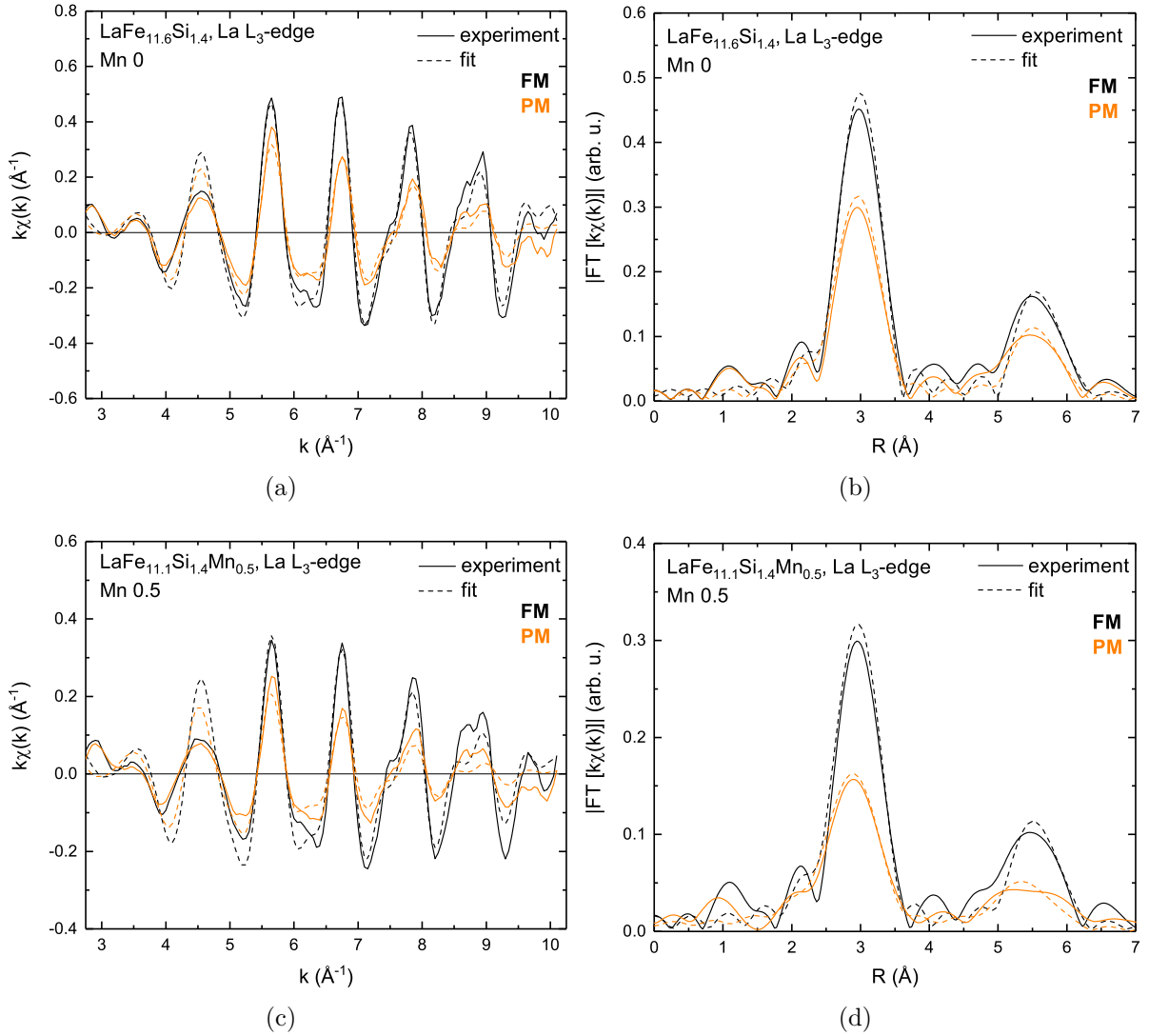


Figure 5.45.: (a, c) EXAFS fit in the FM (black) and PM (orange) phase at the La L_3 -edge at 20 K (black) and 300 K (orange) in $\text{LaFe}_{11.6}\text{Si}_{1.4}$ (a, b) and $\text{LaFe}_{11.1}\text{Si}_{1.4}\text{Mn}_{0.5}$ (c, d) using only La-Fe single scattering paths. (b, d) FT of the first and second coordination shell fit with $\Theta_{\text{DB}} = 370$ K in the FM and $\Theta_{\text{DB}} = 350$ K in the PM phase.

of a smaller lattice constant upon heating, the effect is smaller than the error of the measurement, which is a result from the simplified fits. A trend can be estimated in the mean-squared relative displacement, which is strongly affected by increase in Mn content and gives rise to the static disorder in the system around the absorbing La atom. By increasing the Mn content from $x = 0$ to $x = 0.5$, the static disorder term roughly doubles in value. The dynamic part of the mean-squared relative displacement gives an offset to the obtained values and accounts for both experimental temperatures of $T_{\text{exp}} = 20$ K in the FM phase with a Debye temperature of $\Theta_{\text{DB}} = 370$ K and in the PM phase at $T_{\text{exp}} = 300$ K

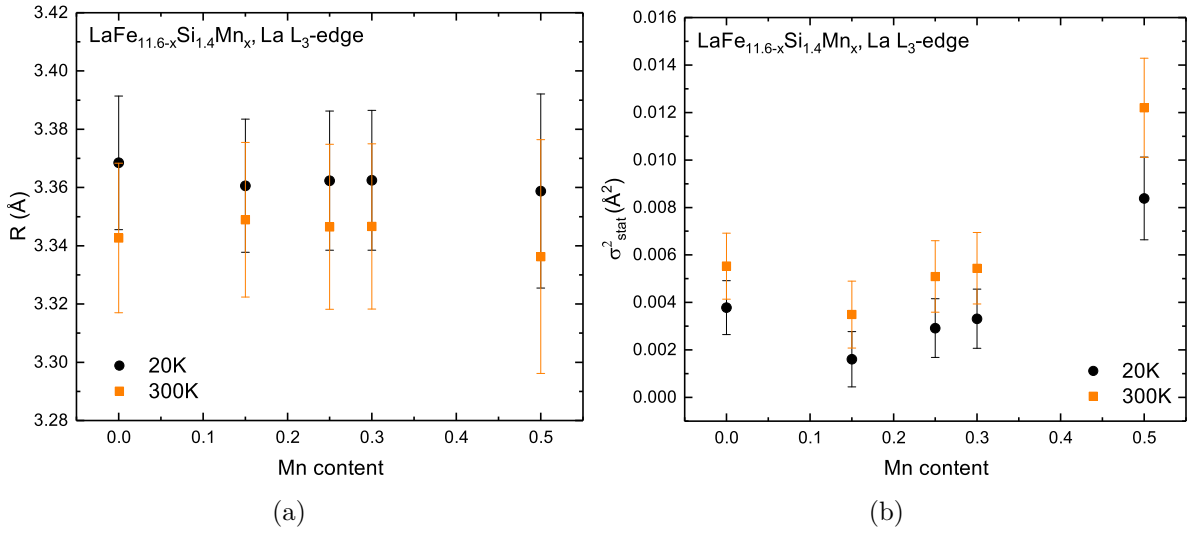


Figure 5.46.: (a) Values for the next neighbor distance of the first coordination shell in the sample series with rising Mn content and (b) the static disorder term in the mean-squared relative displacement as obtained from the fits using the *Larch* code on basis of *FEFF* calculations at the La L_3 -edge at $T_{\text{exp}} = 20$ K (black dots) and at $T_{\text{exp}} = 300$ K (orange squares) with $\Theta_{\text{DB}} = 370$ K in the FM and $\Theta_{\text{DB}} = 350$ K in the PM phase.

and $\Theta_{\text{DB}} = 350$ K. As an increase in the static disorder is visible between fits to the EXAFS in the FM and PM phase for every Mn content shown, the Debye temperature which has been used to account for the dynamic disorder term σ_{dyn}^2 was probably set at a value which is too high and has been compensated by the static disorder term σ_{stat}^2 . The Debye temperatures Θ_{DB} used, represent the values from the Fe subsystem [47] obtained by NRIXS experiments for an undoped specimen and have been used as an approximation due to the large Fe amount in the sample system. The discrepancy in σ_{stat}^2 between the two magnetic phases indicates that the Debye temperature needs to be lowered for the La subsystem for a proper description in the system. The Debye temperature scales with $M^{-\frac{1}{3}}$, with M as the atomic mass, according to the Debye model [114]. From Ref. [130] it is not expected that with rising Mn content, the Debye temperature decreases, but the rising offset between the values for the static disorder in the FM and PM phase, with increasing Mn content might indicate a change in the Debye temperature through Mn doping.

The effect of the Debye temperature is very small for an experimental temperature of 20 K, as the *FEFF* calculations showed a very good agreement between experiment and calculation of the EXAFS using the Fe-partial Debye temperatures of 370 K and 350 K. A consequent fit to the first shell at the La L_3 -edge in the PM state of $\text{LaFe}_{1.6}\text{Si}_{1.4}$ with the Debye temperature as an open parameter gave a value of $\Theta_{\text{DB}} = 313 \pm 24$ K. The

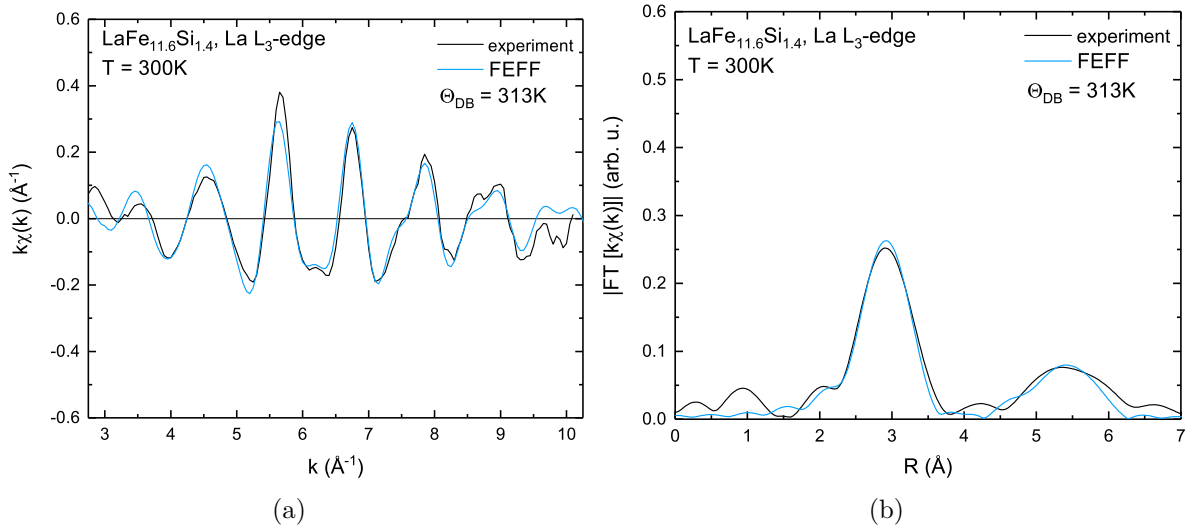


Figure 5.47.: Comparison of the calculation of the La L₃-edge in the PM phase at $T_{\text{exp}} = 300 \text{ K}$ using the *FEFF* code (blue line) to the experimental data (black line). (a) EXAFS and (b) FT. *FEFF* parameters as listed in Table 5.5, but with $\Theta_{\text{DB}} = 313 \pm 24 \text{ K}$.

value for the static disorder $\sigma_{\text{stat}}^2 = 0.0038 \text{ \AA}^2$ as obtained from the FM phase fit was fixed. Using this Debye temperature for the a *FEFF* calculation of the La L₃-edge set up with the same parameters as in subsection 5.3.5 revealed a model, which is suitable to describe the experimental data. The comparison between experiment and calculation is shown in Figure 5.47. Therefore, this rather complex system needs to be modeled with regard to the Debye temperature in the future.

Next neighbor distances in $\text{LaFe}_{11.6-x}\text{Si}_{1.4}\text{Mn}_x$ at the La L_3 -edge						
Mn_x	Temperature [K]	Atomic Pair	N	R_{i-j} [\AA]	σ_{stat}^2 [\AA^2]	
0	20	La(8a)-Fe(96i)	24	3.37 ± 0.03	0.0038 ± 0.0011	
0	20	La(8a)-Fe(96i)	21 ± 1	3.36 ± 0.01	0.0019 ± 0.0010	
		La(8a)-Si(96i)	3 ± 1	3.32 ± 0.05	0.006 ± 0.009	
0.15	20	La(8a)-Fe(96i)	24	3.36 ± 0.02	0.0016 ± 0.0012	
0.25	20	La(8a)-Fe(96i)	24	3.36 ± 0.02	0.0029 ± 0.0012	
0.3	20	La(8a)-Fe(96i)	24	3.36 ± 0.02	0.0031 ± 0.0012	
0.5	20	La(8a)-Fe(96i)	24	3.36 ± 0.03	0.0084 ± 0.0017	
0	300	La(8a)-Fe(96i)	24	3.34 ± 0.03	0.0055 ± 0.0014	
0.15	300	La(8a)-Fe(96i)	24	3.35 ± 0.03	0.0035 ± 0.0014	
0.25	300	La(8a)-Fe(96i)	24	3.35 ± 0.03	0.0051 ± 0.0015	
0.3	300	La(8a)-Fe(96i)	24	3.35 ± 0.03	0.0054 ± 0.0015	
0.5	300	La(8a)-Fe(96i)	24	3.34 ± 0.04	0.0122 ± 0.0021	

Table 5.6.: Extracted La-Fe distances R_{i-j} and static disorder parameter σ_{stat}^2 from the *Larch* fit at the La L_3 -edge for the first shell with $\Theta_{\text{DB}} = 370$ K in the FM and $\Theta_{\text{DB}} = 350$ K in the PM phase.

Fit results of the La L_3 -edge of $\text{LaFe}_{11.6-x}\text{Si}_{1.4}\text{Mn}_x$						
Mn_x	Temperature [K]	Scattering	N	R_{i-j} [\AA]	σ_{stat}^2 [\AA^2]	
0	20	La-Fe single	24	3.37 ± 0.03	0.0038 ± 0.0010	
		La-Fe single	24	5.94 ± 0.02	fixed	
		La-Fe triangle	48	6.01 ± 0.01	0.0033 ± 0.0010	
0	300	La-Fe single	24	3.34 ± 0.03	0.0055 ± 0.0014	
		La-Fe single	24	5.89 ± 0.03	fixed	
		La-Fe triangle	48	5.96 ± 0.01	0.0042 ± 0.0013	
0.5	20	La-Fe single	24	3.36 ± 0.03	0.0084 ± 0.0017	
		La-Fe single	24	5.91 ± 0.05	fixed	
		La-Fe triangle	48	5.98 ± 0.02	0.0073 ± 0.0020	
0.5	300	La-Fe single	24	3.34 ± 0.04	0.0122 ± 0.0021	
		La-Fe single	24	5.87 ± 0.06	fixed	
		La-Fe triangle	48	5.94 ± 0.03	0.0103 ± 0.0028	

Table 5.7.: Extracted La-Fe next neighbor distances R_{i-j} and static disorder parameter σ_{stat}^2 from the *Larch* fit at the La L_3 -edge for the first and second shell with $\Theta_{\text{DB}} = 370$ K in the FM and $\Theta_{\text{DB}} = 350$ K in the PM phase.

The fit of the Fe K-edge had to be simplified and not all paths could be fitted for the first shell. As Fe_{II} is the main constituent in the crystal, the absorbing atom for Fe has been chosen as a Fe_{II} absorber. Again, Fe-Si scattering has been neglected for the fits. At the Fe K-edge, the first coordination shell consists of 4 different Fe-Fe distances with different path degeneracies, as obtained from the *FEFF* calculations. First, all four Fe-Fe scattering paths have been fitted to the structure with the given path degeneracies as depicted in Figure 5.48. A Fe_{II} absorber has 9 surrounding Fe atoms and 4 scattering paths with slightly varying distance.

The main contribution arises from a fourfold degenerated single scattering path between $\text{Fe}_{\text{II}}\text{-Fe}_{\text{II}}$. Furthermore, there are 2 paths, both twofold degenerated also single scattering, between $\text{Fe}_{\text{II}}\text{-Fe}_{\text{II}}$ and one path $\text{Fe}_{\text{II}}\text{-Fe}_{\text{I}}$. After fitting the fourfold degenerated $\text{Fe}_{\text{II}}\text{-Fe}_{\text{II}}$ path to the experimental data, the static disorder estimated from the fit has been fixed and kept the same for the other paths in the first shell. The direct comparison between the fit with all four paths and just one path showed that besides making the fit more complex, the fit with all paths resulted in a slightly more pronounced structure in the FT at $\sim 2.75 \text{ \AA}$. For all further fits at the Fe K-edge, therefore, only the four fold degenerated $\text{Fe}_{\text{II}}\text{-Fe}_{\text{II}}$ single scattering path has been fitted to the data. From the *FEFF* output we found 6

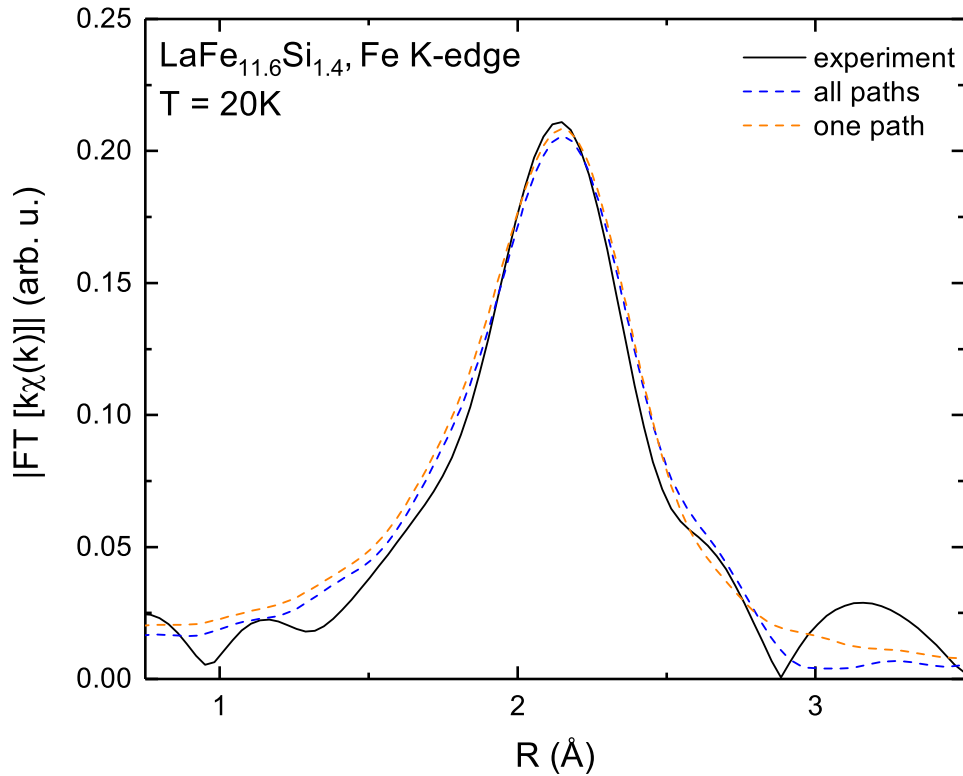


Figure 5.48.: *Larch* fits to the first coordination shell at the Fe K-edge in the sample's FM state with all 4 paths and 9 surrounding atoms.

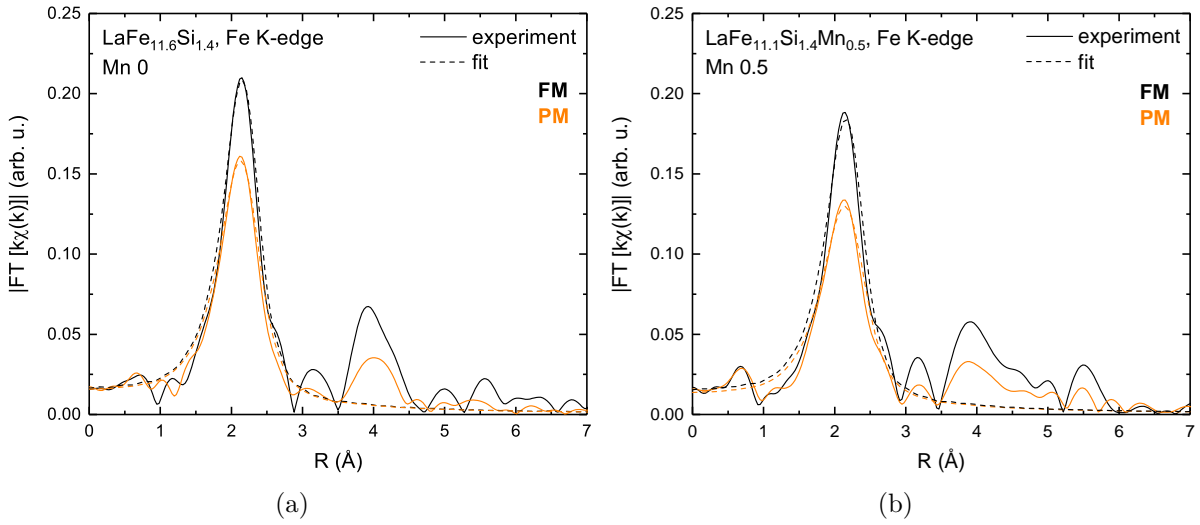


Figure 5.49.: First shell fits in the FM (black) and PM (orange) phase at the Fe K-edge at 20 K (black) and 300 K (orange) in (a) $LaFe_{11.6}Si_{1.4}$ and (b) $LaFe_{11.1}Si_{1.4}Mn_{0.5}$ using only one Fe-Fe single scattering path.

different single scattering paths with a total degeneracy of 13 for the second coordination shell. Due to the complexity, the second shell has not been fitted to the data. Figure 5.49 shows the first shell fit to the FT at the Fe K-edge in both magnetic phases. From the fit, a next neighbor Fe-Fe distance of 2.5 \AA was found in pure $LaFe_{11.6}Si_{1.4}$ as well as in $LaFe_{11.1}Si_{1.4}Mn_{0.5}$. Mn doping, therefore, does not seem to alter the structure in such a way that it results in a smaller Fe-Fe distance. Across the phase transition, from the FM to PM state, a lattice contraction could be extracted for the undoped compound. Here the $Fe_{II}-Fe_{II}$ distance slightly decreases by -0.016 \AA .

In Figure 5.50 the k -weighted $k\chi(k)$ is shown with the fit to the first coordination shell (dashed black line) and the backward Fourier transform of the experimental first shell only (blue line). It can be seen that the fine structure in the oscillation solely arise from scattering events of the second coordination shell. Despite the slight mismatch in the low k -oscillation amplitude (due to the lack of Si, as observed already at the La L_3 -edge), the fit matches very well with the experimental data.

Due to Mn being close to Fe in atomic weight, the fits with a Mn content of $x = 0.5$ have been done without fitting the Fe-Mn single scattering path, as there is only one Mn atom inside of 2 formula units, which is expected to have very little deviation from the La-Fe single scattering amplitude. The fit of the Mn K-edge could not be performed analog to that of the Fe K-edge. Here it was not sufficient enough to use a fixed static disorder term of $\sigma^2 = 0.0065 \text{ \AA}^2$ and add just one path with the main scattering contribution to the first shell.

The fit to the Mn K-edge depicted in Figure 5.51 includes three single scattering paths of

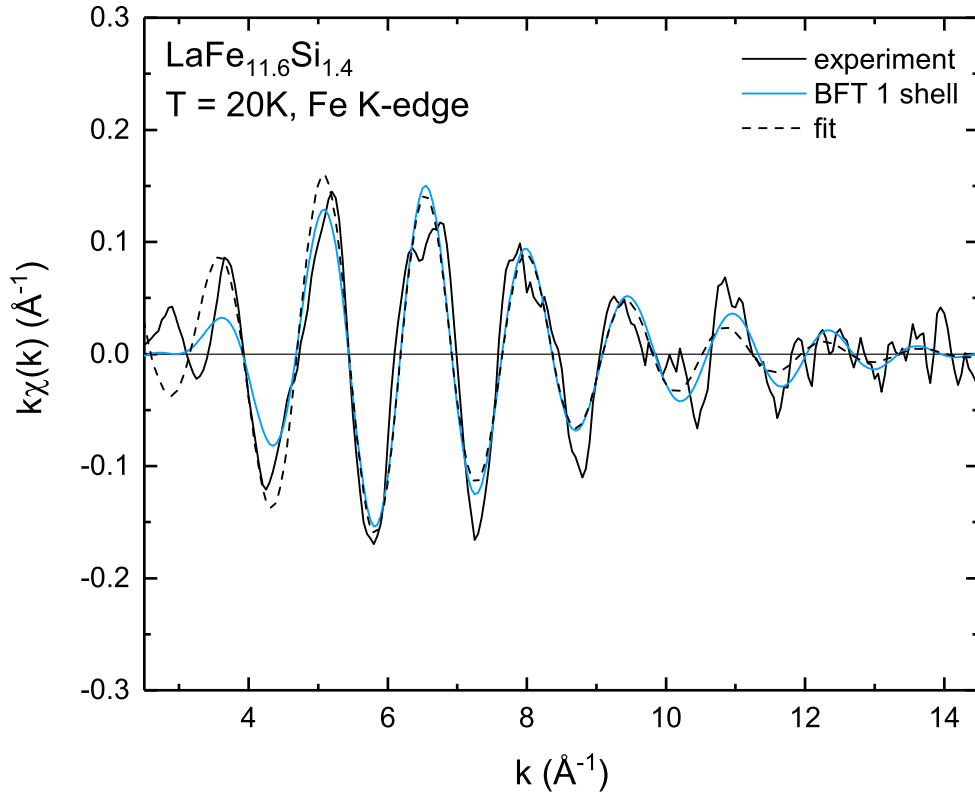


Figure 5.50.: $k\chi(k)$ at the Fe K-edge in $\text{LaFe}_{11.6}\text{Si}_{1.4}$ at 20 K (black line) compared with the first shell fit (black line, dashed) and the backward FT of the first coordination shell of the experimental data (blue line).

Next neighbor distances in $\text{LaFe}_{11.6-x}\text{Si}_{1.4}\text{Mn}_x$ at the Fe K-edge					
Mn_x	Temperature [K]	Atomic Pair	N	R_{i-j} [\AA]	σ_{stat}^2 [\AA^2]
0	20	Fe(96i)-Fe(96i)	4	2.50 ± 0.01	0.0047 ± 0.0005
		Fe(96i)-Fe(96i)	2	2.76 ± 0.02	fixed
		Fe(96i)-Fe(96i)	2	2.96 ± 0.02	fixed
		Fe(96i)-Fe(8b)	1	2.56 ± 0.03	fixed
0.5	20	Fe(96i)-Fe(96i)	4	2.50 ± 0.02	0.006 ± 0.001
0	300	Fe(96i)-Fe(96i)	4	2.484 ± 0.003	0.003 ± 0.001
0.5	300	Fe(96i)-Fe(96i)	4	2.50 ± 0.02	0.005 ± 0.001

Table 5.8.: Extracted next neighbor distances from the *Larch* fit at the first shell at the Fe K-edge with $\Theta_{\text{DB}} = 370$ K in the FM and $\Theta_{\text{DB}} = 350$ K in the PM phase.

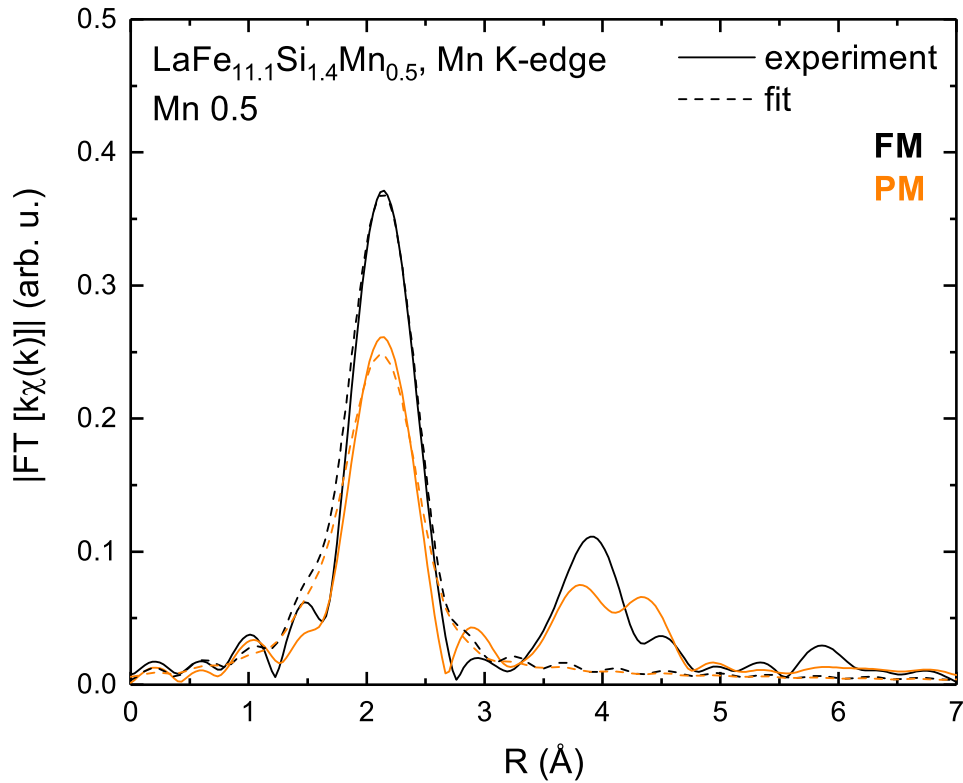


Figure 5.51.: First shell fits in the FM (black) and PM (orange) phase at the Mn K-edge at 20 K (black) and 300 K (orange) in $\text{LaFe}_{11.1}\text{Si}_{1.4}\text{Mn}_{0.5}$ using only one Fe-Fe single scattering path.

Mn-Fe in the first shell with the highest amplitude ratio as obtained from *FEFF*. From the fit, the path with the main amplitude resulted in a next neighbor distance of $2.49 \pm 0.01 \text{ \AA}$ for the low temperature FM phase and $2.49 \pm 0.03 \text{ \AA}$ in the high temperature PM phase, listed in Table 5.9. Due to the very simplified assumption, the contributions from the different paths to the first shell can not be distinguished. Within the error, the extracted distance between the single scattering path Mn-Fe is the same as Fe-Fe as extracted from the Fe K-edge measurement. For the fits of the hydrogenated compounds, the same unrelaxed crystal structure has been used as in the fits before, which did not include hydrogen on the interstitial sites. The *Larch* fits in the FM phase at 20 K for $\text{LaFe}_{11.4}\text{Si}_{1.6}$ and $\text{LaFe}_{11.4}\text{Si}_{1.6}\text{H}_{1.6}$ have been performed at the Fe K-edge and the La L_3 -edge. Analog to the Mn doped sample series, the Fe K-edge has been modeled by only fitting the main single scattering path for the first shell, due to the fit complexity. The La L_3 -edge fit has been performed for both shells. The first shell has been fitted and the parameters have been kept fixed. The second shell, has only been fitted using the La-Fe and La-Fe-Fe contributions, while keeping the static disorder of the single scattering path the same as in the first shell. The fits are compared to the data in Figure 5.52. The backward Fourier transform of the EXAFS over the first shell at the Fe K-edge is compared to

Next neighbor distances in $\text{LaFe}_{11.6-x}\text{Si}_{1.4}\text{Mn}_x$ at the Mn K-edge					
Mn_x	Temperature [K]	Atomic Pair	N	R_{i-j} [\AA]	σ_{stat}^2 [\AA^2]
0.5	20	Mn(96i)-Fe(96i)	4	2.50 ± 0.01	0.0065
		Mn(96i)-Fe(96i)	2	2.50 ± 0.3	fixed
		Mn(96i)-Fe(96i)	2	2.50 ± 0.3	fixed
0.5	300	Mn(96i)-Fe(96i)	4	2.49 ± 0.03	0.0065
		Mn(96i)-Fe(96i)	2	2.52 ± 0.2	fixed
		Mn(96i)-Fe(96i)	2	2.50 ± 0.2	fixed

Table 5.9.: Extracted next Mn-Fe next neighbor distances from the *Larch* fit to the first shell obtained from the Mn K-edge with $\Theta_{\text{DB}} = 370$ K in the FM and $\Theta_{\text{DB}} = 350$ K in the PM phase.

the fit over the first shell in Figure 5.52 (a). It can be seen that both fits, despite the mismatch in the low frequency oscillations, which most likely originate from the missing Si in the fit, match the experimental data for the undoped (black line) as well as the hydrogenated compound (green line). From the Fourier Transform and the fit to the first shell as depicted in Figure 5.52 (a) the significant increase in the next neighbor distance can be confirmed. A list of the values which have been extracted from the datafits are given in Table. 5.10.

Next neighbor distances in $\text{LaFe}_{11.4}\text{Si}_{1.6}$ and $\text{LaFe}_{11.4}\text{Si}_{1.6}\text{H}_{1.6}$					
Composition	T [K]	Atomic Pair	N	R_{i-j} [\AA]	σ_{stat}^2 [\AA^2]
Fe K-edge					
$\text{LaFe}_{11.4}\text{Si}_{1.6}$	20	Fe(96i)-Fe(96i)	4	2.50 ± 0.01	0.0085 ± 0.0008
$\text{LaFe}_{11.4}\text{Si}_{1.6}\text{H}_{1.6}$	20	Fe(96i)-Fe(96i)	4	2.53 ± 0.01	0.0074 ± 0.0006
La L_3 -edge					
$\text{LaFe}_{11.4}\text{Si}_{1.6}$	20	La-Fe single	24	3.36 ± 0.02	0.0024 ± 0.0011
		La-Fe single	24	6.01 ± 0.02	fixed
		La-Fe triangle	48	6.00 ± 0.01	0.0050 ± 0.0009
$\text{LaFe}_{11.4}\text{Si}_{1.6}\text{H}_{1.6}$	20	La-Fe single	24	3.40 ± 0.02	0.0021 ± 0.0012
		La-Fe single	24	6.02 ± 0.02	fixed
		La-Fe triangle	48	5.81 ± 0.04	0.0060 ± 0.0030

Table 5.10.: Extracted next neighbor distances from the *Larch* fit to the first shell at the Fe K-edge and two the first and second shell at the La L_3 -edge.

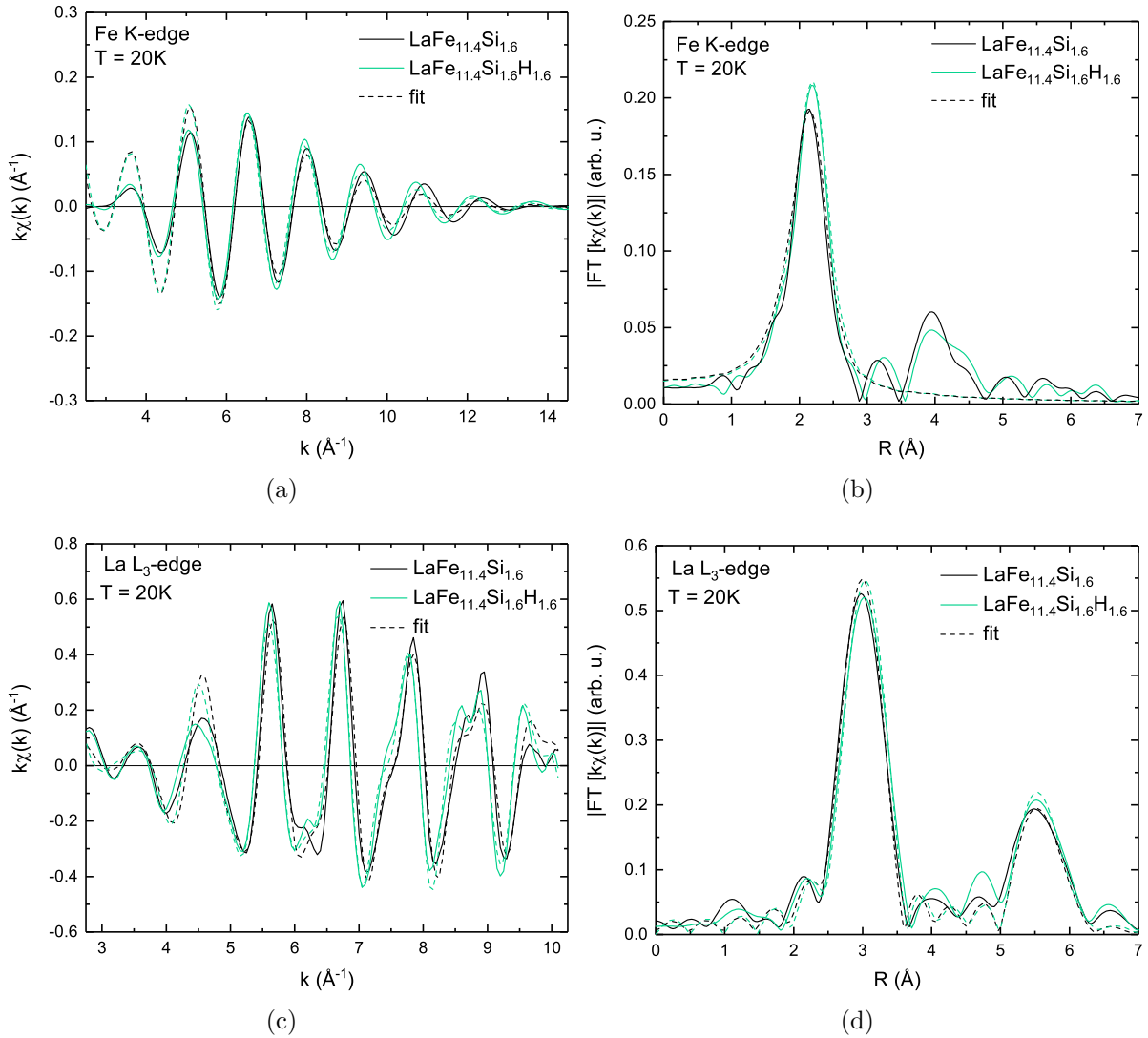


Figure 5.52.: *Larch* fits in the FM phase at 20 K in $\text{LaFe}_{11.4}\text{Si}_{1.6}$ (black line) and $\text{LaFe}_{11.4}\text{Si}_{1.6}\text{H}_{1.6}$ (green line). (a, b) at the Fe K-edge and (c, d) at the La L_3 -edge. (a, c) Fit to the EXAFS, (c, d) fit to the FT.

From the fit, the next neighbor distance at the Fe K-edge in $\text{LaFe}_{11.4}\text{Si}_{1.6}$ is $2.50 \pm 0.01 \text{\AA}$, while hydrogenation in $\text{LaFe}_{11.4}\text{Si}_{1.6}\text{H}_{1.6}$ results in a next neighbor distance of $2.53 \pm 0.01 \text{\AA}$. The value obtained for the undoped sample is the same as obtained from the undoped sample in the Mn sample series, despite the different Fe and Si content. The average Fe-Fe distance in samples with a similar nominal composition of $\text{LaFe}_{11.6}\text{Si}_{1.4}\text{H}_y$ showed an increase of $\sim 0.01 \text{\AA}$, see Ref. [68] through hydrogenation. At the La L_3 -edge, the lattice expansion can be confirmed as well. While the comparison of the EXAFS at the La L_3 -edge in Figure 5.52 (c) shows that most features are well reproduced in the fit, the structural model can not reproduce the kink in the oscillation around $\sim 6.3 \text{\AA}^{-1}$ due to the simplified fit procedure. The shift of the oscillation to lower frequencies is well

reproduced. From the Fourier transform as depicted in Figure 5.52 (d), a change of the La-Fe distance can be inferred. The fit results in a distance of $3.36 \pm 0.02 \text{ \AA}$ in $\text{LaFe}_{11.4}\text{Si}_{1.6}$ and $3.40 \pm 0.02 \text{ \AA}$ through hydrogenation.

5.3.7. Conclusion

The EXAFS measurements revealed a change in the next neighbor distance while undergoing the magnetostructural phase transition from the FM low temperature to the PM high temperature phase at the La L_3 -edge. On the the other hand, at the Fe K- and Mn K-edge, the reduction in the next neighbor distance was barely observable, with nearly no change to be observed at the Fe K-edge. The reduction in the next neighbor distance was furthermore suppressed in the sample with a Mn content of $x = 0.5$, leading to the assumption that Mn addition and the rise in disorder in the sample has a strong effect on the immediate Fe and Mn surrounding. The structural phase transition had a stronger effect on the second coordination shell. While the distances at the La L_3 - and Fe K-edge decreased, the second coordination shell changes its structure at the Mn K-edge and splits into one part which shifts towards smaller and one towards bigger distances. From the EXAFS it could be deduced that the the addition of Mn did not result in any reduction in the atomic distances in comparison to the undoped compound at all measured absorption edges. Only the second coordination shell at the Fe K-edge showed a slight altering of the structure in the FT by Mn addition. Hydrogenation of undoped $\text{LaFe}_{1.4}\text{Si}_{1.6}$ on the other hand, leads to an increase of the next neighbor distance at the Fe K-edge of $0.03 \pm 0.01 \text{ \AA}$ and at the La L_3 -edge by $0.04 \pm 0.02 \text{ \AA}$ as obtained from consequent fits to the experimental data. The second coordination shell showed no change through hydrogenation.

The *FEFF* calculations revealed a good agreement at the La L_3 -edge in the theoretical model and the experimental data. All the features in the fine structure could be reproduced. At the Fe K- and Mn K-edge, the structural model used for the calculations showed strong deviations from the experimental data. It was found that the real structure has a less broad distribution of atoms around the absorbing atom (Fe or Mn), raising the question of the need for an improved structural model. By using simplified fitting models in the *Larch*-fits revealed a rising static disorder at the La L_3 -edge, which doubles with the addition of 1 Mn atom per 2 formular units ($x = 0.5$).

5.4. Mössbauer Spectroscopy on $\text{La}(\text{Fe},\text{Si},\text{Mn})_{13}$

5.4.1. Magnetic Phase Transitions

^{57}Fe Mössbauer spectroscopy was used to study the local magnetism of the Fe sub-lattices under the influence of increasing Mn doping. A series of different Mn concentrations has been measured ranging from Mn contents of $x = 0$ to $x = 1$ in $\text{LaFe}_{11.6-x}\text{Si}_{1.4}\text{Mn}_x$. The whole sample series has been measured at room temperature, in the magnetically disordered, paramagnetic (PM) phase and in the ferromagnetic (FM) low temperature phase at 4.3 K in zero applied magnetic field and in a magnetic field of 5 T (applied along the γ -ray propagation direction). From the Mössbauer spectra the site resolved magnetic behavior has been studied for the Fe sub-lattices. Furthermore, secondary phases in this sample system have been identified and will be discussed. The room temperature spectra are shown exemplary for the Mn concentrations of 0, 0.3, 0.6 and 1 in Figure 5.53 and Figure 5.54 in the top viewgraphs. From the Mössbauer measurements it was possible to identify various secondary phases.

In all samples, bcc α -Fe has been identified. In the paramagnetic phase, the samples with a low Mn concentration ($x < 0.6$) only have one secondary phase, α -Fe. As inferred from field dependent magnetometry measurements (see section A.2), the samples all contained α -Fe as a secondary phase, which has been quantified. To account for the secondary phase, a Zeeman split sextet with a fixed hyperfine field of 33 T and an isomer shift of $-0.107 \frac{\text{mm}}{\text{s}}$ (relative to the ^{57}Co (Rh) source) has been added to the fit of the RT spectra, according to literature values for bcc Fe (calibration standard [166]). The main features in the spectra are a quadrupole doublet and a singlet. The singlet is attributed to the paramagnetic Fe_I -sites on (8b), while the dominant quadrupole doublet originates from the paramagnetic Fe_{II} -sites on (96i). The intensity ratio between the two sites has been calculated from the Mn content in the sample and kept fixed for the equivalent Mn content using the assumption that Mn occupies the (96i)-sites randomly. With Mn contents exceeding 0.6, another secondary phase can be observed in the RT spectra. Here, a sextet with a hyperfine field of 30.6 T and an isomer shift of $-0.023 \frac{\text{mm}}{\text{s}}$ relative to α -Fe has been estimated and this sextet was attributed to a Fe-rich FeSi phase, possibly Fe_3Si [167–170]. The spectra at room temperature give insight into the local electronic properties of the sample series with dependence on the Mn content.

From the quadrupole doublets, the quadrupole splitting ΔE_Q has been extracted as a function of rising Mn concentration. Furthermore, the center line shift ΔCS (relative to α -Fe) at RT has been evaluated. Despite the fact that there is no direct trend observable either in the central shift ΔCS nor in ΔE_Q in the RT measurements (see section A.9), differences in the two inequivalent Fe-sites are visible. Generally, for all Mn concentrations

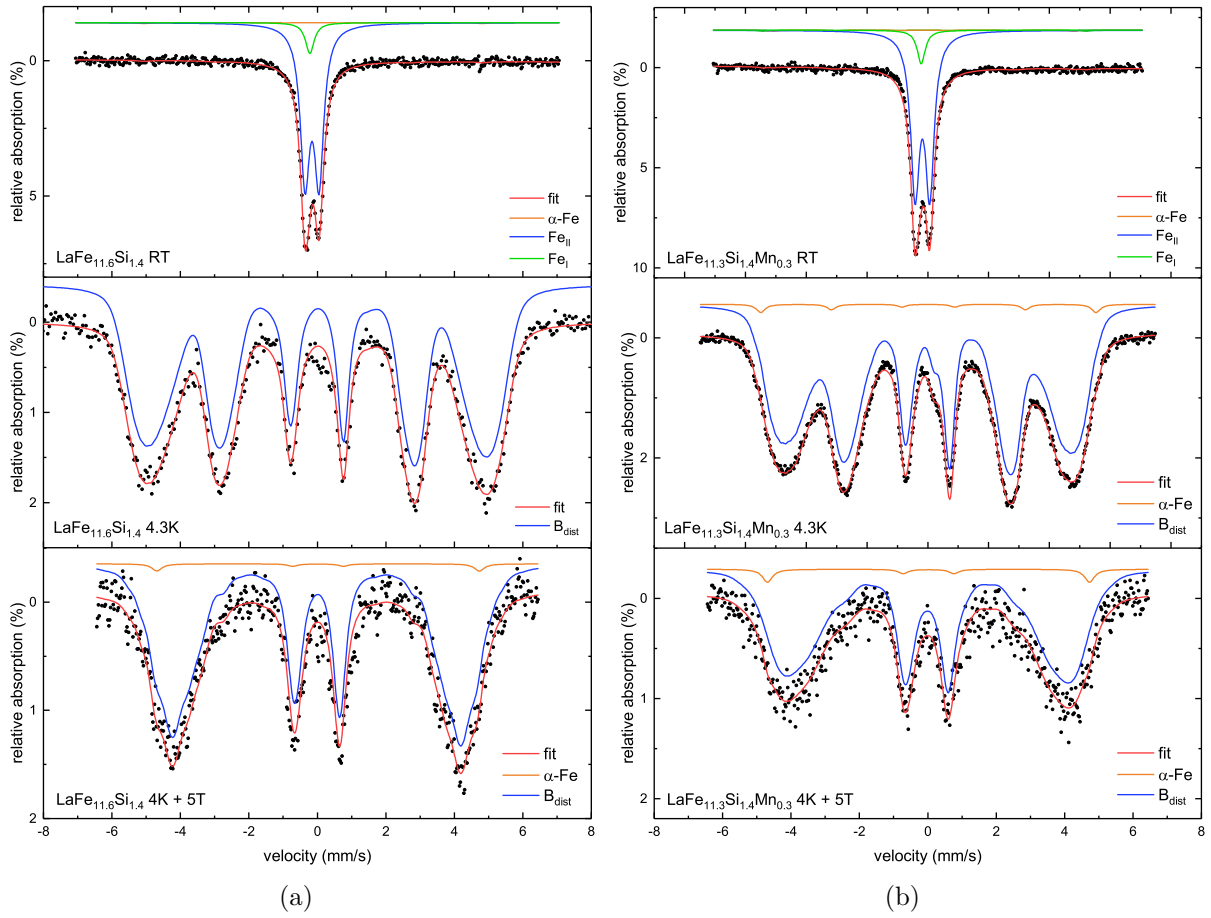


Figure 5.53.: Mössbauer spectra of $\text{LaFe}_{11.6}\text{Si}_{1.4}$ (a) and $\text{LaFe}_{11.3}\text{Si}_{1.4}\text{Mn}_{0.3}$ (b) recorded at room temperature (top viewgraphs), low temperature (4 K, middle viewgraphs) and low temperature 4.3 K and external magnetic field of 5 T (bottom viewgraphs) for Mn contents of (a) 0 and (b) 0.3. The black dots give the data points, the red lines are the least-squares fitted curves. The sub-spectra, which the fits consist of, are displayed with an offset for better visualization.

$\Delta\text{CS}_{\text{FeI}} < \Delta\text{CS}_{\text{FeII}}$ is valid as seen in Table 5.11 for the lowest and highest Mn contents 0 and 1. This finding is in agreement with Ref. [52, 127] and can be explained by a higher symmetry of the Fe_I -sites and thus higher s-electron density at the absorbing nucleus.

To obtain information on the local magnetism, Mössbauer spectra have also been taken at low temperatures in the FM phase for all Mn concentrations at liquid He temperature, 4.3 K, and with and without an applied magnetic field of 5 T. From Figure 5.53 and Figure 5.54 (middle panel) it can be inferred that all low temperature spectra consist of magnetically Zeeman split sextets with broadly distributed lines due to a wide distribution of hyperfine magnetic fields from the Fe sub-lattices, $P(B_{\text{hf}})$. Due to the in-equivalently occupied Fe-sites in the 1:13 phase, the main contribution to the spectral

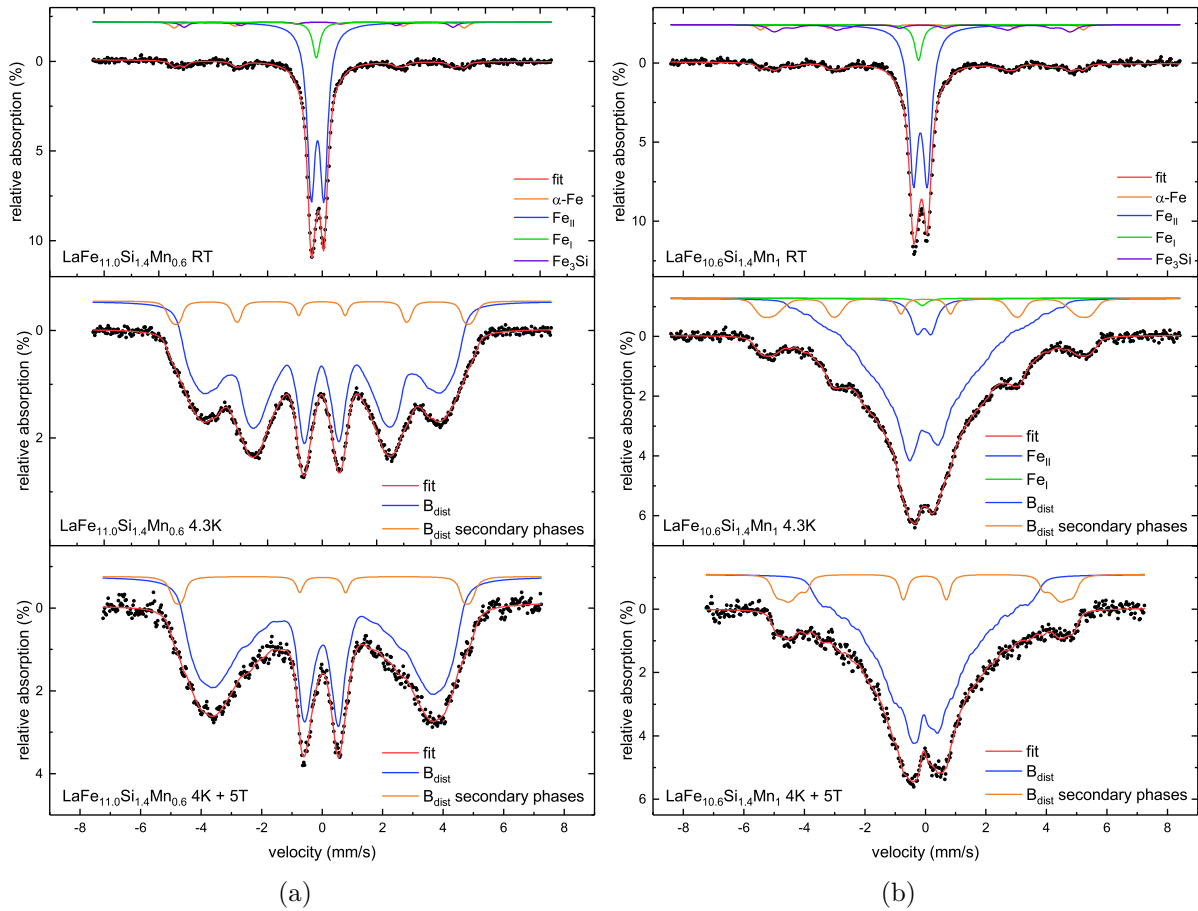


Figure 5.54.: Mössbauer spectra of $\text{LaFe}_{11.0}\text{Si}_{1.4}\text{Mn}_{0.6}$ (a) and $\text{LaFe}_{10.6}\text{Si}_{1.4}\text{Mn}_1$ (b) recorded at room temperature (top viewgraphs), low temperature (4 K, middle viewgraphs) and low temperature 4.3 K and external magnetic field of 5 T (bottom viewgraphs) for Mn contents of (a) 0.6 and (b) 1. The black dots give the data points, the red lines are the least-squares fitted curves. The sub-spectra, which the fits consist of, are displayed with an offset for better visualization.

area relates to Fe_{II} on the (96i)-sites. The fits have been done without a separation of the two Fe-sites, as the sextet contribution from the atoms on the Fe_{I} -sites (8b) is hidden underneath the broad lines of Fe_{II} . In the low temperature spectra for Mn contents exceeding 0.5 it was not possible anymore to distinguish the secondary phases. Therefore, the secondary phase contents of $\alpha\text{-Fe}$ and the Fe_3Si phase have been fitted assuming a hyperfine field distribution $B_{\text{hf}} \sim 30$ T, as seen in Figure 5.54 at low temperatures (middle and bottom viewgraph, orange). Additionally it is possible that there are Mn clusters inside of the secondary $\alpha\text{-Fe}$ phase, which could lead to a hyperfine field distribution of B_{hf} . With a longitudinally applied external magnetic field of 5 T, lines 2 and 5 vanish for the samples with low Mn contents, which indicates very limited spin canting behavior

Center line shift and Quadrupole Splitting of $\text{LaFe}_{11.6-x}\text{Si}_{1.4}\text{Mn}_x$			
Mn_x	Subspectrum	ΔCS [mms ⁻¹]	ΔE_Q [mms ⁻¹]
0	Doublet (Fe_{II})	-0.050 ± 0.001	0.411 ± 0.003
	Singlet (Fe_{I})	-0.113 ± 0.007	
1	Doublet (Fe_{II})	-0.059 ± 0.001	0.454 ± 0.002
	Singlet (Fe_{I})	-0.121 ± 0.004	

Table 5.11.: Mössbauer parameters of the sub-spectra from fitting the RT spectra in Figure 5.53 (a) and Figure 5.54 (b). ΔCS is given relative to an α -Fe absorber at room temperature

in samples with low Mn content. From the low temperature measurements in zero field, the average center line shift $\Delta\langle\text{CS}\rangle$ and the nuclear level quadrupole shift 2ε have been estimated in dependence on the Mn content inside the sample series. Figure 5.55 depicts both, the center line shift $\Delta\langle\text{CS}\rangle$ and the quadrupole nuclear level shift 2ε at 4.3 K in dependence on the Mn concentration. From Figure 5.55 (a) a clear decrease in $\Delta\langle\text{CS}\rangle$, i.e., the isomer shift, is to be seen with rising Mn content. This indicates that with rising Mn doping, the s -electron charge density at the nucleus is increased.

This is a result from the gradual substitution of Fe with Mn, which has only 5 valence electrons, one less than Fe, in its $3d$ shell. Through the hybridization between the Fe and Mn $3d$ -states, the Coulomb interaction between the core and the $4s$ electrons increases. This consequently results in a higher core charge density as the shielding from the $3d$ electrons gets weaker by removing electrons from the system. An opposite trend is observable for the quadrupolar level shift, 2ε , as seen in Figure 5.55 (b). The effect is weak, but clearly visible. Here the value slowly rises with increasing Mn addition. An increase in the quadrupolar level shift is the result of an increasing electric field gradient (EFG) at the nucleus. If the charge density around the absorbing nucleus is non-spheric, the EFG rises. There are two main contributions, which partake in the increase of the EFG. First the ligand field around the nucleus of the Mössbauer isotope, and, second, its own charge density. The trend observable could be explained by the fact that the field gradient is affected when randomly substituting a next neighbor of Fe with Mn, leading to an asymmetry in the charge density around the nucleus.

5.4.2. Changes in Fe Local Magnetic Moment

The changes in the average magnetic hyperfine field $\langle B_{\text{hf}} \rangle$ have been extracted from low temperature measurements at 4.3 K in zero field, as well as via in-field measurements with an applied field of 5 T. As the transition temperature is low for Mn contents $x > 0.5$, even

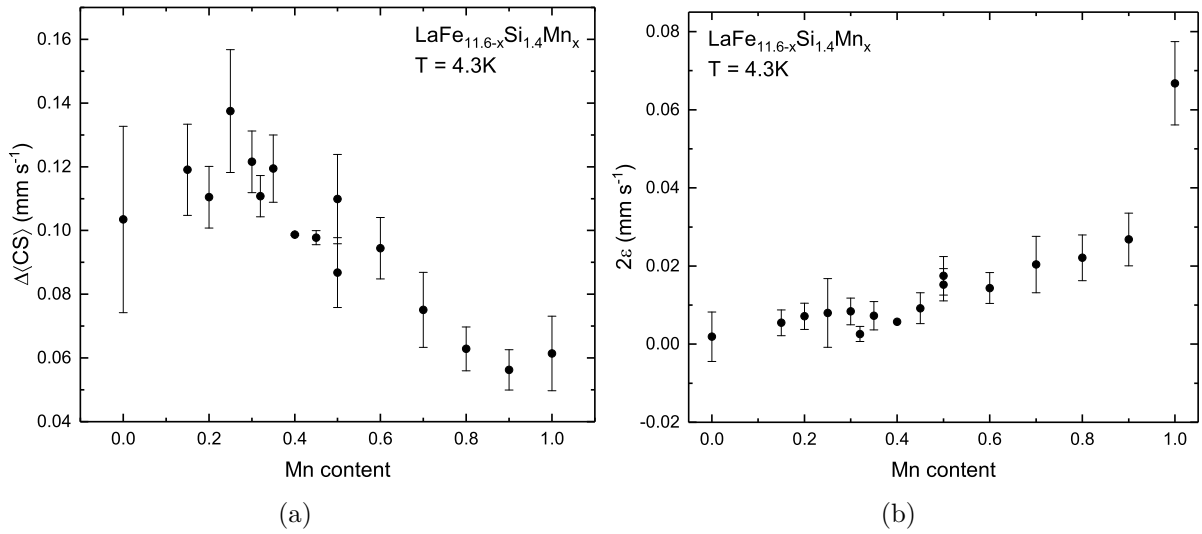


Figure 5.55.: (a) $\Delta\langle\text{CS}\rangle$, which is the center line shift (relative to $\alpha\text{-Fe}$ at RT) and (b) 2ε , the average quadrupolar nuclear level shift, in $\text{La}(\text{Fe}, \text{Si}, \text{Mn})_{13}$ for different Mn contents obtained from the low temperature Mössbauer spectra at 4.3 K.

spectra taken at 80 K (not shown) already have a decrease in $\langle B_{\text{hf}} \rangle$, as expected from the Brillouin function type behavior. Therefore, the local magnetic moment of the Fe sublattices will be extracted from $\langle B_{\text{hf}} \rangle$ of the low temperature (4.3 K) measurements, when $\langle B_{\text{hf}} \rangle$ is close to its ground state. The values extracted for the hyperfine field $\langle B_{\text{hf}} \rangle$ of the dominant Fe_{II} -sites can be assumed to be approximately proportional to the magnetic moment of the corresponding Fe_{II} sub-lattice in the measured compounds. From the in-field measurements in an applied magnetic field of 5 T the effective field is expected to be reduced by the external field. The fields are connected via the following relation

$$\vec{B}_{\text{eff}} = \vec{B}_{\text{hf}} + \vec{B}_{\text{ext}}. \quad (5.1)$$

The effective field \vec{B}_{eff} directly relates to the vector sum of the applied external magnetic field B_{ext} , here 5 T, and the internal hyperfine field \vec{B}_{hf} . Figure 5.56 shows the average hyperfine field values for the whole sample series. Depicted are the values with and without a magnetic field applied with respect to the increasing Mn concentration in the samples. The upward dark blue triangles represent the hyperfine field $\langle B_{\text{hf}} \rangle$, the light blue downward triangles show the values for the effective field $\langle B_{\text{eff}} \rangle$. It is clearly visible that the average hyperfine field is strongly reduced with rising Mn content for both cases. The graph can be parted into two sections. At Mn concentrations ranging between $x = 0$ and $x = 0.6$, values for both $\langle B_{\text{hf}} \rangle$ and $\langle B_{\text{eff}} \rangle$ are reduced, with a difference in magnitude, which roughly corresponds to the value of the applied external magnetic field of 5 T as expected for the γ -photon direction parallel to the aligned magnetic moments ($|B_{\text{eff}}| = |B_{\text{hf}}| - 5 \text{ T}$),

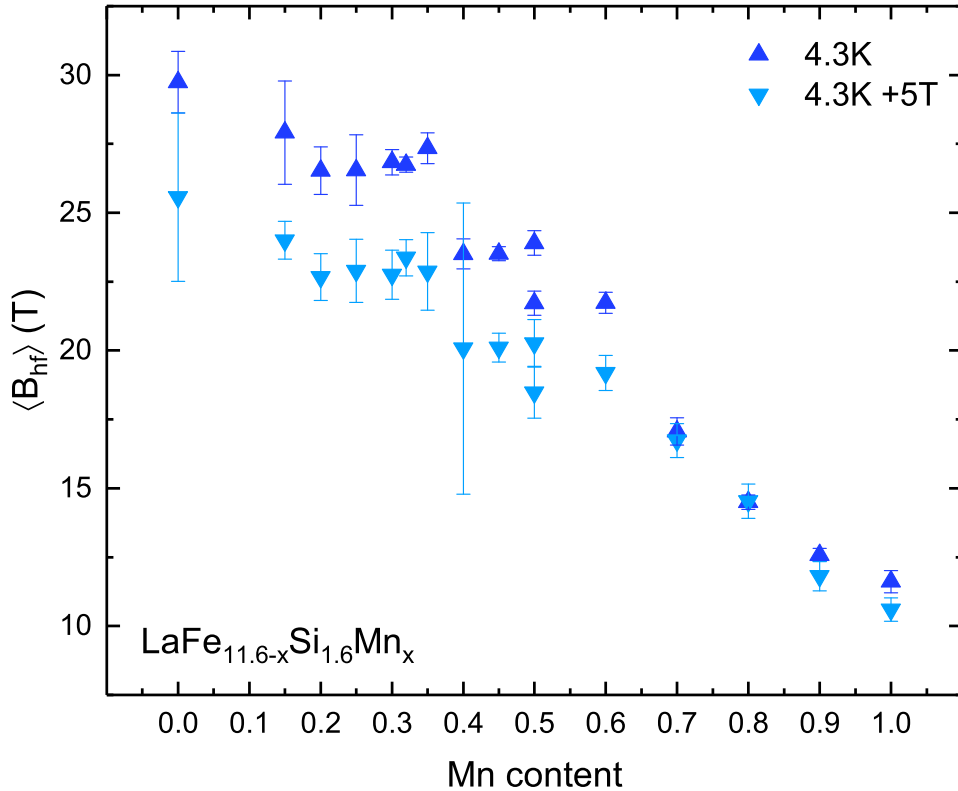


Figure 5.56.: Average magnetic hyperfine field for the Mn doped sample series at low temperatures of 4.3 K (in zero external magnetic field)(dark blue upward triangles) and in 4.3 K in an external field of 5 T (light blue downward triangles).

without spin canting. The average hyperfine magnetic field and the average effective field are very close to each other for Mn concentrations above Mn contents of $x = 0.6$ so that $\langle B_{\text{hf}} \rangle \approx \langle B_{\text{eff}} \rangle$. It can be expected that this trend is observable when there is a strong spin frustration in the system as the Fe moments are not oriented parallel to B_{ext} (parallel to the γ -ray). This observation is in agreement with the data from the temperature dependent magnetometry as discussed in section 2.3. There, above Mn contents of $x = 0.6$, a spin glass phase appears. This behavior could explain why the average hyperfine magnetic field and the effective field are approximately the same for Mn contents above $x = 0.6$. Figure 5.57 exemplary shows the hyperfine field distributions for Mn contents of $x = 0, 0.3, 0.6$ and $x = 1$, respectively. It can be seen that despite the shift in the absolute value of $\langle B_{\text{hf}} \rangle$, also the distribution $p(B_{\text{hf}})$ significantly broadens, indicating a distribution of spin orientations. The upper viewgraphs show the case for zero applied field, the lower in an applied field of 5 T. Apparently, the in field measurements yield much broader $p(B_{\text{hf}})$ distributions. Furthermore, hyperfine field distributions emerge at higher fields for the secondary phase contents at high Mn concentrations. With rising Mn content, the ground state average hyperfine magnetic field $\langle B_{\text{hf}} \rangle$ is reduced by 61 %

and $\langle B_{\text{eff}} \rangle$ by 58 %. Despite the broadening in the hyperfine field distributions, an overall trend can be estimated. The continuous reduction in the average hyperfine field can be directly compared with the (macroscopic) magnetization at 5 K in an applied external field of $\mu_0 H = 9 \text{ T}$, in cases of low spin canting. The macroscopic magnetization measurements as depicted in Figure 5.59, support the conclusions from the Mössbauer experiments as a reduction of the magnetization of 63 % from a Mn content of $x = 0$ to $x = 1$ is evident.

As Mn inside a $\text{La}(\text{Fe},\text{Si})_{13}$ compound holds a magnetic moment, which is approximately in the same range as that of Fe, but with an opposite sign of $-2.35 \mu_{\text{B}}$, the replacement of Fe (with a magnetic moment of $2.2 \mu_{\text{B}}$) [171] by Mn in a stoichiometry of $x = 0.5$ only yields a reduction of the magnetization by approximately $\sim 8 \%$. From the evolution of the Fe magnetic moment according to the Mössbauer experiments, the reduction between a Mn content of $x = 0$ (first sample series) and $x = 0.5$ (second sample series) is 20 %. Thus, the discrepancy must be a combined effect of the reduction in the Fe moment by magnetic exchange interactions and the possible rise of AFM interactions between

Magnetic Hyperfine field and Magnetization of $\text{LaFe}_{11.6-x}\text{Si}_{1.4}\text{Mn}_x$					
Mn_x	$\langle B_{\text{hf}} \rangle$ [T]	μ_{FeII} [μ_{B}]	$\langle B_{\text{eff}} \rangle$ [T]	$M(9 \text{ T})$ [$\frac{\text{emu}}{\text{g}}$]	α -Fe content [%]
0	29.7 ± 1.1	2.09 ± 0.08	25.6 ± 3.1	151	0.5
0.15	27.9 ± 1.9	1.97 ± 0.13	24.00 ± 0.69	140	3
0.2	26.55 ± 1.28	1.87 ± 0.09	22.89 ± 1.2	133	8.5
0.25	26.53 ± 0.87	1.87 ± 0.06	22.67 ± 0.85	146	0.3
0.3	26.84 ± 0.46	1.89 ± 0.03	22.75 ± 0.89	141	0.3
0.32	26.75 ± 0.27	1.88 ± 0.02	23.37 ± 0.66	135	11.4
0.35	27.34 ± 0.56	1.93 ± 0.04	22.87 ± 1.40	140	0.4
0.4	23.50 ± 0.54	1.66 ± 0.04	20.1 ± 5.3	114	20.7
0.5	21.72 ± 0.44	1.53 ± 0.03	18.48 ± 0.94	94	2.9
0.45	23.51 ± 0.26	1.66 ± 0.02	20.11 ± 0.52	125	0.9
0.5	23.90 ± 0.45	1.68 ± 0.03	20.27 ± 0.86	129	9
0.6	21.73 ± 0.39	1.53 ± 0.03	19.19 ± 0.64	122	10.2
0.7	17.06 ± 0.50	1.20 ± 0.04	16.73 ± 0.61	107	15.1
0.8	14.50 ± 0.26	1.02 ± 0.02	14.53 ± 0.62	92	9.8
0.9	12.59 ± 0.23	0.89 ± 0.02	11.81 ± 0.53	73	10
1	11.61 ± 0.40	0.82 ± 0.03	10.60 ± 0.42	55	10.7

Table 5.12.: Extracted average magnetic hyperfine fields at 4.3 K (in zero external magnetic field) ($\langle B_{\text{hf}} \rangle$), Fe moment of (mainly) the Fe_{II} -sites ($\langle B_{\text{eff}} \rangle$) effective field at 4.3 K in a longitudinal applied field of 5 T and magnetization in high field $M(9 \text{ T})$ (corrected for the given residual α -Fe content, the error in the magnetization is around 0.2 %). Shown are the values for the two sample series, $x = 0 \dots 0.5$ (first) and $x = 0.45 \dots 1$ (second).

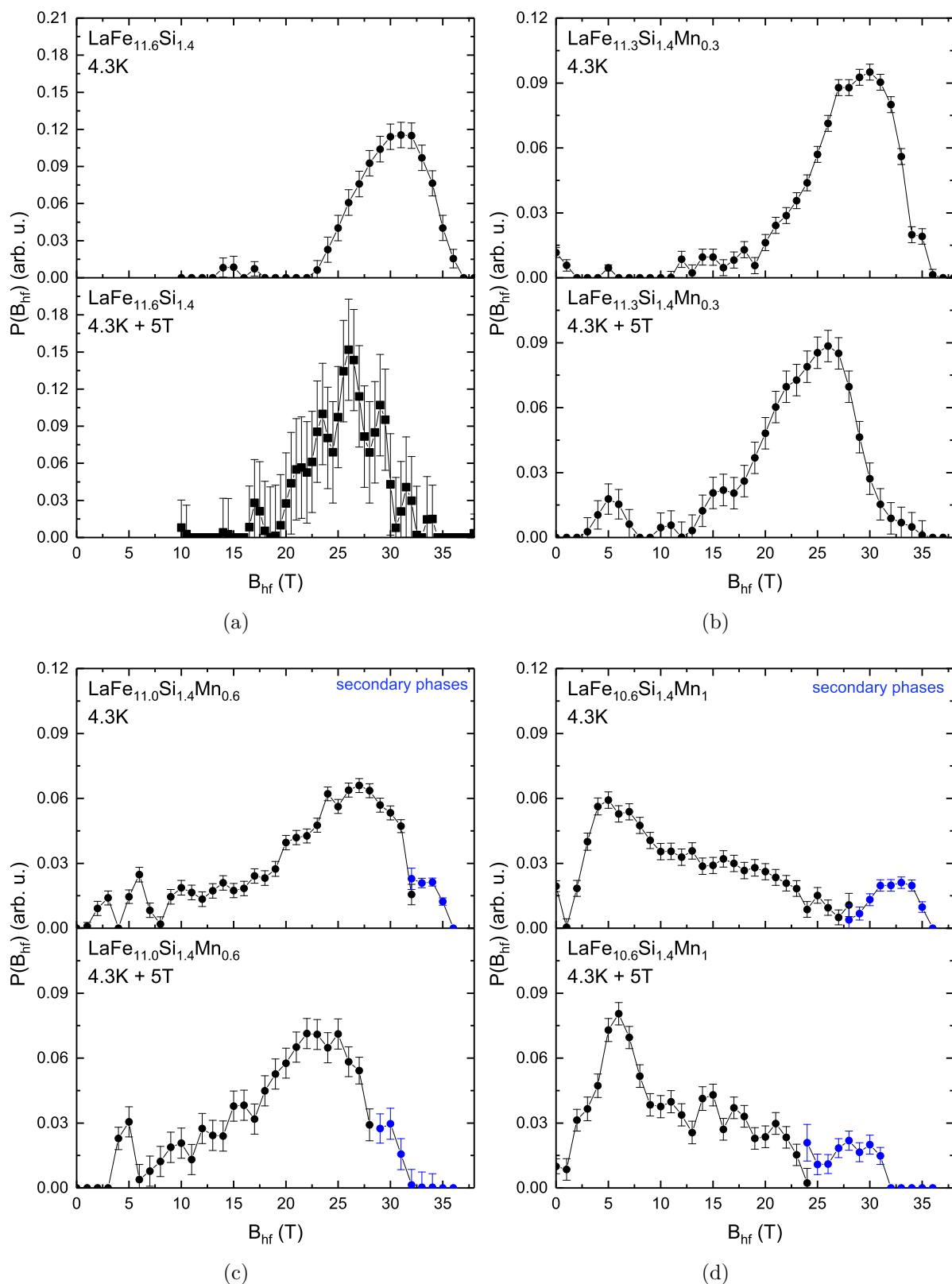


Figure 5.57.: Magnetic hyperfine field distributions at low temperature 4.3 K with and without an applied magnetic field of 5 T for Mn contents of 0 (a), 0.3 (b), 0.6 (c) and 1 (d). The blue lines refer to the distributions of the secondary phases. The average magnetic hyperfine field distributions have been area normalized to the spectral area of the corresponding phases. The distributions are area-normalized to 1.

the Mn and Fe atoms and the substitution of the Fe atoms themselves. Equiatomic Fe₅₀Mn₅₀ in a *fcc* structure has antiferromagnetic coupling between Fe and Mn in various stoichiometries [172]. The next neighbor distance in Fe₅₀Mn₅₀ is 2.5 Å [173]. From Heusler alloys it is known that Mn and Mn couple antiferromagnetically to each other when in a distance $< 3 \text{ \AA}$, whilst ferromagnetic exchange is preferred when the next neighbor distance is $> 4.24 \text{ \AA}$ [174]. As inferred from the EXAFS measurements and consequent fits with *Larch* in section 5.3, Fe_{II} has 10 Fe atoms in its first coordination shell, with four next neighbor Fe_{II} distances of $2.50 \pm 0.01 \text{ \AA}$, where Mn possibly can be substituted. This distance is below the critical distance where both, Mn and Mn as well as Fe and Mn would couple antiferromagnetically. The values for the magnetization have been taken from the low temperature field dependent magnetometry measurements at 9 T and corrected for a residual α -Fe content given in Table 5.12 (following the procedure as described in section A.2).

To estimate the Fe magnetic moment of the Fe sub-lattice, the moment has been extracted from the average magnetic hyperfine field $\langle B_{\text{hf}} \rangle$ with dependence on the Mn content x . The coupling parameter A relates the average hyperfine field to the Fe magnetic moment [175], using

$$\langle B_{\text{hf}} \rangle = A\mu_{\text{Fe}}. \quad (5.2)$$

Within this work, the coupling parameter has been assumed to have a constant value of $A = 14.2 \text{ T}/\mu_{\text{B}}$ [127] for all samples in the series measured in order to approximate the Fe magnetic moment. It has to be noted though that the coupling constant A can change slightly for different dopant concentrations x . This is an effect of the increase in hybridization between the Fe and Mn $3d$ -states, which reduces the hyperfine splitting and thus, results in a potentially different hyperfine coupling constant. Consequently, the values for the Fe magnetic moments μ_{FeII} at high Mn concentrations might be smaller than the ones calculated within this work. In a first approximation, the changes are assumed to be small for low Mn contents [127, 175]. From Figure 5.59 (b) it can be inferred that the assumption of a constant A remains valid at least up to a Mn content of $x = 0.3$, where the magnetic hyperfine field $\langle B_{\text{hf}} \rangle$ is compared to the magnetization. The extracted Fe magnetic moments for (mainly) the Fe_{II}-sites, as the broad magnetic hyperfine field distribution cannot be separated into the two Fe sub-lattices, can be found in Table 5.12. Comparing the value for the magnetic moment of the Fe_{II}-sites, as determined from neutron diffraction data for an undoped compound [176], of $\mu_{\text{FeII}} = 2.16 \mu_{\text{B}}$, to our data, shows that we extract the same Fe magnetic moment within the error margin. The magnetic moment for no Mn doping in our sample series is $\mu_{\text{FeII}} = 2.09 \pm 0.08 \mu_{\text{B}}$. Increasing the Mn content consequently from $x = 0$ to $x = 1$ leads to a reduction of the magnetic moment by 61 %, determined from $\langle B_{\text{hf}} \rangle$. This reduction is in general agreement

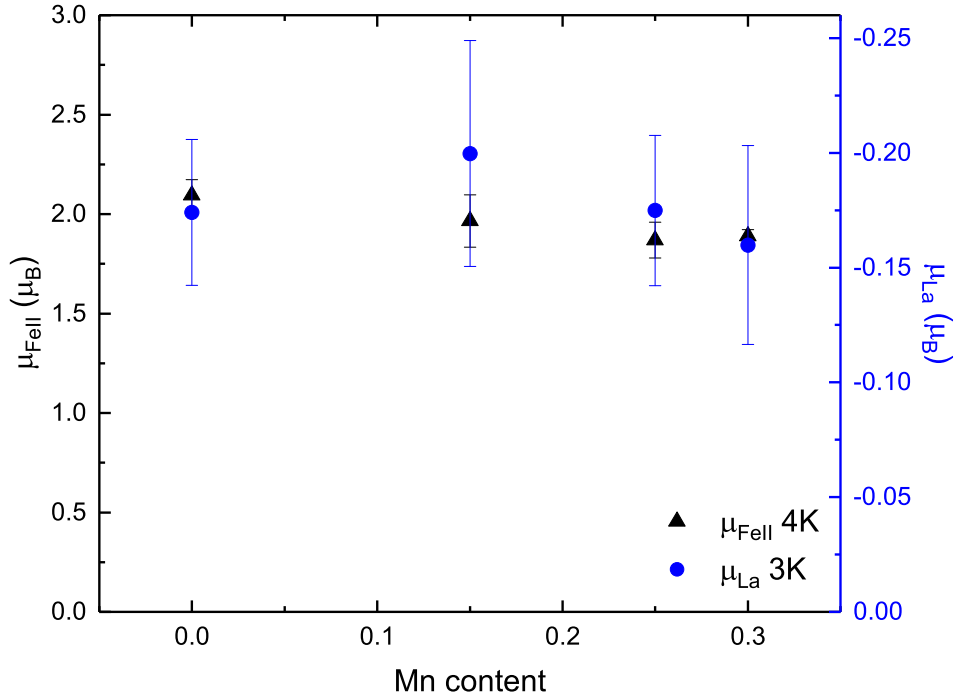


Figure 5.58.: Comparison of the magnetic moments in Fe_{II} (black triangles) and the induced La moments (blue dots) from the XMCD sum rule evaluation at edge step E_0 , versus the Mn content x .

with the value for the reduction of the high field magnetization of 63 %. The reduction in the Fe-moment can be directly correlated to the XMCD measurements on the Fe K-edge as described in section 5.2.2.

Figure 5.58 directly correlates the obtained magnetic moment of the Fe_{II} -sites with the induced spin moments of La obtained from sum rule analysis of the XMCD measurements at the La $L_{2,3}$ -edges. The induced moments of La were calculated from the magnetic spin and orbital moments via $\mu_{\text{La}} = \mu_s + \mu_l$. While μ_{FeII} is reduced by $\sim 9.5\%$ from a Mn concentration of $x = 0$ and $x = 0.3$, a change in the La moment is not clearly proven within the error margin. The magnetic moment of La is exemplary listed in Table 5.13 is that of the evaluation with background correction and the edge step at E_0 and a branching ratio of $\frac{1}{1.48}$. The induced spin moment in La is only $\sim 4 - 10\%$ of that of the Fe moment μ_{Fe} for $x = 0 - 0.3$ for all evaluation methods used to obtain μ_{La} from the sum rule analysis.

Figure 5.59 (a) depicts the evolution of the high field magnetization in dependence of the rising Mn content at low temperature (FM). The values have been corrected for residual α -Fe secondary phase contents. The blue dots take into account the spin canting angles estimated from the Mössbauer spectra for Mn contents above $x = 0.5$ using the relation $M(9\text{T}) = M_{\text{sat}} \cdot \cos(\theta)$. The findings presented are in accordance with studies of the magnetization of Mn doped compounds with a similar stoichiometry $\text{La}(\text{Fe}_{1-x}\text{Mn}_x)_{11.7}\text{Si}_{1.3}$

Comparison of magnetic moments in Fe and La of $\text{LaFe}_{11.6-x}\text{Si}_{1.4}\text{Mn}_x$			
Mn_x	$\mu_{\text{FeII}} [\mu_{\text{B}}]$	$\mu_{\text{La}} [\mu_{\text{B}}]$	$\mu_{\text{La}}/\mu_{\text{FeII}} [\%]$
0	2.09 ± 0.08	-0.17 ± 0.03	8
0.15	1.97 ± 0.13	-0.20 ± 0.04	10
0.25	1.87 ± 0.06	-0.17 ± 0.03	9
0.3	1.89 ± 0.03	-0.16 ± 0.04	9

Table 5.13.: Magnetic moments of Fe_{II} and La as estimated from Mössbauer and XMCD sum rule analysis (E_0 edge step) of XMCD at La $L_{2,3}$ -edges.

for Mn contents of $x = 0 \dots 0.03$, corresponding to nominal stoichiometries ranging from $\text{LaFe}_{11.7}\text{Si}_{1.3}$ to $\text{LaFe}_{11.35}\text{Si}_{1.3}\text{Mn}_{0.35}$, showed a decrease of 7.4% [177]. From Figure 5.59 (a) we find a decrease in the magnetization of $\sim 7.3\%$, when comparing to $\text{LaFe}_{11.6}\text{Si}_{1.4}$ to $\text{LaFe}_{11.25}\text{Si}_{1.4}\text{Mn}_{0.35}$, following the same trend. The reduction in the average magnetic hyperfine field and the Fe_{II} moment is 7.6%. In Figure 5.59 (b) the magnetization, which has been corrected for the spin canting is plotted against the average magnetic hyperfine field at 4.3 K. We can assume that there is no spin canting for Mn contents from $x = 0 - 0.5$, as the average hyperfine field is consistent with the saturation magnetization. From Figure 5.59 (b) it can be inferred that there is no Fe spin canting within the error

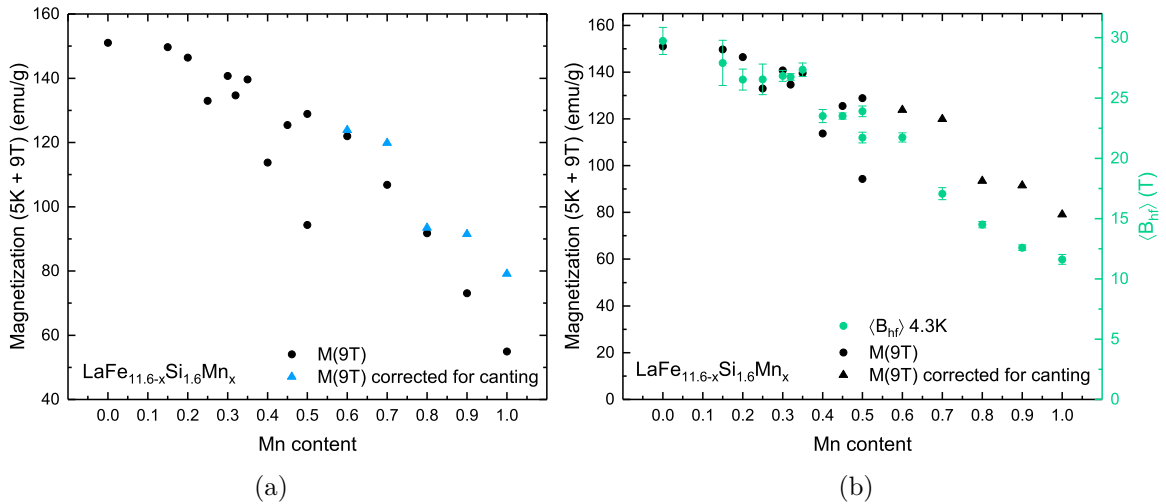


Figure 5.59.: (a) Evolution of the magnetization at 5 K in 9 T. (b) Comparison of the high field magnetization (black dots) versus the hyperfine field (green dots). The magnetization has additionally been corrected for the Fe spin canting (triangles) as obtained by the fits to the Mössbauer spectra. The error of the magnetization is maximum 0.2% and thus smaller than the data points. The deviation of the magnetization for the samples with $x = 0.5$ results from different sample batches with varying secondary phase contents.

bar for Mn contents between $x = 0$ and $x = 0.5$ as the values for the average hyperfine fields are consistent with the saturation magnetization.

It can be seen that both, the reduction in hyperfine fields, as well as the reduction in the saturation magnetization show that the Fe moment is continuously decreased when Mn doping increases, as the local surrounding of the Fe atoms is drastically modified. Mn substitutes the Fe_{II} -sub-lattices and therefore reduces the magnetic moment. The extraction of the static disorder in the system by means of the EXAFS measurements proved that the disorder doubles by adding 1 Mn atom into 2 formula units. The disorder, therefore, also contributes to the decrease in the magnetic moment of Fe by a variation of the local exchange interaction. The magnetic moment of Fe, μ_{FeII} , extracted from the average hyperfine field, has been compared to the value of the maximum XMCD at the Fe K-edge at 7114 – 7115 eV (denoted as energy position 2 in section 5.2.2), which showed a direct correlation between Mn content and magnetic signal. Figure 5.60 shows the extracted magnetic moments of the Fe_{II} -sites and the value of the maximum XMCD at an energy of 7114 – 7115 eV for Mn contents ranging from $x = 0 - 0.5$. From the comparison it is clear that the magnetic moment μ_{FeII} is proportional to the XMCD at the Fe K-edge with exception of the data points in the sample with a Mn content of $x = 0.5$. The

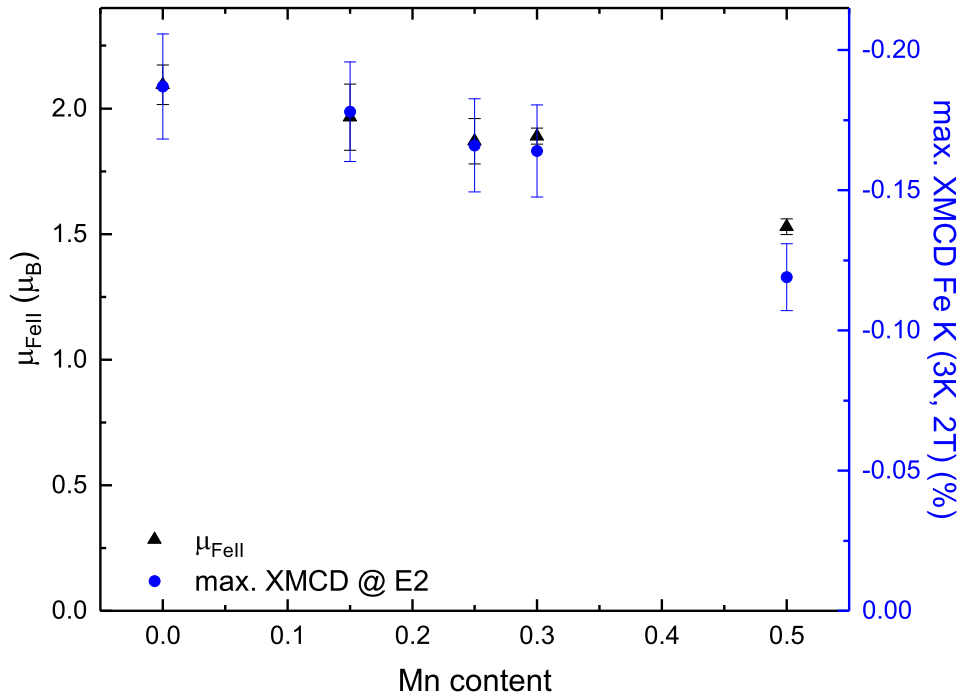


Figure 5.60.: Comparison of the magnetic moments of Fe_{II} (black upward triangles) from the hyperfine field distributions obtained by Mössbauer spectroscopy versus the maximum value of the XMCD (blue dots) of the Fe K-edge at the energetic position in the pre-edge region at the energy denoted as E2 between 7114 – 7115 eV.

deviation between the XMCD and the Fe magnetic moment at $x = 0.5$ could possibly be explained by the changing coupling constant A due to the increase in hybridization between the Fe and Mn $3d$ -states, which then results in spin canting. The canting will be furthermore discussed in the following section. The total magnetic moment of the Fe_{II} -sites reduces by 27 % from a Mn content of $x = 0$ to $x = 0.5$, while the value of the maximum XMCD reduces by 36 % in comparison to the initial magnitude. The absolute error in the given Fe magnetic moments might be a bit bigger than given, due to the possible error originating from the assumed coupling constant A .

5.4.3. Evolution of Spin Frustration

As observed in section 5.3, the increase of Mn contents strongly affects the local surrounding of the Fe sub-lattices. From the measurements at low temperatures and in a high magnetic field (at 4.3 K and an external magnetic field of 5 T) it was possible to extract the Fe spin canting angles of the compounds as a function of Mn content. This has been done to determine whether the reduction of the magnetic moment can be correlated with a possible altering of the magnetic structure in the sample series rather than just substitution of the Fe atoms by adding Mn. The sample series measured ranged from a Mn content of $x = 0 - 1$. Figure 5.61 depicts the extracted spin canting angles estimated from the A_{23} -ratio as described in section 2.5. From the evaluation we can deduce a trend of an increasing spin canting angle with rising Mn content, as soon as latter exceeds $x = 0.6$. Figure 5.61 (black full circles) shows the evaluation via the A_{23} intensity ratio. Here it can be seen that the angles obtained for Mn concentrations below $x = 0.6$ are in a range of $\theta = 0^\circ$ within the error margin (see Table A.5 in the appendix for a list of the values). This evaluation gives no conclusive proof of $\theta = 0^\circ$, but we can expect from the Mössbauer spectra predominantly collinear behavior.

The orange circles depict a manual adjustment and the maximum angle, which can be fitted to the Mössbauer spectra without distorting the shape of the fit. The description of the spin canting angle via the A_{23} intensity ratio yields a physically more accurate description for the system. Here, the spin canting angle also increases as the Mn content exceeds $x = 0.6$, inducing higher spin frustration in the system with higher Mn doping. It has to be noted, though that from the measurements done and also from the evaluation of the A_{23} intensity ratio, it cannot be completely excluded that there is the possibility of a small spin canting angle even at very low Mn concentrations due to a relatively large error in the measurements resulting from the broadened magnetic hyperfine field distributions and overlapping spectral lines. This behavior would, however, contradict the expectation [35, 58, 59] of a collinear spin structure at no Mn content. This indicates the need to measure Mössbauer spectra in a transversal geometry (γ -ray perpendicular to B_{ext}) with

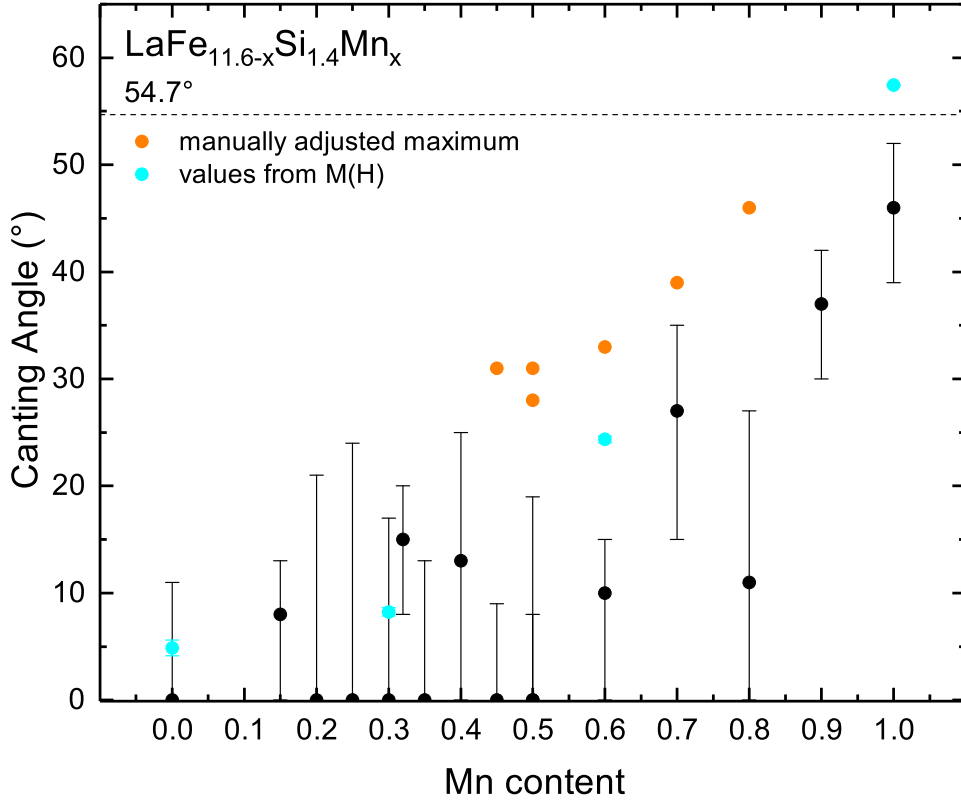


Figure 5.61.: Spin canting angles obtained via the intensity ratio A_{23} from in-field Mössbauer measurements (black circles) for Mn doped $\text{La}(\text{Fe}, \text{Si}, \text{Mn})_{13}$ for different Mn concentrations in an applied external magnetic field of 5 T. The black dashed line refers to the "magic angle" at ~ 55 degree, indicating random spin orientation. The cyan dots refer to the canting angles obtained from the magnetometry measurements for four exemplary Mn contents. The orange dots refer to the maximum value for the canting angle with the respective A_{23} intensity ratio, which could be manually adjusted without distorting the fitted spectrum. They serve as the maximum possible canting angle.

better statistics in the future, as the transversal geometry is somewhat more sensitive to spin canting. The field dependent magnetometry (see chapter 4) already hinted towards stronger spin frustration with rising Mn content, as the magnetization curves did not reach saturation in high fields of ± 9 T, the spin canting has also been estimated from the magnetometry measurements at low temperatures. Figure 5.62 depicts the $M(H)$ curves obtained for Mn contents of $x = 0, 0.3, 0.6$ and $x = 1$. Whilst the high field magnetization reduces with increasing Mn content, the curves for a Mn content of $x = 0.6$ and $x = 1$ clearly do not saturate at 9 T.

In order to extract a value for the saturation magnetization, the following equation has been used [178]:

$$M_{\text{ext}}(B) = M_{\text{S}} \left(1 + \frac{a}{B} + \frac{b}{B^2} \right). \quad (5.3)$$

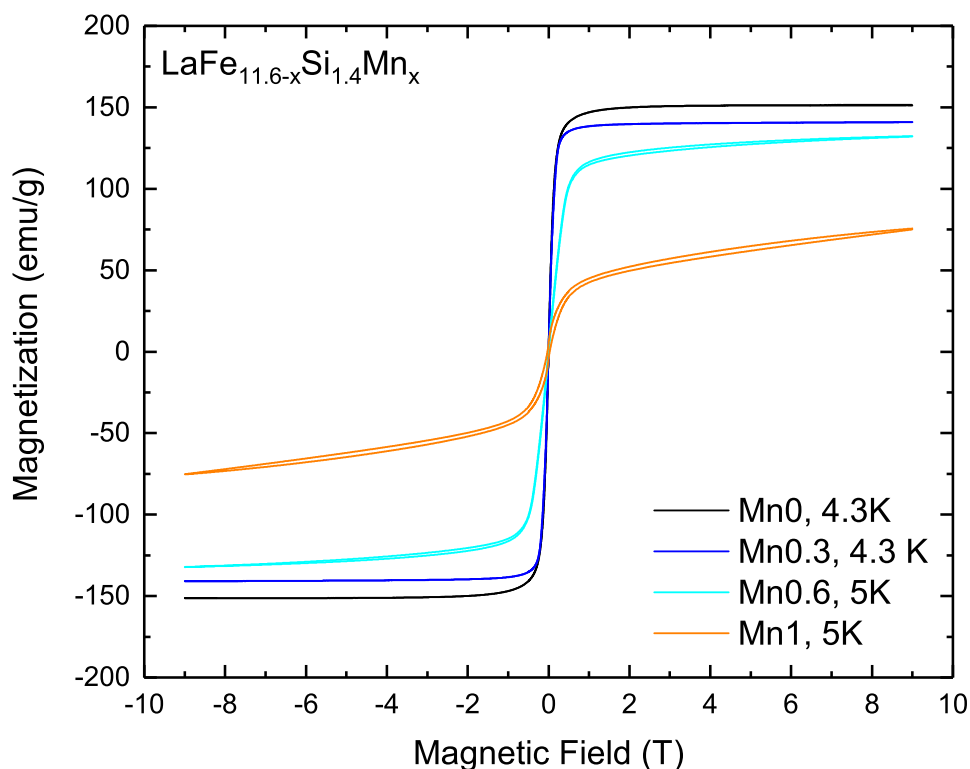


Figure 5.62.: Field dependent magnetization curves for four exemplary stoichiometries of Mn from 0 (black), 0.3 (blue), 0.6 (cyan) to 1 (orange), from which the saturation magnetization has been extrapolated to determine the spin canting angle according to Equation 5.3.

With Equation 5.3, a fit has been performed to the high field quadrant of the field dependent magnetometry curves in a range of 5 – 9 T. From the fit, the curve has then been extrapolated in order to determine the saturation magnetization for the compound. For the extraction of the canting angle θ , the equation

$$M \approx M_S \cdot \cos(\theta), \quad (5.4)$$

has been used, which relates the saturation magnetization to the spin canting angle. The equation can be used for moderate canting angles. The angles have been calculated from $M(5\text{T})$ and $M(9\text{T})$ using the extrapolated value of M_S . The values for the respective magnetization as well as the angles are given in Table 5.14. The angles as calculated with $M(5\text{T})$ have been included in Figure 5.61 (cyan dots) to be directly compared with the results as obtained from the least-squares fits of the Mössbauer spectra via the $A_{2,3}$ ratio. From the comparison between the angles extracted from the magnetization at 5 T and 9 T it is obvious that even 9 T are not sufficient to fully magnetically saturate the samples with high Mn content. Figure 5.63 depicts the fits to the experimental magnetization data for the four exemplary Mn contents, Mn $x = 0, 0.3, 0.6$ and $x = 1$.

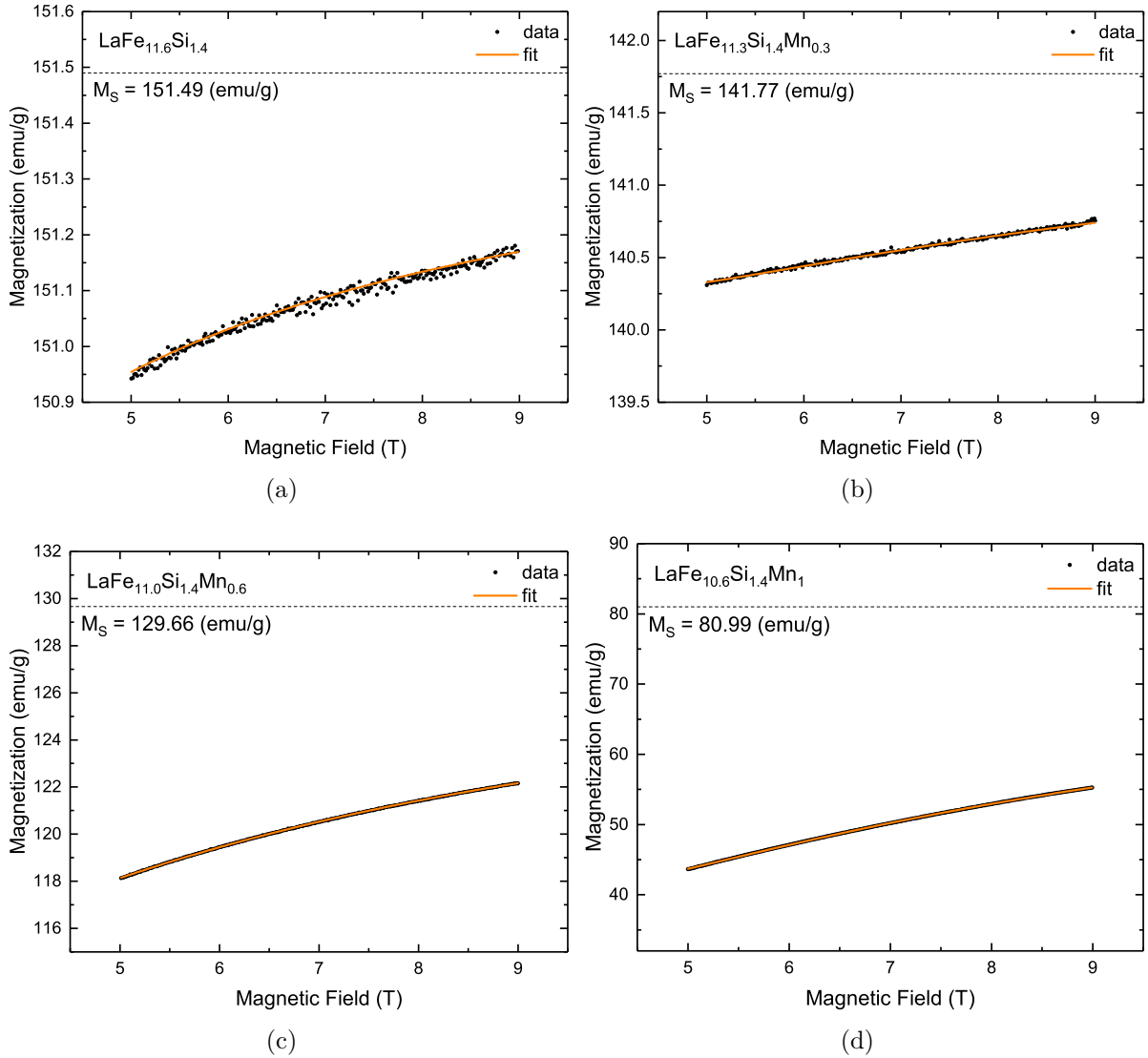


Figure 5.63.: Fit (orange curve) to the data points (black) of the high field magnetization measurements for Mn contents of $x = 0, 0.3, 0.6$ and $x = 1$. The curves have been corrected for the residual α -Fe contents. The black dashed line refers to the extrapolated saturation magnetization according to Equation 5.3.

The field dependent magnetization curves shown have been corrected for the residual α -Fe content. The orange line is the fit to the experimental data (black dots) according to Equation 5.3. The dashed line refers to the value of the extrapolated saturation magnetization. From this evaluation it is apparent that with rising Mn content, the deviation between the high field magnetization and the saturation magnetization increases, leading to a stronger spin frustration. The values for the canting angle, as calculated from Equation 5.4, indicate that Mn contents of $x = 0.6$ and $x = 1$ clearly show a rise in spin frustration. This finding is in general agreement with the evaluation and extracted canting angles from the A_{23} -ratio from the Mössbauer spectra and validates that at high

Mn content, the system exhibits magnetically frustrated behavior. The increase in the hybridization of the Fe and Mn 3*d*-states results in an increase of spin frustration. This is an effect between the competing FM and AFM coupling of the Fe and the added disordered Mn atoms in the system.

Extrapolated saturation Magnetization M_S in $\text{LaFe}_{11.6-x}\text{Si}_{1.4}\text{Mn}_x$					
Mn_x	$M(5\text{T}) [\frac{\text{emu}}{\text{g}}]$	$M(9\text{T}) [\frac{\text{emu}}{\text{g}}]$	$M_S [\frac{\text{emu}}{\text{g}}]$	$\theta(5\text{T}) [^\circ]$	$\theta(9\text{T}) [^\circ]$
0	150.94 ± 0.16	151.17 ± 0.16	151.49 ± 0.003	4.87 ± 0.73	3.73 ± 0.95
0.3	140.31 ± 0.13	140.76 ± 0.13	141.77 ± 0.003	8.23 ± 0.38	6.88 ± 0.45
0.6	118.14 ± 0.27	122.15 ± 0.26	129.66 ± 0.003	24.35 ± 0.32	19.61 ± 0.37
1	43.64 ± 0.03	55.26 ± 0.03	80.99 ± 0.007	57.43 ± 0.05	47.02 ± 0.04

Table 5.14.: Extracted saturation magnetization exemplary for Mn contents of $x = 0, 0.3, 0.6$ and $x = 1$, corrected for residual secondary phase contents. The canting angle has been calculated from $M(9\text{T})$ and $M(5\text{T})$, using Equation 5.3.

5.5. Conclusion

In this chapter the electric and magnetic hyperfine interactions have been studied in Mn containing $\text{LaFe}_{11.6-x}\text{Si}_{1.4}\text{Mn}_x$ -compounds by using ^{57}Fe Mössbauer spectroscopy for a series of Mn contents ranging from $x = 0$ to $x = 1$. From the room temperature measurements in the paramagnetic state, the electric hyperfine parameters have been obtained for the two distinct Fe-sites in the compounds. For the Fe_{II} (96i) and Fe_{I} -sites (8b), respectively, with no Mn and high Mn doping, no difference was observed in the quadrupole splitting ΔE_Q , nor in the center line shift ΔCS . Comparing the two Fe-sites showed that the center line shift ΔCS was generally larger for the Fe_{II} than the Fe_{I} site, $\Delta\text{CS}_{\text{FeI}} < \Delta\text{CS}_{\text{FeII}}$, for all Mn contents, agreeing with the structural information on the system, which has a higher symmetry around the Fe_{I} site. From the temperature dependent measurements it was possible to identify multiple secondary phases in the sample system. Next to the α -Fe secondary phase, FeSi-compounds have been identified, which give rise to the hyperfine magnetic field contributions at high magnetic field values. From the low temperature measurements in zero field, the average center line shift $\Delta\langle\text{CS}\rangle$ as well as the nuclear quadrupole shift 2ε , mainly from the dominant Fe_{II} -sites, have been found to change with rising Mn content. A higher *s*-electron charge density at the ^{57}Fe nucleus results in a decrease of the isomer shift and is in agreement with rising Mn content, due to less electrons in the system. The increase in the quadrupole shift is an effect of

the electric field gradient, which is rising with Mn doping, distorting the spherical charge density around the Fe atom. From the average magnetic hyperfine field the magnetic moment of the Fe_{II}-sites has been determined as a function of Mn content. The total magnetic moment of Fe was found to be $\mu_{\text{FeII}} = 2.09 \mu_{\text{B}}$ without Mn addition, which decreases to only $\mu_{\text{FeII}} = 0.82 \mu_{\text{B}}$ for a Mn content of $x = 1$. This decrease in magnetization is a result from multiple effects in the sample. First, the disorder in the sample is increased by subsequent Mn doping changing the local exchange interaction. Additionally, the magnetic moment reduces by replacing Fe with Mn in the system. Furthermore, a rise in spin frustration, as obtained from the A_{23} line intensity ratio in the low temperature Mössbauer spectra as well as from the field dependent magnetization measurements was observed, which showed non collinear spin alignment for Mn contents exceeding $x = 0.6$. Up to a Mn content of $x = 0.3$ it was found that the coupling constant $A = 14.2 \text{ T}/\mu_{\text{B}}$ can be used to calculate the Fe magnetic moment, while for higher Mn contents, the absolute values might deviate due to the increase in the hybridization of the Fe and Mn $3d$ states and consequently results in spin canting. The competition between the FM coupling of the Fe atoms and the AFM coupling of the Mn atoms to Fe gives rise to the spin canting behavior.

6. Conclusion and Outlook

The goal of this thesis was to connect and investigate the microscopic degrees of freedom in $\text{La}(\text{Fe},\text{Si})_{13}$ -based compounds by means of various element-specific techniques. The combined approach of various element-specific characterization methods, together with *ab-initio* calculations revealed a strong interplay of the electronic, phononic and magnetic subsystems due to the itinerant character of the investigated system. The decomposition of the microscopic degrees of freedom therefore needs to be replaced for a rather inclusive model, which correlates all degrees of freedom.

NRIXS experiments show a significant change in the Fe-partial VDOS originating from hydrogenation. These changes are confirmed by element-resolved first-principles calculations of the electronic and vibrational DOS. While hydrogen is capable of shifting the phase transition to ambient temperatures, the electron-phonon coupling, as well as the large moment volume coupling, which is associated with the itinerant electron metamagnetism as observed in a hydrogen free sample, are both in effect. Originating from adiabatic electron-phonon coupling, a strong redshift and anomalous lattice softening is observed, which indicates a cooperative contribution of the microscopic degrees of the entropy to the entropy change across the first-order phase transition. The entropy enhancement at the phase transition region is reduced by 50 % through hydrogenation in comparison to the hydrogen-free case. This effect is further suppressed through Mn doping. The mechanism of the strong suppression of the vibrational entropy enhancement across the phase transition by Mn is not clear yet, despite an apparent energetic redshift and reproduction of all the features in the VDOS of the undoped compound.

Mn doping does not only change the phononic, but also the magnetic behavior in the sample system. Through the combination of increasing hybridization of the Mn $3d$ - with the Fe $3d$ -states, by consequent substitution of Fe with Mn and rising disorder in the sample system, the magnetism in $\text{La}(\text{Fe},\text{Si})_{13}$ -based compounds changes drastically. The XANES of the K-edge is very sensitive to the changes on the local structure and electronic state and acts as a sensor to the structural transition as well as the disorder arising from Mn doping. The structural changes of the Fe K-edge XAS can directly be correlated to the decrease of the magnetic moment of Fe and are in agreement with magnetometry measurements. To get a better insight on the dynamics of the structural phase transition,

an in-situ measurement of the structural transition in direct correlation to the magnetism could verify whether the structural transition is triggered by the magnetic transition or vice versa. This can be achieved by driving the phase transition with an applied external magnetic field in small field steps at the transition temperature and recording the XMCD for each consequent step.

The decrease in the isomer shift with rising Mn content, from the Mössbauer experiments proves the strong hybridization of the Fe and Mn $3d$ -states. According to the quadrupole shift the rising electric field gradient directly correlates to the change of the shape of the pre-edge feature at the Fe K-edge XAS, which decreases with increasing Mn content due to an increase in local disorder seen by EXAFS measurements. With rising Mn content, the increase in the static disorder contributes to the reduction in the Fe magnetic moment through a variation of the local exchange interaction.

Additionally, the removal of Fe atoms from the compound, and a rise in the Fe and Mn $3d$ -band hybridization lead to stronger spin frustration, resulting in non collinear spin alignment with higher Mn contents. For Mn contents above $x = 0.6$, spin frustration is present and non collinear behavior is emerging, pointing at AFM coupling between Fe and Mn. Due to the big error in the obtained spin canting angles, future experiments have to be performed in transversal and longitudinal measurement geometry with better statistics to conclusively determine the Mn content, where non-collinear magnetic behavior begins. While La does hold a finite induced magnetic moment as a result from the hybridization of the Fe $3d$ and La $5d$ -states, which are coupled antiparallel to the Fe magnetic moment, Mn doping does not have a strong effect on the value of the induced magnetic La moment contrary to the expectation from magnetometry and Mössbauer experiments. The sensitivity of the spectral shape of the XANES to applied fields and sample preparation made it difficult to apply sum rule analysis. The alteration of the spectral shape by Mn doping can therefore not conclusively be explained, as data post-processing and Bragg peaks in the measurement originating from big crystallites additionally distort the spectral shape. This indicates the need of further XMCD experiments with more finely ground samples to avoid spectral distortion.

To clarify the effect of Mn on the whiteness intensity due to hybridization effects, X-ray absorption experiments at the Fe and Mn $L_{2,3}$ -edges in the soft X-ray regime can be done in future with consequently higher Mn contents. Furthermore, it can prove the proposed rise in antiferromagnetic coupling of Fe to Mn due to the increase in spin frustration in combination with theoretically modeling.

Within this thesis, the strong correlation between the various microscopic degrees of freedom could be validated by utilizing the combined approach of NRIXS, XAS, XMCD, EXAFS, Mössbauer spectroscopy and DFT calculations. Through the strong hybridiza-

tion effects in $\text{La}(\text{Fe},\text{Si})_{13}$ -based compounds, the changes in the electronic structure, and thus the magnetism is significantly affected, which correlates to the vibrational behavior and thus, overall, to the thermodynamic performance of the material system.

Due to the combination of various complementary element-specific measurement techniques presented, this thesis shows the importance of understanding the single atomic contribution which partake in the first order phase transition, and thus, the magnetocaloric effect. This makes it possible to specifically tailor $\text{La}(\text{Fe},\text{Si})_{13}$ -based compounds to the application needs.

A. Appendix

A.1. Magnetometry

For a determination of the transition temperatures in the Mn doped sample series with a nominal stoichiometry of $\text{LaFe}_{11.6-x}\text{Si}_{1.4}\text{Mn}_x$, the $M(T)$ curves in an applied field of 50 mT have been normalized to the minimum and maximum value. The approximate transition temperature has been determined by taking the value of the heating branch in the middle of the hysteresis at 0.5, where also the width of the hysteresis has been estimated.

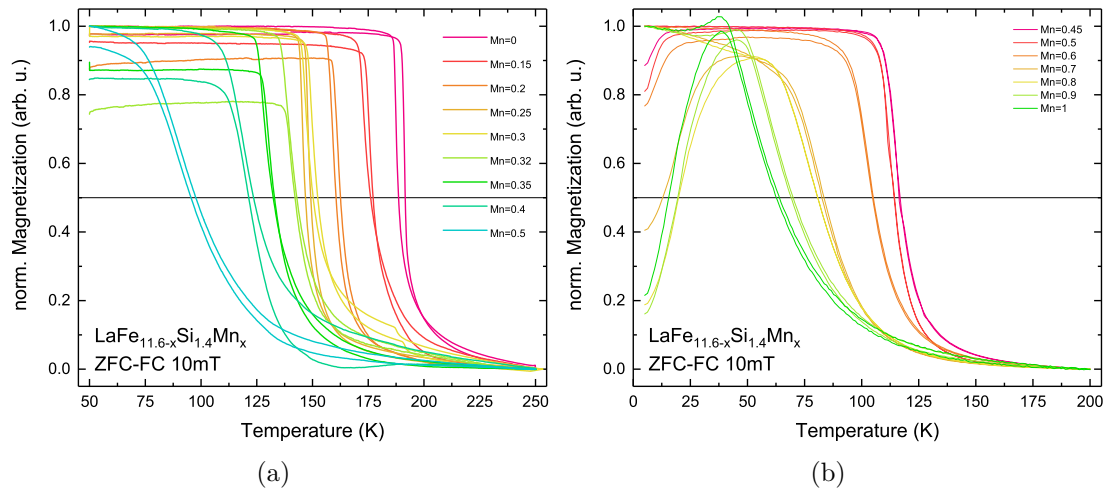


Figure A.1.: Temperature dependent magnetization measurement, normalized to minimal and maximum value in order to determine transition temperatures for the sample series with $\text{LaFe}_{11.6-x}\text{Si}_{1.4}\text{Mn}_x$ with Mn content of (a) $x = 0$ to 0.5 and (b) $x = 0.45$ to 1.

A.2. Determination of the α -Fe Content

As all the samples showed residual secondary phase contents, it was necessary to account for the α -Fe. Here, the high field quadrants of the field dependent magnetization curves at room temperature have been linearly fitted from 1 – 2 to 9 T, in order to extract the secondary phase content. The procedure has been done analogously as described in [127]. With the known value for the magnetization of α -Fe at room temperature of $218 \frac{\text{emu}}{\text{g}}$ and

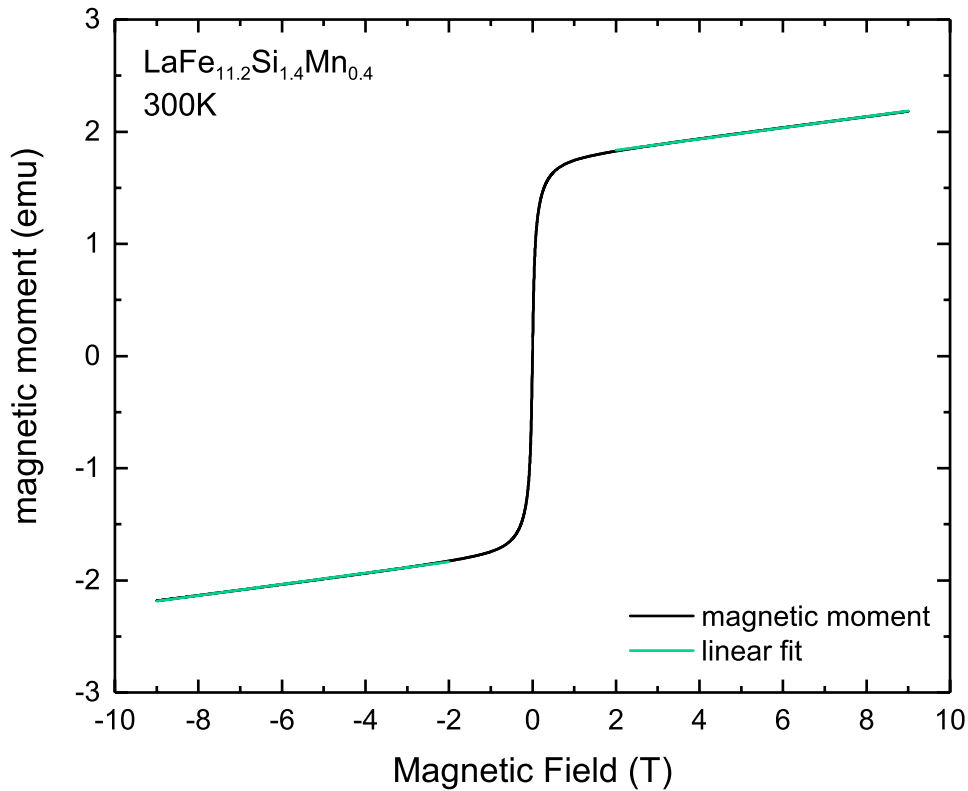


Figure A.2.: Linear fit to the field dependent magnetization curve of $\text{LaFe}_{11.2}\text{Si}_{1.4}\text{Mn}_{0.4}$ in a field range of $\pm(2 - 9)$ T to extract the residual α -Fe content.

the mass of the sample, the respective secondary phase content can be quantified using the value of the determined y-intercept of the linear fit.

A.3. Correction of the α -Fe Content at the Fe K-edge EXAFS

Using the extracted α -Fe contents, the NRIXS data as well as the Fe K-edge EXAFS have been corrected for the respective percentage of the secondary phase. To correct the EXAFS, the absorption spectra for *bcc*-Fe at 60 K (serving as a reference at the FM phase) and at 300 K (PM phase), have been normalized and scaled with the percentage of α -Fe content as found from magnetometry and then subtracted from the Fe K-edge spectra. The corrected spectra have then been renormalized. Figure A.3 shows the normalized $\mu(E)$ before (black line) and after (orange line) subtraction of the α -Fe content of 9.34 %.

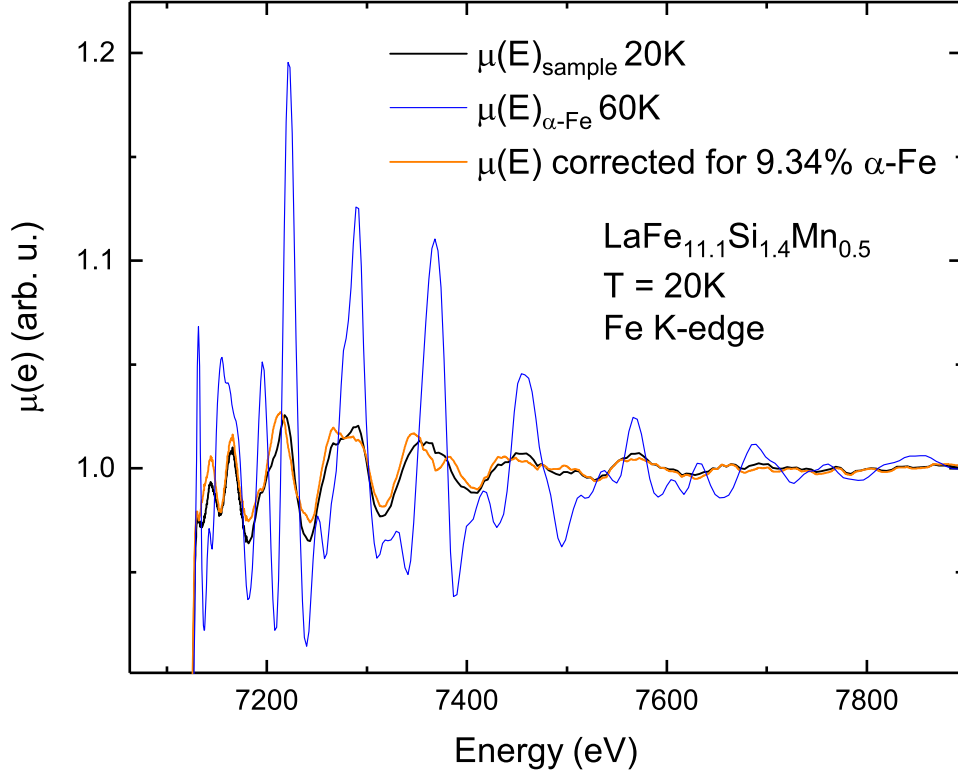


Figure A.3.: Correction of $\mu(E)$ (black line) with the respective α -Fe content of 9.34% (orange line) in $\text{LaFe}_{11.1}\text{Si}_{1.4}\text{Mn}_{0.5}$ as extracted from magnetometry. The blue line refers to the absorption of bcc -Fe at 60 K, which has been used as reference.

A.4. NRIXS - Data Evaluation

The vibrational density of states (VDOS) has been extracted from the raw data by utilizing the *Pi* program package [179]. In Figure A.4, the NRIXS spectra, the raw data, are shown at various temperature points exemplary for hydrogenated $\text{LaFe}_{11.4}\text{Si}_{1.6}\text{H}_{1.6}$. Figure A.5 shows the excitation probability per energy unit versus energy transfer E compared for different temperature points across the phase transition and separated into its phonon contributions per energy. The VDOS used for the evaluation and extraction of the thermodynamic properties directly relates to the single phonon contribution (red line). The elastic peak at 14.412 keV (width at bottom ~ 10 meV) has been removed from the spectra and the data from -5.5 to $+5.5$ meV have been parabolically fitted, thus this part does not give physically relevant information on the VDOS in this energy regime.

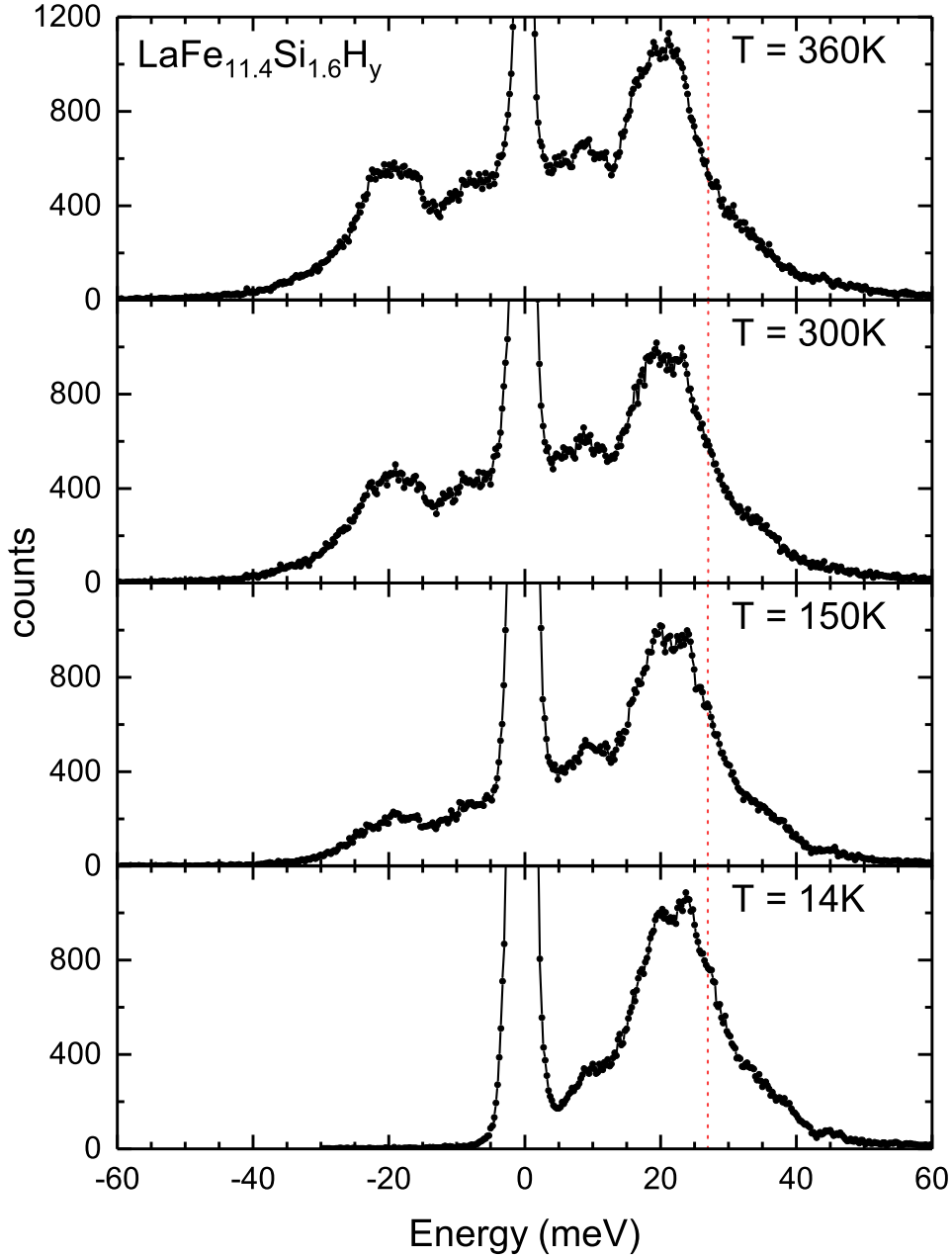


Figure A.4.: Typical ^{57}Fe NRIXS spectra (raw data) of the hydrogenated $\text{LaFe}_{11.4}\text{Si}_{1.6}\text{H}_{1.6}$ sample measured at three temperature points below ($T = 14\text{ K}$ bottom , $T = 150\text{ K}$, and $T = 300\text{ K}$) and at one point above the metamagnetic phase transition ($T = 360\text{ K}$, top) of $T_{\text{tr}} = 329\text{ K}$. The vertical red dotted line indicates the position of the phonon energy of 27 meV , where the main spectral feature in the VDOS (shoulder) disappears upon heating trough the phase transition from FM to PM. The VDOS was extracted using the Pi program [179]. The elastic peak (Mössbauer line) at $E = 0\text{ meV}$ was cut off for clarity.

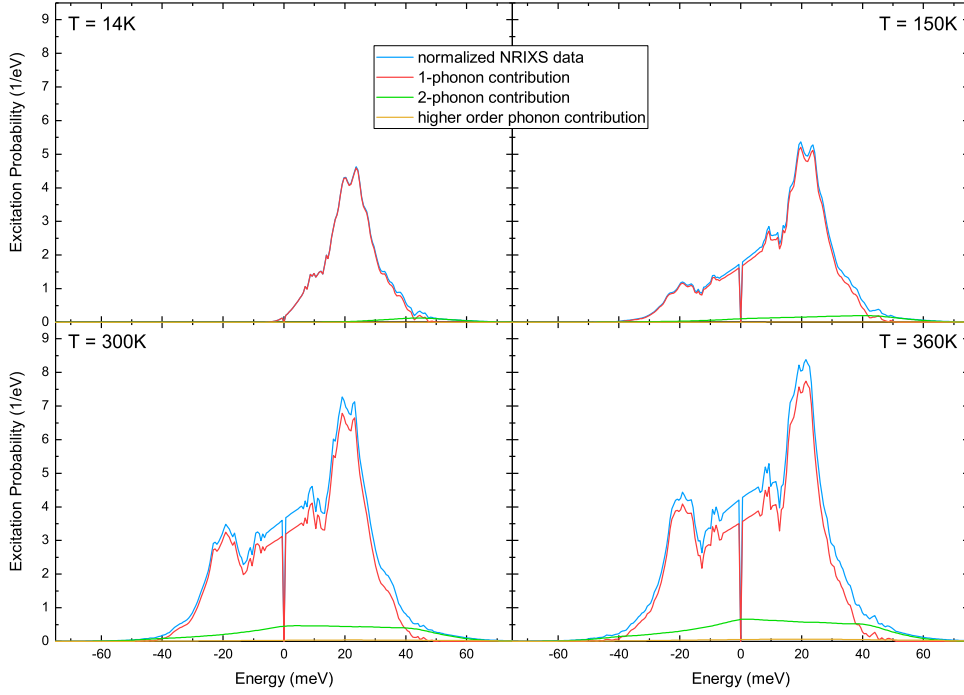


Figure A.5.: Phonon excitation probability versus energy transfer (blue line) of the polycrystalline $\text{LaFe}_{11.4}\text{Si}_{1.6}\text{H}_{1.6}$ sample, measured at: $T_{\text{exp}} = 14\text{ K}$, $T_{\text{exp}} = 150\text{ K}$, $T_{\text{exp}} = 300\text{ K}$ (RT) and $T_{\text{exp}} = 360\text{ K}$. Shown are the one-phonon (red line), two-phonon (green line) and higher order phonon (magenta line) contributions with the one-phonon contribution directly linked to the Fe-partial VDOS $g(E)$. The spectra have been extracted from the data using the Pi program [179]. With increasing temperature an increase of the integrated excitation probability is visible. Conversely, a decrease in multi-phonon excitations is apparent with decreasing temperature. The energy range E within $\pm 5.5\text{ meV}$ is physically not meaningful because of the uncertainty in subtraction of the elastic peak.

The extraction of the VDOS itself has been done with correction for respective α -Fe secondary phase contribution. The data, which has been used for the thermodynamic evaluation across the phase transition has also been corrected for the residual α -Fe content. For the correction bcc Fe-VDOS [180] has been subtracted from data obtained by Kresch et al. [181], which has been extrapolated to our measurement temperatures via the Grüneisen relation $\Delta E/E = -\Gamma\Delta V/V$ using the volume expansion $V(T)$ from Ref. [182] and a Grüneisen constant of $\Gamma = 1.66$ [135, 183]. Figure A.6 (a) shows the VDOS of bcc α -Fe at 360 K, which has been area normalized to the secondary phase content. This spectrum has then been subtracted from the normalized VDOS of the respective sample. Figure A.6 (b) depicts the corrected VDOS at a measurement temperature of 360 K. After subtraction of the secondary phase contents, the VDOS has been renormalized.

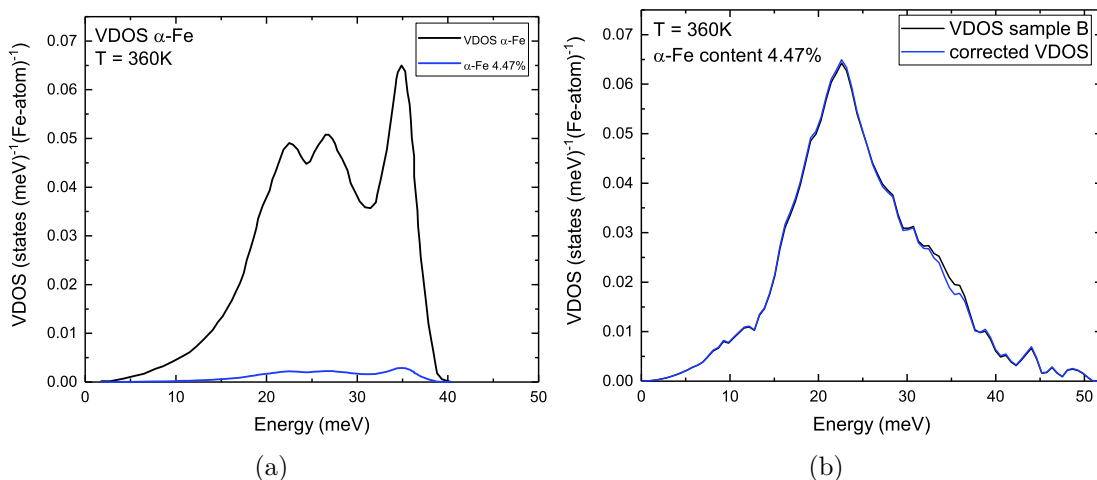


Figure A.6.: Example of the analysis of the experimental Fe-partial VDOS. (a) bcc α -Fe VDOS at 360 K (black curve) area-normalized to 1, and the VDOS corresponding to 4.47% secondary phase content in sample B as derived from magnetometry of α -Fe (blue curve). (b) Uncorrected VDOS (black curve) and VDOS after α -Fe correction and renormalization.

A.5. Thermodynamic Properties in Hydrogenated and Mn Doped La(Fe,Si)₁₃

The isothermal entropy change ΔS_{iso} has been obtained from temperature and field dependent, $M(H, T)$, magnetization measurements in order to be compared with the results from NRIXS. Here the hydrogenated $\text{LaFe}_{11.4}\text{Si}_{1.6}\text{H}_{1.6}$ was measured in a PPMS while being heated up from 300 to 364 K in steps of 2 K with applied magnetic fields from -0.5 to 2.1 T for each temperature and back, using a sweep rate of 50 Oe/s. From these $M(T, H)$ measurements the entropy change could be extracted. The value for ΔS_{iso} in a field of $\mu_0 H = 1.1$ T as corresponding to the field applied in the NRIXS measurements is $|\Delta S_{\text{iso}}| = 9.1 \pm 0.1 \frac{\text{J}}{\text{kgK}}$. Figure A.7 depicts the entropy change for various fields from 0.1 – 2 T with $|\Delta S_{\text{iso}}| = 12.5 \pm 0.1 \frac{\text{J}}{\text{kgK}}$ in $\mu_0 H = 2$ T.

All the Fe-specific thermodynamic properties as obtained from the VDOS are listed in Tables A.1, A.2 and A.3. The values for hydrogenated $\text{LaFe}_{11.4}\text{Si}_{1.6}\text{H}_{1.6}$ are listed in Table A.1, Mn doped and hydrogenated $\text{LaFe}_{11.4}\text{Si}_{1.5}\text{Mn}_{0.1}\text{H}_{1.6}$ in Table A.2, and Mn doped $\text{LaFe}_{11.4}\text{Si}_{1.5}\text{Mn}_{0.1}$ in Table A.3.

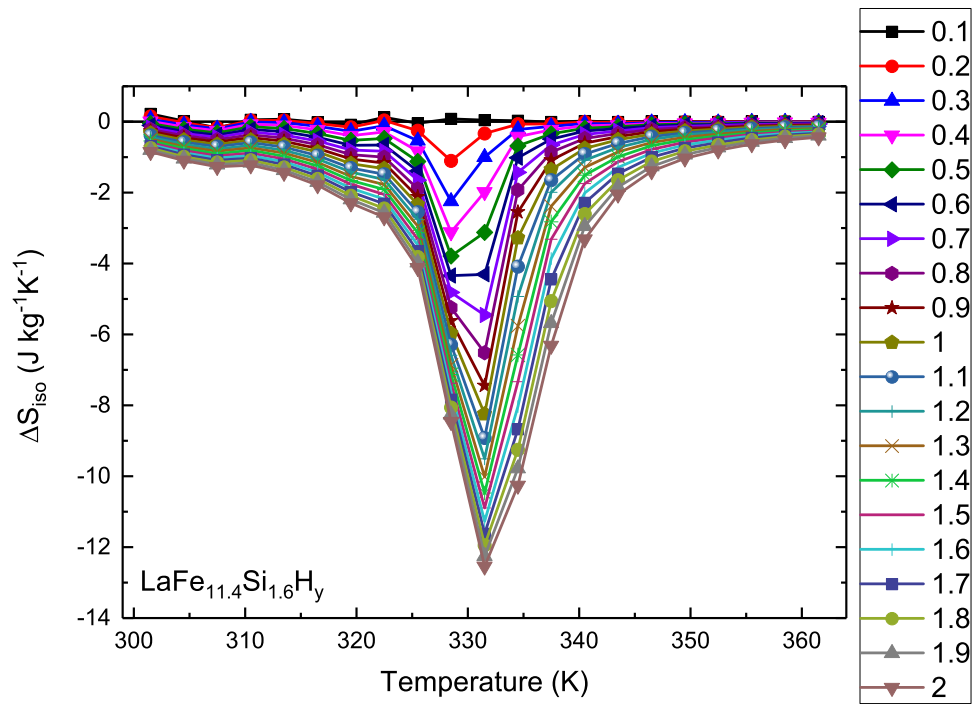


Figure A.7.: Entropy change in $\text{LaFe}_{11.4}\text{Si}_{1.6}\text{H}_{1.6}$ for various magnetic fields. Measurements of the entropy change are courtesy of Dr. I. Radulov, Functional Materials group, TU Darmstadt.

Fe-specific thermodynamic properties of LaFe _{11.4} Si _{1.6} H _{1.6}							
T [K]	S_{lat} [$\frac{\text{k}_B}{\text{Fe-atom}}$]	C_{lat} [$\frac{\text{k}_B}{\text{Fe-atom}}$]	f_{LM}	F_{vib} [$\frac{\text{meV}}{\text{Fe-atom}}$]	U_{vib} [$\frac{\text{meV}}{\text{Fe-atom}}$]	Φ_{kin} [$\frac{\text{N}}{\text{m}}$]	E_{kin} [$\frac{\text{meV}}{\text{Fe-atom}}$]
14	0.0034(2)	0.011(1)	0.9146(6)	37.8(3)	37.8(3)	118(1)	6.1(1)
150	1.63(1)	2.19(1)	0.85(1)	30.0(3)	51.1(3)	108(1)	8.3(1)
300	3.43(2)	2.77(2)	0.742(1)	-4.9(2)	83.9(5)	78(2)	13.6(1)
310	3.51(2)	2.78(2)	0.739(1)	-7.4(2)	86.3(5)	77(2)	13.9(1)
320	3.62(2)	2.79(2)	0.728(1)	-11.2(2)	88.6(5)	74(2)	14.3(1)
325	3.67(2)	2.80(2)	0.722(1)	-13.1(2)	89.8(6)	73(2)	14.5(1)
330	3.72(2)	2.81(2)	0.720(1)	-14.7(2)	91.0(6)	72(2)	14.7(1)
332	3.74(2)	2.81(2)	0.719(1)	-15.6(2)	91.5(6)	72(2)	14.8(1)
335	3.77(2)	2.81(2)	0.714(1)	-16.8(2)	92.2(6)	71(2)	14.9(1)
340	3.82(2)	2.82(2)	0.712(1)	-18.4(2)	93.4(6)	70(2)	5.1(1)
350	3.89(2)	2.83(2)	0.706(1)	-21.3(2)	95.6(5)	69(2)	15.5(1)
360	3.97(2)	2.84(2)	0.698(1)	-24.9(2)	98.3(6)	67(2)	15.8(1)

Table A.1.: Lattice contributions to the thermodynamics extracted from the VDOS $g(E)$ in hydrogenated LaFe_{11.4}Si_{1.6}H_{1.6} in 0 T, given are the obtained parameters for the lattice entropy S_{lat} , specific heat C_{lat} , the Lamb- Mössbauer factor f_{LM} , the free energy per atom F_{vib} , the inner energy U_{vib} , the average force constant Φ_{kin} and the mean kinetic energy E_{kin} . The temperature points below 300 K are from the beamtime in 2016, the others from 2017.

Fe-specific thermodynamic properties of LaFe _{11.4} Si _{1.5} Mn _{0.1} H _{1.6}									
T [K]	S_{lat} [$\frac{\text{k}_B}{\text{Fe-atom}}$]	C_{lat} [$\frac{\text{k}_B}{\text{Fe-atom}}$]	f_{LM}	$\Theta_{\text{DB}}(0)$ [K]	$\Theta_{\text{DB}}(2)$ [K]	F_{vib} [$\frac{\text{meV}}{\text{Fe-atom}}$]	U_{vib} [$\frac{\text{meV}}{\text{Fe-atom}}$]	Φ_{kin} [$\frac{\text{N}}{\text{m}}$]	E_{kin} [$\frac{\text{meV}}{\text{Fe-atom}}$]
14	0.0038(2)	0.0113(2)	0.914(1)	383(8)	393(2)	37.6(3)	37.6(3)	116(1)	6.10(4)
298	3.42(2)	2.76(2)	0.743(2)	377(1)	387(3)	-4.4(3)	83.4(6)	79(2)	13.5(1)
310	3.57(3)	2.79(3)	0.728(3)	371(1)	382(4)	-9.1(4)	86.1(8)	75(3)	13.9(1)
315	3.60(3)	2.79(3)	0.728(3)	373(1)	384(4)	-10.3(4)	87.4(9)	75(3)	14.1(1)
320	3.66(3)	2.80(2)	0.719(3)	372(1)	382(3)	-12.3(3)	88.5(8)	74(3)	14.3(1)
323	3.69(3)	2.80(2)	0.719(3)	371(1)	381(3)	-13.4(3)	89.2(8)	73(3)	14.4(1)
325	3.69(3)	2.80(2)	0.722(3)	373(1)	383(4)	-13.6(3)	89.7(9)	73(3)	14.5(1)
330	3.73(3)	2.81(3)	0.716(3)	373(1)	384(1)	-15.1(4)	91.0(9)	73(3)	14.7(1)
340	3.83(3)	2.82(2)	0.707(3)	372(1)	382(4)	-18.7(4)	93.4(9)	70(3)	15.1(1)
350	3.91(4)	2.83(2)	0.707(3)	371(1)	379(3)	-22.4(3)	95.7(8)	70(3)	15.5(1)

Table A.2.: Lattice contributions to the thermodynamics extracted from the VDOS $g(E)$ in hydrogenated and Mn doped LaFe_{11.4}Si_{1.5}Mn_{0.1}H_{1.6} in 0 T, given are the obtained parameters for the lattice entropy S_{lat} , specific heat C_{lat} , the Lamb- Mössbauer factor f_{LM} , the entropy Debye temperature $\Theta_{\text{DB}}(0)$, the specific heat Debye temperature $\Theta_{\text{DB}}(2)$, the free energy per atom F_{vib} , the inner energy U_{vib} , the average force constant Φ_{kin} and the mean kinetic energy E_{kin} .

Fe-specific thermodynamic of LaFe _{11.4} Si _{1.5} Mn _{0.1}									
T [K]	$S_{\text{lat}} [\frac{\text{k}_B}{\text{Fe-atom}}]$	$C_{\text{lat}} [\frac{\text{k}_B}{\text{Fe-atom}}]$	f_{LM}	$\Theta_{\text{DB}}(0)$ [K]	$\Theta_{\text{DB}}(2)$ [K]	$F_{\text{vib}} [\frac{\text{meV}}{\text{Fe-atom}}]$	$U_{\text{vib}} [\frac{\text{meV}}{\text{Fe-atom}}]$	$\Phi_{\text{kin}} [\frac{\text{N}}{\text{m}}]$	$E_{\text{kin}} [\frac{\text{meV}}{\text{Fe-atom}}]$
14	0.0069(1)	0.020(1)	0.909(1)	374(8)	390(2)	37.1(3)	37.1(3)	115(2)	6.0(1)
165	1.96(1)	2.34(2)	0.808(2)	368(2)	384(3)	25.6(3)	53.4(5)	101(2)	8.7(1)
170	2.04(1)	2.37(2)	0.802(2)	366(2)	382(2)	24.5(3)	54.3(4)	99(2)	8.9(1)
175	2.10(1)	2.40(1)	0.801(2)	368(2)	385(2)	23.9(3)	55.5(4)	100(2)	9.0(1)
180	2.18(1)	2.43(2)	0.799(2)	366(2)	381(3)	22.6(3)	56.4(5)	98(2)	9.2(1)
185	2.24(2)	2.45(2)	0.792(2)	368(2)	385(3)	21.9(3)	57.6(5)	99(2)	9.4(1)
190	2.31(2)	2.48(2)	0.787(2)	366(2)	382(3)	20.7(3)	58.6(5)	97(2)	9.5(1)
195	2.37(2)	2.50(2)	0.788(2)	367(2)	383(3)	19.9(3)	59.7(5)	96(2)	9.7(1)
298	3.51(2)	2.77(2)	0.702(2)	366(1)	382(3)	-6.8(3)	83.2(6)	77(2)	13.5(1)

Table A.3.: Lattice contributions to the thermodynamics extracted from the VDOS $g(E)$ in Mn doped LaFe_{11.4}Si_{1.5}Mn_{0.1} in 0 T, given are the obtained parameters for the lattice entropy S_{lat} , specific heat C_{lat} , the Lamb- Mössbauer factor f_{LM} , the entropy Debye temperature $\Theta_{\text{DB}}(0)$, the specific heat Debye temperature $\Theta_{\text{DB}}(2)$, the free energy per atom F_{vib} , the inner energy U_{vib} , the average force constant Φ_{kin} and the mean kinetic energy E_{kin} .

A.6. XMCD Background Correction

As a linear background subtraction was not sufficient enough to correct the XAS in the high temperature and high field spectra, a linear background has been subtracted from the derivative of the XAS, as to be seen in Figure A.8 in order to have the pre-edge and post-edge region parallel to each other.

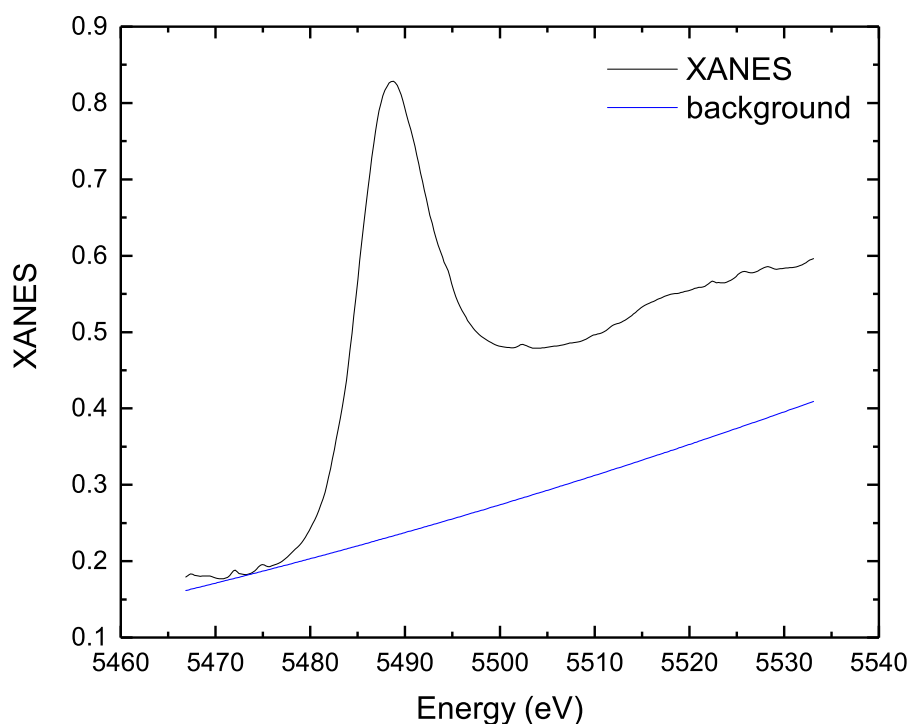
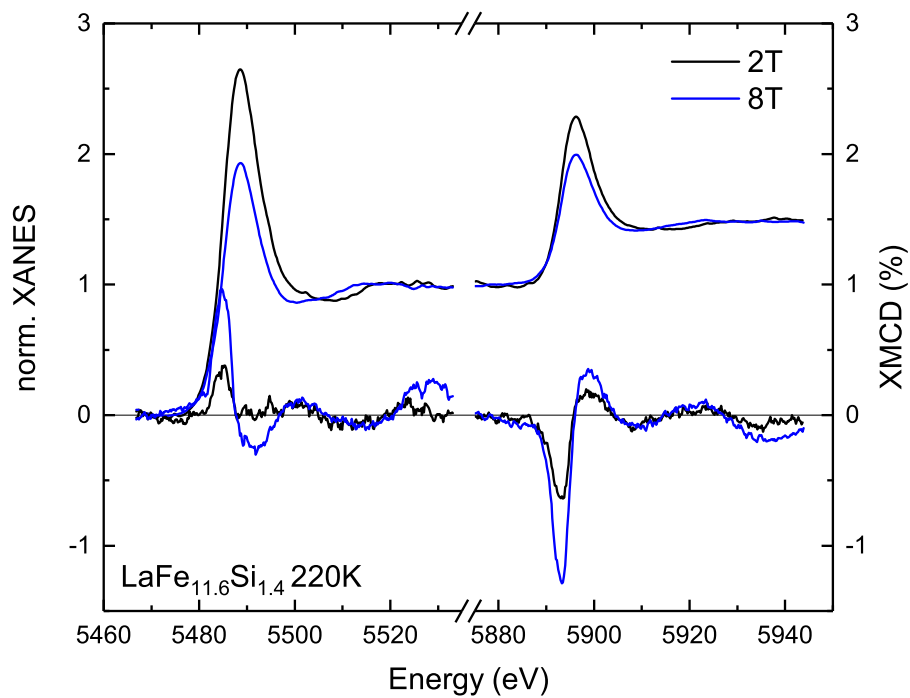


Figure A.8.: Example of the background subtraction from the high field XAS. Depicted is the La L_3 -edge of $\text{LaFe}_{11.6}\text{Si}_{1.4}$ at 220 K and 2 T. The black line is the measured XAS, the blue line refers to the background which has been subtracted from the XAS.

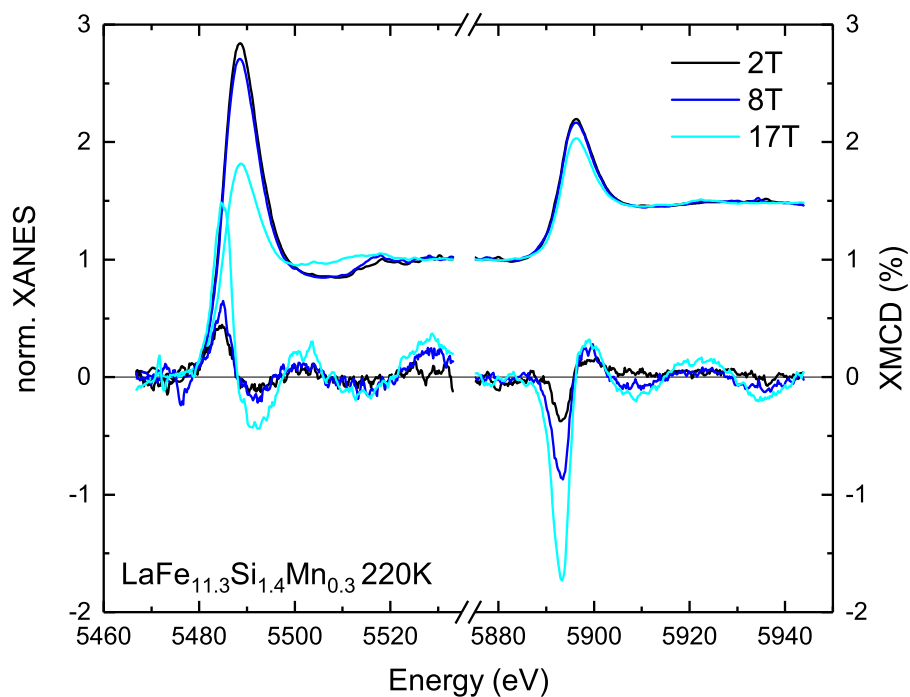
Figure A.9 shows the strong effect of background correction and change in the whiteline intensity for the two samples measured. It can be seen that a background correction results in unphysical large whiteline intensities, which makes it apparent that background correction should be used with caution.

A.7. Sum Rule Analysis of High Field XMCD

The sum rule analysis has been done only with the step function at the maximum of the XAS, as the evaluation in the FM phase showed the same development of the magnetic moments, regardless of the choice of the step function, which just gave an offset in the absolute value. The sum rule analysis has been performed with a quadratic background



(a)



(b)

Figure A.9.: XANES and XMCD of La(Fe,Si,Mn)₁₃ with an Mn content of (a) 0 and (b) 0.3, both taken above their respective phase transition temperature T_{tr} at 2 T at $T_{exp} = 220$ K with high applied magnetic fields.

correction as seen in section A.6. It has to be noted that the error in the sum rule analysis relies strongly on the background correction and therefore it is questionable whether a difference can be estimated between the two stoichiometries of $\text{LaFe}_{11.6}\text{Si}_{1.4}$ and $\text{LaFe}_{11.3}\text{Si}_{1.4}\text{Mn}_{0.3}$ due to the unphysical large whiteline intensities. Figure A.10 (a) depicts the extracted magnetic spin and orbital moments taken at 220 K. For a Mn content of 0 (black triangles), the magnetic spin moment is reduced from $-0.13 \mu_{\text{B}}$ in the FM phase at 2 T and 3 K down to $-0.024 \mu_{\text{B}}$ in the PM phase, still holding a residual magnetic spin moment (corresponding step function for the sum rule evaluation at maximum of XAS). The application of an external magnetic field of $\mu_0 H = 8 \text{ T}$, increases the induced magnetic spin moment from $-0.024 \mu_{\text{B}}$ by 30 % to $-0.073 \mu_{\text{B}}$. It can be seen that the value for the induced magnetic moment in the undoped compound is slightly bigger than the sample with a stoichiometry of $\text{LaFe}_{11.3}\text{Si}_{1.4}\text{Mn}_{0.3}$ (blue dots). The direct comparison of the spin magnetic moment from the FM to the PM phase for the Mn content of 0.3 also shows a reduction in the moment from $-0.1 \mu_{\text{B}}$ to only $-0.015 \mu_{\text{B}}$. Applying 8 T doubles the spin magnetic moment and is only an effect of the external field. The applied field of 17 T leads to an increase of the spin magnetic moment by 64 % to a value of $-0.095 \mu_{\text{B}}$. The light blue dot in Figure A.10 refers the measurement below the phase transition temperature of $\text{LaFe}_{11.3}\text{Si}_{1.4}\text{Mn}_{0.3}$ at $T_{\text{exp}} = 180 \text{ K}$ and shows that high fields can stabilize the ferromagnetic phase as the magnetic spin moment at 17 T at 220 K in the PM phase has the same value within the error. The orbital magnetic moment is depicted in Figure A.10 (b). Within the error, the orbital moment lies in the same range as in the FM state as seen for the complete sample series as discussed in section 5.2.3. The orbital moment is positive and has the opposite sign to the magnetic spin moment. The magnetic orbital moment of the undoped sample has a bigger absolute value than the sample with a Mn content of 0.3. Application of high magnetic fields seems to slightly increase the orbital moment, which is in accordance with a rise of the orbital moment when a ligand field and strong exchange splitting, as is the case for high applied magnetic fields, is present. Yet, within the error margin it is questionable to attribute this effect to possible orbital distortion, which could lead to an anisotropy in the orbital moment.

Induced moments of $\text{LaFe}_{11.6}\text{Si}_{1.4}$ and $\text{LaFe}_{11.3}\text{Si}_{1.4}\text{Mn}_{0.3}$ edge step at max XAS				
Mn_x	B [T]	T [K]	μ_s [μ_B]	μ_l [μ_B]
0	2	220	-0.024 ± 0.014	0.003 ± 0.002
	8		-0.073 ± 0.023	0.005 ± 0.011
0.3	2	180	-0.015 ± 0.033	-0.001 ± 0.002
	8		-0.029 ± 0.032	0.003 ± 0.004
	17		-0.095 ± 0.033	0.005 ± 0.009
	17		-0.096 ± 0.040	0.004 ± 0.008

Table A.4.: Magnetic spin and orbital moments extracted via sum rule analysis for the Mn doped sample series with the edge jump at the max XAS and a branching ratio of $\frac{1}{1.48}$.

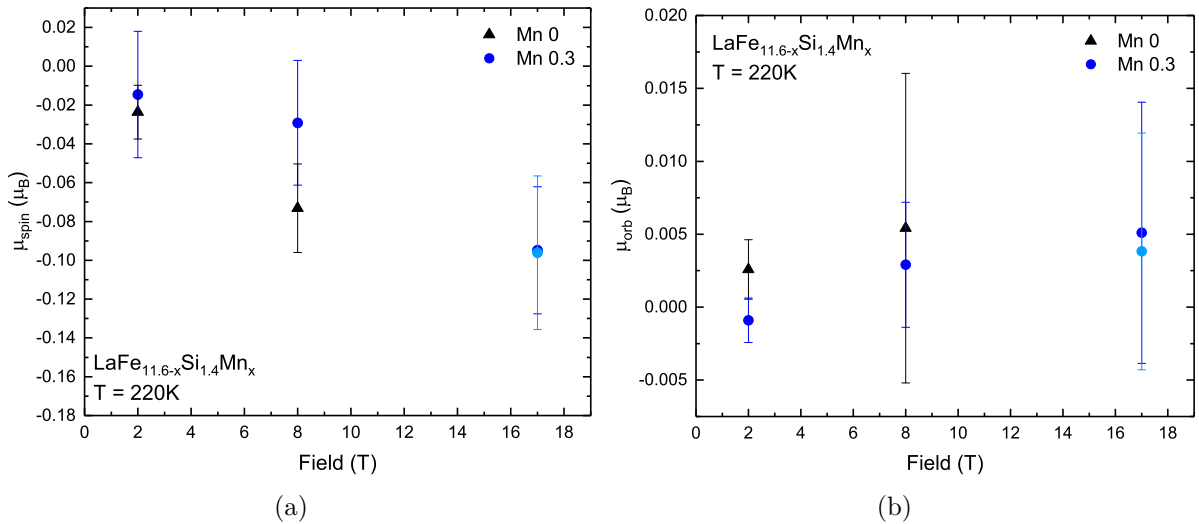


Figure A.10.: Induced magnetic moments in $\text{La}(\text{Fe},\text{Si},\text{Mn})_{13}$ with an Mn content of (a) 0 (black triangles) and (b) 0.3 (blue dots), both taken above their respective phase transition temperature T_{tr} at 2 T at $T_{exp} = 220$ K with various high applied magnetic fields. The light blue dot refers to a temperature of 180 K.

A.8. Canting Angle

As the relative spin orientation in the sample series can be extracted via two different methods, from the A_{23} line ratio, as described in section 2.5, and the law of cosines, both have been done for the Mn doped sample series. The law of cosines directly uses the hyperfine field parameters and the cosine relation for the spin canting. Using the

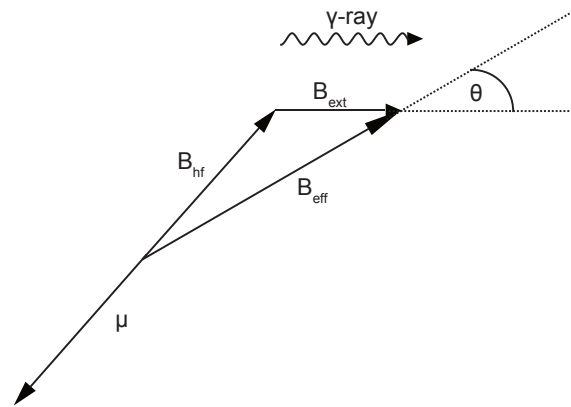


Figure A.11.: Schematic of the magnetic field relation in the Mössbauer measurement geometry. Depicted is the vector addition with the directions of the hyperfine magnetic field B_{hf} , the applied magnetic field B_{ext} and the respective effective hyperfine field B_{eff} as well as the resulting canting angle θ .

following equation for the canting angle θ :

$$B_{\text{eff}}^2 = B_{\text{hf}}^2 - B_{\text{ext}}^2 + 2B_{\text{ext}}B_{\text{hf}} \cos \theta, \quad \theta = \arccos \frac{B_{\text{eff}}^2 - B_{\text{hf}}^2 - B_{\text{ext}}^2}{2B_{\text{ext}}B_{\text{hf}}}, \quad (\text{A.1})$$

with the hyperfine magnetic field B_{hf} , the applied magnetic field B_{ext} and the respective effective hyperfine field B_{eff} and the canting angle θ . This evaluation holds various disadvantages in comparison to the evaluation via the A_{23} ratio. For the evaluation with the cosine relation sharp sextets are needed. The low temperature in-field spectra all showed a very broad hyperfine field distributions, which made it difficult to determine the right value for B_{hf} . Furthermore the effective field B_{eff} can be reduced by, for example, a demagnetization field within the sample. In case of a homogeneous disk (as is the case for the pressed powder samples used in the Mössbauer experiments, the reduction of the effective field would be in a range of a few hundred mT, increasing the spin canting angle artificially if the demagnetization effect is not taken into account at evaluation. Furthermore it is unclear whether the hyperfine field changes and the magnetic moment μ increases by the application of an external magnetic field as is the case for the split coil measurement geometry. From Figure A.12 it can be seen that the evaluation holds unphysical large values with big errors. Angles above the magic angle, which is defined as the angle where a random spin orientation is to be expected, show that the evaluation with the law of cosines yields wrong results. A full list of the angles obtained from the A_{23} line intensity ratio (which have been shown in subsection 5.4.3, Figure 5.61) can be found in Table A.5.

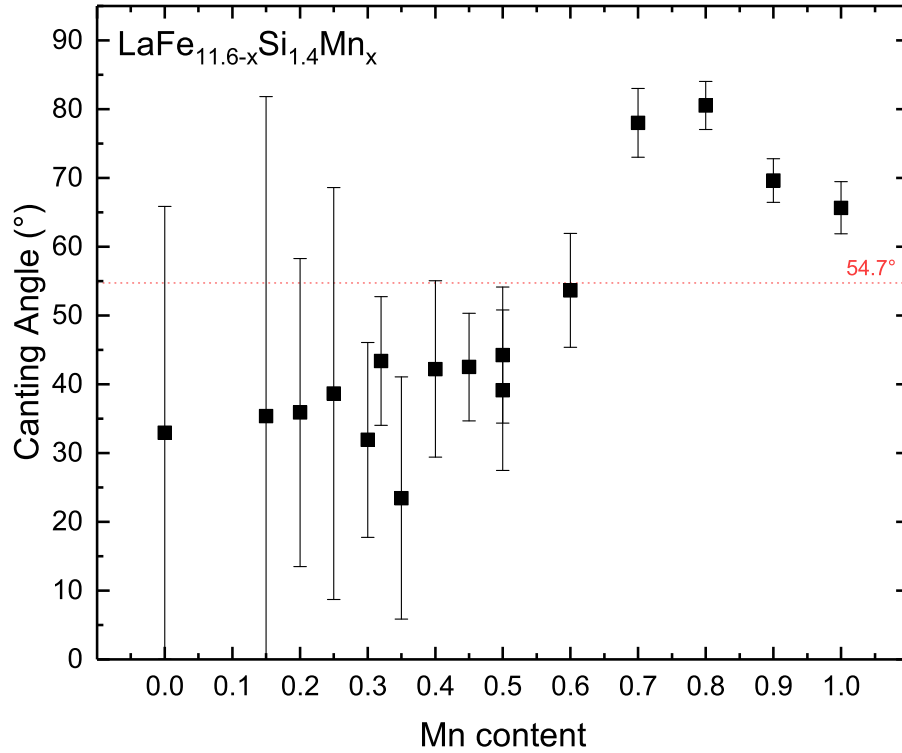


Figure A.12.: Spin canting angles obtained from law of cosines from low temperature measurements for Mn doped $\text{La}(\text{Fe}, \text{Si}, \text{Mn})_{13}$ for different Mn concentrations in an applied external magnetic field of 5 T. The red dashed line indicates the "magic angle" at ~ 55 degree, indicating random spin orientation.

Spin Canting Angles of $\text{LaFe}_{11.6-x}\text{Si}_{1.4}\text{Mn}_x$, extracted from the A_{23} -ratio			
Mn_x	Canting Angle θ [°]	θ_{\max} [°]	θ_{\min} [°]
0	0	11	0
0.15	8	13	0
0.2	0	21	0
0.25	0	24	0
0.3	0	17	0
0.32	15	20	8
0.35	0	13	0
0.4	13	25	0
0.5	0	19	0
0.45	0	9	0
0.5	0	8	0
0.6	10	15	0
0.7	27	35	15
0.8	11	27	0
0.9	37	42	30
1	46	52	39

Table A.5.: Spin canting angles calculated from the $A_{2,3}$ -ratio as obtained from the least square fits of the Mössbauer spectra at 5 K in 5 T.

A.9. Center Line Shift and Quadrupole Splitting

Center line shift and Quadrupole Splitting of $\text{LaFe}_{11.6-x}\text{Si}_{1.4}\text{Mn}_x$			
Mn_x	Subspectrum	ΔCS [mms^{-1}]	ΔE_Q [mms^{-1}]
0	Doublet (Fe_{II})	-0.050 ± 0.001	0.411 ± 0.003
	Singlet (Fe_{I})	-0.113 ± 0.007	
0.15	Doublet (Fe_{II})	-0.064 ± 0.001	0.480 ± 0.002
	Singlet (Fe_{I})	-0.105 ± 0.004	
0.2	Doublet (Fe_{II})	-0.070 ± 0.001	0.481 ± 0.002
	Singlet (Fe_{I})	-0.102 ± 0.006	
0.25	Doublet (Fe_{II})	-0.064 ± 0.001	0.451 ± 0.002
	Singlet (Fe_{I})	-0.113 ± 0.006	
0.3	Doublet (Fe_{II})	-0.071 ± 0.001	0.482 ± 0.003
	Singlet (Fe_{I})	-0.110 ± 0.006	
0.32	Doublet (Fe_{II})	-0.067 ± 0.001	0.456 ± 0.002
	Singlet (Fe_{I})	-0.121 ± 0.003	
0.35	Doublet (Fe_{II})	-0.071 ± 0.001	0.477 ± 0.003
	Singlet (Fe_{I})	-0.122 ± 0.007	
0.4	Doublet (Fe_{II})	-0.054 ± 0.003	0.406 ± 0.008
	Singlet (Fe_{I})	-0.161 ± 0.030	
0.5	Doublet (Fe_{II})	-0.060 ± 0.001	0.444 ± 0.002
	Singlet (Fe_{I})	-0.081 ± 0.005	
0.45	Doublet (Fe_{II})	-0.055 ± 0.001	0.460 ± 0.002
	Singlet (Fe_{I})	-0.109 ± 0.004	
0.5	Doublet (Fe_{II})	-0.059 ± 0.001	0.464 ± 0.001
	Singlet (Fe_{I})	-0.115 ± 0.003	
0.6	Doublet (Fe_{II})	-0.061 ± 0.001	0.462 ± 0.002
	Singlet (Fe_{I})	-0.105 ± 0.005	
0.7	Doublet (Fe_{II})	-0.060 ± 0.001	0.467 ± 0.002
	Singlet (Fe_{I})	-0.115 ± 0.005	
0.8	Doublet (Fe_{II})	-0.057 ± 0.001	0.460 ± 0.002
	Singlet (Fe_{I})	-0.111 ± 0.004	
0.9	Doublet (Fe_{II})	-0.059 ± 0.001	0.454 ± 0.002
	Singlet (Fe_{I})	-0.121 ± 0.004	
1	Doublet (Fe_{II})	-0.059 ± 0.001	0.454 ± 0.002
	Singlet (Fe_{I})	-0.121 ± 0.004	

Table A.6.: Obtained values for the center line shift ΔCS and the quadrupole splitting ΔE_Q in $\text{LaFe}_{11.6-x}\text{Si}_{1.6}\text{Mn}_x$ from room temperature measurements at 300 K, relative to $\alpha\text{-Fe}$.

A.10. FEFF Code

```

* This feff8 file was generated by Demeter 0.9.26
* Demeter written by and copyright (c) Bruce Ravel, 2006-2018
*-----*
* space = 1
* a = 8.08251 b = 8.08251 c = 8.08251
* alpha = 60.00000 beta = 60.00000 gamma = 60.00000
* rmax = 8.00000 core = La1
* polarization = 0 0 0
* shift = 0 0 0
* atoms
* # el. x y z tag
* La 0.75024 0.75024 0.75024 La1
* La 0.24895 0.24895 0.24895 La2
* Si 0.70760 0.06779 0.28892 Si1
* Si 0.28892 0.70760 0.06779 Si2
* Si 0.06779 0.28892 0.70760 Si3
* Fe 0.00038 0.00038 0.00038 FeI1
* Fe 0.50127 0.50127 0.50127 FeI2
* Fe 0.56470 0.20304 0.79529 FeII1
* Fe 0.79529 0.56470 0.20304 FeII2
* Fe 0.20304 0.79529 0.56470 FeII3
* Fe 0.06625 0.70175 0.93626 FeII4
* Fe 0.93626 0.06625 0.70175 FeII5
* Fe 0.70175 0.93626 0.06625 FeII6
* Fe 0.29157 0.93115 0.71206 FeII7
* Fe 0.71206 0.29157 0.93115 FeII8
* Fe 0.93115 0.71206 0.29157 FeII9
* Fe 0.93266 0.30041 0.06427 FeII10
* Fe 0.06427 0.93266 0.30041 FeII11
* Fe 0.30041 0.06427 0.93266 FeII12
* Fe 0.43403 0.79532 0.20484 FeII13
* Fe 0.20484 0.43403 0.79532 FeII14
* Fe 0.79532 0.20484 0.43403 FeII15
* Fe 0.80405 0.43970 0.55997 FeII16
* Fe 0.55997 0.80405 0.43970 FeII17
* Fe 0.43970 0.55997 0.80405 FeII18
* Fe 0.19884 0.55781 0.44087 FeII19
* Fe 0.44087 0.19884 0.55781 FeII20
* Fe 0.55781 0.44087 0.19884 FeII21
*-----*
* total mu*x=1: 7.294 microns, unit edge step: 24.743 microns
* specific gravity: 7.324
*-----*
* normalization correction: 0.00072 ang^2
*-----*
* La L3 edge energy = 5483 eV
EDGE L3
S02 0.85

* pot xsph fms paths genfmt ff2chi
CONTROL 0 1 1 1 1 1

PRINT 1 0 0 0 3

* ixc [ Vr Vi ] *** ixc=0 means to use Hedin-Lundqvist
EXCHANGE 0 0 0 0 -1
*** Radius for self-consistent pots (2 shells is a good choice)
* r_scf [ l_scf n_scf ca ] *** l_scf = 0 for a solid, 1 for a molecule
SCF 6 0 100 0.2 1
* kmax [ delta_k delta_e ] *** Upper limit of XANES calculation.
* XANES 4.0
* r_fms l_fms *** Radius for Full Mult. Scatt. l_fms = 0 for a solid, 1 for a molecule
* FMS 24.09799 0
* emin emax eimag *** Energy grid over which to calculate DOS functions
* LDOS -30 20 0.1
*** for EXAFS: RPATH 6.0 and uncomment the EXAFS card
* POLARIZATION 0 0 0
COREHOLE FSR
DEBYE 20 370 0
SIG2 0.002

RMULTIPLIER 1.003

EXAFS 12.0

RPATH 6.0
POTENTIALS
0 57 La 3 3 0.0010
1 57 La 3 3 2.0
2 14 Si 2 2 3.0
3 26 Fe 2 2 23.0

ATOMS
0.00000 0.00000 0.00000 0 La1 0.00000
0.35510 -3.06144 -1.20629 3 FeII16.1 3.30963
-1.25567 -1.58901 -2.61763 3 FeII17.1 3.30963
-2.04937 -2.57540 -0.34792 3 FeII18.1 3.30963
1.20300 -1.62954 2.62366 3 FeII10.1 3.31484
-2.96859 1.45739 0.22727 3 FeII12.1 3.31484
2.07235 0.92551 -2.41598 3 FeII11.1 3.31484

```

Figure A.13.: Example for an *FEFF* input file *feff.inp* used for the *ab-initio* calculations of the EXAFS at the La L_2 -edge, created using *Atoms* [163] with a magnetic relaxed structure provided by M. E. Gruner. The complete list of next neighbor distances has been cut off after 7 atoms.

Bibliography

- [1] International Energy Agency - The Future of Cooling Opportunities for energy-efficient air conditioning (2018).
- [2] M. Isaac and D. P. van Vuuren, *Energy Policy* **37**, 507 (2009).
- [3] International Institute of Refrigeration, 29th Informatory Note on Refrigeration Technologies (2015).
- [4] S. Fähler, U. K. Röbber, O. Kastner, J. Eckert, G. Eggeler, H. Emmerich, P. Entel, S. Müller, E. Quandt, and K. Albe, *Advanced Energy Materials* **14**, 10 (2012).
- [5] X. Moya, S. Kar-Narayan, and N. D. Mathur, *Nature Materials* **13**, 439 (2014).
- [6] C. Zimm, A. Jastrab, A. Sternberg, V. Pecharsky, K. Gschneidner, M. Osborne, and I. Anderson, in *Advances in Cryogenic Engineering* (Springer US, 1998) pp. 1759–1766.
- [7] V. K. Pecharsky and K. A. Gschneidner, *Physical Review Letters* **78**, 4494 (1997).
- [8] K. A. Gschneidner Jr. and V. K. Pecharsky, *Annual Review of Material Science* **30**, 387 (2000).
- [9] K. A. Gschneidner Jr., V. K. Pecharsky, and A. O. Tsokol, *Reports on Progress in Physics* **68**, 1479 (2005).
- [10] N. H. Dung, Z. Q. Ou, L. Caron, L. Zhang, D. T. C. Than, G. A. de Wijs, R. A. de Groot, K. H. J. Buschow, and E. Brück, *Advanced Energy Materials* **1**, 1215 (2011).
- [11] M. F. J. Boeijs, P. Roy, F. Guillou, H. Yibole, X. Miao, L. Caron, D. Banerjee, N. H. van Dijk, R. A. de Groot, and E. Brück, *Chemistry of Materials* **28**, 4901 (2016).
- [12] A. Waske, M. E. Gruner, T. Gottschall, and O. Gutfleisch, *MRS Bulletin* **43**, 269 (2018).

- [13] A. Waske, D. Dzekan, K. Sellschopp, D. Berger, A. Stork, K. Nielsch, and S. Fähler, *Nature Energy* **4**, 68 (2018).
- [14] M. Krautz, M. Beyer, C. Jäschke, L. Schinke, A. Waske, and J. Seifert, *Crystals* **9**, 76 (2019).
- [15] F. Scheibel, T. Gottschall, A. Taubel, M. Fries, K. P. Skokov, A. Terwey, W. Keune, K. Ollefs, H. Wende, M. Farle, M. Acet, O. Gutfleisch, and M. E. Gruner, *Energy Technology* **6**, 1397 (2018).
- [16] P. Weiss and A. Piccard, *Journal de Physique Théorique et Appliquée* **7**, 103 (1917).
- [17] W. F. Giauque, *Journal of the American Chemical Society* **49**, 1864 (1927).
- [18] W. F. Giauque and D. P. MacDougall, *Physical Review* **43**, 768 (1933).
- [19] <https://www.basf.com/global/en/media/news-releases/2015/01/p-15-100.html> last accessed 18.02.2019.
- [20] <https://www.vacuumschmelze.com/en/products/permanent-magnets-assemblies/magnetocaloric-materials.html> last accessed on 28.02.2019.
- [21] K. G. Sandeman, *Scripta Materialia* **67**, 566 (2012).
- [22] J. Lyubina, R. Schäfer, N. Martin, L. Schultz, and O. Gutfleisch, *Advanced Materials* **22**, 3735 (2010).
- [23] S. Fujieda, A. Fujita, and K. Fukamichi, *Applied Physics Letters* **81**, 1276 (2002).
- [24] S. Fujieda, A. Fujita, K. Fukamichi, Y. Yamazaki, and Y. Iijima, *Applied Physics Letters* **79**, 653 (2001).
- [25] F. Hu, M. Ilyn, A. M. Tishin, J. R. Sun, G. J. Wang, Y. F. Chen, F. Wang, Z. H. Cheng, and B. G. Shen, *Journal of Applied Physics* **93**, 5503 (2003).
- [26] A. M. Tishin and Y. I. Spichkin, *The Magnetocaloric Effect and its Applications* (Institute of Physics Publishing, 2003).
- [27] O. Gutfleisch, M. A. Willard, E. Brück, C. H. Chen, S. G. Sankar, and J. P. Liu, *Advanced Materials* **23**, 821 (2011).
- [28] A. Fujita, Y. Akamatsu, and K. Fukamichi, *Journal of Applied Physics* **85**, 4756 (1999).
- [29] O. Tegus, E. Brück, K. H. J. Buschow, and F. R. de Boer, *Nature* **415**, 150 (2002).

-
- [30] H. S. J. Stöhr, *Magnetism, From Fundamentals to Nanoscale Dynamics* (Springer, 2006).
- [31] O. Gutfleisch, T. Gottschall, M. Fries, D. Benke, I. Radulov, K. P. Skokov, H. Wende, M. Gruner, M. Acet, P. Entel, and M. Farle, *Philosophical Transactions of the Royal Society A: Mathematical, Physical and Engineering Sciences* **374**, 20150308 (2016).
- [32] T. Gottschall, *On the magnetocaloric properties of Heusler compounds: Reversible, time- and size-dependent effects of the martensitic phase transition*, Ph.D. thesis, Technische Universität Darmstadt (2017).
- [33] K. A. Gschneidner and V. K. Pecharsky, *Journal of Applied Physics* **85**, 5365 (1999).
- [34] M. Gruner, W. Keune, B. R. Cuenya, C. Weis, J. Landers, S. Makarov, D. Klar, M. Hu, E. Alp, J. Zhao, M. Krautz, O. Gutfleisch, and H. Wende, *Physical Review Letters* **114** (2015).
- [35] M. E. Gruner, W. Keune, J. Landers, S. Salamon, M. Krautz, J. Zhao, M. Y. Hu, T. Toellner, E. E. Alp, O. Gutfleisch, and H. Wende, *physica status solidi (b)* **255**, 1700465 (2018).
- [36] A. Fujita, S. Fujieda, Y. Hasegawa, and K. Fukamichi, *Physical Review B* **67** (2003).
- [37] Z. Gercsi, N. Fuller, K. G. Sandeman, and A. Fujita, *Journal of Physics D: Applied Physics* **51**, 034003 (2018).
- [38] C. P. Opeil, B. Mihaila, R. K. Schulze, L. Mañosa, A. Planes, W. L. Hults, R. A. Fisher, P. S. Riseborough, P. B. Littlewood, J. L. Smith, and J. C. Lashley, *Physical Review Letters* **100** (2008).
- [39] H. Wende, *Reports on Progress in Physics* **67**, 2105 (2004).
- [40] H. J. Elmers, “Element-specific magnetic and electronic properties of epitaxial heusler films-heusler alloys,” (Springer Series in Materials Science, 2016).
- [41] A. Rogalev, K. Ollefs, and F. Wilhelm, in *X-Ray Absorption and X-Ray Emission Spectroscopy* (John Wiley & Sons, Ltd, 2016) pp. 671–694.
- [42] G. van der Laan and A. I. Figueroa, *Coordination Chemistry Reviews* **277-278**, 95 (2014).

- [43] S. Ener, J. Neuhaus, W. Petry, R. Mole, K. Hradil, M. Siewert, M. E. Gruner, P. Entel, I. Titov, and M. Acet, *Physical Review B* **86** (2012).
- [44] P. J. Stonaha, M. E. Manley, N. M. Bruno, I. Karaman, R. Arroyave, N. Singh, D. L. Abernathy, and S. Chi, *Physical Review B* **92** (2015).
- [45] W. Sturhahn, *Journal of Physics: Condensed Matter* **16**, S497 (2004).
- [46] M. Wolloch, M. E. Gruner, W. Keune, P. Mohn, J. Redinger, F. Hofer, D. Suess, R. Podloucky, J. Landers, S. Salamon, F. Scheibel, D. Spoddig, R. Witte, B. R. Cuenya, O. Gutfleisch, M. Y. Hu, J. Zhao, T. Toellner, E. E. Alp, M. Siewert, P. Entel, R. Pentcheva, and H. Wende, *Physical Review B* **94** (2016).
- [47] J. Landers, S. Salamon, W. Keune, M. E. Gruner, M. Krautz, J. Zhao, M. Y. Hu, T. Toellner, E. E. Alp, O. Gutfleisch, and H. Wende, *Physical Review B* **98**, 024417 (2018).
- [48] C. Kittel, *Introduction to Solid State Physics*, 5th ed. (John Wiley & Sons, New York, London, Sidney, Toronto, 1976) p. 152.
- [49] P. I. Kryptiakewytsch, O. S. Zaretschniuk, E. I. Hladyschewskyj, and O. I. Bodak, *Zeitschrift für anorganische und allgemeine Chemie* **358**, 90 (1968).
- [50] T. Palstra, J. Mydosh, G. Nieuwenhuys, A. van der Kraan, and K. Buschow, *Journal of Magnetism and Magnetic Materials* **36**, 290 (1983).
- [51] R. B. Helmholdt, T. T. M. Palstra, G. J. Nieuwenhuys, J. A. Mydosh, A. M. van der Kraan, and K. H. J. Buschow, *Physical Review B* **34**, 169 (1986).
- [52] H. Hamdeh, H. Al-Ghanem, W. Hikal, S. Taher, J. Ho, D. Anh, N. Thuy, N. Duc, and P. Thang, *Journal of Magnetism and Magnetic Materials* **269**, 404 (2004).
- [53] M. Rosca, M. Balli, D. Fruchart, D. Gignoux, E. Hlil, S. Miraglia, B. Ouladdiaf, and P. Wolfers, *Journal of Alloys and Compounds* **490**, 50 (2010).
- [54] J. Lyubina, *Journal of Applied Physics* **109**, 07A902 (2011).
- [55] F. Hu, B. Shen, J. Sun, Z. Cheng, G. Rao, and X. Zhang, *Applied Physics Letters* **78**, 3675 (2001).
- [56] A. Fujita, S. Fujieda, K. Fukamichi, H. Mitamura, and T. Goto, *Physical Review B* **65** (2001).
- [57] M. D. Kuz'min and M. Richter, *Physical Review B* **76** (2007).

-
- [58] M. Phejar, V. Paul-Boncour, and L. Bessais, *Intermetallics* **18**, 2301 (2010).
- [59] V. H. Vuong, K. A. D. Thi, K. T. Nguyen, V. H. Le, and N. N. Hoang, *Journal of Applied Physics* **120**, 142120 (2016).
- [60] L. Jia, G. J. Liu, J. R. Sun, H. W. Zhang, F. X. Hu, C. Dong, G. H. Rao, and B. G. Shen, *Journal of Applied Physics* **100**, 123904 (2006).
- [61] J. Y. Law, V. Franco, L. M. Moreno-Ramírez, A. Conde, D. Y. Karpenkov, I. Radulov, K. P. Skokov, and O. Gutfleisch, *Nature Communications* **9** (2018).
- [62] G.-J. Wang, F. Wang, N.-L. Di, B.-G. Shen, and Z.-H. Cheng, *Journal of Magnetism and Magnetic Materials* **303**, 84 (2006).
- [63] W. Fang, C. Yuan-Fu, W. Guang-Jun, S. Ji-Rong, and S. Bao-Gen, *Chinese Physics* **12**, 911 (2003).
- [64] A. Barcza, M. Katter, V. Zellmann, S. Russek, S. Jacobs, and C. Zimm, *IEEE Transactions on Magnetics* **47**, 3391 (2011).
- [65] L. Jia, J. Sun, J. Shen, B. Gao, T. Zhao, H. Zhang, F. Hu, and B. Shen, *Journal of Alloys and Compounds* **509**, 5804 (2011).
- [66] K. Irisawa, A. Fujita, K. Fukamichi, Y. Yamazaki, Y. Iijima, and E. Matsubara, *Journal of Alloys and Compounds* **316**, 70 (2001).
- [67] S. Fujieda, A. Fujita, K. Fukamichi, Y. Yamaguchi, and K. Ohoyama, *Journal of the Physical Society of Japan* **77**, 074722 (2008).
- [68] M. Krautz, K. Skokov, T. Gottschall, C. S. Teixeira, A. Waske, J. Liu, L. Schultz, and O. Gutfleisch, *Journal of Alloys and Compounds* **598**, 27 (2014).
- [69] J. Lyubina, K. Nenkov, L. Schultz, and O. Gutfleisch, *Physical Review Letters* **101** (2008).
- [70] H. N. Bez, B. G. Eggert, J. A. Lozano, C. R. Bahl, J. R. Barbosa, C. S. Teixeira, and P. A. Wendhausen, *Journal of Magnetism and Magnetic Materials* **386**, 125 (2015).
- [71] X. Hai, C. Mayer, C. V. Colin, and S. Miraglia, *Journal of Magnetism and Magnetic Materials* **400**, 344 (2016).
- [72] J. Wang, Y. Chen, Y. Tang, S. Xiao, T. Liu, and E. Zhang, *Journal of Alloys and Compounds* **485**, 313 (2009).

- [73] M. Phejar, V. Paul-Boncour, and L. Bessais, *Journal of Solid State Chemistry* **233**, 95 (2016).
- [74] S. Rundqvist, R. Tellgren, and Y. Andersson, *Journal of the Less Common Metals* **101**, 145 (1984).
- [75] D. Westlake, *Journal of the Less Common Metals* **90**, 251 (1983).
- [76] X. Hai, F. Porcher, C. Mayer, and S. Miraglia, *Journal of Applied Physics* **123**, 085115 (2018).
- [77] Private communication with PD. Dr. M. E. Gruner.
- [78] M. Krautz, J. D. Moore, K. P. Skokov, J. Liu, C. S. Teixeira, R. Schäfer, L. Schultz, and O. Gutfleisch, *Journal of Applied Physics* **112**, 083918 (2012).
- [79] M. Bratko, E. Lovell, A. D. Caplin, V. Basso, A. Barcza, M. Katter, and L. F. Cohen, *Physical Review B* **95** (2017).
- [80] O. L. Baumfeld, Z. Gercsi, M. Krautz, O. Gutfleisch, and K. G. Sandeman, *Journal of Applied Physics* **115** (2014).
- [81] B. K. Teo, *EXAFS: Basic Principles and Data Analysis* (Springer Verlag, 1986).
- [82] J. L. Erskine and E. A. Stern, *Physical Review B* **12**, 5016 (1975).
- [83] G. Schütz, W. Wagner, W. Wilhelm, P. Kienle, R. Zeller, R. Frahm, and G. Materlik, *Physical Review Letters* **58**, 737 (1987).
- [84] J. Igarashi and M. Takahashi, *Physica Scripta* **72**, CC1 (2005).
- [85] S. W. Lovesey, *Journal of Physics: Condensed Matter* **10** (1998).
- [86] G. Dräger, R. Frahm, G. Materlik, and O. Brümmer, *physica status solidi (b)* **146**, 287 (1988).
- [87] T. E. Westre, P. Kennepohl, J. G. DeWitt, B. Hedman, K. O. Hodgson, and E. I. Solomon, *Journal of the American Chemical Society* **119**, 6297 (1997).
- [88] P. Glatzel, M. Sikora, and M. Fernández-García, *The European Physical Journal Special Topics* **169**, 207 (2009).
- [89] S. D. George, T. Petrenko, and F. Neese, *The Journal of Physical Chemistry A* **112**, 12936 (2008).

-
- [90] P. Carra and M. Altarelli, *Physical Review Letters* **64**, 1286 (1990).
- [91] C. Giorgetti, E. Dartyge, C. Brouder, F. Baudelet, C. Meyer, S. Pizzini, A. Fontaine, and R.-M. Galéra, *Physical Review Letters* **75**, 3186 (1995).
- [92] J. Chaboy, F. Bartolomé, L. M. García, and G. Cibin, *Physical Review B* **57**, R5598 (1998).
- [93] B. T. Thole, P. Carra, F. Sette, and G. van der Laan, *Physical Review Letters* **68**, 1943 (1992).
- [94] P. Carra, B. T. Thole, M. Altarelli, and X. Wang, *Physical Review Letters* **70**, 694 (1993).
- [95] C. T. Chen, Y. U. Idzerda, H.-J. Lin, N. V. Smith, G. Meigs, E. Chaban, G. H. Ho, E. Pellegrin, and F. Sette, *Physical Review Letters* **75**, 152 (1995).
- [96] J. Stöhr and H. König, *Physical Review Letters* **75**, 3748 (1995).
- [97] E. Beaurepaire, F. Scheurer, G. Krill, and J.-P. Kappler, eds., *Magnetism and Synchrotron Radiation* (Springer, 2010).
- [98] M. Newville, *Reviews in Mineralogy and Geochemistry* **78**, 33 (2014).
- [99] K. B. A. Vertés, L. Korecz, *Mössbauer Spectroscopy* (Elsevier Scientific Publishing, 1979).
- [100] R. L. Mössbauer, *Zeitschrift für Physik* **151**, 124 (1958).
- [101] W. M. Visscher, *Annals of Physics* **9**, 194 (1960).
- [102] H. J. Lipkin, *Annals of Physics* **9**, 332 (1960).
- [103] D. Barb, *Grundlagen und Anwendungen der Mössbauerspektroskopie* (Akademie-Verlag Berlin, 1980).
- [104] J. Landers, *Study of magnetic relaxation dynamics in soft matter nanoparticle composite systems*, Ph.D. thesis, Universität Duisburg-Essen (2016).
- [105] N. N. Greenwood and T. C. Gibb (Chapman and Hall Ltd, 1971) pp. 633–707.
- [106] Y.-L. Chen and D.-P. Yang, *Mössbauer Effect in Lattice Dynamics* (Wiley-VHC Verlag GmbH & Co. KGaA, 2007).

- [107] W. Sturhahn, T. S. Toellner, E. E. Alp, X. Zhang, M. Ando, Y. Yoda, S. Kikuta, M. Seto, C. W. Kimball, and B. Dabrowski, *Physical Review Letters* **74**, 3832 (1995).
- [108] A. Chumakov and W. Sturhahn, *Hyperfine Interactions* **123/124**, 781 (1999).
- [109] R. Röhlberger, *Nuclear Condensed Matter Physics with Synchrotron Radiation* (Springer Berlin Heidelberg, 2004).
- [110] M. Y. Hu, T. S. Toellner, N. Dauphas, E. E. Alp, and J. Zhao, *Physical Review B* **87** (2013).
- [111] K. S. Singwi and A. Sjölander, *Physical Review* **120**, 1093 (1960).
- [112] A. I. Chumakov, R. Rüffer, H. Grünsteudel, H. F. Grünsteudel, G. Grübel, J. Metge, O. Leupold, and H. A. Goodwin, *Europhysics Letters* **30** (1995).
- [113] M. Seto, Y. Yoda, S. Kikuta, X. W. Zhang, and M. Ando, *Physical Review Letters* **74**, 3828 (1995).
- [114] G. Grimvall, *Thermophysical Properties of Materials*, Selected Topics in Solid State Physics, Vol. 18 (North-Holland, Amsterdam, 1986).
- [115] J. Rosén and G. Grimvall, *Physical Review B* **27**, 7199 (1983).
- [116] O. Eriksson, J. M. Wills, and D. Wallace, *Physical Review B* **46**, 5221 (1992).
- [117] <https://www.esrf.eu/home/UsersAndScience/Accelerators/parameters.html> last accessed on 24.12.2018.
- [118] <https://www.aps.anl.gov/Beamline-Selection/Technical-Information/Storage-Ring-Parameters> last accessed on 24.12.2018.
- [119] A. Rogalev, J. Goulon, C. Goulon-Ginet, and C. Malgrange, in *Magnetism and Synchrotron Radiation* (Springer Berlin Heidelberg, 2001) pp. 60–86.
- [120] A. Rogalev and F. Wilhelm, *Synchrotron Radiation News* **26**, 33 (2013).
- [121] CRG-FAME mode d'emploi <http://www.esrf.eu/files/live/sites/www/files/UsersAndScience/Experiments/CRG/BM30B/ModeOp.pdf> last accessed on 27.12.2018.
- [122] W. Sturhahn and V. Kohn, *Hyperfine Interactions* **123/124**, 367 (1999).
- [123] T. Toellner, *Hyperfine Interactions* **125**, 3 (2000).

-
- [124] J. Liu, M. Krautz, K. Skokov, T. G. Woodcock, and O. Gutfleisch, *Acta Materialia* **59**, 3602 (2011).
- [125] F. Wang, J. Zhang, Y.-F. Chen, G.-J. Wang, J.-R. Sun, S.-Y. Zhang, and B.-G. Shen, *Physical Review B* **69** (2004).
- [126] H. Wakabayashi, T. Goto, K. Fukamichi, and H. Komatsu, *Journal of Physics: Condensed Matter* **2**, 417 (1990).
- [127] S. I. Makarov, M. Krautz, S. Salamon, K. Skokov, C. S. Teixeira, O. Gutfleisch, H. Wende, and W. Keune, *Journal of Physics D: Applied Physics* **48**, 305006 (2015).
- [128] B. D. Cullity and C. D. Graham, *Introduction to Magnetic Materials* (John Wiley & Sons, Inc., 2009).
- [129] A. Terwey, M. E. Gruner, W. Keune, J. Landers, S. Salamon, B. Eggert, K. Ollefs, V. Brabänder, I. Radulov, K. Skokov, M. Y. Hu, J. Zhao, E. E. Alp, C. Giacobbe, O. Gutfleisch, and H. Wende, (2019), submitted to *Physical Review B*.
- [130] E. Lovell, L. Ghivelder, A. Nicotina, J. Turcaud, M. Bratko, A. D. Caplin, V. Basso, A. Barcza, M. Katter, and L. F. Cohen, *Physical Review B* **94** (2016).
- [131] B. Fultz, *Progress in Materials Science* **55**, 247 (2010).
- [132] L. Hung and T. Yildirim, *Physical Review B* **97**, 224501 (2018).
- [133] F. Körmann, Y. Ikeda, B. Grabowski, and M. H. F. Sluiter, *npj Computational Materials* **3** (2017).
- [134] O. Delaire, M. S. Lucas, J. A. Muñoz, M. Kresch, and B. Fultz, *Physical Review Letters* **101** (2008).
- [135] M. S. Lucas, J. A. Muñoz, O. Delaire, N. D. Markovskiy, M. B. Stone, D. L. Abernathy, I. Halevy, L. Mauger, J. B. Keith, M. L. Winterrose, Y. Xiao, M. Lerche, and B. Fultz, *Physical Review B* **82**, 144306 (2010).
- [136] O. Delaire, K. Marty, M. B. Stone, P. R. C. Kent, M. S. Lucas, D. L. Abernathy, D. Mandrus, and B. C. Sales, *Proceedings of the National Academy of Sciences* **108**, 4725 (2011).
- [137] U. Hannemann, J. Lyubina, M. P. Ryan, N. M. Alford, and L. F. Cohen, *Europhysics Letters* **100**, 57009 (2012).

- [138] F. Baudelet, S. Pascarelli, O. Mathon, J. P. Itié, A. Polian, M. d' Astuto, and J. C. Chervin, *Journal of Physics: Condensed Matter* **17**, S957 (2005).
- [139] G. A. Waychunas, M. J. Apter, and G. E. Brown, *Physics and Chemistry of Minerals* **10**, 1 (1983).
- [140] F. de Groot, G. Vankó, and P. Glatzel, *Journal of Physics: Condensed Matter* **21**, 104207 (2009).
- [141] M.-A. Arrio, S. Rossano, C. Brouder, L. Galois, and G. Calas, *Europhysics Letters* **51**, 454 (2000).
- [142] H. Wende, Z. Li, A. Scherz, G. Ceballos, K. Baberschke, A. Ankudinov, J. J. Rehr, F. Wilhelm, A. Rogalev, D. L. Schlage, and T. A. Lograsso, *Journal of Applied Physics* **91**, 7361 (2002).
- [143] M. S. S. Brooks, O. Eriksson, and B. Johansson, *Journal of Physics: Condensed Matter* **1**, 5861 (1989).
- [144] H. Yamada and M. Shimizu, *Journal of Physics F: Metal Physics* **15**, L175 (1985).
- [145] F. Wilhelm, P. Pouloupoulos, H. Wende, A. Scherz, K. Baberschke, M. Angelakeris, N. K. Flevaris, and A. Rogalev, *Physical Review Letters* **87** (2001).
- [146] F. Klose, O. Schulte, F. Rose, W. Felsch, S. Pizzini, C. Giorgetti, F. Baudelet, E. Dartyge, G. Krill, and A. Fontaine, *Physical Review B* **50**, 6174 (1994).
- [147] F. Rose, O. Schulte, P. Schaaf, W. Lohstroh, and W. Felsch, *Applied Physics A Materials Science & Processing* **63**, 183 (1996).
- [148] L. Sève, N. Jaouen, J. M. Tonnerre, D. Raoux, F. Bartolomé, M. Arend, W. Felsch, A. Rogalev, J. Goulon, C. Gautier, and J. F. Bézar, *Physical Review B* **60**, 9662 (1999).
- [149] E. A. Tereshina, O. Isnard, A. Smekhova, A. V. Andreev, A. Rogalev, and S. Khmelevskiy, *Physical Review B* **89** (2014).
- [150] Y. Shao, B. Lu, M. Zhang, and J. Liu, *Acta Materialia* **150**, 206 (2018).
- [151] R. Kurian, K. Kunnus, P. Wernet, S. M. Butorin, P. Glatzel, and F. M. F. de Groot, *Journal of Physics: Condensed Matter* **24**, 452201 (2012).
- [152] S. Eisebitt, T. Böske, J.-E. Rubensson, and W. Eberhardt, *Physical Review B* **47**, 14103 (1993).

-
- [153] F. de Groot, *Coordination Chemistry Reviews* **249**, 31 (2005).
- [154] G. van der Laan, *Physical Review B* **57**, 5250 (1998).
- [155] J. J. Rehr, J. J. Kas, F. D. Vila, M. P. Prange, and K. Jorissen, *Physical Chemistry Chemical Physics* **12**, 5503 (2010).
- [156] B. Ravel and M. Newville, *Physica Scripta* , 1007 (2005).
- [157] B. Ravel 'Demeter'-Program Package for X-Ray Absorption Analysis <https://bruceravel.github.io/demeter/> last accessed 22.01.2019.
- [158] D. C. Koningsberger and R. Prins, in *Chemical Analysis*, Vol. 92, edited by J. Windefordner (John Wiley and Sons, 1988).
- [159] M. Newville, *Journal of Physics: Conference Series* **430**, 012007 (2013).
- [160] S. I. Zabinsky, J. J. Rehr, A. Ankudinov, R. C. Albers, and M. J. Eller, *Physical Review B* **52**, 2995 (1995).
- [161] A. Ankudinov and J. J. Rehr, *Physical Review B* **52**, 10214 (1995).
- [162] A. V. Poiarkova and J. J. Rehr, *Physical Review B* **59**, 948 (1999).
- [163] B. Ravel, *Journal of Synchrotron Radiation* **8**, 314 (2001).
- [164] C. M. Pillich, *Lokale strukturelle Untersuchungen an magnetokalorischem La(Fe, Si, Mn)₁₃*, Master's thesis, Universität Duisburg-Essen (2019).
- [165] M. Newville 'Larch' Data Analysis Tools for X-ray spectroscopy <https://xrappy.github.io/xraylarch/> last accessed 22.01.2019.
- [166] R. S. Preston, S. S. Hanna, and J. Heberle, *Physical Review* **128**, 2207 (1962).
- [167] B. Krumme, *Einfluss von Unordnung und Grenzflächen auf elektronische und magnetische Eigenschaften von Heusler-Systemen*, Ph.D. thesis, Universität Duisburg-Essen (2012).
- [168] F. Stromberg, *Mössbauerspektroskopische Untersuchung von Struktur und Magnetismus der austauschgekoppelten Schichtsysteme Fe/FeSn₂ und Fe/FeSi/Si und des ionenimplantierten verdünnten magnetischen Halbleiters SiC(Fe)*, Ph.D. thesis, Universität Duisburg-Essen (2009).
- [169] K. Trunov, M. Walterfang, W. Keune, N. Utochkina, and A. Trunova, *Thin Solid Films* **516**, 6205 (2008).

- [170] G. A. Pasquevich, P. M. Zélis, M. B. F. van Raap, and F. H. Sánchez, *Physica B: Condensed Matter* **354**, 369 (2004).
- [171] Z. Gercsi, *Europhysics Letters* **110**, 47006 (2015).
- [172] E. Wohlfarth and K. Buschow, eds., *Handbook of Magnetic Materials*, Vol. 5 (ELSEVIER LTD, 1990).
- [173] K. H. J. Buschow, *Handbook of Magnetic Materials*, Vol. 15 (NORTH HOLLAND, 2003).
- [174] T. Krenke, *Untersuchung der martensitischen Umwandlung und der magnetischen Eigenschaften mangan-reicher Ni-Mn-In und Ni-Mn-Sn-Heusler-Legierungen*, Ph.D. thesis (2007), duisburg, Essen, Univ., Diss., 2007.
- [175] I. Vincze, D. Kaptás, T. Kemény, L. F. Kiss, and J. Balogh, *Physical Review Letters* **73**, 496 (1994).
- [176] F. Wang, G. Wang, F. Hu, A. Kurbakov, B. Shen, and Z. Cheng, *Journal of Physics: Condensed Matter* **15**, 5269 (2003).
- [177] F. Wang, Y.-F. Chen, G.-J. Wang, and B.-G. Shen, *Journal of Physics D: Applied Physics* **36**, 1 (2002).
- [178] C. Cannas, A. Musinu, G. Piccaluga, D. Fiorani, D. Peddis, H. K. Rasmussen, and S. Mørup, *The Journal of Chemical Physics* **125**, 164714 (2006).
- [179] U. von Hörsten 2017 Pi Program Package www.uni-due.de/hm236ap/hoersten/home.html last accessed 22.01.2019.
- [180] J. Neuhaus, M. Leitner, K. Nicolaus, W. Petry, B. Hennion, and A. Hiess, *Physical Review B* **89** (2014).
- [181] M. Kresch, *Temperature Dependence of Phonons in Elemental Cubic Metals Studied by Inelastic Scattering of Neutrons and X-Rays*, Ph.D. thesis, California Institute of Technology (2009).
- [182] H. Hasegawa, M. W. Finnis, and D. G. Pettifor, *Journal of Physics F: Metal Physics* **15**, 19 (1985).
- [183] R. Boehler and J. Ramakrishnan, *Journal of Geophysical Research* **85**, 6996 (1980).

List of Figures

2.1. Schematic of a magnetocaloric cooling cycle	10
2.2. Magnetization and Entropy versus temperature at a Second Order Phase Transition.	12
2.3. Magnetization and Entropy versus temperature at a First Order Phase Transition.	13
2.4. Ordered $\text{La}(\text{Fe}, \text{Si})_{13}$ unit cell containing 112 atoms.	15
2.5. Reduced ordered unit cell of $\text{La}(\text{Fe}, \text{Si})_{13}$ in a <i>fcc</i> basis containing 28 atoms.	16
2.6. Reduced ordered unit cell of $\text{LaFe}_{11.5}\text{Si}_{1.5}\text{H}_{1.5}$ on <i>fcc</i> basis with interstitial hydrogen.	17
2.7. Schematic depiction of X-ray attenuation according to Lambert Beer law.	18
2.8. XMCD effect at the $L_{2,3}$ -edges.	21
2.9. Integrated whiteline intensity for sum rule analysis.	22
2.10. Amplitude modulation of the X-ray absorption coefficient.	24
2.11. Decay scheme of ^{57}Co to ^{57}Fe	25
2.12. Relative absorption probability of a γ -photon.	26
2.13. Influence of hyperfine interactions on the Mössbauer transmission spectra.	28
2.14. Relative absorption intensities, A_{23} ratio, dependent on incident γ -photon direction.	29
2.15. Schematic of phonon annihilation and creation in a NRIXS process.	31
3.1. Schematic of a synchrotron radiation facility.	36
3.2. Experimental setup at the ID12 beam line, ESRF.	37
3.3. Experimental setup at the beam line BM30b, ESRF.	38
3.4. Experimental setup at the beam line 3-ID, APS.	39
3.5. Experimental setup of the transmission Mössbauer experiments.	41
4.1. Temperature dependent magnetometry of $\text{La}(\text{Fe}, \text{Si}, \text{Mn})_{13}$ from Mn 0-1.	44
4.2. All transition temperatures of $\text{La}(\text{Fe}, \text{Si}, \text{Mn})_{13}$ from Mn 0-1.	46
4.3. Field dependent magnetometry measurements in $\text{LaFe}_{1.6-x}\text{Si}_{1.4}\text{Mn}_x$	47
4.4. $M(T)$ measurements on enriched NRIXS samples.	48

4.5. Shift of transition temperature with rising magnetic fields in the NRIXS samples.	49
4.6. HR-PXRD measurements on $\text{LaFe}_{11.4}\text{Si}_{1.6}\text{H}_{1.6}$	50
5.1. Fe-partial VDOS of $\text{LaFe}_{11.6}\text{Si}_{1.4}$, $\text{LaFe}_{11.4}\text{Si}_{1.5}\text{Mn}_{0.1}$ (green line), hydrogenated $\text{LaFe}_{11.4}\text{Si}_{1.6}\text{H}_{1.6}$ and $\text{LaFe}_{11.4}\text{Si}_{1.5}\text{Mn}_{0.1}\text{H}_{1.6}$	52
5.2. VDOS of $\text{LaFe}_{11.4}\text{Si}_{1.5}\text{Mn}_{0.1}$ and $\text{LaFe}_{11.4}\text{Si}_{1.6}\text{H}_{1.6}$ each compared to $\text{LaFe}_{11.6}\text{Si}_{1.4}$	54
5.3. VDOS in FM and PM phase of $\text{LaFe}_{11.4}\text{Si}_{1.6}\text{H}_{1.6}$	55
5.4. VDOS in FM and PM state of (a) $\text{LaFe}_{11.4}\text{Si}_{1.5}\text{Mn}_{0.1}$ (b) $\text{LaFe}_{11.4}\text{Si}_{1.5}\text{Mn}_{0.1}\text{H}_{1.6}$	57
5.5. Temperature series of the VDOS across the phase transition in $\text{LaFe}_{11.4}\text{Si}_{1.6}\text{H}_{1.6}$	58
5.6. Temperature series of the VDOS across the phase transition in (a) $\text{LaFe}_{11.4}\text{Si}_{1.5}\text{Mn}_{0.1}$ and (b) $\text{LaFe}_{11.4}\text{Si}_{1.5}\text{Mn}_{0.1}\text{H}_{1.6}$	59
5.7. Lattice entropy of $\text{LaFe}_{11.4}\text{Si}_{1.6}\text{H}_{1.6}$ across the phase transition.	60
5.8. Vibrational specific heat in $\text{LaFe}_{11.4}\text{Si}_{1.6}\text{H}_{1.6}$ across the phase transition.	62
5.9. Vibrational entropy of $\text{LaFe}_{11.4}\text{Si}_{1.6}\text{H}_{1.6}$ from $g(E)$ and from Θ_{DB}	64
5.10. (a) Θ_{DB} and (b) f_{LM} over temperature in $\text{LaFe}_{11.4}\text{Si}_{1.6}\text{H}_{1.6}$	65
5.11. S_{lat} of $\text{LaFe}_{11.4}\text{Si}_{1.5}\text{Mn}_{0.1}$ across the phase transition.	67
5.12. Temperature evolution of the VDOS of $\text{LaFe}_{11.4}\text{Si}_{1.5}\text{Mn}_{0.1}$	68
5.13. S_{lat} in $\text{LaFe}_{11.4}\text{Si}_{1.5}\text{Mn}_{0.1}\text{H}_{1.6}$ across the phase transition.	69
5.14. Comparison of the VDOS in hydrogenated $\text{LaFe}_{11.5}\text{Si}_{1.5}\text{H}_{1.5}$ with element-resolved DFT calculations.	70
5.15. Spin-resolved element- and site-resolved electronic DOS of hydrogenated $\text{LaFe}_{11.5}\text{Si}_{1.5}\text{H}_{1.5}$ in its FM and PM state.	72
5.16. Site resolved entropy difference over temperature and plotted against site projected minority spin channel at Fermi level from DFT calculations.	73
5.17. Temperature dependence of XANES and XMCD at Fe K-edge of $\text{LaFe}_{11.6}\text{Si}_{1.4}$	79
5.18. Comparison of the evolution of the XMCD and the XAS with rising temperature in $\text{LaFe}_{11.4}\text{Si}_{1.6}$ at the Fe K-edge.	80
5.19. Comparison of the structural transition (XAS) and the magnetic FOPT in $\text{LaFe}_{11.4}\text{Si}_{1.6}$	81
5.20. Change of the XAS and XMCD with rising Mn content in $\text{LaFe}_{11.6-x}\text{Si}_{1.4}\text{Mn}_x$ at the Fe K-edge.	83
5.21. Pre-edge XAS and XMCD versus Mn content.	84
5.22. XMCD of FOPT in $\text{La}(\text{Fe},\text{Si},\text{Mn})_{13}$	86

5.23. XANES and XMCD of $\text{LaFe}_{11.6-x}\text{Si}_{1.6}\text{Mn}_x$ at La $L_{2,3}$ -edges.	88
5.24. XANES and XMCD of $\text{LaFe}_{11.6-x}\text{Si}_{1.4}\text{Mn}_x$ at La $L_{2,3}$ -edges with and with- out background correction.	90
5.25. Whiteline intensity at the La $L_{2,3}$ -edges vs. Mn content.	91
5.26. Branching ratio at the La $L_{2,3}$ -edges.	92
5.27. Step functions used for sum rule analysis, depicted for $\text{LaFe}_{11.4}\text{Si}_{1.6}$ at the L_3 -edge.	93
5.28. Induced magnetic spin and orbital moments at the La $L_{2,3}$ -edges calculated via sum rule analysis	94
5.29. (a) Total magnetic moment μ_{La} in dependence of the Mn content. (b) Comparison of μ_{La} to Fe K-edge XMCD.	96
5.30. XANES and XMCD at the La $L_{2,3}$ -edges in $\text{LaFe}_{11.6}\text{Si}_{1.4}$ in the FM and PM phase.	97
5.31. XANES and XMCD at the La $L_{2,3}$ -edges of (a) $\text{LaFe}_{11.6}\text{Si}_{1.4}$ and (b) $\text{LaFe}_{11.3}\text{Si}_{1.4}\text{Mn}_{0.3}$	99
5.32. Absorption and Fourier transform of $\text{LaFe}_{11.6}\text{Si}_{1.4}$ at the La L_3 -edge.	102
5.33. EXAFS and Fourier transform of $\text{LaFe}_{11.6-x}\text{Si}_{1.4}\text{Mn}_x$	104
5.34. Absorption and EXAFS in FM and PM phase of $\text{LaFe}_{11.6}\text{Si}_{1.6}$ at the Fe K-edge.	105
5.35. Fourier transform at the La L_3 -, Fe K- and Mn K-edges in the FM and PM phase for no and high Mn content.	107
5.36. Absorption in FM phase of $\text{LaFe}_{11.6-x}\text{Si}_{1.4}\text{Mn}_x$ at the La L_3 -edge	109
5.37. Comparison of the EXAFS and Fourier transform in the FM phase for low and high Mn content.	110
5.38. Absorption in FM phase of $\text{LaFe}_{11.4}\text{Si}_{1.6}$ (black line) and $\text{LaFe}_{11.4}\text{Si}_{1.6}\text{H}_{1.6}$ at the La L_3 -edge	111
5.39. Comparison of the EXAFS and Fourier transform in the FM phase for low and high Mn content.	112
5.40. Crystal structures used for <i>FEFF</i> calculations.	114
5.41. Comparison experiment and <i>FEFF</i> at the La L_3 -edge.	115
5.42. Comparison experiment and <i>FEFF</i> at the Fe K-edge.	117
5.43. Comparison experiment and <i>FEFF</i> at the Mn K-edge.	118
5.44. <i>Larch</i> Fit at the La L_3 -edge with Si.	119
5.45. <i>Larch</i> fit at the La L_3 -edge in the FM and PM phase.	121
5.46. Evolution of the radial distance and static disorder with rising Mn content at the LA L_3 -edge.	122
5.47. <i>FEFF</i> calculation of the La L_3 -edge in the PM phase.	123

5.48. <i>Larch</i> fits to the first coordination shell at the Fe K-edge in the sample's FM state with all 4 paths and 9 surrounding atoms.	125
5.49. <i>Larch</i> fit at the Fe K-edge in the FM and PM phase.	126
5.50. <i>Larch</i> fit compared to the BFT at the Fe K-edge.	127
5.51. <i>Larch</i> fits at Mn K-edge.	128
5.52. <i>Larch</i> fit at the Fe K- and La L ₃ -edge in the FM phase with and without hydrogenation	130
5.53. Mössbauer spectra at RT, low temperature and in high magnetic field for Mn content 0 and 0.3	134
5.54. Mössbauer spectra at RT, low temperature and in high magnetic field for Mn content 0.6 and 1	135
5.55. Evolution of $\Delta\langle CS \rangle$ and ε with rising Mn content	137
5.56. Average magnetic hyperfine field in Magnetic moments of Fe and La in LaFe _{11.6-x} Si _{1.4} Mn _x	138
5.57. Hyperfine field distributions for main and secondary phases in samples with Mn contents 0, 0.3, 0.6 an 1.	140
5.58. Magnetic moments of Fe and La in LaFe _{11.6-x} Si _{1.4} Mn _x	142
5.59. Magnetization and magnetic Hyperfine field in LaFe _{11.6-x} Si _{1.4} Mn _x	143
5.60. Comparison of Fe magnetic moment with XMCD at Fe K-edge.	144
5.61. Canting angles in LaFe _{11.6-x} Si _{1.4} Mn _x from A ₂₃ -ratio.	146
5.62. M(H) in LaFe _{11.6-x} Si _{1.4} Mn _x	147
5.63. High field extrapolation of M(H) in LaFe _{11.6-x} Si _{1.4} Mn _x	148
A.1. M(T) LaFe _{11.6-x} Si _{1.4} Mn _x	155
A.2. M(H) curve with fit for α -Fe correction.	156
A.3. Correction of the EXAFS for α -Fe.	157
A.4. NRIXS raw data of LaFe _{11.4} Si _{1.6} H _{1.6}	158
A.5. Multi-phonon contributions in the VDOS	159
A.6. α -Fe correction of the VDOS	160
A.7. Entropy change in hydrogenated LaFe _{11.4} Si _{1.6} H _{1.6}	161
A.8. Quadratic background correction	165
A.9. XANES and XMCD of La(Fe,Si,Mn) ₁₃ in high magnetic fields.	166
A.10. Magnetic moments of La from sum rule analysis in high magnetic fields. . .	168
A.11. Schematic of the magnetic field relation in the Mössbauer measurement geometry.	169
A.12. Spin canting angles from law of cosines.	170
A.13. <i>FEFF</i> input file	172

List of Tables

2.1. Mössbauer transition probabilities and intensity ratio according to magnetic quantum numbers.	29
4.1. Sample list of all samples used within this work.	45
4.2. Sample list of $\text{LaFe}_{1.6-x}\text{Si}_{1.4}\text{Mn}_x$ EXAFS samples.	47
4.3. Sample list of NRIXS samples.	50
5.1. Thermodynamic Properties of $\text{LaFe}_{1.4}\text{Si}_{1.6}\text{H}_{1.6}$	63
5.2. List of Θ_{DB} in $\text{LaFe}_{1.4}\text{Si}_{1.6}\text{H}_{1.6}$	66
5.3. Sample list of XMCD experiments.	82
5.4. Magnetic moments of La with all sum rule analysis methods.	95
5.5. Parameters of the <i>FEFF</i> calculation	116
5.6. Extracted La-Fe distances R_{i-j} and static disorder parameter σ_{stat}^2 from the <i>Larch</i> fit at the La L_3 -edge for the first shell with $\Theta_{\text{DB}} = 370$ K in the FM and $\Theta_{\text{DB}} = 350$ K in the PM phase.	124
5.7. Extracted La-Fe next neighbor distances R_{i-j} and static disorder parameter σ_{stat}^2 from the <i>Larch</i> fit at the La L_3 -edge for the first and second shell with $\Theta_{\text{DB}} = 370$ K in the FM and $\Theta_{\text{DB}} = 350$ K in the PM phase.	124
5.8. Extracted next neighbor distances from the <i>Larch</i> fit at the first shell at the Fe K-edge with $\Theta_{\text{DB}} = 370$ K in the FM and $\Theta_{\text{DB}} = 350$ K in the PM phase.	127
5.9. Extracted next Mn-Fe next neighbor distances from the <i>Larch</i> fit to the first shell obtained from the Mn K-edge with $\Theta_{\text{DB}} = 370$ K in the FM and $\Theta_{\text{DB}} = 350$ K in the PM phase.	129
5.10. Extracted next neighbor distances from the <i>Larch</i> fit to the first shell at the Fe K-edge and two the first and second shell at the La L_3 -edge.	129
5.11. Center Line shift and Quadrupole splitting in $\text{La}(\text{Fe},\text{Si},\text{Mn})_{13}$	136
5.12. Average magnetic hyperfine field and Fe moment for various Mn contents.	139
5.13. Magnetic moments of Fe and La in $\text{LaFe}_{11.6-x}\text{Si}_{1.4}\text{Mn}_x$	143
5.14. Saturation Magnetization and canting angle in $\text{LaFe}_{11.6-x}\text{Si}_{1.4}\text{Mn}_x$	149

A.1. Fe-specific thermodynamic properties of $\text{LaFe}_{11.4}\text{Si}_{1.6}\text{H}_{1.6}$	162
A.2. Fe-specific thermodynamic properties of $\text{LaFe}_{11.4}\text{Si}_{1.5}\text{Mn}_{0.1}\text{H}_{1.6}$	163
A.3. Fe-specific thermodynamic properties of $\text{LaFe}_{11.4}\text{Si}_{1.5}\text{Mn}_{0.1}$	164
A.4. Magnetic moments of La from sum rule analysis in high magnetic fields. . .	168
A.5. Spin Canting angles in $\text{LaFe}_{11.6-x}\text{Si}_{1.4}\text{Mn}_x$ from $A_{2,3}$ -ratio.	170
A.6. Center line shift the quadrupole splitting in $\text{LaFe}_{11.6-x}\text{Si}_{1.6}\text{Mn}_x$	171

Abbreviations

APD - Avalanche Photo Diode

APS - Advanced Photon Source

DOS - Density Of States

DFT - Density Functional Theory

EFG - Electric Field Gradient

ESRF - European Synchrotron Radiation Facility

EXAFS - Extended X-ray Absorption Fine Structure

FM - Ferromagnetic

FT - Fourier Transform

FOPT - First Order Phase Transition

HR-PXRD - High Resolution Powder X-ray Diffraction

LINAC - Linear Accelerator

MCE - Magnetocaloric Effect

NRIXS - Nuclear Resonant Inelastic X-ray Scattering

PM - Paramagnetic

PPMS - Physical Property Measurement System

SG - Spin Glass

SOPT - Second Order Phase Transition

VDOS - Vibrational Density of States

VSM - Vibrating Sample Magnetometer

XANES - X-ray Absorption Near Edge Structure

XAS - X-ray Absorption Spectroscopy

XMCD - X-ray Magnetic Circular Dichroism

Acknowledgements

Here I would like to thank everyone who participated in this work.

First of all, I would like to thank **Prof. Dr. Heiko Wende** for giving me the opportunity to write my thesis in this workgroup.

Special thanks belongs to **Dr. Katharina Ollefs**, who not only participated nearly every synchrotron beamtime, but also had to cope with all the questions I had.

Many thanks to **Prof. Dr. Werner Keune**, who always had time for many of my questions and invaluable input concerning Mössbauer spectroscopy and NRIXS experiments. Thank you for all the important and fruitful discussions.

I would like to thank **Dr. Markus Gruner** for his theoretical input and the DFT calculations and all the discussions we had, which greatly contributed to this thesis.

Another big thanks belongs to **Prof. Dr. Oliver Gutfleisch**, **Dr. Konstantin Skokov**, **Dr. Iliya Radulov** and the Functional Materials Group from the TU Darmstadt for the sample preparation and the very successful collaboration.

Furthermore, I would like to thank **Dr. Joachim Landers**, **Dr. Soma Salamon** and **Benedikt Eggert** for the help and discussions concerning Mössbauer experiments and the beam times we had at the APS.

Another big thanks belongs to **Dipl. Ing. Ulrich von Hörsten** for all the help with the "Pi" program package, and all the technical assistance and support.

Thanks to **Cynthia Pillich** who joined me on a few beamtimes and participated in the EXAFS experiments and did many of the *FEFF* calculations. I would like to thank **Daniela Trienes** for the first Mössbauer experiments.

Another special thanks belongs to my office colleagues **Nico Rothenbach** and **Alexander Herman** who had to endure me during the writing phase and for all the discussions we had. Thanks to all the colleagues in the **AG Wende**, whom I did not mention specifically.

I would like to thank the team at the 3ID at the APS, **Dr. E. Ercan Alp**, **Dr. Michael J. Hu** and **Dr. Jiyong Zhao**, for the help during the NRIXS beamtimes, the team of the ID12 at the ESRF, **Dr. Andrei Rogalev**, **Dr. Fabrice Wilhelm** and **Dr. Amir Hen** for beamtime support during the XMCD experiments and **Dr. Mauro Rovezzi** from the BM30, ESRF, for all the help with the EXAFS experiments.

Thanks to **Dr. Carlotta Giacobbe** for the HR-PXRD measurement at the ESRF.

Thanks to everyone, who had the time to critically read this thesis and provided me with suggestions for improvement.

Special thanks belongs to all my friends, especially **Stella, Eltje, Dominik and Petros**, who really supported me on the last few meters.

At last, I would like to thank **my family** that is always there. Thank you for supporting me throughout my whole studies.

Funding by the DFG via the **SPP 1599, Ferroic Cooling** is gratefully acknowledged.